

**„Auf Kraft basierender Nachweis  
biomolekularer Wechselwirkung im Chipformat:  
Anwendung und Theorie des DNA-Kraftsensors“**



Dissertation der Fakultät für Physik  
der  
Ludwig-Maximilians-Universität München

vorgelegt von **Dominik Ho**  
aus Heidelberg

München, den 21. September 2009

Erstgutachter:

Prof. Dr. Hermann E. Gaub

Zweitgutachter:

Prof. Dr. Roland R. Netz (TU München)

Datum der mündlichen Prüfung:

21.10.2009

## INHALTSVERZEICHNIS

<b>Inhaltsverzeichnis</b>	<b>1</b>
<b>Zusammenfassung</b>	<b>2</b>
<b>1 Einleitung</b>	<b>4</b>
<b>2 Experimentelle Grundlagen</b>	<b>15</b>
2.1 Oberflächenfunktionalisierung	16
2.2 Kontakteinheit	18
2.3 Fluoreszenz und Datenanalyse	20
2.4 Fluidiksystem	23
<b>3 Theoretische Grundlagen</b>	<b>25</b>
<b>4 Nachweis von DNA·Ligand Wechselwirkungen</b>	<b>29</b>
<b>5 Nachweis von Aptamer·Ligand Wechselwirkungen</b>	<b>38</b>
<b>6 Nachweis von Membranproteinen auf lebenden Zellen</b>	<b>44</b>
<b>7 AD-Wandler molekularer Kräfte</b>	<b>51</b>
<b>8 Schlussbemerkung</b>	<b>56</b>
<b>Anhang</b>	<b>58</b>
A.1 Publikationen	58
P1 „Recognition of "Mirror-Image" DNA by Small Molecules.“	59
P2 „Quantitative Detection of Small Molecule/DNA Complexes Employing a Force-Based and Label-Free DNA-Microarray.“	67
P3 „DNA as a Force Sensor in an Aptamer-Based Biochip for Adenosine.“	83
A.2 Manuskripte	91
M1 „Force-driven separation of short double stranded DNA“	92
A.3 Publikationen unabhängig von der Dissertation	132
P4 „Tethering Forces of Secretory Granules Measured with Optical Tweezers.“	133
P5 „Photoactivated release of cargo from the cavity of polyelectrolyte capsules to the cytosol of cells.“	141
<b>Lebenslauf</b>	<b>145</b>
<b>Danksagung</b>	<b>147</b>

## ZUSAMMENFASSUNG

Die Sequenzierung des menschlichen Genoms lieferte eine Fülle von Informationen über bislang unbekannte Gene und damit assoziierte Proteine, die nicht nur für die molekularbiologische Forschung relevant sind, sondern auch direkt in der modernen Arzneimittelentwicklung, der klinischen Diagnostik sowie der Nahrungsmittel- und Umweltforschung Anwendung finden. Um dieser Menge an neuen Untersuchungsobjekten gerecht zu werden, sind Nachweisverfahren entwickelt worden, die es erlauben, in kurzer Zeit eine Vielzahl von Wechselwirkungen zwischen Molekülen aufzudecken. Herkömmlich wird dabei eines der beiden wechselwirkenden Moleküle (Analyt) direkt mit einer fluoreszierenden oder radioaktiven Markierung versehen. Solche Verfahren sind sehr sensitiv und lassen sich einfach in Hochdurchsatzformate wie beispielsweise einem Biochip implementieren. Eine Markierung birgt jedoch das Risiko in sich, die Funktion des Analyten zu beeinträchtigen. Deswegen wird mit hohem Aufwand die Erforschung und Entwicklung von alternativen Nachweisverfahren vorangetrieben, die zum einen markierungsfrei arbeiten und zum anderen hohe Durchsatzraten erreichen. Die vorliegende Dissertation befasst sich mit der Anwendung und der zugrunde liegenden Theorie einer auf Kraft basierenden Methode, die molekulare Wechselwirkungen auf einem Biochip mit Hilfe eines nur molekülgroßen DNA-Kraftsensors nachweist.

Die drei im Rahmen dieser Dissertation veröffentlichten Artikel befassen sich mit der Entwicklung einer Biochipplattform für den markierungsfreien Nachweis der Wechselwirkung doppelsträngiger DNA mit kleinen Molekülen, Peptiden sowie Proteinen. Das Prinzip des Nachweisverfahrens beruht auf der erhöhten Abrisskraft von doppelsträngiger DNA im gebundenen Zustand im Vergleich zum ungebundenen Zustand. Dies wird mit Hilfe eines auf dem Biochip integrierten DNA-Kraftsensors realisiert. Das Verfahren erlaubt den simultanen Nachweis vieler unterschiedlicher Wechselwirkungen in komplexen Medien wie beispielsweise Blut und ist auf Grund des auf Kraft basierenden Messprinzips spezifischer und sensitiver als konventionelle Biochiptechnologien.

Weiterhin wurde in einer noch nicht publizierten Arbeit die DNA-Kraftsensor-Plattform angewandt, um Zellmembranproteine auf lebenden Zellen nachzuweisen. Der Nachweis von Zellmembranproteinen ist ein wichtiger Vorgang in der Krebsforschung und Behandlung, um neue Biomarker oder Arzneimittelziele zu identifizieren oder um Tumore in histologischen Untersuchungen zu detektieren und klassifizieren. Das auf dem DNA-Kraftsensor basierende Nachweisverfahren verspricht erhöhte Sensitivität, erhöhte Spezifität

und den simultanen Nachweis vieler verschiedener Membranproteine. Erste Ergebnisse der beschriebenen Experimente werden in dieser Dissertation vorgestellt.

Ein Manuskript, welches derzeit den Peer-Review-Prozess durchläuft, befasst sich mit einer Theorie des kraftinduzierten Bindungsbruchs doppelsträngiger DNA. Diese wurde anhand der Kombination eines thermodynamischen Gleichgewichtsmodells und der kanonischen Übergangszustandstheorie entwickelt und durch kraftspektroskopische Einzelmolekülmessungen verifiziert. Die Theorie bietet die Grundlage einer theoretischen Beschreibung der DNA-Kraftsensor-Experimente.

Zuletzt wird im Rahmen dieser Dissertation sowohl das Konzept als auch erste experimentelle Ergebnisse eines auf dem DNA-Kraftsensor basierenden Analog-Digital-Wandlers vorgestellt. Mithilfe der mathematischen Hilfsmittel, die für den elektronischen Analog-Digital-Wandler entwickelt worden sind, soll es zukünftig möglich sein, die Abrisskraftverteilung unbekannter molekularer Wechselwirkungen anhand einer einzigen Biochipmessung zu rekonstruieren. Mittels konventioneller kraftspektroskopischer Messmethoden werden dafür bislang tausende Messungen benötigt.

## 1. EINLEITUNG

Ziel der Molekularbiologie ist es, biologische Prozesse auf der molekularen Ebene zu verstehen, um ausgehend von diesen Erkenntnissen, Störungen der molekularen Abläufe mittels Arzneimitteln gezielt zu korrigieren und Krankheiten zu heilen [1]. Untersuchungsobjekte sind biologische Einheiten wie Proteine und DNA sowie deren dynamisches Wechselspiel. Der Begriff Molekularbiologie selbst wurde von dem englischen Physiker und Molekularbiologen William T. Astbury geprägt und folgendermaßen definiert:

*"[...] not so much a technique as an approach, an approach from the viewpoint of the so-called basic sciences with the leading idea of searching below the large-scale manifestations of classical biology for the corresponding molecular plan. It is concerned particularly with the forms of biological molecules and [...] is predominantly three-dimensional and structural - which does not mean, however, that it is merely a refinement of morphology. It must at the same time inquire into genesis and function."*

Einen Meilenstein der Molekularbiologie stellt die Fertigstellung der Sequenzierung des kompletten menschlichen Genoms im Jahre 2003 dar [2]. Aus den daraus gewonnenen Informationen lässt sich ableiten, dass das menschliche Genom etwa 20.000-25.000 verschiedene Gene besitzt [3]. Da einerseits ein Gen häufig mehr als ein Protein kodiert und andererseits es zu posttranskriptionellen Modifikationen kommt, wird die Anzahl der im menschlichen Körper existierenden Proteine viel höher geschätzt. Allein die Anzahl der im *International Protein Index* [4] gelisteten Proteine ist aktuell bereits bei über 84.000 [5]. Die Molekularbiologie studiert Form, Ursprung und insbesondere Funktion dieser Einheiten. Dies bewerkstellt sie anhand eines reduktionistischen Paradigmas [6]. Einzelne Einheiten, von denen bekannt ist, dass sie miteinander wechselwirken, werden isoliert und vom Ensemble der restlichen Zellmoleküle getrennt untersucht. Die eingesetzten Technologien sind beispielsweise Kristallographie [7], Einzelmolekülfloreszenz [8] [9] und Einzelmolekülkraftspektroskopie [10] [11] [12]. Am Anfang der meisten funktionellen und strukturellen Untersuchungen steht jedoch der Nachweis einer Wechselwirkung zwischen zwei Biomolekülen.

Der Nachweis von Wechselwirkungen zwischen Biomolekülen ist nicht nur für die Molekularbiologie, sondern auch für die moderne Arzneimittelentwicklung, die klinische Diagnostik sowie die Nahrungsmittel- und Umweltforschung ein grundlegender Prozess. Der Entwicklung und Anwendung von bioanalytischen

Verfahren wird dementsprechend eine hohe Bedeutung beigemessen. Gegenwärtig wird die Bioanalytik durch verschiedene Ziele vorangetrieben: darunter sind die Analyse von extrem kleinen Probenvolumina, der simultane Nachweis von riesigen Bibliotheken von Aktivitäten und die Entwicklung von Nachweisverfahren, die ohne Markierung des Analyten auskommen [13]. Biochip Formate liefern hierbei einen signifikanten Vorteil für die ersten beiden genannten Ziele, denn auf jedem einzelnen dieser Chips können auf engstem Raum sehr viele unterschiedliche Biomoleküle (Sonden) räumlich getrennt, aber dicht nebeneinander aufgebracht werden. Probenmaterial wird auf den Biochip gegeben und spezifisch mit den Sonden wechselwirkende Moleküle bleiben an dem jeweiligen Ort der Sonde haften und können dann mittels verschiedenster Techniken nachgewiesen werden. Dies erlaubt es, mit geringstem Probenvolumen zahlreiche unterschiedliche Wechselwirkungen in nur einer einzigen Messung zu identifizieren.

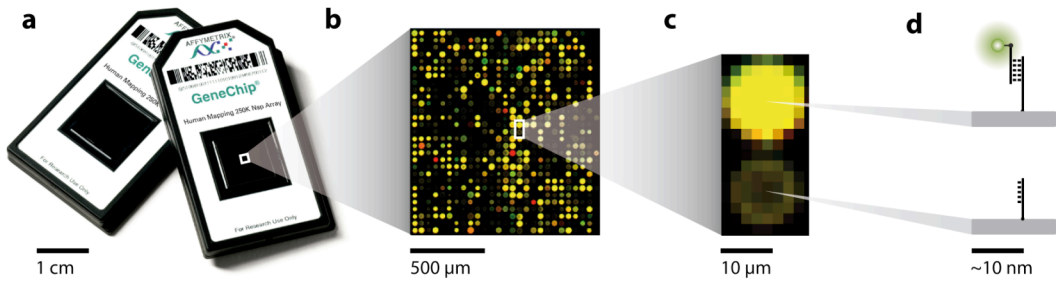


**Abbildung 1.** (a) Kommerziell verfügbarer DNA-Biochip der Firma Affymetrix. Auf einem typischen DNA-Biochip sind örtlich getrennt DNA-Oligonukleotide unterschiedlicher Basensequenz aufgebracht (DNA-Sonden). In diesem Beispiel besitzt der „GeneChip“ eine Dichte von etwa 40.000 DNA-Punkte/cm<sup>2</sup> und ermöglicht die Identifikation von RNA-Transkripten in Zellproben. Die Proben-DNA wird fluoreszenzmarkiert auf den DNA-Biochip aufgebracht. Proben-DNA, welche komplementär zu den an der Oberfläche befestigten DNA-Sonden ist, hybridisiert und wird anschließend mittels Fluoreszenzmikroskopie quantifiziert, um beispielsweise die Genexpression einer bestimmten zellulären Aktivität zu charakterisieren. (b) Ausschnitt eines Fluoreszenzbildes der Biochipoberfläche nach der Inkubation mit einer Probe verschiedener DNA-Oligonukleotide. (c) Dieses Bild zeigt eine nochmals vergrößerte Fluoreszenzaufnahme zweier DNA-Punkte. Der obere DNA-Punkt leuchtet hell, während der untere DNA-Punkt keine nennenswerte Fluoreszenz aufweist. Das heißt, dass der Komplementärstrang zu den oberen DNA-Sonden in signifikanter Menge in der Probe vorlag. Dagegen war der Komplementärstrang zu den unteren DNA-Sonden nur in geringfügiger Menge in der Probe vorhanden. (d) Schematische Zeichnung der molekularen Wechselwirkung. Oben hat ein Komplementärstrang an die DNA-Sonde gebunden, unten nicht.

Den ersten Biochip entwickelten Fodor und Kollegen bereits 1991 [14]. Ein solcher Chip hatte Dichten von etwa 100.000 unterschiedlichen, räumlich getrennten DNA-Punkte/cm<sup>2</sup> und ermöglichte die simultane Erkennung von transkribierter RNA in Zellproben mittels Fluoreszenz [15]. In den letzten Jahren wurde diese Technologie immer weiter vorangetrieben und mittlerweile sind DNA-Biochips mit mehreren Millionen von Sonden-DNAs kommerziell verfügbar [16]. Der durchschlagende Erfolg der DNA-nachweisenden Biochips trieb auch die Entwicklung analoger Biochips voran, welche Wechselwirkungen zwischen Peptiden, Proteinen, Kohlenhydraten sowie kleinen Molekülen nachweisen. Jedoch hat sich die Entwicklung dieser konzeptionell nahezu identischen Technologien als sehr viel schwieriger herausgestellt und eine breite Kommerzialisierung findet noch nicht statt [17]. Die technologischen Schwierigkeiten resultieren vor allem aus einer Ursache: während verschiedene DNA-Moleküle - unabhängig von der Sequenz - ein uniformes Erscheinungsbild teilen, unterscheiden sich insbesondere Proteine in Molekulargewicht, Faltung, Ladung und Stabilität. Dies erschwert die Herstellung geeigneter Oberflächen, die

die Adsorption aller Arten von Proteinen universell reduzieren. Daraus resultiert folgendes Problem: Proteine in Lösung komplexer Zusammensetzung adsorbieren unspezifisch an der Oberfläche [18] [19] [20] [21]. Dies führt zu einem Hintergrundsignal, weil konventionelle Biochip- Nachweismethoden [22], die beispielsweise auf Fluoreszenz [23], Oberflächenplasmonenresonanz [24] oder MALDI-TOF (Matrix Assisted Laser Desorption/Ionisation – Time of Flight) [25] basieren, prinzipiell nur die Präsenz eines Wechselwirkungspartners an der Biochipoberfläche nachweisen und nicht die Wechselwirkung selbst. Um unspezifisch adsorbierte und spezifische Wechselwirkungen unterscheiden zu können, bedarf es einer Methode, welche die Wechselwirkung direkt nachweist und nicht nur die Präsenz von Biomolekülen nahe der Biochipoberfläche. Da molekulare Wechselwirkungen aus Kraftfeldern resultieren, bietet sich Kraft als experimentelle Observable an, um spezifische Wechselwirkung von nicht spezifischer zu unterscheiden.

Kraft ist der zugrunde liegende Faktor für das dynamische Zusammenspiel biologischer Einheiten wie Proteine und DNA [26]. Sie bestimmt nicht nur wie stark einzelne Moleküle [27] oder Zellen [28] aneinander haften, sondern sie wird auch in der Zelle aktiv erzeugt [29] oder sogar in biochemische Signale übersetzt, um biologische Prozesse zu regulieren [30]. Experimentell konnte dieser Parameter jedoch erst Anfang der 90er Jahre erschlossen werden. Pionierarbeit auf diesem Gebiet wurde durch die Gruppen von Carlos Bustamante [31], Steven Block [31] sowie Hermann E. Gaub [27] geleistet. In diesen Einzelmolekül-Kraftexperimenten kommen mikroskopische Kraftsensoren, darunter sowohl auslenkbare mikroskopische Kugeln in optischen [33] oder magnetischen [34] Fallen, biegsame Blattfedern [35] und Glasnadeln [36] als auch deformierbare künstliche Membranen [37] zum Einsatz. Der Kraftsensor wird über biotechnologische Methoden mit einem auf einer Oberfläche immobilisierten Biomolekül verbunden, um anschließend aktiv Kräfte auszuüben [27] [36] oder um passiv die Kraft von molekularen Motoren zu untersuchen [31].

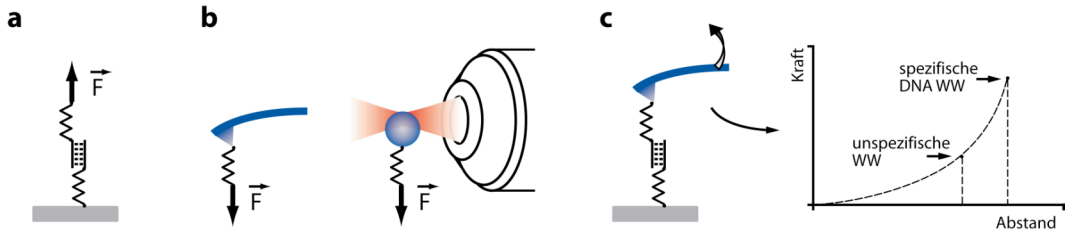


**Abbildung 2.** Prinzip einer DNA-Einzelmolekülkraftmessung. Die Wechselwirkung einer doppelsträngigen DNA-Wechselwirkung soll durch kraftspektroskopische Untersuchungen charakterisiert werden. Dazu wird einer der beiden komplementären DNA-Stränge auf einer Oberfläche und der andere an eine mikroskopische Feder über Polymerverbindungen, wie beispielsweise poly(ethylene glycol) (PEG), befestigt. (a) Werden Oberfläche und Feder separiert, baut sich eine Kraft in den Polymerverbindungen auf, bis sich die molekulare Bindung zwischen den beiden DNA-Strängen öffnet. Diese maximale Kraft wird als Abrisskraft bezeichnet. (b) Beispiele für mikroskopische Federn sind Mikrokugeln (rechts), die durch einen fokussierten Laserstrahl eingefangen sind, oder auch mikroskopisch kleine Blattfedern (links). Wird auf diese Federn eine Kraft ausgeübt, lenken sie sich proportional zur Kraft aus der Ruheposition aus. Die Auslenkung wird typischerweise über optische Verfahren ermittelt und dann auf einem Messrechner gespeichert. (c) Solche Experimente liefern für die Polymerbindung charakteristische Kraft-Abstandskurven. Ist die untersuchte Wechselwirkung tatsächlich eine DNA-DNA Wechselwirkung, das heißt spezifisch, so wird eine hohe Abrisskraft gemessen. Ist der DNA-Strang nur unspezifisch auf der Oberfläche adsorbiert, wird eine niedrige Abrisskraft gemessen.

Eine Vielzahl von Biomolekülen sequentiell auf einem Chip anzufahren und deren Wechselwirkung zu testen ist prinzipiell möglich, jedoch zeitaufwändig und technologisch sehr anspruchsvoll [38]. Um solch einen Prozess zu beschleunigen, entwickelte IBM die *Millipede* Technologie [39], eine Anordnung von tausenden miniaturisierten Blattfedern, welche ebenso viele Wechselwirkungen simultan nachweisen kann. Führen wir den Gedankengang der Miniaturisierung und Parallelisierung weiter, gelangen wir im Extremfall zu nur noch molekulargroßen Kraftsensoren. In der Tat hat die Natur solche funktionellen Einheiten bereits selbst hervorgebracht. Beispielsweise befinden sich Enzyme tief vergraben in globulären Proteinen, die erst dann aktiviert werden, wenn eine Kraft größer als ein bestimmter Schwellwert ausgeübt worden ist und dadurch das globuläre Protein teilweise entfaltet wurde [10] [30]. Solch ein biomolekularer Kraftsensor unterscheidet sich in seiner Funktionsweise grundlegend von den oben vorgestellten nanotechnologischen Methoden. Während die Nanotechnologie federwaagenähnliche Aufbauten benutzt (Abbildung 3a, 3b), um absolute Kräfte zu messen (Abbildung 3c), entspricht das Konzept des biomolekularen Kraftsensors einer Balkenwaage (Abbildung 3d). Liegt die angelegte Kraft unter einem Schwellwert (Referenz) passiert nichts. Übersteigt sie diesen Schwellwert

wird eine chemische Reaktion katalysiert und beispielsweise ein Genregulationspfad aktiviert. Dass solch ein Konzept auch für auf Kraft basierenden Biochips nutzbar ist, zeigten zum ersten Mal Christian Albrecht und Kollegen im Jahr 2003 [40]. Zwei doppelsträngige DNA-Einheiten wurden mittels biotechnologischer Methoden in Serie zwischen zwei Oberflächen eingespannt, so dass sich bei der Separation der Oberflächen genau einer der beiden Doppelstränge öffnet (Abbildung 3e). Experimentell wird das Resultat des Experiments über die Lokalisation des farbstoffmarkierten Verbindungsstücks zwischen der untersuchten Bindung und Referenzbindung, die im Folgenden als DNA-Kraftsensor bezeichnet wird, bestimmt (Abbildung 3f). Die benötigten Öffnungs- oder Abrisskräfte der beiden DNA-Stränge werden also direkt miteinander verglichen. Werden zwei identische DNA-Doppelstränge miteinander verglichen ist die Wahrscheinlichkeit der beiden Endzustände gleich groß. Werden zwei unterschiedliche DNA-Doppelstränge verglichen ist die Symmetrie des Experiments gebrochen und die Wahrscheinlichkeit höher, dass die Fluoreszenzmarkierung auf der Seite der stärkeren Bindung anstatt auf der Seite der schwächeren Bindung verbleibt. Dieser Prozess verhält sich wie eine 1-bit Analog-Digital-Wandlung, welche durch thermische Fluktuationen verschmiert ist. Zur Erhöhung der Aussagekraft der Messung werden daher viele identisch präparierte Einzelmolekülexperimente simultan zwischen den beiden Oberflächen durchgeführt. Das Zählen der Fluoreszenzmarkierung auf jeder Seite, beispielsweise mittels Einzelmolekülfloreszenz, liefert ein quantitatives Ergebnis für den Vergleich der Abrisskräfte der beiden molekularen Bindungen. Äquivalente Informationen bieten die Fluoreszenzintensitäten pro Flächeneinheit, welche proportional zu der Dichte der Fluoreszenzmarkierungen sind.

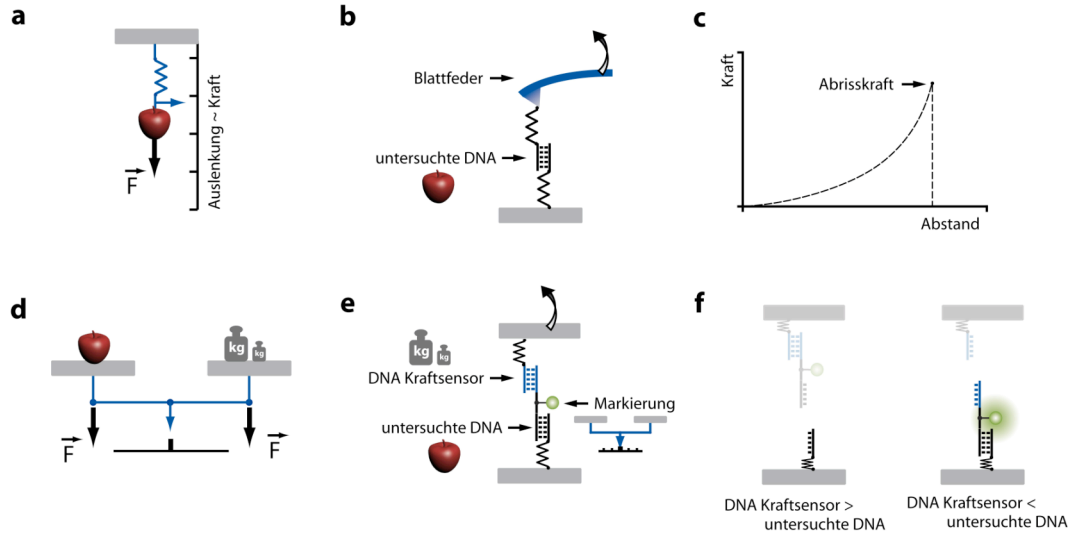


**Abbildung 3.** Vergleich zwischen dem Messprinzip einer Federwaage und einer Balkenwaage. (a) Bei einer Federwaage wird die zu messende Kraft an einen elastischen Kraftsensor angelegt. Die Auslenkung des Kraftsensors ist normalerweise proportional zur Kraft und eine einzelne Eichmessung reicht aus, um den dazugehörigen Proportionalitätsfaktor zu bestimmen und eine unbekannte angelegte Kraft (Gewichtskraft Apfel) absolut zu beziffern. (b) Konventionelle Einzelmolekulkraftmessungen wie die hier dargestellte Kraftmessung an einem DNA-Doppelstrang mittels einer Blattfeder folgen diesem Messprinzip. (c) Das Messergebnis ist eine Kraft-Abstandskurve. (d) Bei einer Balkenwaage wird eine unbekannte Kraft (Gewichtskraft Apfel) direkt mit einer bekannten Kraft (Gewichtskraft Referenz) verglichen. Die bekannte Kraft wird solange erhöht oder erniedrigt bis die Balkenwaage ausgeglichen ist. Die unbekannte Kraft entspricht dann der eingestellten Kraft. (e) Das Messprinzip der Balkenwaage wurde von Albrecht und Kollegen [40] bereits auf Einzelmolekülmessungen angewandt. Zwei DNA-Doppelstränge werden in Serie über lange Polymer Verbindungsstücke zwischen zwei Oberflächen eingespannt. Der eine der beiden DNA-Doppelstränge entspricht der untersuchten DNA-Bindung und der andere dem DNA-Kraftsensor (Referenz). Die beiden Oberflächen werden separiert und die schwächere der beiden Bindungen reißt ab. (f) Das Messergebnis lässt sich über den fluoreszenzmarkierten Verbindungsstrang ermitteln. Ist die Abrisskraft des DNA-Kraftsensors höher als die der untersuchten Bindung verbleibt der fluoreszenzmarkierte Strang auf der Seite des DNA-Kraftsensors. Ist die Abrisskraft der untersuchten DNA höher als die des DNA-Kraftsensors, so verbleibt der fluoreszenzmarkierte Strang auf der Seite der untersuchten Bindung.

Der DNA-Kraftsensor ist in einer Reihe von Anwendungen zum Einsatz gekommen. Darunter befinden sich der Nachweis einzelner Nukleotid-Polymorphismen [40], der Vergleich verschiedener Antikörper-Antigen-Wechselwirkungen [41], das Verhindern von Kreuzreaktionen auf ELISA-Sandwich-Biochips [42], die Untersuchung molekularen Bindungsbruchs in Serie [43] und die Untersuchung des Entbindungsverlaufs kurzer doppelsträngiger DNA [44].

Zentrales Thema der vorliegenden Dissertation ist der auf Kraft basierende Nachweis von Wechselwirkungen zwischen doppelsträngiger DNA und kleinen Molekülen, Peptiden und Proteinen. Hierbei kommt das von Albrecht und Kollegen entwickelte Biochip-Format zum Einsatz, das die Öffnungskraft zweier DNA-Doppelstränge direkt miteinander vergleicht [40]. Bindet ein Molekül an einen der beiden Stränge, so wird dieser in der Regel stabilisiert. Vergleicht man nun die Abrisskraft der beiden Doppelstränge, indem sie in Serie zwischen zwei Oberflächen eingespannt werden und die Oberflächen trennt, so wird erwartet, dass der Doppelstrang ohne gebundenes Molekül mit einer erhöhten Wahrscheinlichkeit reißt. Das experimentelle Resultat spiegelt sich in der Verteilung der Verbindungsstücke auf den beiden Oberflächen wieder, die mittels Fluoreszenz nachgewiesen werden. Der Wechselwirkungsnachweis erfolgt ohne Markierung des Analyten und ist auf Kraft basierend, weshalb unspezifisch auf der Biochipoberfläche adsorbierte Moleküle das Messergebnis nicht beeinflussen. Dies erlaubt es, Messungen auch an komplexen molekularen Proben wie beispielsweise an Blut oder Urin durchzuführen.

Im Einzelnen untersuchten wir mit Hilfe des DNA-Kraftsensors das chirale [P1] und sequenzspezifische Bindeverhalten [P2] von Pyrrole-Imidazole-Polyamiden an doppelsträngiger DNA. Weiterhin demonstrierten wir den Nachweis von Adenosinen mittels eines aus zwei Untereinheiten bestehenden DNA-Aptamers [P3]. Um die DNA-Kraftsensor-Experimente besser beschreiben und vorhersagen zu können, erarbeiteten wir eine theoretische Beschreibung des DNA-Bindungsbruchs [M1]. Erste Ergebnisse liegen für die Untersuchung von Zellrezeptor-Ligand-Wechselwirkungen sowie eines molekularen Analog-Digital-Kraftsignalwandlers bereits vor.

## Literaturverzeichnis Kapitel 1.

- [1] Morange, M. 2000. A History of Molecular Biology. Harvard University Press, Cambridge.
- [2] The Human Genome Project. 2003. <http://genomics.energy.gov/>.
- [3] Claverie, J. 2005. Fewer Genes, More Noncoding RNA. *Science*. 309:1529-1530.
- [4] Kersey, P., J. Duarte, A. Williams, Y. Karavidopoulou, E. Birney, and R. Apweiler. 2004. The International Protein Index: An integrated database for proteomics experiments. *Proteomics*. 4:1985-1988.
- [5] International Protein Index: Statistics Page. 2009. <http://www.ebi.ac.uk/IPI/IPIhuman.html/>.
- [6] Hull, D. L., and M. Ruse. 2007. The Cambridge Companion to the Philosophy of Biology. Cambridge University Press, Cambridge.
- [7] Gaffney, K. J., and H. N. Chapman. 2007. Imaging Atomic Structure and Dynamics with Ultrafast X-ray Scattering. *Science*. 316:1444-1448.
- [8] Eggeling, C., C. Ringemann, R. Medda, G. Schwarzmann, K. Sandhoff, S. Polyakova, V. N. Belov, B. Hein, C. v. Middendorff, A. Schönle, and S. W. Hell. 2008. Direct observation of the nanoscale dynamics of membrane lipids in a living cell. *Nature*. 457:1159-1163.
- [9] Liu, S., E. Abbondanzieri, J. Rausch, S. Grice, and X. Zhuang. 2008. Slide into Action: Dynamic Shuttling of HIV Reverse Transcriptase on Nucleic Acid Substrates. *Science* 322:1092-1097.
- [10] Puchner, E. M., A. Alexandrovich, A. L. Kho, U. Hensen, L. V. Schäfer, B. Brandmeier, F. Gräter, H. Grubmüller, H. E. Gaub, and M. Gautel. 2008. Mechanoenzymatics of titin kinase. *Proc. Natl. Acad. Sci. USA*. 105:13385-90.
- [11] Guydosh, N. R., and S. Block. 2009. Direct observation of the binding state of the kinesin head to the microtubule. *Nature*. in press.
- [12] Hodges, C., L. Bintu, L. Lubkowska, M. Kashlev, and C. Bustamante. 2009. Nucleosomal Fluctuations Govern the Transcription Dynamics of RNA Polymerase II. *Science*. 325:626-628
- [13] Gurard-Levin, Z. A., and M. Mrksich. 2008. Combining Self-Assembled Monolayers and Mass Spectrometry for Applications in Biochips. *Annu. Rev. Anal. Chem.* 1:767-800.
- [14] Fodor, S. P., J. L. Read, M. C. Pirrung, L. Stryer, A. T. Lu, and D. Solas, 1991. Light-directed, spatially addressable parallel chemical analysis. *Science*. 251:767–773.
- [15] Schena, M., D. Shalon, R. W. Davis, and P. O. Brown. 1995. Quantitative monitoring of gene-expression patterns with a complementary-DNA microarray. *Science* 270:467–70.
- [16] Haushalter RC. 2004. Method for in situ, on-chip chemical synthesis. U.S. Patent No. 20040175710.
- [17] Bodovitz, S., T. Joos, J. Bachmann. 2005. Protein biochips: the calm before the storm. *Drug Discovery Today*. 10:283-287.

- [18] Mrksich, M., G. B. Sigal, and G. M. Whitesides. 1995. Surface-plasmon resonance permits in-situ measurement of protein adsorption on self-assembled monolayers of alkanethiolates on gold. *Langmuir*. 11:4383–85.
- [19] Tengvall, P., I. Lundstrom, B. Liedberg. 1998. Protein adsorption studies on model organic surfaces: an ellipsometric and infrared spectroscopic approach. *Biomaterials* 19:407–22
- [20] Elwing, H. 1998. Protein absorption and ellipsometry in biomaterial research. *Biomaterials* 19:397–406
- [21] Margel, S., E. A. Vogler, L. Firment, T. Watt, S. Haynie, and D. Y. Sogah. 1993. Peptide, protein, and cellular interactions with self-assembled monolayer model surfaces. *J. Biomed. Mater. Res.* 27:1463–76.
- [22] Weinberger, S. R., T. S. Morris, and M. Pawlak. 2000. Recent trends in protein biochip technology. *Pharmacogenomics*. 1:395-416.
- [23] Kopf, E., D. Zharhary. 2007. Antibody arrays-An emerging tool in cancer proteomics. *Int. J. Biochem. Cell Biol.* 39:1305-1317.
- [24] Boozer, C., G. Kim, S. Cong, H. Guan, and T. Londergan. 2006. Looking towards label-free biomolecular interaction analysis in a high-throughput format: a review of new surface plasmon resonance technologies. *Curr. Opin. Cell Biol.* 17: 400-405.
- [25] Min, D. H., J. Su, and M. Mrksich. 2004. Profiling kinase activities by using a peptide chip and mass spectrometry. *Angew. Chem. Int. Edit.* 43:5973–5977.
- [26] Stone, A. J. 1997. The theory of intermolecular forces. Oxford University Press, Oxford.
- [27] Florin, E. L., V. T. Moy, and H. E. Gaub. 1994. Adhesion forces between individual ligand-receptor pairs. *Science*. 264:415-417.
- [28] Benoit, M., D. Gabriel, G. Gerisch, and H. E. Gaub. 2000. Discrete interactions in cell adhesion measured by single-molecule force spectroscopy. *Nat. Cell Biol.* 2:313-317.
- [29] Du Roure, O., A. Saez, A. Buguin, and R. H. Austin. 2005 Force mapping in epithelial cell migration. *Proc. Natl. Acad. Sci. USA*. 102:2390-2395.
- [30] Vogel, V., and M. Sheetz. 2006. Local force and geometry sensing regulate cell functions. *Nat. Rev. Mol. Cell Biol.* 7:265-275.
- [31] Smith, S., L. Finzi, and C. Bustamante. 1992. Direct mechanical measurements of the elasticity of single DNA molecules by using magnetic beads. *Science* 258:1122-1126.
- [32] Svoboda, K., and S. M. Block. 1994. Force and velocity measured for single kinesin molecules. *Cell*. 7:773-794.
- [33] Neuman, K. C., and S. M. Block. 2004. Optical trapping. *Rev. Sci. Instrum.* 75:2787-2809.
- [34] Gosse, C., and V. Croquette. 2008. Magnetic Tweezers: Micromanipulation and Force Measurement at the Molecular Level. *Biophys. J.* 82:3314-3329.
- [35] Zlatanova, J., S. M. Lindsay, and S. H. Leuba. 2000. Single molecule force spectroscopy in biology using the atomic force microscope. *Prog. Biophys. Mol. Biol.* 74:37–61.

- [36] Cluzel, P., A. Lebrun, C. Heller, R. Lavery, J. Viovy, D. Chatenay and F. Caron. 1996. DNA: an extensible molecule. *Science* 271:792-794.
- [37] Evans, E., K. Ritchie, and R. Merkel. 1995. Sensitive force technique to probe molecular adhesion and structural linkages at biological interfaces. *Biophys. J.* 68:2580–2587.
- [38] Kufer, S. K., E. M. Puchner, H. Gumpf, T. Liedl, and H. E. Gaub 2008. Single-Molecule Cut-and-Paste Surface Assembly. *Science* 319:594-596.
- [39] Vettiger, P., G. Cross, M. Despont, U. Drechsler, U. Durig, B. Gotsmann, W. Haberle, M. A. Lantz, H. E. Rothuizen, R. Stutz, and G. K. Binnig. The "millipede" - nanotechnology entering data storage. *IEEE Transactions on Nanotechnology*. 1:39-55.
- [40] Albrecht, C., K. Blank, M. Lalic-Multhaler, S. Hirler, T. Mai, I. Gilbert, S. Schiffmann, T. Bayer, H. Clausen-Schaumann, and H. E. Gaub. 2003. DNA: a programmable force sensor. *Science*. 301:367-370.
- [41] Blank, K., A. Lankenau, T. Mai, S. Schiffmann, I. Gilbert, S. Hirler, C. Albrecht, M. Benoit, H. E. Gaub, and H. Clausen-Schaumann. 2004. Double-chip protein arrays: force-based multiplex sandwich immunoassays with increased specificity. *Anal. Bioanal. Chem.* 379:974-981.
- [42] Blank, K., T. Mai, I. Gilbert, S. Schiffmann, J. Rankl, R. Zivin, C. Tackney, T. Nicolaus, K. Spinnler, F. Oesterhelt, M. Benoit, H. Clausen-Schaumann, and H. E. Gaub. 2003. A force-based protein biochip. *Proc. Natl. Acad. Sci. USA*. 100:11356-11360.
- [43] Neuert, G., C. H. Albrecht, and H. E. Gaub. 2007. Predicting the Rupture Probabilities of Molecular Bonds in Series. *Biophys. J.* 93:1215-1223.
- [44] Albrecht, C., G. Neuert, R. Lugmaier, and H. E. Gaub. 2008. Molecular Force Balance Measurements Reveal that Double-Stranded DNA Unbinds Under Force in Rate-Dependent Pathways. *Biophys. J.* 94:4766-4774.

## 2. EXPERIMENTELLE GRUNDLAGEN

Die in den nächsten Kapiteln beschriebenen Experimente laufen im Wesentlichen sehr ähnlich ab [1] [2]. Viele identische Einzelmolekülexperimente werden zwischen zwei Oberflächen präpariert. Jedes einzelne Konstrukt besteht aus einer Kette von zwei molekularen Bindungen, in der Regel DNA-Wechselwirkungen, die über lange, inerte Polymere zwischen den beiden Oberflächen eingespannt ist. Separiert man die beiden Oberflächen, baut sich eine Kraft in den Polymeren auf, die gleichzeitig auch auf die molekularen Bindungen wirkt, bis sich eine der beiden molekularen Bindungen öffnet [3] [4]. Experimentell lässt sich bestimmen, welche der beiden Bindungen sich geöffnet hat, indem der Ort des Verbindungsstücks bestimmt wird. Dies ist ohne großen Aufwand mittels einer Fluoreszenzmarkierung zu bewerkstelligen. Da es sich bei einem molekularen Bindungsbruch um einen thermisch aktivierten Prozess handelt [5], ist das Resultat des Experiments nicht determiniert. Wird das Experiment einige Male wiederholt, so wird - gerade wenn die beiden Bindungen sehr ähnlich sind - eine Verteilung der beiden möglichen Endzustände erwartet. Daher ist es zwingend notwendig, eine ausreichende Statistik zu generieren, indem das Einzelmolekülexperiment häufig wiederholt wird oder, wie in unserem Fall, eine Vielzahl identischer Experimente simultan durchgeführt wird. Dazu werden viele Kopien des gleichen Einzelmolekülexperiments zwischen zwei Oberflächen präpariert. Die Oberflächen werden anschließend separiert und mittels Fluoreszenz ausgelesen. Eine der Oberflächen ist ein konventioneller Glasträger, während die andere Oberfläche aus PDMS besteht und einem elastischen Stempel ähnelt.

Dieses Kapitel beschreibt in Kürze folgende Komponenten des Experiments: (1) die Oberflächenfunktionalisierung; (2) die Kontakteinheit, welche die beiden kongruenten Oberflächen zusammenführt und separiert; (3) den Fluoreszenzaufbau und die Datenanalyse; (4) das Fluidiksystem, das es erlaubt, auf einem Chip an verschiedenen Punkten unterschiedliche Probenflüssigkeiten aufzubringen. Eine ausführlichere Diskussion der verwendeten Protokolle und Materialen findet sich in den publizierten Manuskripten [P1] [P2] [P3] [2] und der Diplomarbeit von Philip Severin [6].

## 2.1. Oberflächenfunktionalisierung

**Biochip.** Der Biochip besteht aus einem konventionellen Glasträger auf dem, in unserem Fall, bis zu sechzehn verschiedene Funktionalisierungen in einer vier-mal-vier-Anordnung aufgebracht werden (Abbildung 4d). Jede dieser Funktionalisierungen besteht aus zwei in Serie aufgebauten DNA-Bindungen, **1·2** und **2·3** (Abbildung 4f). Das **1** Ende ist fest mit der Oberfläche verankert, während das **3** Ende frei in Richtung Lösung zeigt. Mit Hilfe von Standardprotokollen lässt sich der aminofunktionalisierte DNA-Oligomer **1** auf den aldehydfunktionalisierten Glasträger lokalisiert anbringen. Dann wird ein Komplementärstrang **2** an den immobilisierten DNA-Strang **1** hybridisiert. **2** besitzt einen einzelsträngigen Überlapp, der es wiederum erlaubt, den zu **2** komplementären DNA-Oligomer **3** an **2** zu hybridisieren. Es entstehen also Ketten von insgesamt drei Biomolekülen, die auf dem Glasträger immobilisiert sind. Das freie Ende von **3** ist mit einer Biotin-Gruppe funktionalisiert und erlaubt im weiteren Verlauf des Experiments eine Kraft an der Kette **1·2·3** anzulegen. **2** ist mit einer Fluoreszenzmarkierung versehen, die es dann ermöglicht, zu bestimmen, ob sich die **1·2** oder die **2·3** Bindung geöffnet hat. Über die Fluoreszenzmarkierung wurde auch eine Oberflächendichte von einer **1·2·3** Kette/100 nm<sup>2</sup> auf dem Biochip ermittelt (Abbildung 4e).

**Stempel.** Der elastische Stempel besteht aus einem quervernetzten Polymer. Poly(dimethylsiloxane) wird zusammen mit einem Quervernetzer in eine eigens hergestellte Gussform gefüllt und über Nacht ausgehärtet [7]. Anschließend wird das PDMS aus der Gussform genommen und in Stücke geschnitten, so dass jedes Stück vier-mal-vier zylinderförmige Noppen vorweist (Abbildung 4a). Auf den Kontaktflächen dieser Noppen befindet sich eine Mikrostruktur von siebenunddreißig um 5 µm erhöhte 100 µm x 100 µm große Quader (Abbildung 4b). Diese erlauben beim Kontaktieren und Separieren der beiden Oberflächen den Ein- und Abfluss der umgebenden Flüssigkeit. Die Kontaktfläche wird mit einem Epoxysilan beschichtet und über dieses mit poly(ethylene glycol) Polymeren funktionalisiert. Das Ende der PEG-Polymeren ist mit einer Biotin-Gruppe versehen, über welche multivalentes Streptavidin angebunden wird (Abbildung 4c). Dies ermöglicht im späteren Verlauf des Experiments, die **1·2·3** Ketten zwischen Biochip und Stempel einzuspannen.

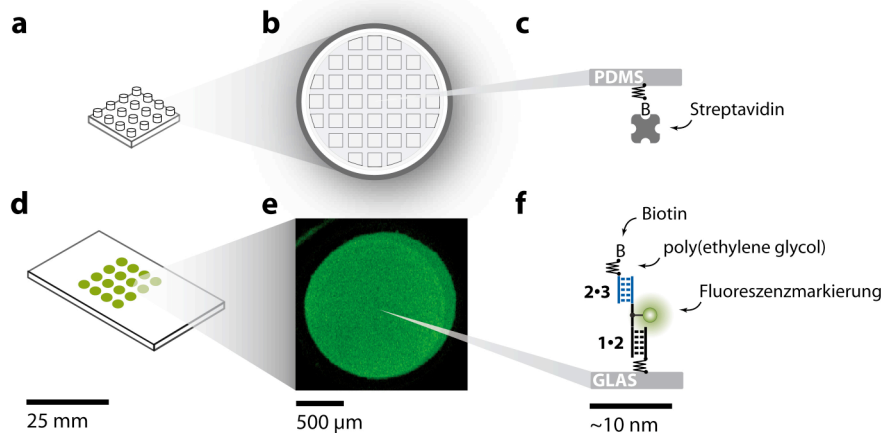


**Abbildung 4.** (a) Der PDMS-Stempel, wie er bei den beschriebenen Experimenten zum Einsatz kommt, hat vier-mal-vier zylindrische Noppen. (b) Auf den Kontaktflächen dieser Noppen befindet sich eine Mikrostruktur von siebenunddreißig um 5 µm erhöhte 100 µm x 100 µm große Quader. (c) Die Oberfläche ist mit poly(ethylene glycol) Polymeren functionalisiert, die an ihrem freien Ende eine Biotinmodifikation besitzen, über welche multivalentes Streptavidin angebunden wird. (d) Der Biochip ist analog zum Stempel in einer vier-mal-vier-Anordnung mit DNA-Punkten functionalisiert. (e) Jeder DNA-Punkt ist zwischen 1 mm und 1,5 mm groß. (f) Schematische Darstellung des DNA-Konstrukts. Zwei DNA-Bindungen sind über poly(ethylene glycol) Verbindungen in Serie an den Biochip gebunden. Normalerweise ist die **1·2** DNA-Bindung die untersuchte Bindung, während die **2·3** DNA-Bindung die Funktion des DNA-Kraftsensors übernimmt.

## 2.2. Kontakteinheit

Im Verlauf eines DNA-Kraftsensor-Experiments wird der - wie oben beschrieben -beschichtete Biochip und der PDMS-Stempel kontrolliert zusammengeführt und wieder separiert. Dafür wurde eigens eine Kontakteinheit gebaut, die auf einem invertierten Epifluoreszenzmikroskop montiert ist (Abbildung 5a). Der Biochip wird mittels Magneten auf einer Edelstahlplatte fixiert. Diese kann mittels Steppermotoren (Abbildung 5c) relativ zum Mikroskop in x- und y-Richtung bewegt werden, um mit hoher Vergrößerung alle Bereiche des Biochips abzufahren und Fluoreszenzbilder aufzunehmen. Über der Edelstahlplatte ist ein Glasblock montiert, welcher sowohl über einen Steppermotor als auch einen Piezo relativ zu der Edelstahlplatte in z-Richtung bewegt werden kann. An den Glasblock wird der PDMS-Stempel angebracht (Abbildung 5d). Biochip und Stempel werden von Hand aufeinander ausgerichtet, so dass die vier-mal-vier Noppen des Stempels genau über den vier-mal-vier Punkten auf dem Biochip liegen und die beiden Oberflächen parallel zueinander ausgerichtet sind. Die parallele Ausrichtung erfolgt dabei anhand von Interferenzmustern, die über Reflektions-Interferenz-Kontrast-Mikroskopie beobachtet werden [8]. Anschließend werden die Oberflächen mit Hilfe des Steppermotors und des Piezos kontrolliert zusammengeführt und zehn Minuten in Kontakt inkubiert, damit sich Biotin·Streptavidin Bindungen ausbilden können, welche die 1·2·3 Ketten zwischen dem Biochip und dem Stempel einspannen. Daraufhin werden die beiden Oberflächen mit konstanter Geschwindigkeit, die zwischen 10 nm/s und 10 µm/s liegt, separiert. Prinzipiell muss jetzt nur noch gezählt werden wie viele Verbindungsstücke **2** auf dem Biochip und dem Stempel zurückbleiben, um die relative Stabilität der beiden Bindungen zu bestimmen. Dies erfolgt anhand von Fluoreszenzaufnahmen.

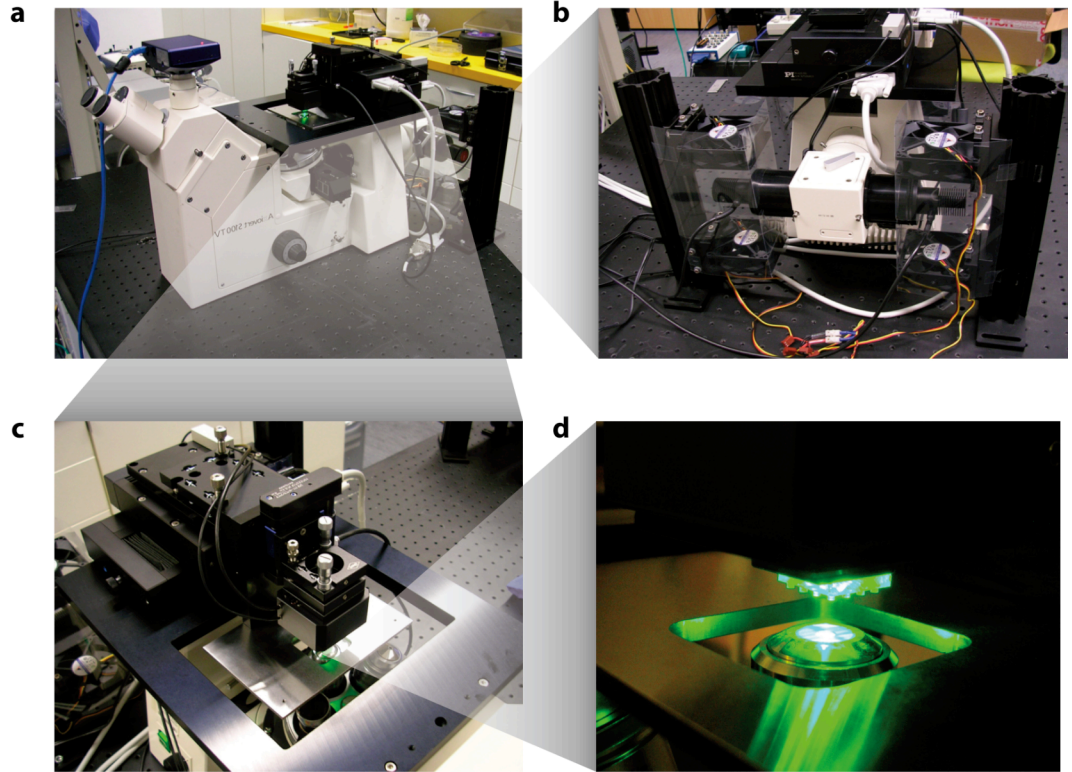


**Abbildung 5.** Kontakteinheit. (a) Die Kontakteinheit ist auf ein Epifluoreszenzmikroskop montiert. (b) Die Beleuchtungsquellen des Epifluoreszenzmikroskops sind zwei luftgekühlte LEDs. (c) Auf einer Edelstahlplatte lässt sich der Biochip über Magneten fixieren. Diese kann mittels Steppermotoren relativ zum Mikroskop in x- und y-Richtung bewegt werden, um mit hoher Vergrößerung alle Bereiche des Biochips abzufahren und Fluoreszenzbilder aufzunehmen. Über der Edelstahlplatte ist ein Glasblock montiert, welcher sowohl über einen Steppermotor als auch einen Piezo relativ zu der Edelstahlplatte in z-Richtung bewegt werden kann. (d) An den Glasblock wird der PDMS-Stempel angebracht.

### 2.3. Fluoreszenz und Datenanalyse

Während eines DNA-Kraftsensor-Experiments werden keine absoluten Kräfte aufgezeichnet wie es beispielsweise bei einem Blattfeder-Experiment der Fall ist. Die Kraftmessung geschieht inhärent durch den Vergleich einer zu untersuchenden molekularen Bindung **1·2** mit dem DNA-Kraftsensor **2·3** (Abbildung 6a). Physikalisch relevant ist daher das Verhältnis von gebrochenen **1·2** Bindungen zu gebrochenen **1·2** und **2·3** Bindungen. Diese beiden Zustände werden über den Ort des fluoreszenzmarkierten **2** Konstrukts ermittelt. Dazu können die einzelnen **2** Konstrukte mittels Einzelmolekülfloreszenz gezählt oder äquivalent die Fluoreszenzintensität pro Einheitsfläche betrachtet werden, welche proportional zur Anzahl der Fluoreszenzfarbstoffe pro Einheitsfläche ist [P2]. Einzige experimentelle Observable ist daher die Fluoreszenzintensität auf dem Biochip. Diese wird mittels eines invertierten Epifluoreszenzmikroskops oder mittels eines Biochip-Fluoreszenzscanners aufgezeichnet. In der Regel werden dazu drei Fluoreszenzbilder aufgenommen: ein Bild vor dem Kontakt, ein Bild nach dem Kontakt und ein Bild, in dem freie Biotine mit Hilfe von Streptavidin-AlexaFluor 647 (AF) angefärbt worden sind. Auf dem Bild vor dem Kontakt ist typischerweise ein homogener Fluoreszenzpunkt mit einem Durchmesser von etwa 1 mm zu sehen (Abbildung 6d). Das Bild nach dem Kontakt zeigt den gleichen Fluoreszenzpunkt mit dunklen, quadratischen Strukturen (Abbildung 6e). Diese resultieren aus dem Kontakt des mikrostrukturierten Stempels mit der Biochipoberfläche. Das letzte Bild zeigt die Biochipoberfläche nach der Inkubation mit AF, das spezifisch an nicht gebundene Biotin-Gruppen haftet (Abbildung 6f). Der letzte Schritt wird durchgeführt, weil die Konstrukte nach dem Experiment in drei verschiedenen Zuständen vorliegen. Entweder ist die **1·2** Bindung gebrochen (S1), oder es ist die **2·3** Bindung gebrochen (S2) oder das Konstrukt war überhaupt nicht über die Biotin-Streptavidin Bindung zwischen den beiden Oberflächen eingespannt (S0) (Abbildung 6c). Von Interesse sind in unseren Experimenten nur das Verhältnis gebrochener **2·3** Bindung (S2) zu allen Konstrukten, auf die eine Kraft ausgeübt worden ist (S1+S2). Nicht eingespannte Konstrukte (S0), die nicht an dem Experiment teilgenommen haben, können jedoch nicht von dem Fall einer gebrochenen **2·3** Bindung (S2) unterschieden werden, weil bei beiden Zuständen das fluoreszenzmarkierte **2** Konstrukt auf der Seite des Biochips verbleibt. In den hier durchgeföhrten Experimenten wurde der Anteil dieser Konstrukte abgezogen. Dazu wurde der Biochip nach der Aufnahme der ersten beiden Fluoreszenzbilder mit einem farbstoffmarkierten Streptavidin inkubiert. Dieses bindet die freien Biotin-Gruppen der nicht eingespannten Konstrukte und erlaubt die Bestimmung des Anteils der molekularen Ketten, auf die keine Kraft ausgeübt wurde (S0) (Abbildung 6d).

Für die eigentliche Berechnung der normalisierten Fluoreszenzverteilung wurden nur die letzten beiden Fluoreszenzbilder herangezogen, d.h. das Bild nach dem Stempelkontakt (Abbildung 6f) und das Bild nach der Inkubation mit farbstoffmarkiertem Streptavidin (Abbildung 6g). Das Fluoreszenzbild vor dem Stempelkontakt kann ebenfalls zur Analyse herangezogen werden, dient jedoch in allen im Anschluss gezeigten Experimenten nur als Kontrolle. Aus diesen beiden Bildern lassen sich für jedes quadratische Muster vier verschiedene gemittelte Fluoreszenzintensitäten bestimmen.  $Cy3_{Start}$  wird aus den nicht-kontaktierten Bereichen, die direkt an die quadratischen Flächen angrenzen, bestimmt.  $Cy3_{Rem}$  wird über die quadratischen Flächen selbst bestimmt. Analog werden  $AF_{Start}$  und  $AF_{Rem}$  aus dem zweiten Fluoreszenzbild ermittelt. Folgende Annahmen wurden getroffen, um die normalisierte Fluoreszenzverteilung zu bestimmen:

- $Cy3_{Start}$  und  $AF_{Start}$  weichen nur unwesentlich von der Fluoreszenzintensität der kontaktierten Fläche vor dem Kontakt ab.
- Die Fluoreszenzintensität pro Einheitsfläche ist proportional zur Anzahl der Farbstoffe pro Einheitsfläche.

Dadurch ergibt sich die normalisierte Fluoreszenzintensität folgendermaßen:

(Gleichung 1)

$$S0 = AF_{Ratio}$$

(Gleichung 2)

$$S1 = Cy3_{Ratio} - AF_{Ratio}$$

(Gleichung 3)

$$S2 = 1 - Cy3_{Ratio}$$

(Gleichung 4A, 4B)

$$Cy3_{Ratio} = \frac{Cy3_{Rem}}{Cy3_{Initial}}, AF_{Ratio} = \frac{AF_{Rem}}{AF_{Initial}}$$

$S0$ ,  $S1$  und  $S2$  sind normalisiert, so dass die Relation  $S0+S1+S2=1$  immer eingehalten wird. Wie oben definiert wird das normalisierte Fluoreszenzverhältnis (NF) durch die Anzahl der gebrochenen **2·3** Bindungen ( $S1$ ) geteilt durch die Anzahl aller Bindungen, auf die eine Kraft ausgeübt wurde, ( $S1+S2$ ) berechnet.

(Gleichung 5)

$$NF = \frac{S1}{S1 + S2} = \frac{Cy3_{Ratio} - AF_{Ratio}}{1 - AF_{Ratio}}$$

Das NF spiegelt direkt das Verhältnis der Abrisskräfte zwischen **1·2** und **2·3** wider und ist eine physikalische Messgröße, die einem Paar von molekularen Bindungen inhärent ist und nicht abhängig von der Anzahl der molekularen Ketten, auf die eine Kraft ausgeübt wurde. Deswegen sollte das NF nicht mit  $Cy3_{Ratio}$  verwechselt werden. Für ein Paar von molekularen Bindungen hängt dieser Wert von dem Anteil der zwischen den beiden Oberflächen eingespannten Bindungen ab, während das NF unabhängig davon ist.

Die in dieser Dissertation präsentierten NFs sind Mittelwerte von allen  $100 \mu\text{m} \times 100 \mu\text{m}$  großen Strukturen eines Experiments. Einen Messfehler von 0.018 ermittelten wir aus wiederholten Messungen an demselben **1·2 2·3** molekularen Bindungspaar bei gleich bleibenden experimentellen Bedingungen.

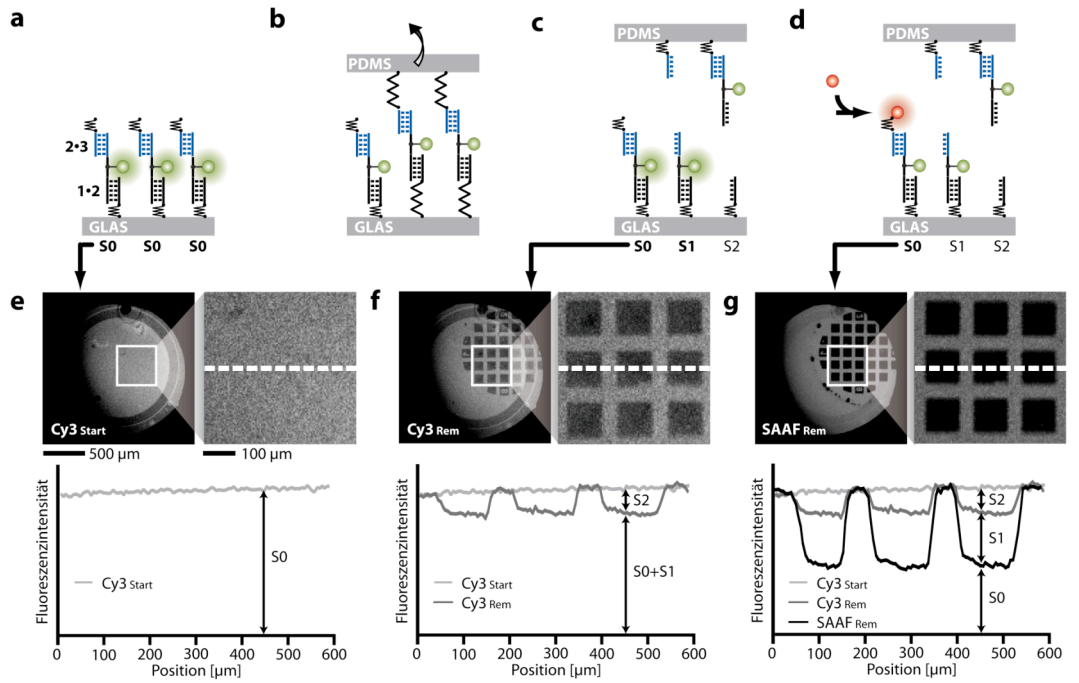


**Abbildung 6.** Schematische Darstellung eines DNA-Kraftsensor-Experiments. (a) Die zu untersuchende DNA-Bindung **1·2** und der DNA-Kraftsensor **2·3** sind in Serie und über PEG-Verbindungen an den Biochip gebunden. Der Zustand **1·2·3** wird fortan als **S0** bezeichnet. Der Streptavidin-funktionalisierten PDMS-Stempel wird an die Biochipoberfläche herangefahren. (b) Der Stempel koppelt an die 3 Oligomere über die Bildung eines Biotin-Streptavidin Komplexes. Die beiden Oberflächen werden separiert und eine Kraft baut sich in der **1·2·3** Kette auf, bis sich einer der beiden DNA-Komplexe öffnet. (c) Es liegen drei verschiedene Zustände vor. Entweder hat der Stempel nicht gekoppelt (**S0**), der DNA-Kraftsensor **2·3** hat sich geöffnet (**S1**), oder die zu untersuchende DNA-Bindung **1·2** hat sich geöffnet (**S2**). (d) Um den Zustand **S0** und **S1** über Fluoreszenz unterscheiden zu können, wird der Zustand **S0** mittels eines farbstoffmarkierten Streptavidin markiert, welches auf einer anderen Wellenlänge als der **2** Mittelstrang fluoresziert. (e) Fluoreszenz auf dem Biochip vor dem Kontakt. (f) Fluoreszenz auf dem Biochip nach dem Kontakt. Die quadratischen Muster resultieren aus der Mikrostruktur des PDMS-Stempels. (g) Fluoreszenz auf dem Biochip nach dem Kontakt und Inkubation mit fluoreszenzmarkiertem Streptavidin bei einer anderen Wellenlänge. Zusammen erlauben die drei Bilder die Bestimmung der Anteile der Zustände **S0**, **S1** und **S2** nach der Durchführung des Experiments.

## 2.4. Fluidiksystem

In Experimenten, in denen molekulare Wechselwirkungen zwischen DNA-bindenden Molekülen und einem DNA-Doppelstrang untersucht werden, ist es von Vorteil, das gleiche DNA-Konstrukt, bestehend aus **1·2** und **2·3** Bindung, an räumlich getrennten Punkten mit unterschiedlichen Konzentrationen des DNA-bindenden Moleküls zu inkubieren. Die jetzige Geometrie erlaubt die gleichzeitige Untersuchung von sechzehn DNA-Punkten auf einem Biochip (Abbildung 7a), weshalb wir im Rahmen dieser Doktorarbeit ein Fluidiksystem aufbauen, das es ermöglicht, die sechzehn verschiedenen DNA-Punkte auf dem Biochip mit sechzehn unterschiedlichen Konzentrationen des DNA-bindenden Konstrukts zu inkubieren (Abbildung 7b). Dafür wurden PDMS- Masken mit sechzehn Öffnungen so auf den Biochips platziert, dass die Öffnungen konzentrisch über den DNA-Punkten lagen. Mittels jeweils zwei Kanülen und zwei Peristaltikpumpenkanälen wurde zwischen 1 ml und 50 ml Lösung über jeden der DNA-Punkte gespült. Dadurch konnten komplette Titrationskurven anhand einer einzelnen DNA-Kraftsensor-Messung aufgenommen werden (Abbildung 7d). Aus solchen Titrationskurven lässt sich die für die untersuchte Wechselwirkung charakteristische Dissoziationskonstante  $K_D$  ermitteln.

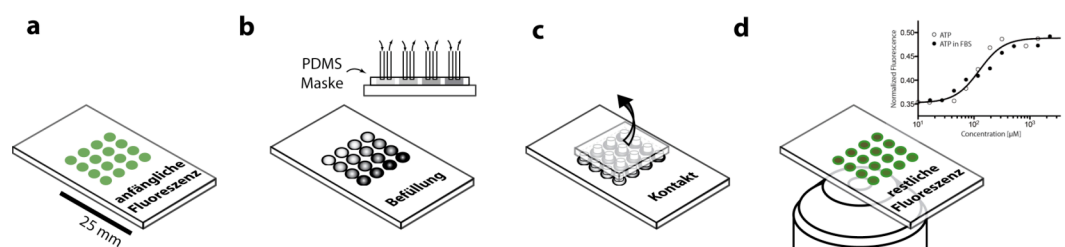


**Abbildung 7.** Ein Fluidiksystem wurde aufgebaut, um identische DNA-Punkte mit verschiedenen Proben zu inkubieren. (a) Die Fluoreszenz vor dem Experiment wird aufgenommen. (b) Eine PDMS-Maske mit vier-mal-vier Öffnungen wird auf den Biochip aufgelegt und erlaubt die Inkubation der sechzehn DNA-Punkte mit jeweils einer anderen Probenflüssigkeit. Die Fluidik wird über zwei Sechzehn-Kanal-Peristaltikpumpen getrieben. (c) Kontakt zwischen Biochip und PDMS-Stempel. (d) Auslesen der Fluoreszenz. Wurde beispielsweise das Bindeverhalten eines Moleküls an DNA anhand sechzehn verschiedener Konzentrationen des Binders untersucht, ergibt sich aus der Auswertung eines einzelnen Biochips bereits eine komplett Titrationskurve.

## Literaturverzeichnis Kapitel 2.

- [1] Albrecht, C., K. Blank, M. Lalic-Multhaler, S. Hirler, T. Mai, I. Gilbert, S. Schiffmann, T. Bayer, H. Clausen-Schaumann, and H. E. Gaub. 2003. DNA: a programmable force sensor. *Science*. 301:367-370.
- [2] Albrecht, C., H. Clausen-Schaumann, and H. E. Gaub. 2006. Differential analysis of biomolecular rupture forces. *J. Phys.: Condens. Matter*. 18:S581-S599
- [3] Strunz, T., K. Oroszlan, R. Schäfer and H. Güntherodt. 1999. Dynamic force spectroscopy of single DNA molecules. *Proc. Natl. Acad. Sci. USA*. 96:11277-11282.
- [4] Morfill, J., F. Kuhner, K. Blank, R. Lugmaier, J. Sedlmair and H. E. Gaub. 2007. B-S Transition in Short Oligonucleotides. *Biophys. J.* 93:2400-2409.
- [5] Evans, E. and K. Ritchie. 1997. Dynamic strength of molecular adhesion bonds. *Biophys. J.*, 72:1541-1555.
- [6] Severin, P., 2008. Hochparallelisierte Kraftmessungen von Protein-DNA Wechselwirkungen. Diplomarbeit.
- [7] Delamarche, M., and H. Biebuyck. 1997. Stability of molded polydimethylsiloxane microstructures. *Adv. Mater.* 9:741-746.
- [8] Wiegand, G., K. R. Neumaier and E. Sackmann. 1998. Microinterferometry: three-dimensional reconstruction of surface microtopography for thin-film and wetting studies by reflection interference contrast microscopy (RICM). *Applied Optics*, 37:6892-6905.

### 3. THEORETISCHE GRUNDLAGEN

Das folgende Kapitel befasst sich mit der theoretischen Beschreibung des DNA-Kraftsensors. Experimente, in denen zwei 15-45 basenpaarlange DNA-Doppelstränge in Serie über PEG-Polymeren zwischen zwei Oberflächen eingespannt werden, sind konzeptionell am einfachsten zu beschreiben. Die Separation der Oberflächen resultiert in einer Erhöhung des End-zu-End-Abstands des molekularen Konstrukts, bestehend aus den PEG-Verbindungen, der zu untersuchenden **1·2** DNA-Bindung sowie dem **2·3** DNA-Kraftsensor. Dadurch baut sich eine immer größer werdende Kraft auf, bis sich eine der beiden Bindungen öffnet (Abbildung 8). Theoretisch lässt sich die vorliegende Situation anhand einer gekoppelten Differentialgleichung formulieren [1]:

$$(Gleichung 1) \quad dS_0 = -(k_1(t) + k_2(t))S_0 dt$$

$$(Gleichung 2) \quad dS_1 = k_1(t) S_0$$

$$(Gleichung 3) \quad dS_2 = k_2(t) S_0,$$

wobei  $S_0$  der Anteil der **1·2·3** Zustände ist, der über die Raten  $k_1(t)$  und  $k_2(t)$  in die Zustände **1·2** ( $S_1$ ) und **1** ( $S_2$ ) übergeht (Abbildung 8). Die  $k_i(t)$  folgen aus kraftabhängigen Dissoziationsraten  $k_i(f)$  der molekularen Komplexe. Diese werden über die Kraft-Abstandsrelation  $f(x)$  und die Abstands-Zeitrelation  $x(t)$  in zeitabhängige Raten überführt. Die Kraft-Abstandsrelation  $f(x)$  erhält man aus bekannten Polymertheorien für PEG-Linker [2], ssDNA [3] und dsDNA [4] [5] [6].

$$(Gleichung 4) \quad f(x) = f_{PEG}(x) + f_{ssDNA}(x) + f_{dsDNA}(x)$$

Die Kraft-Zeitrelation ist durch das Experiment vorgegeben. Die Glas- und PDMS-Oberflächen werden mit konstanter Geschwindigkeit  $v$  separiert.

$$(Gleichung 5) \quad x(t) = v \cdot t$$

Mit Hilfe von Gleichung 4 und 5 lässt sich die kraftabhängige Rate  $k_i(f)$  folgendermaßen als zeitabhängige Rate umschreiben

$$(Gleichung 6) \quad k_i(t) = k_i(f(v \cdot t)).$$

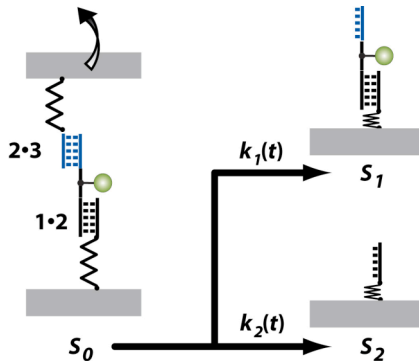


**Abbildung 8.** Herleitung der Differentialgleichung, die den Bindungsbruch in Serie beschreibt. Anfangs liegt der Zustand  $S_0$  vor. Zwei DNA- Bindungen, **1·2** und **2·3**, sind über PEG-Verbindung zwischen zwei Oberflächen eingespannt. Werden die beiden Oberflächen separiert, zerfällt der Zustand  $S_0$  über die Raten  $k_1(t)$  und  $k_2(t)$  in die beiden Zustände  $S_1$  und  $S_2$ . Das heißt entweder die **2·3** Bindung ( $S_1$ ) oder die **1·2** Bindung ( $S_2$ ) öffnet sich.

Ausgehend von diesem System gekoppelter Differentialgleichungen (Gleichung 1-3) lässt sich das Ergebnis des Kraftsensor-Experiments vorhersagen, falls die kraftabhängige Dissoziationsrate von doppelsträngiger DNA bekannt ist. Bislang wurde der DNA- Bindungsbruch in der Literatur nur phänomenologisch mittels des Bell-Evan Modells beschrieben [7] [8] [9] [10]. Dieses setzt ein harmonisches Bindungspotential voraus, aus dem eine dem Arrhenius-Gesetz folgende, thermisch aktivierte Dissoziation der Bindung über eine Potentialbarriere stattfindet. Das Bindungspotential verkippt durch eine äußere angelegte Kraft, so dass die Energie zwischen dem Gleichgewichtszustand und dem Übergangszustand proportional zur angelegten Kraft abnimmt. Ein solches Bindungspotential ist durch zwei Parameter vollständig charakterisiert: die Dissoziationsrate ohne angelegte Kraft und den Abstand zwischen Gleichgewichtszustand und Übergangszustand projiziert auf den Richtungsvektor der angelegten Kraft.

Aus zwei Gründen ist es wünschenswert, eine neue Theorie für Kraft-induzierte doppelsträngige DNA-Separation aufzustellen. Zum einen lassen sich - ausgehend von der Bindungssequenz des jeweiligen DNA-Doppelstrangs - die beiden Bell-Evans Parameter nicht berechnen. Um die Bell-Evans Theorie auf den DNA-Kraftsensor anzuwenden, müssten die Parameter für den jeweiligen DNA-Doppelstrang anhand von Einzelmolekülexperimenten zeitaufwändig bestimmt werden. Zum anderen erfüllt die doppelsträngige DNA-Bindung nicht die Bell-Evans Annahme eines kraftunabhängigen Abstands zwischen Gleichgewichts- und Übergangszustand, weshalb die Energiedifferenz zwischen diesen beiden Zuständen nicht mehr linear mit der Kraft abnimmt. Aus diesen

Gründen entwickelten wir im Rahmen dieser Dissertation ein detaillierteres Modell [M1] für die kraftabhängige Dissoziationsrate für 15-45 basenpaar lange DNA-Doppelstränge, welche unter Zug entlang ihrer langen Achse stehen („Schergeometrie“). Explizit stellen wir ein Drei-Zustands-Gleichgewichtsmodell [11] auf und wenden darauf die kanonische Übergangszustandstheorie [12] an, um die kinetischen Raten für die Strangseparation und die Abrisskraftverteilung als Funktion der Separationsgeschwindigkeit zu berechnen. Die Theorie ist nicht nur in exzellenter Übereinstimmung mit experimentellen Einzelmolekülkraftspektroskopie Ergebnissen, sondern erlaubt auch die Vorhersage der Abrisskraftverteilung für gegebene DNA-Sequenz und Separationsgeschwindigkeit.

**Ausblick.** Die in [M1] vorgestellte DNA-Theorie basiert auf einem Drei-Zustands-Gleichgewichtsmodell. Das heißt, dass die Basen der doppelsträngigen DNA einen von drei möglichen Zuständen annehmen: einzelsträngige DNA (ssDNA), Watson-Crick doppelsträngige DNA (B-DNA) oder eine überstreckte Konformation der DNA (S-DNA). Dabei wird nicht unterschieden, ob sich die ssDNA am Ende des Doppelstrangs abspaltet, oder sich sogenannte einzelsträngige Loops innerhalb des DNA-Doppelstrangs ausbilden. Die beiden Zustände sind jedoch energetisch unterschiedlich zu beschreiben. Zum einen liegt im Loop-Zustand die Kraft an beiden Einzelsträngen an und nicht nur an einem Einzelstrang wie im abgepellten Zustand. Zum anderen ist der Loop-Zustand durch einen entropischen Beitrag energetisch zusätzlich begünstigt [13] [14] [15]. Mit Hilfe eines Vier-Zustands-Gleichgewichtsmodells lässt sich diese Unterscheidung explizit modellieren. Auch der entropische Beitrag, der logarithmisch zur Größe des Loops (weitreichende Wechselwirkung) in die Berechnung eingeht, lässt sich explizit in die Berechnung mit aufnehmen. Zwar ist das in [M1] verwendete Gleichgewichtsmodell ein Nächster-Nachbar-Modell [16] und berücksichtigt keine weitreichenden Wechselwirkungen, jedoch treten für den hier untersuchten Fall von kurzen DNA-Doppelsträngen nur kleine Loops von wenigen Basenpaaren auf. Aus diesem Grund lässt sich der entropische Beitrag linear nähern (kurzreichende Wechselwirkung) und in unser Modell implementieren.

### Literaturverzeichnis Kapitel 3.

- [1] Neuert, G., C. H. Albrecht, and H. E. Gaub. 2007. Predicting the Rupture Probabilities of Molecular Bonds in Series. *Biophys. J.* 93:1215-1223.
- [2] Oesterhelt, F., M. Rief, and H. E. Gaub. 1999. Single molecule force spectroscopy by AFM indicates helical structure of poly(ethylene- glycol) in water. *N. J. Phys.* 1:1-11.
- [3] Smith, S. B., Y. J. Cui, and C. Bustamante. 1996. Overstretching B-DNA: the elastic response of individual double-stranded and single-stranded DNA molecules. *Science.* 271:795-799.
- [4] Smith, S., L. Finzi, and C. Bustamante. 1992. Direct mechanical measurements of the elasticity of single DNA molecules by using magnetic beads. *Science* 258:1122-1126.
- [5] Cluzel, P., A. Lebrun, C. Heller, R. Lavery, J. Viovy, D. Chatenay and F. Caron. 1996. DNA: an extensible molecule. *Science* 271:792-794.
- [6] Rief, M., H. Clausen-Schaumann, and H. E. Gaub. 1999. Sequence dependent mechanics of single DNA molecules. *Nat. Struct. Biol.* 6:346-349.
- [7] Strunz, T., K. Oroszlan, R. Schäfer and H. Güntherodt. 1999. Dynamic force spectroscopy of single DNA molecules. *Proc. Natl. Acad. Sci. USA.* 96:11277-11282.
- [8] Morfill, J., F. Kuhner, K. Blank, R. Lugmaier, J. Sedlmair and H. E. Gaub. 2007. B-S Transition in Short Oligonucleotides. *Biophys. J.* 93:2400-2409.
- [9] Friedsam, C., A. K. Wehle, F. Kuhner and H. E. Gaub. 2003. Dynamic single-molecule force spectroscopy: bond rupture analysis with variable spacer length. *J. Phys.: Condens. Matter*, 15:S1709-S1723.
- [10] Evans, E. and K. Ritchie. 1997. Dynamic strength of molecular adhesion bonds. *Biophys. J.*, 72:1541-1555.
- [11] Cocco, S., J. Yan, J. Léger, D. Chatenay, J. Marko. 2004. Overstretching and force-driven strand separation of double-helix DNA. *Phys. Rev. E.* 70:011910.
- [12] Hänggi, P., P. Talkner, and M. Borkovec. 1990. Reaction-rate theory: fifty years after Kramers. *Rev. Mod. Phys.* 62:251-342.
- [13] Hanke, A., M. G. Ochoa and, R. Metzler. 2008. Denaturation Transition of Stretched DNA. *Phys. Rev. Lett.* 100: 018106.
- [14] Y. Kafri, D. Mukamel, and L. Peliti. 2002. Melting and unzipping of DNA. *Eur. Phys. J. B.* 27:135-146.
- [15] T. R. Einert, P. Naeger, H. Orland, and R. R. Netz. 2008. Impact of Loop Statistics on the Thermodynamics of RNA Folding. *Phys. Rev. Lett.* 101:048103.
- [16] Zimm, B. H., and J. K. Bragg. 1959. Theory of the phase transition between helix and random coil in polypeptide chains. *J. Chem. Phys.* 31:526 –535.

#### 4. NACHWEIS VON DNA·LIGAND WECHSELWIRKUNGEN

Das folgende Kapitel beschreibt den Nachweis von DNA·Ligand Wechselwirkungen anhand eines auf dem DNA-Kraftsensor basierenden Biochips. Eine ausführlichere Diskussion der Experimente und Messergebnisse findet sich in [P1] und [P2].

**Einleitung.** Kleine DNA-bindende Moleküle sind im Mittelpunkt des Interesses vieler Forschungsgebiete. Sei es Systembiologie [1], Diagnostik [2] oder Molekularmedizin [3]: das Wissen, ob und wie stark ein Molekül mit einer spezifischen DNA-Sequenz wechselwirkt, ist von höchstem Interesse. Bilden sich solche Komplexe, dann ist dieser Prozess typischerweise mit Änderungen in der Struktur der Doppelhelix verbunden und resultiert beispielsweise in der Verdrängung oder Blockierung, aber auch Rekrutierung anderer DNA-bindender Moleküle. Dadurch übernehmen DNA-bindende Moleküle wichtige Funktionen in der Transkription, Rekombination und DNA-Reparatur [4] [5].

Aufgrund der Bedeutung der molekularen Erkennung zwischen Ligand und doppelsträngiger DNA sind unterschiedlichste Nachweismethoden entwickelt worden, die eine schnelle, sensitive und quantitative Erkennung von DNA·Ligand Komplexen ermöglichen. Konventionell werden DNase-Footprinting-Experimente herangezogen, um die Bindestellen eines Liganden auf doppelsträngiger DNA zu identifizieren und deren jeweiligen Affinitäten zu bestimmen. Diese Methode ist einerseits robust und in Forschung und Entwicklung etabliert, andererseits komplex und zeitaufwändig [6]. Ein sehr viel schnellerer und ebenfalls markierungsfreier Nachweis von kleinsten Mengen an Liganden ist mittels Mikroblattfedern möglich geworden [7]. Diese Methode hat jedoch den Kostennachteil, der mit Fabrikation und chemischer Modifizierung einer großen Anzahl von Blattfedern verbunden ist.

Für eine Vielzahl von Anwendungen ist es zudem wünschenswert, das komplette DNA-Erkennungsprofil eines bestimmten DNA-Binders zu identifizieren, um im Detail zu verstehen, welche Rollen ein Ligand in einem lebenden Organismus spielt. Auf Biochips basierende Methoden tragen dem Wunsch nach hochparalleler Untersuchung von DNA-Ligand-Wechselwirkungen Rechnung: Chromatin-Immunoprecipitation-on-chip (ChIP-on-chip) ist eine mittlerweile weit verbreitete und kommerziell verfügbare Technik, die genomweit Proteinbindestellen aufspürt [8] [9]. Jedoch beruht ChIP-on-chip auf unspezifischem Kreuzverbinden von DNA mit dem zu untersuchenden DNA-bindenden Molekül in-vivo. Kreuzverbindungseffizienzen variieren von

Molekül zu Molekül und manche Wechselwirkungen werden überhaupt nicht erkannt [10]. Insbesondere die Erkennung von kleinen Molekülen, die mit DNA wechselwirken, ist nicht trivial. Auch aufgrund dieser Unzulänglichkeiten von ChIP-on-chip werden immer mehr in-vitro-Biochip-Nachweismethoden entwickelt, die die DNA-Ligand Wechselwirkung unter kontrollierten Bedingungen untersuchen. Beispielsweise führten Warren und Kollegen [11] Experimente durch, in denen alle Permutationen einer acht basenpaarlangen doppelsträngigen DNA örtlich getrennt auf einem einzelnen Biochip präsentiert werden. Ligandbindung wurde direkt mittels Fluoreszenz nachgewiesen und die erkannten Sequenzen als Funktion der Affinität aufgetragen [12]. Jedoch handelt man sich mit auf Fluoreszenz basierenden Methoden im Tausch für sensitives und schnelles Auslesen einen markierten Liganden ein. Markierungen am Liganden beeinflussen das Erkennungsprofil des Liganden in einer unvorhersehbaren Art und Weise. Dies treibt die Entwicklung markierungsfreier Nachweisverfahren voran. Eine weit verbreitete Methode markierungsfreien Nachweises auf Biochips basiert auf der Oberflächenplasmonenresonanz-Technologie (SPR). Da kleine Moleküle den Brechungsindex nur sehr schwach verändern, ist der Nachweis von diesen mit Hilfe von SPR schwierig und benötigt im Vergleich zu auf Fluoreszenz basierenden Techniken größere Flächen auf dem Biochip [13] [14]. Abhängig von der Anwendung kann das Hintergrundsignal durch nichtspezifisch adsorbierte Biomoleküle eine erhebliche Einschränkung für alle auf Oberflächen zugrunde liegenden Nachweismethoden darstellen. Die Fabrikation von inerten Oberflächen ist sogar das Hauptproblem für die Weiterentwicklung von Biochips [15].

In dieser Dissertation präsentieren wir ein biochip-kompatibles DNA-Ligand Nachweisverfahren, das auf dem DNA-Kraftsensor basiert [16] [17] [18]. Dieses Verfahren beruht auf der Veränderung der Abrisskräfte des Ligand-gebundenen DNA-Doppelstrangs (Ziel-DNA) [19] [20] [21], ein Effekt der bereits in Einzmolekulkraftexperimenten mittels AFM [22] [23] [24], optischer [25] und magnetischer Fallen [26] bestätigt wurde.

**Messprinzip.** Das Prinzip dieses DNA-Kraftsensor-Experiments beruht darauf, dass sich die Abrisskräfte einer doppelsträngigen Ziel-DNA erhöhen, falls die Ziel-DNA einen Komplex mit einem Liganden bildet [19] [20] [21]. Um den Anstieg der Abrisskräfte nachzuweisen, verwenden wir anstelle eines mikroskopischen, federartigen Objekts, wie beispielsweise eine AFM Blattfeder, einen nur molekulargroßen DNA-Kraftsensor. Die Ziel-DNA und der DNA-Kraftsensor werden hierzu als molekulare Kette zwischen zwei Oberflächen eingespannt. Werden die beiden Oberflächen separiert, baut sich eine Kraft in der molekularen Kette auf, bis sich die Ziel-DNA oder der DNA-Kraftsensor öffnet.

Der Verbindungsstrang ist fluoreszenzmarkiert und landet auf der Seite der Ziel-DNA, falls der DNA-Kraftsensor abreißt, oder auf der Seite des DNA- Kraftsensors, falls die Ziel-DNA abreißt. Bindet ein Ligand an die Ziel-DNA, wird diese stabilisiert und die Wahrscheinlichkeit, dass der Kraftsensor abreißt, erhöht sich (Abbildung 9a).

Aufgrund des nur molekülgroßen Kraftsensors sind solche Experimente dafür prädestiniert, viele identische Kopien des Experiments simultan auf einem Biochip durchzuführen. Die hohe Anzahl der gleichzeitig durchgeführten Experimente trägt zu der exzellenten Sensitivität der Messung bei. Das Resultat der Messung, das heißt das Verhältnis von gebrochenen Ziel-DNAs zu gebrochenen DNA-Kraftsensoren, lässt sich über den Ort des fluoreszenzmarkierten Verbindungsstrangs bestimmen. Dieses Verhältnis verschiebt sich zu einem höheren Anteil gerissener DNA-Kraftsensoren, falls ein Ligand an die Ziel- DNA bindet und diese stabilisiert. Das resultierende Messverfahren ist dabei zwar Fluoreszenz basierend, jedoch benötigt es keinen markierten Liganden. Der Hauptvorteil dieser Messmethode liegt darin, dass anstelle der Präsenz von Biomolekülen in der Nähe des Biochips, die Änderung der Abrisskräfte nachgewiesen wird. Dadurch weist unser Verfahren keine nichtspezifischen adsorbierten Moleküle auf der Biochipoberfläche nach und umgeht damit eines der Hauptprobleme heutiger Biochips [15].

**Zusammenfassung der Experimente.** Als Modelsystem untersuchten wir in Kooperation mit der Forschungsgruppe von Peter B. Dervan vom California Institute of Technology sequenzspezifisch bindende Pyrol-Imidazol-Haarnadel Polyamide [27]. Diese Moleküle erkennen die kleine Fuge der DNA mit Affinitäten und Spezifitäten vergleichbar zu natürlich vorkommenden, DNA-bindenden Proteinen [28] [29]. Die Sequenzspezifität entsteht durch Wechselwirkungen von Paaren von aromatischen Aminosäuren N-methylpyrrol (Py), N-methylimidazol (Im) und N-methylhydroxypyrrrol (Hp) mit den Kanten der Watson-Crick DNA Basenpaaren [31]. Eine Paarung von Im mit Py bindet ein G·C Basenpaar und Py/Im erkennt ein C·G Basenpaar, während Py/Py eine Präferenz für A·T und T·A Basenpaare verleiht. Die Unterscheidung von T·A von A·T mittels Hp/Py Paarung vervollständigt die Erkennung des DNA-Basenpaarcodes. Haarnadel-Polyamide, welche aus insgesamt acht Ringen bestehen, liefern einen guten Kompromiss zwischen einfacher Synthesierung und molekularer Erkennungseigenschaften. Diese Haarnadelkonstrukte verwenden einen  $\gamma$ -Aminobuttersäurerückstand, welcher das Carboxylenende des einen Polyamidstrangs mit dem Aminoende des anderen Polyamidstrangs verbindet [32]. Der Umkehrpunkt dient als ein DNA-Erkennungselement für A·T und T·A Basenpaare. Außerdem verleiht eine  $\beta$ -Alaningruppe und ein

Dimethylaminopropylamidende am Carboxylende jeweils ein Erkennungselement für A·T und T·A Basenpaare [33]. Diese allgemeine Ansprechbarkeit der kleinen DNA-Furche wird durch kristallographische und NMR- Untersuchungen [34] [35] unterstützt und in verschiedensten Anwendungen, wie zum Beispiel DNA-Nanostrukturen [36] [37], der Rekrutierung von DNA-bindenden Proteinen [38] [39] und der Inhibierung der Genexpression in lebenden Zellen [40] [41] [42] angewandt.

Die erste im Rahmen dieser Dissertation veröffentlichte Studie [P1] befasst sich mit der Untersuchung der Selektivität der Polyamide gegenüber den Enantiomeren D-DNA und L-DNA mit Hilfe des DNA-Kraftsensors [P1]. Anhand dieser Studien wurde gezeigt, dass Polyamiden über einen Aminsubstituent am Wendepunkt des Haarnadelkonstrukts ( $\gamma$ -Aminobuttersäurerückstand) eine chirale Selektivität verliehen wird. Weiterhin wurde gezeigt, dass die chirale Selektivität sich über die Konfiguration des Aminsubstituent schalten lässt: die *R*-Konfiguration verleiht dem Polyamid eine Präferenz für reguläre D-DNA, während die *S*-Konfiguration dem Polyamid eine Präferenz für gespiegelte L-DNA verleiht.

Eine weitere veröffentlichte Studie [P2] befasst sich mit der Bestimmung der Dissoziationskonstante  $K_D$  für verschiedene DNA·Polyamid Wechselwirkungen (Abbildung 9a) anhand einer einzelnen DNA-Kraftsensor-Messung. Mittels eines Fluidiksystems werden identisch präparierte DNA-Punkte auf einem Biochip mit verschiedenen Konzentrationen eines Polyamids inkubiert. Eine erhöhte Polyamidkonzentration resultierte in einer Stabilisierung der Ziel-DNA und einer erhöhten Wahrscheinlichkeit, dass der DNA-Kraftsensor abreißt (Abbildung 9c und 9d). Insgesamt wurden drei DNA·Polyamid Wechselwirkungen untersucht und deren Dissoziationskonstanten bestimmt (Abbildung 9b). Die Dissoziationskonstanten stimmen sehr gut mit bereits publizierten Werten [43] überein (Abbildung 9).

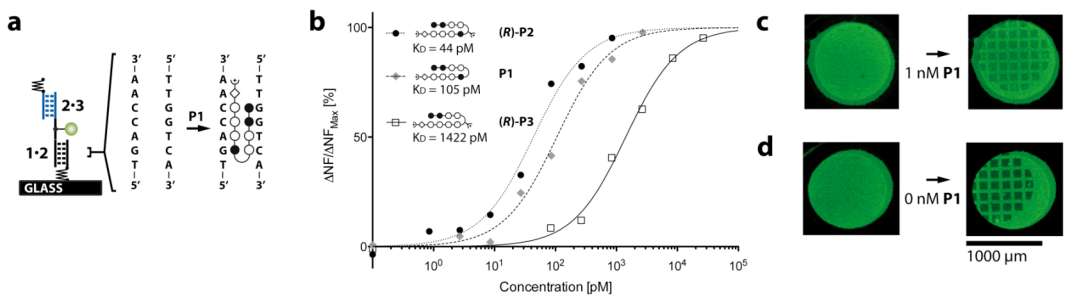


**Abbildung 9.** Der Nachweis von DNA-Polyamid Wechselwirkungen. (a) Zwei DNA-Bindungen werden auf einem Biochip in Serie befestigt. Die **1·2** Ziel-DNA beinhaltet die 5'-TGACCAA-3' Sequenz, die bevorzugt von den untersuchten Polyamiden (in Stick-and-Ball Darstellung siehe [P1] und [P2]) gebunden wird. **2·3** dient als DNA-Kraftsensor. (b) Die Fluoreszenz, die auf dem Biochip zurückbleibt, erhöht sich mit steigender Konzentration der Polyamide **P1**, **(R)-P2** und **(R)-P3**. Aus der Fluoreszenz-Polyamidkonzentrationskurve lässt sich die Gleichgewichtsbindungsconstante der DNA-Polyamid-Komplexe bestimmen. (c) Fluoreszenz vor und nach dem Biochip-Stempelkontakt in der Präsenz von 1 nM **P1**. (d) Fluoreszenz vor und nach dem Biochip-Stempelkontakt ohne Präsenz von **P1**. Die Fluoreszenz, die auf dem Biochip zurückbleibt, ist mit Polyamid **P1** signifikant höher als ohne.

**Ausblick.** Das DNA-Kraftsensorprinzip wurde erfolgreich angewendet, um zum einen die Selektivität von Polyamiden gegenüber verschiedenen Chiralitäten und Sequenzen doppelsträngiger DNA zu untersuchen und zum anderen die Gleichgewichtsdissoziationskonstanten von drei verschiedenen DNA·Polyamid-Komplexen markierungsfrei zu quantifizieren. Für diesen Zweck sind Polyamidkonzentrationen von gerade einmal 10 pM nachgewiesen worden. Eine solche Sensitivität ist mit konventionellen Biochipmethoden vergleichbar, die jedoch mit fluoreszenzmarkierten Proben arbeiten. In weiteren Experimenten zeigten wir, dass selbst schwache Wechselwirkungen bei komplexem molekularem Hintergrund nachgewiesen werden können [P3]. Die Spanne der Sensitivität reicht also aus, um Gleichgewichtskonstanten molekularer Komplexe von mikromolaren bis zu pikomolaren Konzentrationen zu bestimmen.

Das Nachweisverfahren ist multiplexingfähig, das heißt, dass sich viele verschiedene Experimente auf einem Biochip simultan durchführen lassen. Mit Hilfe von Microarray-Spottern sollen die jetzigen DNA-Punktgrößen von hunderten von Mikrometern auf einige Mikrometer Durchmesser reduziert werden. In Zukunft ließe sich dadurch das ganze menschliche Genom auf einem DNA-Kraftsensor Biochip präsentieren, um das vollständige Sequenzerkennungsprofil eines DNA-Binders anhand nur einer Messung

quantitativ zu bestimmen. Mit einem solchen Biochip lassen sich auch alle in einem Zellextrakt vorkommenden DNA-bindenden Proteine, sogenannte Transkriptionsfaktoren, nachweisen. Transkriptionsfaktoren sind zum einen allein deshalb von herausragender Bedeutung, weil sie bereits 10% oder 2600 der Gene des menschlichen Genoms ausmachen, und zum anderen, weil sie Schlüsselmoleküle bei der Diagnose und klinischen Behandlung von Krebs sind. Demgemäß könnte sich ein Transkriptionsfaktor-Biochip im speziellen für die Entwicklung neuer Arzneimittel und die Entdeckung neuer Biomarker als sehr nützlich erweisen.

Die Durchführung des Experiments ist außerdem denkbar einfach: Ein Biochip wird mit dem zu untersuchenden Molekül/Zellextrakt inkubiert und daraufhin mit einer zweiten Oberfläche kontaktiert. Das Ergebnis wird mittels eines Fluoreszenzscanners ausgelesen. Dadurch ist der DNA-Kraftsensor das ideale Werkzeug, um Wechselwirkungen zwischen Molekülen und DNA markierungsfrei und in hohem Durchsatz quantitativ nachzuweisen.

## Literaturverzeichnis Kapitel 4.

- [1] Fernie, A.R., R. N. Trethewey, A. J. Krotzky AJ. 2004. Metabolite profiling: from diagnostics to systems biology. *Nat. Rev. Mol. Cell Biol.* 5:763-769.
- [2] Hanash, S. 2004. Opinion: Integrated global profiling of cancer. *Nat. Rev. Cancer.* 4:638-644.
- [3] Kramer, R., D. Cohen. 2004. Functional genomics to new drug targets. *Nat. Rev. Drug Discov.* 3: 965-972.
- [4] Gottesfeld, J. M., L. Neely, J. W. Trauger, E. E. Baird and P. B. Dervan. 1997. Regulation of gene expression by small molecules. *Nature.* 387:202-205.
- [5] Majmudar, C. Y. and A. K. Mapp. 2005. Chemical approaches to transcriptional regulation. *Curr. Opin. Chem. Biol.* 9:467-474.
- [6] Connaghan-Jones, K., A. Moody and D. Bain. 2008 Quantitative DNase footprint titration: a tool for analyzing the energetics of protein–DNA interactions. *Nature Protocols.* 3:900-914.
- [7] Zhang, J., H. Lang, F. Huber, A. Bietsch, W. Grange, U. Certa, R. Mckendry, H. Güntherodt, M. Hegner and C. Gerber. 2006. Rapid and label-free nanomechanical detection of biomarker transcripts in human RNA. *Nature Nanotechnol.* 1:214-220.
- [8] Ren, B. 2000. Genome-Wide Location and Function of DNA Binding Proteins. *Science.* 290:2306-2309.
- [9] Harbison, C. T., D. B. Gordon, T. I. Lee, N. J. Rinaldi, K. D. Macisaac, T. W. Danford, N. M. Hannett, J. B. Tagne, D. B. Reynolds, J. Yoo, E. G. Jennings, J. Zeitlinger, D. K. Pokholok, M. Kellis, P. A. Rolfe, K. T. Takusagawa, E. S. Lander, D. K. Gifford, E. Fraenkel and R. A. Young. 2004. Transcriptional regulatory code of a eukaryotic genome. *Nature.* 431:99 –104.
- [10] Solomon, M. J. and A. Varshavsky. 1985. Formaldehyde-mediated DNA-protein crosslinking: a probe for in vivo chromatin structures. *Proc. Natl. Acad. Sci. USA.* 82:6470-6474.
- [11] Warren, C., N. Kratochvil, K. Hauschild, S. Foister, M. Brezinski, P. B. Dervan, Jr G. Phillips and A. Ansari. 2006. Defining the sequence-recognition profile of DNA-binding molecules. *Proc. Natl. Acad. Sci. USA.* 103:867-872.
- [12] Puckett, J., K. Muzikar, J. Tietjen, C. Warren, A. Ansari and P. B. Dervan. 2007. Quantitative microarray profiling of DNA-binding molecules. *J. Am. Chem. Soc* 129:12310-12319.
- [13] Boozer, C., G. Kim, S. Cong, H. Guan and T. Lonergan. 2006. Looking towards label-free biomolecular interaction analysis in a high-throughput format: a review of new surface plasmon resonance technologies. *Curr. Opin. Biotechnol.* 17:400-405.
- [14] Wang, J. and H.S. Zhou. 2008 Aptamer-based Au nanoparticles-enhanced surface plasmon resonance detection of small molecules. *Anal. Chem.* 80:7174-7178.
- [15] Gurard-Levin, Z. A. and M. A. Mrksich. 2008. Combining Self-Assembled Monolayers and Mass Spectrometry for Applications in Biochips. *Annu. Rev. Anal. Chem.* 1:767-800.

- [16] Albrecht, C., K. Blank, M. Lalic-Multhaler, S. Hirler, T. Mai, I. Gilbert, S. Schiffmann, T. Bayer, H. Clausen-Schaumann and H. E. Gaub. 2003. DNA: a programmable force sensor. *Science*. 301:367-370.
- [17] Blank, K., T. Mai, I. Gilbert, S. Schiffmann, J. Rankl, R. Zivin, C. Tackney, T. Nicolaus, K. Spinnler, F. Oesterhelt, M. Benoit, H. Clausen-Schaumann and H. E. Gaub. 2003. A force-based protein biochip. *Proc. Natl. Acad. Sci. USA*. 100:11356-11360.
- [18] Blank, K., A. Lankenau, T. Mai, S. Schiffmann, I. Gilbert, S. Hirler, C. Albrecht, M. Benoit, H. E. Gaub and H. Clausen-Schaumann. Double-chip protein arrays: force-based multiplex sandwich immunoassays with increased specificity. *Anal. Bioanal. Chem.* 379:974-981.
- [19] Krautbauer, R., S. Fischerlander, S. Allen and H. E. Gaub. 2002. Mechanical fingerprints of DNA drug complexes. *Single Mol.* 3:97-103.
- [20] Koch, S. J., A. Shundrovsky, B. C. Jantzen and M. D. Wang. 2002. Probing protein-DNA interactions by unzipping a single DNA double helix. *Biophys. J.* 83:1098-1105.
- [21] Leuba, S. H., M. A. Karymov, M. Tomschik and R. Ramjit. 2003. Assembly of single chromatin fibers depends on the tension in the DNA molecule: Magnetic tweezers study. *Proc. Natl. Acad. Sci. USA*. 100:495-500.
- [22] Puchner, E. M., A. Alexandrovich, A. L. Kho, U. Hensen, L. V. Schäfer, B. Brandmeier, F. Gräter, H. Grubmüller, H. E. Gaub and M. Gautel M. 2008. Mechanoenzymatics of titin kinase. *Proc. Natl. Acad. Sci. USA*. 105:13385-13390.
- [23] Schlierf, M., F. Berkemeier and M. Rief. 2007. Direct Observation of Active Protein Folding Using Lock-in Force Spectroscopy. *Biophys. J.* 93:3989-3998.
- [24] Wiita, A., R. Perez-Jimenez, K. Walther, F. Gräter, B. Berne, A. Holmgren, J. Sanchez-Ruiz and J. Fernandez. 2007. Probing the chemistry of thioredoxin catalysis with force. *Nature*. 450:124-127.
- [25] Clemen, A. E. M., M. Vilfan, J. Jaud, J. S. Zhang, M. Barmann and M. Rief. 2005. Force-dependent stepping kinetics of myosin-V. *Biophys. J.* 88:4402-4410.
- [26] Gosse, C. and V. Croquette. 2002. Magnetic tweezers: Micromanipulation and force measurement at the molecular level. *Biophys. J.* 82:3314-3329.
- [27] Dervan, P. B., A. T. Poulin-Kerstien, E. J. Fechter, and B. S. Edelson. 2005. Regulation of gene expression by synthetic DNA-binding ligands. *Top. Curr. Chem.* 253:1-31.
- [28] Dervan, P. B. and B. S. Edelson, 2003. Recognition of the DNA minor groove by pyrrole-imidazole polyamides. *Curr. Opin. Struct. Biol.* 13:284-299.
- [29] Dervan, P. B. 2001. Molecular recognition of DNA by small molecules. *Bioorg. Med. Chem.* 9:2215-2235.
- [30] White, S., J. W. Szewczyk, J. M. Turner, E. E. Baird and P. B. Dervan. 1998. Recognition of the four Watson-Crick base pairs in the DNA minor groove by synthetic ligands. *Nature*. 391:468-471.
- [31] Kielkopf, C. L., R. E. Bremer, S. White, J. W. Szewczyk, J. M. Turner, E. E. Baird, P. B. Dervan and D. C. Rees. 2000. Structural effects of DNA sequence on T.A

- recognition by hydroxypyrrrole/pyrrole pairs in the minor groove. *J. Mol. Biol.* 295:557-567.
- [32] Mrksich, M., M. E. Parks and P. B. Dervan. 1994. Hairpin Peptide Motif - A New Class of Oligopeptides for Sequence-Specific Recognition in the Minor-Groove of Double-Helical DNA. *J. Am. Chem. Soc.* 116:7983-7988.
- [33] Swalley, S. E., E. E. Baird and P. B. Dervan. 1999. *J. Am. Chem. Soc.* 121:1113-1120.
- [34] Kielkopf, C. L., S. White, J. W. Szewczyk, J. M. Turner, E. E. Baird, P. B. Dervan and D. C. Rees. 1998. A structural basis for recognition of A center dot T and T center dot A base pairs in the minor groove of B-DNA. *Science.* 282:111-115.
- [35] deClairac, R. P. L., B. H. Geierstanger, M. Mrksich, P. B. Dervan and D. E. Wemmer 1997. NMR characterization of hairpin polyamide complexes with the minor groove of DNA. *J. Am. Chem. Soc.* 119:7909-7916.
- [36] Cohen, J. D., J. P. Sadowski and P. B. Dervan. 2007. Adressing Single Molecules on DNA Nanostructures. *Angew. Chem.* 46:7956-7959.
- [37] Schmidt, T. L., C. K. Nandi, G. Rasched, P. P. Parui, B. Brutschy, M. Famulok and A. Heckel. 2007. Polyamide struts for DNA architectures. *Angew. Chem.* 46:4382-4384.
- [38] Arndt, H. D., K. E. Hauschild, D. P. Sullivan, K. Lake, P. B. Dervan, and A. Z. Ansari. 2003. Toward artificial developmental regulators. *J. Am. Chem. Soc.* 125:13322-13323.
- [39] Stafford, R. L., H. D. Arndt, M. L. Brezinski, A. Z. Ansari and P. B. Dervan. 2007. Minimization of a protein-DNA dimerizer. *J. Am. Chem. Soc.* 129:2660-2668.
- [40] Olenyuk, B. Z., G. J. Zhang, J. M. Klco, N. G. Nickols, W. G. Kaelin Jr. and P. B. Dervan. 2004. Inhibition of vascular endothelial growth factor with a sequence-specific hypoxia response element antagonist. *Proc. Natl. Acad. Sci. USA.* 101:16768-16773.
- [41] Nickols, N. G. and Dervan, P.B. 2007. Suppression of androgen receptor-mediated gene expression by a sequence-specific DNA-binding polyamide. *Proc. Natl. Acad. Sci. USA.* 104:10418-10423.
- [42] Nickols, N. G., C. S. Jacobs, M. E. Farkas and P. B. Dervan. 2007. Modulating hypoxia-inducible transcription by disrupting the HIF-1-DNA interface. *ACS Chem. Biol.* 2:561-571.
- [43] Hsu, C. F., J. W. Phillips, J. W. Trauger, M. E. Farkas, J. M. Belitsky, A. Heckel, B. Z. Olenyuk, J. W. Puckett, C. C. C. Wang and P. B. Dervan. 2007. Completion of a Programmable DNA-Binding Small Molecule Library. *Tetrahedron.* 63:6146-6151.

## 5. NACHWEIS VON APTAMER·LIGAND WECHSELWIRKUNGEN

Das folgende Kapitel beschreibt den Nachweis von Aptamer·Ligand Wechselwirkungen anhand eines auf dem DNA-Kraftsensor basierenden Biochips. Eine ausführlichere Diskussion der Experimente und Ergebnisse findet sich in [P3].

**Einleitung.** Eines der derzeitigen Ziele auf dem Gebiet bioanalytischer Methoden ist die Entwicklung von markierungsfreien Verfahren, die eine Vielzahl von Wechselwirkungen gleichzeitig nachweisen [1]. Der durchschlagende Erfolg von Nukleinsäuren nachweisenden Biochips auf das Feld der Molekularbiologie liefert den Anstoß, Biochips für den Nachweis anderer Molekülarten wie zum Beispiel Peptide, Proteine und kleine Moleküle zu entwickeln [1]. Für die Fabrikation von Biochipoberflächen sind Aptamere aus verschiedensten Gründen vielversprechende Kandidaten, um einfach und effektiv die oben genannte Analyten aus der Lösung an designierten Stellen auf dem Biochip einzufangen. Aptamere sind DNA- oder RNA-Oligonukleotide, die alle möglichen Arten von Molekülen spezifisch über ihre dreidimensionale Struktur binden können [3]. Sie werden zunehmend als Konkurrenz für Antikörper in der in-vitro-Diagnostik [4] und Biosensoranwendungen [5] [6] [7] erkannt, weil sie diese durch kleineres Molekulargewicht, Einfachheit der Modifizierbarkeit und der Möglichkeit, mit ihnen auch Toxine nachzuweisen [8], übertreffen. Im Gegensatz zu den aus Aminosäuren bestehenden Antikörpern, welche nur schwer funktionstüchtig befestigt werden können [9], werden standardisierte DNA-Biochipprotokolle verwendet, um Aptamer-Biochips zu fabrizieren. Trotzdem hat sich die Herstellung solcher Biochips als schwieriger herausgestellt als angenommen. Insbesondere kleine Moleküle können kaum nachgewiesen werden: Kleine Moleküle verursachen bei konventionellen markierungsfreien Techniken wie beispielsweise auf Oberflächenresonanz [10], Elektrochemie [11] oder Blattfedern [12] basierenden Sensoren nur kleine Signale. Hintergrundsignale sind bei Biochipnachweisverfahren aufgrund unspezifischer Adsorption recht hoch [13] [14] [15]. Außerdem sind Aptamere, die gegen kleine Moleküle entwickelt worden sind, im Allgemeinen von geringer Affinität [16], weshalb man auch keine Waschschrifte durchführen kann, um die Oberflächen von unspezifisch adsorbierten Molekülen zu reinigen. Diese Kombination aus kleinem Signal, hohem Hintergrundrauschen und der methodische Verzicht auf stringente Waschschrifte, schafft erschwert den technologischen Nachweis kleiner Moleküle mittels Aptameren. In dieser Dissertation präsentieren wir eine generell anwendbare Strategie, um kleine-Molekül·Aptamer Komplexe nachzuweisen. Unser Ansatz identifiziert die Wechselwirkungen zwischen kleinen Molekülen

und Aptameren anstelle der reinen Präsenz von Molekülen nahe der Sensoroberfläche. Dadurch wird das Problem der unspezifischen Adhäsion, eines der Hauptprobleme in der Entwicklung der nächsten Generation von Biochips, gelöst.

**Messprinzip.** Das Prinzip dieses DNA-Kraftsensor-Experiments beruht darauf, dass sich die Abrisskräfte eines aus zwei Untereinheiten bestehenden Aptamer erhöhen, wenn dieser einen Komplex mit seinem spezifischen Ligand bildet. Dies wird mit Hilfe des DNA-Kraftsensor Ansatzes nachgewiesen [17] [18] [19]. Der DNA-Kraftsensor kombiniert die Vorteile von auf Fluoreszenz basierender Methoden, d.h. schnelle und sensitive Detektion mittels kommerziell verfügbaren Fluoreszenzscannern oder Mikroskopen, mit den Vorteilen von markierungsfreien Methoden, d.h. keine ungewollten Markierungswechselwirkungen und der Möglichkeit, eine Vielzahl von molekularen Wechselwirkungen gleichzeitig zu untersuchen. Die eigentliche Stärke des Nachweisverfahrens liegt jedoch in der hohen Spezifität. Konventionelle Biochip-Nachweismethoden unterscheiden nicht zwischen spezifischen und unspezifisch haftenden Analyten, was zu falsch-positiven Messergebnissen führen kann. Waschschritte werden durchgeführt, um unspezifisch haftende Moleküle zu entfernen. Sind jedoch Wechselwirkungen mit Gleichgewichtsdissoziationskonstanten im mikromolar Bereich Gegenstand der Untersuchung, werden spezifisch aber schwach bindende Moleküle ebenfalls durch den Waschschritt entfernt. Dies führt zu falsch-negativen Ergebnissen. Der DNA-Kraftsensor Ansatz löst dieses Problem dadurch, dass nicht die Präsenz irgendeines Moleküls nachgewiesen wird, sondern nur die Wechselwirkung zwischen Aptamer und dem dazugehörigen Ligand.

**Zusammenfassung der Experimente.** Im Speziellen untersuchten wir im Rahmen dieser Dissertation die Wechselwirkung zwischen Adenosin und einem Adenosin spezifischen Aptamer [P3]. Dieses Modellsystem ist deshalb so aufschlussreich, weil der Aptamer sehr gut charakterisiert ist [20] [21] [22] [23]. Die Wechselwirkung ist außerdem sehr schwach und der Analyt so klein, dass er nicht direkt mittels Oberflächenplasmonenresonanz nachgewiesen werden kann [6]. Der zweigeteilte Aptamer wird dazu in großer Anzahl über kurze DNA-Doppelstränge auf einem DNA-Chip aufgebracht (Abbildung 10b und 10c). Die DNA-Doppelstränge übernehmen die Funktion des DNA-Kraftsensors gegen den die Abrisskraft der Aptamer verglichen wird. Verbindet man die molekularen Ketten, die jeweils aus einem DNA-Kraftsensor und einem zweigeteilten Aptamer bestehen, zwischen einer Glas- und PDMS-Oberfläche und separiert die beiden Oberflächen, werden die beiden molekularen Bindungen direkt miteinander verglichen. Mit Hilfe von Fluoreszenz lässt sich das Verhältnis zwischen

gebrochenen Aptamerbindungen und DNA-Kraftsensoren bestimmen. Das Vorhandensein von mikromolarer Adenosin Konzentrationen verursachte eine Verschiebung zu einem höheren Anteil an gebrochenen DNA-Kraftsensoren. Aufgrund des auf Kraft basierenden Designs werden nur die Wechselwirkungen zwischen zweigeteilten Aptamer und dem Analyten anstelle der Präsenz des Analyten allein nachgewiesen. Außerdem wird kein Waschschritt vor dem Auslesen des Experiments und kein sekundärer Antikörper benötigt. Das Nachweisverfahren besticht durch exzellente Selektivität gegenüber anderen Nukleotiden und detektiert nur Adenosin, selbst wenn ein komplexer molekularer Hintergrund vorhanden ist. Multiplexing wurde gezeigt, indem gesamte Titrationsexperimente auf einem einzelnen Chip durchgeführt wurden (Abbildung 10a). Diese bestimmten einen effektiven Halbwertskonzentrationswert von 124.8  $\mu\text{M}$ , der sehr gut mit Literaturwerten übereinstimmt [20] [21] [22] [23] [24].

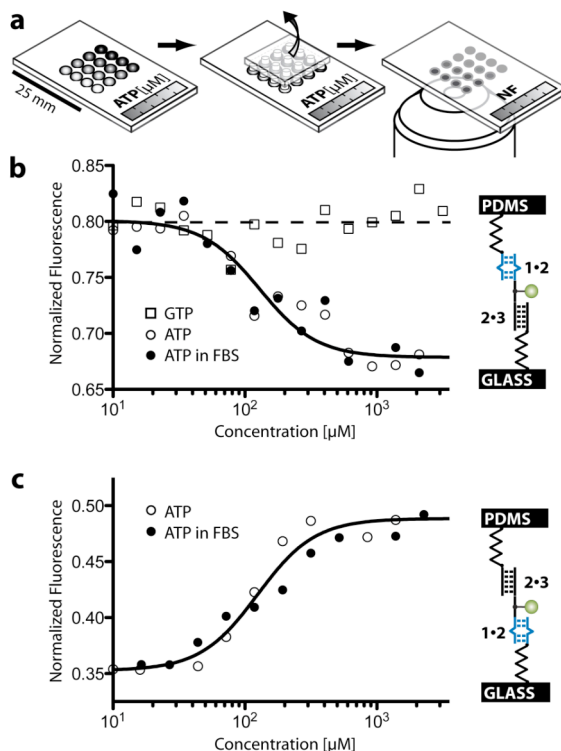


**Abbildung 10.** Nachweis einer Aptamer-ATP Wechselwirkung mittels des DNA-Kraftsensors. (a) Ein Fluidiksystem erlaubt die Inkubation von 16 identisch präparierten DNA-Kraftsensor-Aptamer Punkten mit verschiedenen ATP-Konzentrationen auf einem Biochip. In Anwesenheit von Adenosintriphosphat (ATP) wird der Biochip mit einem PDMS-Stempel kontaktiert. Anschließend wird die Fluoreszenz ausgelesen. (b) Die Fluoreszenz nimmt für zunehmende ATP-Konzentrationen ab. GTP hat keinen Einfluss auf die Fluoreszenz. (c) Werden die DNA-Kraftsensor-Aptamer Konstrukte verkehrt herum auf dem Biochip aufgebracht, ist auch das gemessene Fluoreszenzsignal invertiert. Das heißt das Fluoreszenzsignal nimmt mit zunehmender ATP-Konzentration zu.

**Ausblick.** In der vorliegenden Untersuchung wurde der DNA-Kraftsensor für einen markierungsfreien, auf einem Aptamer basierenden Biochip für den Nachweis von Adenosin verwendet. Dabei beruht das Konzept auf einer erhöhten Abrisskraft des zweigeteilten Aptamers, falls dieser einen Komplex mit seinem Liganden gebildet hat. Das Nachweisverfahren weist Adenosinkonzentrationen höher als 53.5 µM nach und erlaubt die Quantifizierung von Adenosin für Konzentrationen zwischen 53.5 µM und 310.3 µM. Das Signal des Nachweisverfahrens folgt der Hill-Gleichung mit einer halbmaximalen Konzentrationswert von  $EC_{50} = 124,8 \mu\text{M}$ , der sehr gut mit Literaturwerten für die Dissoziationskonstante des Antiadenosinaptamers übereinstimmt [17] [21] [22] [23] [24].

Aufgrund der limitierten Sensitivität und Abhängigkeit der Gleichgewichtskonstante von der Salz- und Magnesiumkonzentration ist der quantitative Nachweis von Adenosin in der Praxis nicht relevant. Die Salzkonzentration von echten Proben ist selten bekannt und es existieren Adenosin-Nachweisverfahren mit wesentlich höherer Sensitivität. Die Stärke des Verfahrens könnte in der Charakterisierung der Gleichgewichtskonstante von schwachen Wechselwirkungen liegen. Dies wurde in diesem Fall anhand eines kleinen Moleküls, Adenosin, und einem niedrigen Affinitäts-Aptamer gezeigt. Die Messungen wurden dabei in reinem SSC-Puffer als auch mit molekularem Hintergrund erfolgreich durchgeführt. Verlässliche Gleichgewichtskonstanten im mikromolaren Regime nachzuweisen, stellt immer noch eine Herausforderung für heutige Hochdurchsatzverfahren dar [25]. Andererseits bieten hochaffine Aptamere die Möglichkeit, sensitivere Nachweisverfahren für Liganden mit höherem Molekulargewicht herzustellen. Aufgrund des markierungsfreien, biochipkompatiblen Konzepts ist es einfach vorstellbar, die Präsenz einer Vielzahl verschiedener Analyten parallel nachzuweisen – prinzipiell nur durch die Anzahl der verschiedenen Aptamerstrukturen beschränkt.

## Literaturverzeichnis Kapitel 5.

- [1] Gurard-Levin, Z. A., and M. Mrksich. 2008. Combining Self-Assembled Monolayers and Mass Spectrometry for Applications in Biochips. *Annu. Rev. Anal. Chem.* 1:767-800.
- [2] Lockhart, D. J., and E. A. Winzeler. 2000. Genomics, gene expression and DNA arrays. *Nature*. 405:827-836.
- [3] Hermann, T., and D. J. Patel. 2000. Biochemistry - Adaptive recognition by nucleic acid aptamers. *Science*. 287:820-825.
- [4] Rimmele, M. 2003. Nucleic Acid Aptamers as Tools and Drugs: Recent Developments . *ChemBioChem*. 4:963-971.
- [5] Zhang, S., J. Xia, and X. Li. 2008. Electrochemical Biosensor for Detection of Adenosine Based on Structure-Switching Aptamer and Amplification with Reporter Probe DNA Modified Au Nanoparticles. *Anal. Chem.* 80:8382-8388.
- [6] Wang, J., and H. S. Zhou. 2008. Aptamer-based Au nanoparticles-enhanced surface plasmon resonance detection of small molecules. *Anal. Chem.* 2008, 80:7174-7178.
- [7] Navani, N. K., and Y. F. Li. 2006. Nucleic acid aptamers and enzymes as sensors. *Curr. Opin. Chem. Biol.* 10:272-281.
- [8] Tang, J., J. Xie, N. Shao, and Y. Yan. 2006. The DNA aptamers that specifically recognize ricin toxin are selected by two in vitro selection methods. *Electrophoresis*. 27:1303-1311.
- [9] Kusnezow, W., and J. J. Hoheisel. 2003. Solid supports for microarray immunoassays. *Mol. Recogn.* 16:165-176.
- [10] Boozer, C., G. Kim, G. Cong, H. Guan, and T. Londergan. 2006. Looking towards label-free biomolecular interaction analysis in a high-throughput format: a review of new surface plasmon resonance technologies. *Curr. Opin.* 17:400-405.
- [11] Xu, D., D. Xu, X. Yu, Z. Liu, W. He, and Z. Ma. 2005. Label-free electrochemical detection for aptamer-based array electrodes. *Anal. Chem.* 77:5107-5113.
- [12] Zhang, J., H. Lang, F. Huber, A. Bietsch, W. Grange, U. Certa, R. Mckendry, H. Güntherodt, M. Hegner, and C. Gerber. 2006. Rapid and label-free nanomechanical detection of biomarker transcripts in human RNA. *Nature. Nanotech.* 2006, 1:214-220.
- [13] Haab, B. B., M. J. Dunham, and P. O. Brown. 2001. Protein microarrays for highly parallel detection and quantitation of specific proteins and antibodies in complex solutions. *Genome Biol.* 2:0004.1-0004.13.
- [14] Michaud, G., M. Salcius; F. Zhou, R. Bangham, J. Bonin, H. Guo, M. Snyder, P. Predki, and B. Schweitzer. 2003. Analyzing antibody specificity with whole proteome microarrays. *Nat. Biotech.* 21:1509-1512.
- [15] Ma, H., and K. Horiuchi. 2006. Chemical microarray: a new tool for drug screening and discovery. *Drug Discovery Today*. 11:661-668.
- [16] Hamula, C., J. Guthrie, H. Zhang, X. Li, and X. Le. 2006. Selection and analytical applications of aptamers. *TrAC, Trends Anal. Chem.* 25:681-691.

- [17] Albrecht, C., K. Blank, M. Lalic-Multhaler, S. Hirler, T. Mai, I. Gilbert, S. Schiffmann, T. Bayer, H. Clausen-Schaumann and H. E. Gaub. 2003. DNA: a programmable force sensor. *Science*. 301:367-370.
- [18] Blank, K., T. Mai, I. Gilbert, S. Schiffmann, J. Rankl, R. Zivin, C. Tackney, T. Nicolaus, K. Spinnler, F. Oesterhelt, M. Benoit, H. Clausen-Schaumann and H. E. Gaub. 2003. A force-based protein biochip. *Proc. Natl. Acad. Sci. USA*. 100:11356-11360.
- [19] Blank, K., A. Lankenau, T. Mai, S. Schiffmann, I. Gilbert, S. Hirler, C. Albrecht, M. Benoit, H. E. Gaub and H. Clausen-Schaumann. 2004. Double-chip protein arrays: force-based multiplex sandwich immunoassays with increased specificity. *Anal. Bioanal. Chem.* 379:974-981.
- [20] Huizenga, D. E., and J. W. Szostak. 1995. A DNA Aptamer That Binds Adenosine and ATP. *Biochemistry*. 34:656-665.
- [21] Lin, C. H., and D. J. Patel. 1997. Structural basis of DNA folding and recognition in an AMP-DNA aptamer complex: distinct architectures but common recognition motifs for DNA and RNA aptamers complexed to AMP. *Chem. Biol.* 4:817-832.
- [22] Stojanovic, M.N., P. de Prada, and D. W. Landry. 2000. Fluorescent sensors based on aptamer self-assembly. *J. Am. Chem. Soc.* 122:11547-11548.
- [23] Stojanovic, M.N., P. de Prada, and D. W. Landry. 2001. Aptamer-based folding fluorescent sensor for cocaine. *J. Am. Chem. Soc.* 123:4928-4931.
- [24] Jhaveri, S. D., R. Kirby, R. Conrad, E. J. Maglott, M. Bowser, R. T. Kennedy, G. Glick, and A. D. Ellington. 2000. Designed signaling aptamers that transduce molecular recognition to changes in fluorescence intensity. *J. Am. Chem. Soc.* 122:2469-2473.
- [25] Titz, B., M. Schlesner, and P. Uetz. 2004. What do we learn from high-throughput protein interaction data?. *Expert Rev. Proteomics*. 1:111-121.

## 6. NACHWEIS VON MEMBRANPROTEINEN AUF LEBENDEN ZELLEN

Das folgende Kapitel beschreibt den Nachweis von Membranproteinen auf lebenden Zellen anhand eines auf dem DNA-Kraftsensor basierenden Verfahrens. Eine ausführlichere Diskussion der Experimente und Ergebnisse findet sich in der Diplomarbeit von Uta Steinbach [1].

**Einleitung.** Zellmembranproteine übernehmen in einer Vielzahl von biologischen Prozessen wichtige Funktionen. Beispiele hierfür sind der Transport von Molekülen, Signalübertragung, Zellverbindung, Zell-Zell-Erkennung und die Verankerung der Zellmembran am Cytoskelett und an der extrazellulären Matrix. Es wird geschätzt, dass etwa 20-30% der menschlichen Proteine Membranproteine sind [1]. Jeder Zelltyp präsentiert eine ganz charakteristische Zusammenstellung dieser Proteine auf seiner Membran und das Gleiche gilt auch für Tumorzellen. Es verwundert daher nicht, dass man insbesondere in der Krebsforschung das erhöhte Vorhandensein tumorspezifischer Membranproteine ausnützt, um diese mit Antikörpern zu markieren, zu lokalisieren [3] [4] und im besten Falle im Patienten direkt zu bekämpfen [5] [6] [7]. Ein kritischer Prozess, der in verschiedensten Schritten in der Krebsforschung und Behandlung immer wieder durchgeführt wird, ist der Nachweis von Membranproteinen auf der Zelloberfläche, um zum Beispiel neue Krebsbiomarker oder Arzneimittelziele zu identifizieren [8] oder um Krebs in histologischen Untersuchungen zu detektieren und zu klassifizieren [9] [10]. Wie in der Bioanalytik ist die Entwicklung neuer Nachweisverfahren maßgeblich durch drei Ziele motiviert: erhöhte Sensitivität, erhöhte Spezifität und der simultane Nachweis vieler verschiedener Membranrezeptoren [9]. Im Rahmen der vorliegenden Dissertation wurde untersucht, ob das Konzept des DNA-Kraftsensors verwendet werden kann, um diesen Zielen Rechnung zu tragen.

**Messprinzip.** Um Rezeptoren auf der Zelloberfläche mittels des DNA-Kraftsensorenprinzips nachzuweisen, wurde die Oberflächenfunktionalisierung im Vergleich zu den Messungen aus Kapitel IV und V leicht verändert. Das Membranprotein erkennende Molekül (Ligand oder Antikörper) wird über eine PEG-Verbindung und einen DNA-Kraftsensor an dem PDMS-Stempel angebracht (Abbildung 11a). Die Oberflächenfunktionalisierung verläuft analog zu der von Blank und Kollegen [11] entwickelten Methode. Die zu untersuchenden Zellen werden auf einer Petrischale bis zur Konfluenz kultiviert oder ausgesät. Der PDMS-Stempel wird dann über die Kontakteinheit mit dem Zellrasen kontaktiert, um dem Erkennungsmolekül zu erlauben, mit dem

Membranprotein zu wechselwirken (Abbildung 11b). Nach einer kurzen Inkubationsphase werden die beiden Oberflächen wieder voneinander getrennt. Dadurch baut sich in der molekularen Kette PEG-Verbindung, **1·2** DNA-Kraftsensor und Erkennungsmolekül-Membranprotein eine Kraft auf bis sich entweder der DNA-Kraftsensor oder die Erkennungsmolekül-Membranprotein Wechselwirkung öffnet. In diesem Experiment ist der DNA-Kraftsensor in der Zipperkonfiguration eingebaut. Das heißt, dass sich der Kraftsensor schon bei einer geringen Belastung von etwa 15 pN öffnet [12]. Diese Abrisskraft ist signifikant niedriger als die Abrisskräfte, die für Antikörper-Antigen Wechselwirkungen gemessen wurden [13], jedoch höher als die meisten unspezifischen Wechselwirkungen. Ist die Wechselwirkung spezifisch, d.h. hat das Erkennungsmolekül seinen korrespondierenden Gegenspieler auf der Zelloberfläche gebunden, so öffnet sich der **1·2** DNA-Kraftsensor und das Erkennungsmolekül sowie der **2** Strang des DNA-Kraftsensors bleiben auf der Zelloberfläche zurück. Diese werden anschließend über Fluoreszenz nachgewiesen (Abbildung 11c). Ist die Wechselwirkung nicht spezifisch, dann wird das Erkennungsmolekül wieder von der Zelloberfläche desorbiert. Dadurch verringert sich im Vergleich zur Inkubation mit einem fluoreszenzmarkierten Erkennungsmolekül in Lösung das Hintergrundsignal, denn unspezifisch adsorbierte Moleküle lassen sich auch durch Waschschritte häufig nicht mehr entfernen. Des Weiteren lassen sich in derselben Zellkultur verschiedenste Zellmoleküle simultan nachweisen, da die Erkennungsmoleküle räumlich getrennt auf dem PDMS-Stempel aufgetragen werden können.

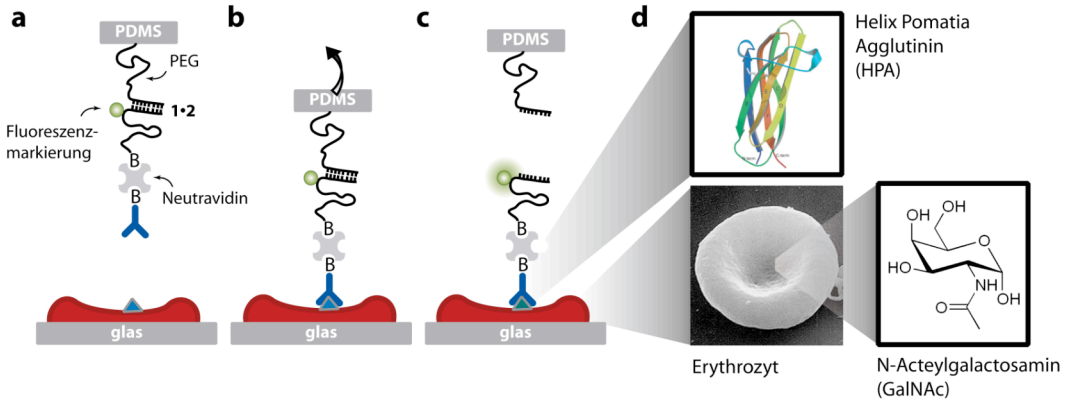


**Abbildung 11.** Nachweis von Glykolipiden auf Zelloberflächen mit Hilfe des DNA-Kraftsensors. (a) Helix Pomatia Agglutinin (HPA) ist über einen Biotin·Neutravidin·Biotin Komplex, dem **1·2** Kraftsensor und poly(ethylene glycol) (PEG) Verbindungen an einem PDMS-Stempel angebracht. Auf einer Petrischale wurden Erythrozyten der Blutgruppe A ausgesät, die über eine hohe Dichte des N-Acetylgalactosamin (GalNAc) auf ihrer Zellmembran verfügen. (b) Der PDMS-Stempel wird vorsichtig mit den Erythrozyten in Verbindung gebracht, so dass sich Komplexe zwischen HPA und GalNAc bilden. Die beiden Oberflächen werden getrennt. Falls sich ein HPA·GalNAc Komplex gebildet hat, baut sich eine Kraft in der molekularen Kette auf und die **1·2** DNA-Kraftsensorkontaktion öffnet sich. (c) Der **2** DNA-Strang bleibt auf der Zelle zurück und kann mittels Fluoreszenz nachgewiesen werden. (d) HPA ist ein Lektin, welches die Struktur eines  $\beta$ -Sandwiches besitzt (oben). Elektronenmikroskopbild eines Erythrozyten (unten). Erythrozyten der Blutgruppe A verfügen über eine hohe Dichte des N-Acetylgalactosamin (GalNAc) auf ihrer Zellmembran (rechts).

**Zusammenfassung der Experimente.** Im Rahmen dieser Dissertation wurden N-Acetylgalactosamin (galNAc) terminierte Glykolipide auf der Zelloberfläche von Erythrozyten mit Hilfe von Helix-Pomatia-Agglutinin (HPA) [14] als Erkennungsmolekül nachgewiesen (Abbildung 11d). Das System ist aus verschiedenen Gründen als Modellsystem geeignet. Zum einen ist die Wechselwirkung gut studiert [15] und wurde in unserem Labor bereits anhand von AFM-Einzelmolekülkraftmessung untersucht [16]. Zum anderen kommen GalNAc terminierte Glykolipide auf der Oberfläche von Erythrozyten der Blutgruppe A in einer hohen Dichte vor, während Erythrozyten der Blutgruppe 0 und B diesen Kohlenhydratrest nicht besitzen und sich somit gut für Kontrollmessungen eignen. Die von Granbois und Kollegen [16] beschriebenen Abrisskräfte bei AFM-Messungen auf der Erythrozytenoberfläche liegen bei 65 pN und somit weit über den Abrisskräften des **1·2** DNA-Kraftsensors, welche bei etwa 15 pN liegen. Das so konstruierte Experiment wurde sowohl an Erythrozyten der Blutgruppe A und 0 als auch an einer Mischung der beiden Blutgruppen durchgeführt.

Die Blutzellen wurden kurz vor dem Experiment auf Petrischalen ausgesät. Der PDMS-Stempel wird vorsichtig mit den Erythrozyten in Verbindung gebracht, so dass sich Komplexe zwischen HPA und GalNAc bilden. Die beiden Oberflächen werden getrennt. Falls sich ein HPA-GalNAc Komplex gebildet hat, baut sich eine Kraft in der molekularen Kette auf und die **1·2** DNA-Kraftsensorbindung öffnet sich. (Abbildung 11b). Die Fluoreszenzbilder der an Blutgruppe A durchgeföhrten Messungen zeigen deutlich die Mikrostruktur des Stempels, da nur die flächigen Erhöhungen des Stempels mit den Zellen in Kontakt waren und nur dort die farbstoffmarkierte DNA zusammen mit dem Liganden HPA auf die Zelloberfläche übertragen wurde (Abbildung 12a). Die Bilder von Messungen an Blutgruppe 0 weisen keinerlei Fluoreszenzübertrag auf die Zellen auf. Dies zeigt, dass unspezifisches Binden an die Zelloberfläche unterbunden wird (Abbildung 12b). Die Kraft von 15 pN zur Öffnung des DNA- Stranges ist demnach größer als die von unspezifischen Wechselwirkungen. Bilder von Messungen an gemischten Blutzellen der Gruppen A und 0 zeigen ebenfalls die Mikrostruktur des Stempels, aber weisen neben den hell gefärbten fluoreszenzmarkierten Zellen dunkle Bereiche auf, die Zellen der Blutgruppe 0 darstellen (Abbildung 12c).

Es lässt sich leicht erkennen, ob die Zellen nach dem Versuch noch intakt oder zerquetscht sind. Erythrozyten weisen durch das im Zellinneren in hohen Konzentrationen vorkommende Hämoglobin einen guten Kontrast bei der Durchlichtmikroskopie auf. Sind die Zellen jedoch zerquetscht, so entweicht das Hämoglobin und der Kontrast geht verloren. In diesem Fall ist die Mikrostruktur des Stempels als kontrastarme Stelle erkennbar.

Kontrollmessungen wurden durchgeführt, bei denen nur die **1·2** Bindung am Stempel angebracht wurde, jedoch nicht HPA. Diese Kontrollmessungen zeigen, dass kein unspezifischer Fluoreszenzübertrag stattfindet. Werte für die mittlere Fluoreszenz pro Fläche liegen im gleichen Bereich wie Werte für Kontrollmessungen mit Blutgruppe 0.

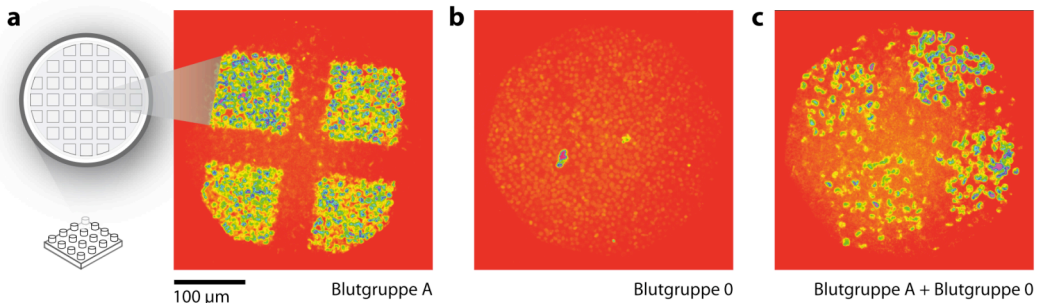


**Abbildung 12.** Fluoreszenzbilder von Erythrozyten nach den Kraftsensorexperimenten.

(a) Bei Zellen der Blutgruppe A ist ein deutlicher Fluoreszenzübertrag erkennbar. Sie besitzen GalNAc terminierte Glykolipide gegen die HPA gerichtet ist. Das quadratische Muster resultiert aus der Mikrostruktur des PDMS-Stempels. (b) Bei Zellen der Blutgruppe 0 fehlt GalNAc auf der Oberfläche. Deshalb findet kein Fluoreszenzübertrag statt. (c) Bei Experimenten mit einem Gemisch der Blutgruppen A und 0 weisen nur Zellen der Gruppe A Fluoreszenz auf, die anderen Zellen bleiben dunkel. Für alle drei hier dargestellten Fluoreszenzbilder wurde dieselbe Helligkeits- und Kontrasteinstellung verwendet.

**Ausblick.** Die Experimente an dem Rezeptor-Ligand Paar GalNAc·HPA konnten zeigen, dass es prinzipiell möglich ist, die molekulare Kraftwaage auf Zellen anzuwenden und damit Blutgruppen von einander zu unterscheiden. Eine solche Messmethode bietet vielerlei Anwendungsmöglichkeiten: Beispielsweise lassen sich funktionelle Kraftmessungen an Zellrezeptoren in hohem Durchsatz durchführen. Da die angelegte Maximalkraft über den verwendeten DNA-Kraftsensorstrang eingestellt werden kann, könnte kraftinduzierte Genexpression [17] [18] [19] mit der angelegten Kraft als Parameter untersucht werden. Des Weiteren ließen sich histologische Untersuchungen an Gewebeproben durch höhere Sensitivität und Spezifität verbessern und parallelisieren [20]: Zum einen verringert sich durch den DNA-Kraftsensoransatz der Hintergrund, der von nicht spezifisch bindenden Antikörpern resultiert [11]. Zum anderen lässt sich dieselbe Gewebsprobe auf das Vorhandensein einer Vielzahl von Biomarkern untersuchen [21]. Dies ist in konventionellen Immunofärbungen nicht möglich, weil sich hier fluoreszenzmarkierte Detektionsantikörper in Lösung befinden und die Signale der verschiedenen gebundenen Antikörper überlagern und nicht mehr separierbar sind [22]. Auf dem PDMS-Stempel sollen in Zukunft verschiedene Antikörper angebracht werden, so dass eine Zellkultur auf viele verschiedene Zellmembranproteine untersucht werden kann.

## Literaturverzeichnis Kapitel 6.

- [1] Steinbach, U. 2009. Differentielle Kraftmessungen an Zelloberflächen. Diplomarbeit.
- [2] Krogh, A., B. Larsson, G. Von Heijne, and E. Sonnhammer E. 2001. Predicting transmembrane protein topology with a hidden markov model: application to complete genomes. *J. Mol. Biol.* 305:567-580.
- [3] Beck, V., H. Herold, A. Benge, B. Luber, P. Hutzler, H. Tschesche, H. Kessler, M. Schmitt, H. Geppert, and U. Reuning. 2005. ADAM15 decreases integrin  $\alpha_v\beta_3$ /vitronectin-mediated ovarian cancer cell adhesion and motility in an RGD-dependent fashion. *Int. J. Biochem. Cell Biol.* 37:590-603.
- [4] Hapke, S., H. Kessler, N. A. de Prada, A. Benge, M. Schmitt, E. Lengyel, and U. Reuning. 2001. Integrin  $\alpha_v\beta_3$ /vitronectin interaction affects expression of the urokinase system in human ovarian cancer cells. *J. Biol. Chem.* 276:26340-26348.
- [5] Reichert, J. M., and V. E. Valge-Archer. 2007. Development trends for monoclonal antibody cancer therapeutics. *Nat. Rev. Drug Discov.* 6:349-356.
- [6] Imai, K., and A. Takaoka. 2006. Comparing antibody and small-molecule therapies for cancer. *Nat. Rev. Cancer.* 6:714-727.
- [7] Schrama, D., R. Reisfeld, and J. Becker. 2006. Antibody targeted drugs as cancer therapeutics. *Nat. Rev. Drug Discov.* 5:147-159.
- [8] Wulfkuhle, J., L. Liotta, and E. Petricoin. 2003. Early detection: Proteomic applications for the early detection of cancer. *Nat. Rev. Cancer.* 3:267-275.
- [9] Hartwell, L., D. Mankoff, A. Paulovich, and S. Ramsey. 2006. Cancer biomarkers: a systems approach. *Nat. Biotechnol.* 24:905-908.
- [10] Cho, W. C. S. 2007. Contribution of oncoproteomics to cancer biomarker discovery. *Mol. Cancer.* 6:25.
- [11] Blank, K., T. Mai, I. Gilbert, S. Schiffmann, J. Rankl, R. Zivin, C. Tackney, T. Nicolaus, K. Spinnler, F. Oesterhelt, M. Benoit, H. Clausen-Schaumann and H. E. Gaub. 2003. A force-based protein biochip. *Proc. Natl. Acad. Sci. USA.* 100:11356-11360.
- [12] Essevaz-Roulet, B., U. Bockelmann, and F. Heslot. 1997. Mechanical separation of the complementary strands of DNA. *Proc. Natl. Acad. Sci. USA.* 94:11935-11940.
- [13] Morfill, J., K. Blank, C. Zahnd, B. Luginbuhl, F. Kuhner, K. E. Gottschalk, A. Pluckthun, and H. E. Gaub. 2007. Affinity-Matured Recombinant Antibody Fragments Analyzed by Single-Molecule Force Spectroscopy. *Biophys. J.* 93:3583-3590.
- [14] Sanchez, J. F., J. Lescar, V. Chazalet, A. Audfray, J. Gagnon, R. Alvarez, C. Breton, A. Imbert, and E. P. Mitchel. 2006. Biochemical and structural analysis of *Helix pomatia* agglutinin. A hexameric lectin with a novel fold. *J. Biol. Chem.* 281:20171-20180.
- [15] Brooks, S., D. Hall, and I. Buley. 2001. GalNAc glycoprotein expression by breast cell lines, primary breast cancer and normal breast epithelial membrane. *Br J Cancer.* 85:1014-1022.

- [16] Grandbois, M., W. Dettmann, M. Benoit, and H. E. Gaub. 2000. Affinity imaging of red blood cells using an atomic force microscope. *J. Histochem. Cytochem.* 48:719-724.
- [17] Vogel, V. 2006. Mechanotransduction involving multimodular proteins: Converting force into biochemical signals. *Annu. Rev. Biophys. Biomol. Struct.* 35:459-488.
- [18] Puchner, E. M., A. Alexandrovich, A. L. Kho, U. Hensen, L. V. Schäfer, B. Brandmeier, F. Gräter, H. Grubmüller, H. E. Gaub and M. Gautel M. 2008. Mechanoenzymatics of titin kinase. *Proc. Natl. Acad. Sci. USA.* 105:13385-13390.
- [19] Katsumi, A. 2003. Integrins in Mechanotransduction. *J. Biol. Chem.* 279:12001-12004.
- [20] Kallioniemi, O. P., U. Wagner, J. Kononen, and G. Sauter. 2001. Tissue microarray technology for high-throughput molecular profiling of cancer. *Hum. Mol. Genet.* 10:657-662.
- [21] Blank, K., A. Lankenau, T. Mai, S. Schiffmann, I. Gilbert, S. Hirler, C. Albrecht, M. Benoit, H. E. Gaub and H. Clausen-Schaumann. 2004. Double-chip protein arrays: force-based multiplex sandwich immunoassays with increased specificity. *Anal. Bioanal. Chem.* 379:974-981.
- [22] Portela-Gomes, G. M. 2004. Immunostaining Techniques for Co-Localization of Multiple Peptide Antigens in Light Microscopy. CRC Press, Boca Raton.

## 7. AD-WANDLER MOLEKÜLARER KRÄFTE

Dieses Kapitel beschäftigt sich mit der Fragestellung, ob Konzepte der analog-digitalen Signalverarbeitung auch für den DNA-Kraftsensor herangezogen werden können. Eine ausführlichere Diskussion der Experimente und Ergebnisse findet sich in der Diplomarbeit von Florian A. Dehmelt [1].

**Einleitung.** Der Analog-Digitalwandler (AD-Wandler) ist ein Konzept, das aus der elektrischen Signalverarbeitung kommt und hauptsächlich in diesem Gebiet Anwendung findet [1] [3]. Die zugrunde liegende Theorie und mathematischen Hilfsmittel [4] sind aber keineswegs auf das Gebiet der Elektronik beschränkt. Das grundlegende Element eines AD-Wandlers ist der Komparator (Abbildung 13a). Der Komparator verarbeitet zwei analoge Eingaben zu einer booleschen (digitalen) Antwort. Typischerweise ist die eine analoge Eingabe das zu untersuchende Signal und die andere analoge Eingabe ein Referenzsignal. Die Ausgabe ist 1 falls das Signal größer ist als die Referenz und 0 falls das Signal kleiner ist als die Referenz. Um das kontinuierliche Eingangssignal genauer zu quantifizieren, werden häufig Parallel-Umsetzer verwendet (Abbildung 14a). Diese basieren auf einer Parallelschaltung vieler Komparatoren, um simultan das gleiche Eingangssignal mit vielen verschiedenen Referenzen zu vergleichen. Je engmaschiger die Referenzen gewählt werden, desto präziser kann damit der digitale Wert des analogen Signals bestimmt werden.

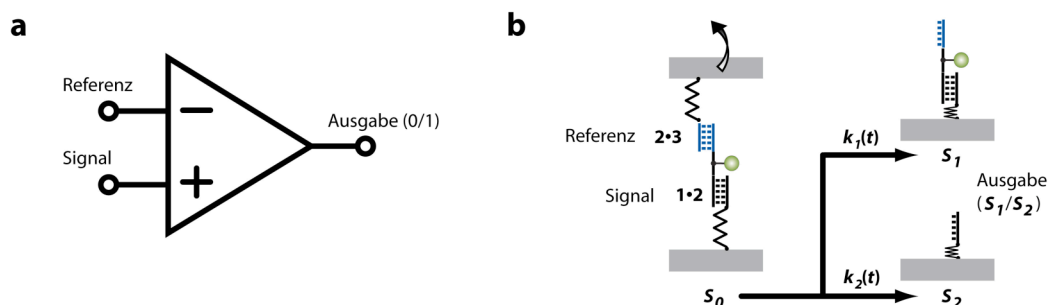


**Abbildung 13.** Vergleich zwischen dem elektronischen Komparator und dem DNA-Kraftsensorprinzip. (a) Der Komparator besitzt einen analogen Referenzeingang und einen analogen Signaleingang. Die beiden Eingänge werden miteinander verglichen und in ein boolesches (digitales) Ausgabesignal umgewandelt. Die Ausgabe ist 0 falls das Signal größer als die Referenz ist und 1 im umgekehrten Fall. (b) Der DNA-Kraftsensor besteht aus einer **1·2** DNA-Bindung (Signal) und einer **2·3** DNA-Bindung (Referenz), die in Serie zwischen zwei Oberflächen eingespannt sind. Werden die beiden Oberflächen separiert, öffnet sich mit einer höheren Wahrscheinlichkeit die **1·2** Bindung, falls die **2·3** DNA-Bindung stabiler als diese ist ( $S_2$ ). Die **2·3** Bindung öffnet sich im umgekehrten Fall ( $S_1$ ).

**Messprinzip.** Die Ähnlichkeit eines Komparators mit dem in dieser Dissertation vorgestellten DNA-Kraftsensors ist bemerkenswert. Hier werden ebenfalls zwei analoge Signale, die Abrisskraft einer zu untersuchenden DNA **1·2** und die Abrisskraft des DNA-Kraftsensors **2·3**, miteinander verglichen (Abbildung 13b). Wie in den vorhergehenden Kapiteln beschrieben werden die zu untersuchende DNA **1·2** und der DNA-Kraftsensor **2·3** in Serie zwischen zwei Oberflächen eingespannt. Das Verbindungsstück **2** ist dabei mit einer Fluoreszenzmarkierung versehen. Werden die beiden Oberflächen separiert, baut sich in den **1·2·3** Ketten eine Kraft auf bis sich eine der beiden Bindungen öffnet. Ist die Abrisskraft des DNA-Kraftsensors größer als die Abrisskraft der zu untersuchenden DNA, verbleibt der Fluoreszenzmarker auf der Seite des DNA-Kraftsensors. Andernfalls verbleibt der Fluoreszenzmarker auf der Seite der zu untersuchenden DNA. Um einen Parallelumsetzer zu realisieren, wird auf einem Biochip an verschiedenen Stellen die Abrisskraft der gleichen zu untersuchenden DNA-Bindung mit den Abrisskräften verschieden eingestellter DNA-Kraftsensoren verglichen (Abbildung 14b).

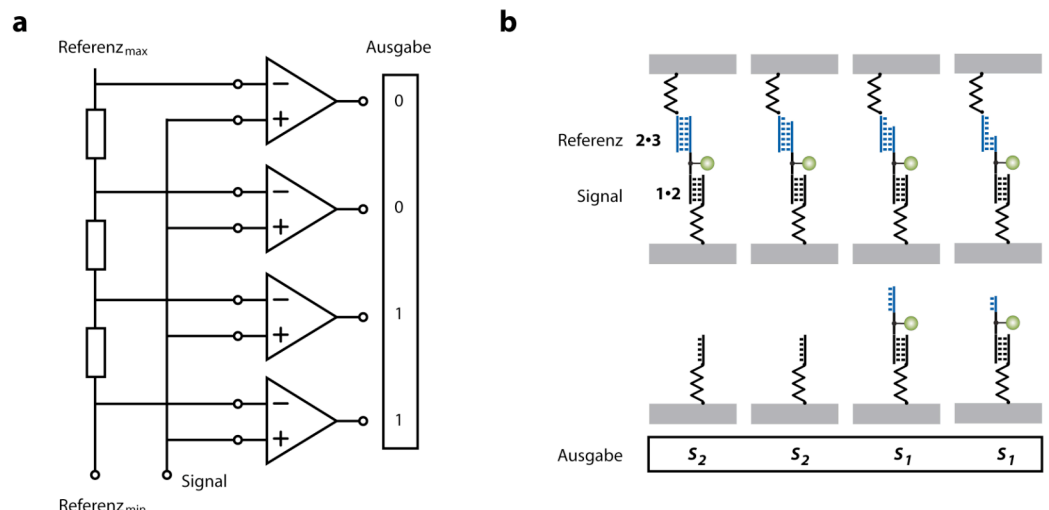


**Abbildung 14.** Flash-AD-Wandler. (a) Das analoge Eingangssignal wird im Flash-Wandler gleichzeitig von mehreren Komparatoren mit den über einen mehrstufigen Spannungsteiler erzeugten Referenzgrößen verglichen. (b) Die gleiche **1·2** DNA-Bindung (Signal) wird simultan gegen verschiedene **2·3** DNA-Kraftsensoren (Referenzen) verglichen.

**Zusammenfassung der Experimente.** In Modellversuchen untersuchten wir das Abrissverhältnis zwischen ein und demselben zwanzig basenpaarlangen DNA-Doppelstrang **1·2** und sechs verschiedenen DNA-Kraftsensoren **2·3** von einer Länge zwischen zwanzig und fünfundvierzig Basenpaaren (Abbildung 14b). Das Verhältnis von gebrochenen DNA-Kraftsensoren zu untersuchender DNA ist in Abbildung 15a zu sehen. Für das normalisierte Fluoreszenzverhältnis einer zwanzig basenpaarlangen DNA, die gegen eine identische Bindung verglichen wird, ermittelten wir reproduzierbar 62%. Theoretisch erwartet wird eine Fluoreszenzverteilung von 50%. Für diese Abweichung gibt es verschiedene Erklärungsmöglichkeiten: Zum einen könnte das DNA-Konstrukt nicht so synthetisiert worden sein wie erwartet, weil beispielsweise eine Base fehlt. Solch eine fehlerhafte Synthesierung lässt sich mittels konventionellen DNA-Schmelzkurven feststellen, was jedoch experimentell noch nicht überprüft wurde. Zum anderen könnte die Symmetrie gebrochen sein, weil sich eine Bindung näher an Glas und die andere näher an PDMS befindet. Verschiedene Mikroumgebungen (Ionenkonzentrationen) führen zu verschiedenen Abrisskräften der DNA-Bindungen.

Mit zunehmender Länge des DNA-Kraftsensors **2·3** nimmt das Fluoreszenzverhältnis ab. Dies entspricht den Erwartungen: ein längerer DNA-Doppelstrang mit mehr Basenpaaren, resultiert in einer höheren Abrisskraft [8] [9]. Die Abrisskraft des DNA-Kraftsensors **2·3** ist also höher als die Abrisskraft der zu untersuchenden DNA **1·2**, weshalb mehr Fluorophore auf der Seite des Kraftsensors landen. Interessanterweise ergibt sich keine scharfe ja-oder-nein Entscheidung. Dies liegt an einem Effekt, der in der Elektronik weitläufig als Quantisierungsrauschen bezeichnet wird [4] [5]. Quantisierungsrauschen tritt auf, wenn das Rauschen, welches auf dem Signal liegt, größer ist als der Abstand zwischen zwei Referenzen. Dadurch treten im zeitlichen Mittel beide Zustände 0 und 1 auf. Der molekulare AD-Wandler verhält sich ganz analog: die Abrisskräfte unterliegen einer Verteilung, weil der Abriss ein thermisch getriebener Prozess ist [6] [7]. Typischerweise sind DNA-Abrisskraftverteilungen etwa 5-10 pN breit [8] [9]. Die Verschiebung der wahrscheinlichsten Abrisskraft durch die Verlängerung des DNA-Kraftsensors befindet sich in einer ähnlichen Größenordnung (schematisch dargestellt in Abbildung 15b). Daher beobachten wir eine graduelle Verschiebung des Fluoreszenzverhältnisses von 62% für einen 20 basenpaarlangen DNA-Kraftsensor, bis 30% für den 45 basenpaarlangen DNA-Kraftsensor.

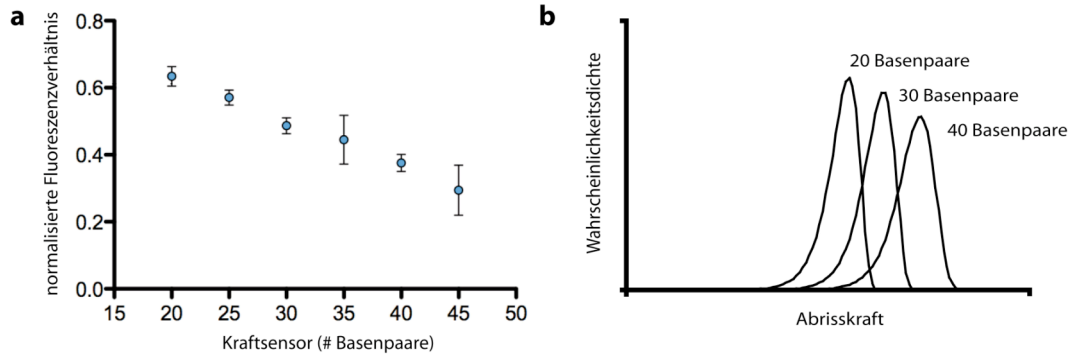


**Abbildung 15.** (a) Fluoreszenzverhältnisse für den DNA-Kraftsensor AD-Wandler. Die gleiche zwanzig basenpaar lange **1·2** Bindung wurde mit 20, 25, 30, 35, 40 und 45 basenpaar lange **2·3** DNA-Kraftsensoren verglichen. (b) Schematische Darstellung der Abrisskraftverteilung verschieden langer DNA-Doppelstränge. Die Verteilungen überlappen sich signifikant, weshalb die Fluoreszenzverhältnisse nicht genau 0 und 1 ergeben, sondern verschmiert sind. Dieser Effekt ist dem Quantisierungsrauschen elektrischer AD-Wandler ähnlich.

**Ausblick.** In ersten Experimenten zeigten wir, wie sich ein einfacher molekularer Kraft-AD-Wandler mit Hilfe des DNA-Kraftsensors realisieren lässt. Bis jetzt fehlt jedoch eine zufrieden stellende theoretische Beschreibung dieser Experimente. Zwar wurde im Rahmen dieser Dissertation eine Theorie zur kraftinduzierten Separation von doppelsträngiger DNA entwickelt [M1], jedoch ist die Abrisskraftverteilung stark abhängig von der Separationsgeschwindigkeit der beiden Oberflächen. Diese lässt sich auf Grund der elastischen Eigenschaften des PDMS-Stempels nicht ermitteln [10]. Drei Strategien würden jedoch die theoretische Beschreibung trotzdem erlauben. (1) Die in Kapitel IV und [M1] erarbeitete Theorie zur DNA-Separation wird benutzt, um durch DNA-DNA-Kraftsensormessungen das System zu eichen. (2) Der PDMS-Stempel wird durch eine starre Oberfläche ersetzt, was eine genaue Ausrichtung der beiden Oberflächen voraussetzt. Dass dies technisch realisierbar ist, wurde bereits am Surface Force Aparatus demonstriert [11]. (3) Eine von Albrecht und Kollegen publizierte Methode [10] macht sich der optischen Interferenzen, welche durch die Biochip- und PDMS-Stempeloberfläche entstehen, zunutze, um die Separationsgeschwindigkeit zwischen den Oberflächen abzuschätzen. Eine Weiterentwicklung dieser Methode ermöglicht unter Umständen die Separationsgeschwindigkeit zu quantifizieren.

## Literaturverzeichnis Kapitel 7.

- [1] Dehmelt, F. A. 2009. Molecular Force Balances as Biological Analog-to-Digital Converters. Diplomarbeit.
- [2] Walden, R. H. 1999. Analog-to-digital converter survey and analysis. IEEE Journal on Selected Areas in Communications 17:539-550.
- [3] Horowitz, P., and W. Hill 1989. The Art of Electronics, Cambridge University Press, Second edition, Cambridge.
- [4] Widrow, B., and I. Kollár. 2008. Quantization Noise: Roundoff Error in Digital Computation, Signal Processing, Control, and Communications. Cambridge University Press, Cambridge.
- [5] Gray, R. M., D. L. Neuhoff. 2000. Quantization. IEEE Press, Piscataway, NJ.
- [6] Evans, E. and K. Ritchie. 1997. Dynamic strength of molecular adhesion bonds. Biophys. J., 72:1541-1555.
- [7] Hänggi, P., P. Talkner, and M. Borkovec. 1990. Reaction-rate theory: fifty years after Kramers. Rev. Mod. Phys. 62:251-342.
- [8] Strunz, T., K. Oroszlan, R. Schäfer and H. Güntherodt. 1999. Dynamic force spectroscopy of single DNA molecules. Proc. Natl. Acad. Sci. USA. 96:11277-11282.
- [9] Morfill, J., F. Kuhner, K. Blank, R. Lugmaier, J. Sedlmair and H. E. Gaub. 2007. B-S Transition in Short Oligonucleotides. Biophys. J. 93:2400-2409.
- [10] Albrecht, C., G. Neuert, R. Lugmaier, and H. E. Gaub. 2008. Molecular Force Balance Measurements Reveal that Double-Stranded DNA Unbinds Under Force in Rate-Dependent Pathways. Biophys. J. 94:4766-4774.
- [11] Israelachvili, J. N., 1992. Intermolecular and Surface Forces. Academic Press, London.

## 8. SCHLUSSBEMERKUNG

Die vorliegende Arbeit „*Auf Kraft basierender Nachweis biomolekularer Wechselwirkungen im Chipformat: Anwendung und Theorie des DNA-Kraftsensors*“ demonstriert den Grad der Kontrolle über molekulare Einheiten wie den DNA-Kraftsensor, der mittels der Konvergenz von nano- und biotechnologischer Methoden möglich geworden ist. Gleichzeitig stellt die Arbeit anschaulich dar wie aus rein wissenschaftlichen Studien – in diesem Fall der Untersuchung der mechanischen Eigenschaften von DNA [1] [2] und der DNA als molekularem Kraftsensor [3] [4] [5] [6] [7] – mehrere für die Industrie relevante Verfahren entstehen können. Einige davon wurden in den vorangegangen Kapiteln bereits vorgestellt. Dazu gehört der Transkriptionsfaktor-Biochip (Kapitel 4) [P1] [P2], ein auf Aptameren basierender Proteinbiochip (Kapitel 5) [P3] und ein Biochip für den Nachweis von Membranproteinen in Gewebeschnitten und Zellkulturen (Kapitel 6). Ein weiteres Projekt wurde kürzlich zusammen mit der Firma Randox Laboratories initiiert. Randox entwickelt, fabriziert und vertreibt Sandwich-ELISA-Biochips [8], zu deren Anwendungsgebieten eine Vielzahl von diagnostischen Verfahren gehören [9]. In einer gemeinschaftlichen Studie soll evaluiert werden, ob der DNA-Kraftsensor die Sensitivität, Spezifität und den Durchsatz von Sandwich-ELISA-Biochips erhöht [4] [5]. Die zahlreichen Anwendungsmöglichkeiten, die auf der Technologie des DNA-Kraftsensors basieren, werden auch in Zukunft die Forschung und Entwicklung in diesem Bereich vorantrieben.

Der DNA-Kraftsensor ist dabei nur ein Beispiel dafür, wie das Verständnis und die Kontrolle über die Eigenschaften nanometergroßer Strukturen die Grundlage der alltäglichen Technik von morgen liefert. Schon heute setzt Pacific Bioscience – ein Startup gegründet von Harold G. Craighead und Watt W. Webb – molekulare Sequenziermaschinen in Nanostrukturen ein, um die Dechiffrierung des menschlichen Genoms für weniger als \$1.000 zu ermöglichen [12]. Nanomaterialien sind auch die Grundlage der nächsten Generation schmutzabweisender Oberflächen [13] und selbsttonender Gläser [14]. Man darf also gespannt sein, ob die Nanotechnologie unser Leben auf ähnliche Art und Weise ändern wird wie die Halbleitertechnologie es in den letzten Jahrzehnten getan hat.

## Literaturverweise Kapitel 8.

- [1] Cluzel, P., A. Lebrun, C. Heller, R. Lavery, J. Viovy, D. Chatenay and F. Caron. 1996. DNA: an extensible molecule. *Science* 271:792-794.
- [2] Rief, M., H. Clausen-Schaumann, and H. E. Gaub. 1999. Sequence-dependent mechanics of single DNA molecules. *Nat. Struct. Biol.* 6:346-349.
- [3] Albrecht, C., K. Blank, M. Lalic-Multhaler, S. Hirler, T. Mai, I. Gilbert, S. Schiffmann, T. Bayer, H. Clausen-Schaumann, and H. E. Gaub. 2003. DNA: a programmable force sensor. *Science*. 301:367-370.
- [4] Blank, K., A. Lankenau, T. Mai, S. Schiffmann, I. Gilbert, S. Hirler, C. Albrecht, M. Benoit, H. E. Gaub, and H. Clausen-Schaumann. 2004. Double-chip protein arrays: force-based multiplex sandwich immunoassays with increased specificity. *Anal. Bioanal. Chem.* 379:974-981.
- [5] Blank, K., T. Mai, I. Gilbert, S. Schiffmann, J. Rankl, R. Zivin, C. Tackney, T. Nicolaus, K. Spinnler, F. Oesterhelt, M. Benoit, H. Clausen-Schaumann, and H. E. Gaub. 2003. A force-based protein biochip. *Proc. Natl. Acad. Sci. USA*. 100:11356-11360.
- [6] Neuert, G., C. H. Albrecht, and H. E. Gaub. 2007. Predicting the Rupture Probabilities of Molecular Bonds in Series. *Biophys. J.* 93:1215-1223.
- [7] Albrecht, C., G. Neuert, R. Lugmaier, and H. E. Gaub. 2008. Molecular Force Balance Measurements Reveal that Double-Stranded DNA Unbinds Under Force in Rate-Dependent Pathways. *Biophys. J.* 94:4766-4774.
- [8] Fitzgerald, S. P., J. V. Lamont, R. I. McConnell, and E. O. Benchikh. 2005. Development of a high-throughput automated analyzer using biochip array technology. *Clin. Chem.* 51:1165-1176.
- [9] Randox Laboratories Biochip Immunoassays. <http://www.randox.com/>.
- [10] Blank, K., A. Lankenau, T. Mai, S. Schiffmann, I. Gilbert, S. Hirler, C. Albrecht, M. Benoit, H. E. Gaub, and H. Clausen-Schaumann. 2004. Double-chip protein arrays: force-based multiplex sandwich immunoassays with increased specificity. *Anal. Bioanal. Chem.* 379:974-981.
- [11] Blank, K., T. Mai, I. Gilbert, S. Schiffmann, J. Rankl, R. Zivin, C. Tackney, T. Nicolaus, K. Spinnler, F. Oesterhelt, M. Benoit, H. Clausen-Schaumann, and H. E. Gaub. 2003. A force-based protein biochip. *Proc. Natl. Acad. Sci. USA*. 100:11356-11360.
- [12] Levene, M. J., J. Korlach, S. W. Turner, M. Foquet, H. G. Craighead, and W. W. Webb. 2003. Zero-mode waveguides for single-molecule analysis at high concentrations. *Science*. 299:682-686.
- [13] Solga, A., Z. Cerman, B. F. Striffler, M. Spaeth, and W. Barthlott. 2007. The dream of staying clean: Lotus and biomimetic surfaces. *Bioinspiration Biomimetics*. 2:1-9.
- [14] Ohko, Y., T. Tatsuma, T. Fujii, K. Naoi, C. Niwa, Y. Kubota, and A. Fujishima. 2003. Multicolour photochromism of TiO<sub>2</sub> films loaded with silver nanoparticles. *Nat. Mat.* 2:29-31.

## ANHANG

### A.1. PUBLIKATIONEN

#### P1:

Dose, C.\* , **D. Ho\***, H. E. Gaub, P. B. Dervan, and C. H. Albrecht. 2007. Recognition of "Mirror-Image" DNA by Small Molecules. *Angewandte Chemie, International Edition*. 46:8384-8387.

Bemerkung: (\*) geteilte Erstautorschaft.

#### P2:

**Ho, D.**, C. Dose, C. H. Albrecht, P. Severin, K. Falter, P. B. Dervan, and H. E. Gaub. 2009. Quantitative Detection of Small Molecule/DNA Complexes Employing a Force-Based and Label-Free DNA-Microarray. *Biophysical Journal*. 96:4661-4671.

#### P3:

**Ho, D.**, K. Falter, P. Severin, H. E. Gaub. 2009. DNA as a Force Sensor in an Aptamer-Based Biochip for Adenosine. *Analytical chemistry*. 81:3159-3164.

## Recognition of “Mirror-Image” DNA by Small Molecules\*\*

Christian Dose, Dominik Ho, Hermann E. Gaub, Peter B. Dervan,\* and Christian H. Albrecht\*

Pyrrole-imidazole polyamides are synthetic oligomers with affinities and specificities for DNA comparable to naturally occurring DNA-binding proteins.<sup>[1]</sup> The molecular recognition of the minor groove of DNA by polyamides arises from interactions of pairs of the aromatic amino acids *N*-methylpyrrole, *N*-methylimidazole, and *N*-methylhydroxypyrrrole with the edges of Watson–Crick DNA base pairs.<sup>[2]</sup> Introduction of an amino group in the *R* configuration to the  $\gamma$ -turn unit of hairpin polyamide oligomers confers a chiral substituent and increases the DNA-binding affinity, whereas *S*-configured molecules provide lower affinities relative to unsubstituted hairpins.<sup>[3]</sup> L-DNA is the “mirror-image” of the natural occurring D conformation<sup>[4]</sup> and has been applied in nucleic acid chemistry for developing anti-HIV agents,<sup>[5]</sup> in the study of aptamers,<sup>[6]</sup> transcription factors,<sup>[7]</sup> mechanisms of antitumor drugs,<sup>[8]</sup> and as microarray platforms.<sup>[9]</sup> Herein we report that mirror-image hairpin polyamides can distinguish L-DNA in presence of natural DNA. To detect this specificity we introduce a symmetric molecular force balance to simultaneously measure rupture forces of diastereomeric DNA–ligand complexes. We show that the chirality of polyamides is suitable to enhance the sensitivity of the measurement to determine effects of subtle structural changes in a single experiment.

Single-molecule force spectroscopy that operates in the range of piconewton forces has contributed detailed insights into the understanding of host–ligand interactions.<sup>[10]</sup> A differential approach to study binding forces was recently introduced, wherein rupture forces of a target complex are directly probed against a known reference complex.<sup>[11]</sup> This differential measurement format has been applied to distin-

guish single base-pair mismatches within 30mer DNA duplexes,<sup>[12]</sup> for studying differences of antibody/antigen interactions,<sup>[13]</sup> and to eliminate cross-reactions on protein microarrays.<sup>[14]</sup> Although a large number of molecules are measured simultaneously, the actual measurement is performed at a single-molecule level. One duplex is compared to one reference duplex.

Our design of the molecular force balance comprises D-DNA duplex **1·2**, which is covalently linked to a glass slide (bottom), and L-DNA duplex **3·4**, which is attached by a biotin–streptavidin bond to a silicone stamp (top, Figure 1a). These DNA duplexes contain identical DNA sequences (20 base pairs) and are linked by an oligothymine spacer (12 bases) that is fluorescently labeled. Upon separation of the two surfaces, force is applied to the molecular balance until one of the duplexes ruptures. If no ligand is bound to the balance, there is a 50% probability for each of the duplexes to survive and the fluorophore will distribute equally between stamp and slide. When ligands are bound to one of the duplexes, the symmetry of the assay is broken and, as a result, there is a higher probability for the fluorophore to end up on the side of the stronger DNA duplex. Parent hairpin polyamide **5**, and mirror-image polyamides (*R*)-**6** and (*S*)-**6** were programmed to bind the six-base-pair DNA sequence 5'-TGGTCA-3' embedded in D-DNA and L-DNA duplexes **1·2** and **3·4**, respectively (Figure 1b). To investigate the difference in rupture forces, we first examined chiral hairpin polyamide (*R*)-**6** in the molecular force balance. The survival probability of D-DNA duplex **1·2**, which corresponds to the remaining Cy3-fluorescence intensity on the glass slide, was monitored in presence of increasing polyamide concentrations (0–100 nm). Background fluorescence intensities, caused by incomplete biotin–streptavidin bond formations, were subtracted to ensure that the determined values were only the result of ruptured DNA complexes.<sup>[12]</sup> Figure 2a shows that the survival probability was significantly changed by increasing the polyamide concentration; for example, the probability was 0.69 at 25 nm. Interestingly, at 100 nm (*R*)-**6**, a reduced survival probability of 0.56 was observed. We assume that both DNA duplexes were occupied at higher concentrations of polyamide (*R*)-**6**, but stabilization of D-DNA duplex relative to L-DNA duplex was still favored. Mirror-image polyamide (*S*)-**6** should bind to the L-DNA duplex rather than the D-DNA duplex. Indeed, addition of (*S*)-**6** to the molecular force balance provided an inverted analysis course containing a survival probability of 0.21 at 25 nm. Removal of the chiral information in the polyamides (as in **5**) abolished the mirror-image specificity, as represented by an almost consistent survival probability course across the entire concentration gradient.

Next, we examined the difference in rupture forces between D-DNA duplex and L-DNA duplex by introducing

[\*] Dr. C. Dose,<sup>[+]</sup> Prof. P. B. Dervan  
Division of Chemistry and Chemical Engineering  
California Institute of Technology  
Pasadena, California 91125 (USA)  
Fax: (+1) 626-683-8753  
E-mail: dervan@caltech.edu  
Homepage: <http://dervan.caltech.edu/>  
D. Ho,<sup>[+]</sup> Prof. H. E. Gaub, Dr. C. H. Albrecht  
Lehrstuhl für Angewandte Physik and Center for Nanoscience,  
Ludwig-Maximilians-Universität  
Amalienstrasse 54, 80799 Munich (Germany)  
Fax: (+49) 89-2180-2050  
E-mail: christian.albrecht@physik.uni-muenchen.de

[+] These authors contributed equally to this work.

[\*\*] Support was provided by the National Institutes of Health, the Deutsche Forschungsgemeinschaft, and the Fonds der Chemischen Industrie. C.D. is grateful to the Alexander von Humboldt foundation for a postdoctoral fellowship. D.H. is grateful to the Elite Network of Bavaria (IDK-NBT) for a doctoral fellowship.

 Supporting information for this article is available on the WWW under <http://www.angewandte.org> or from the author.

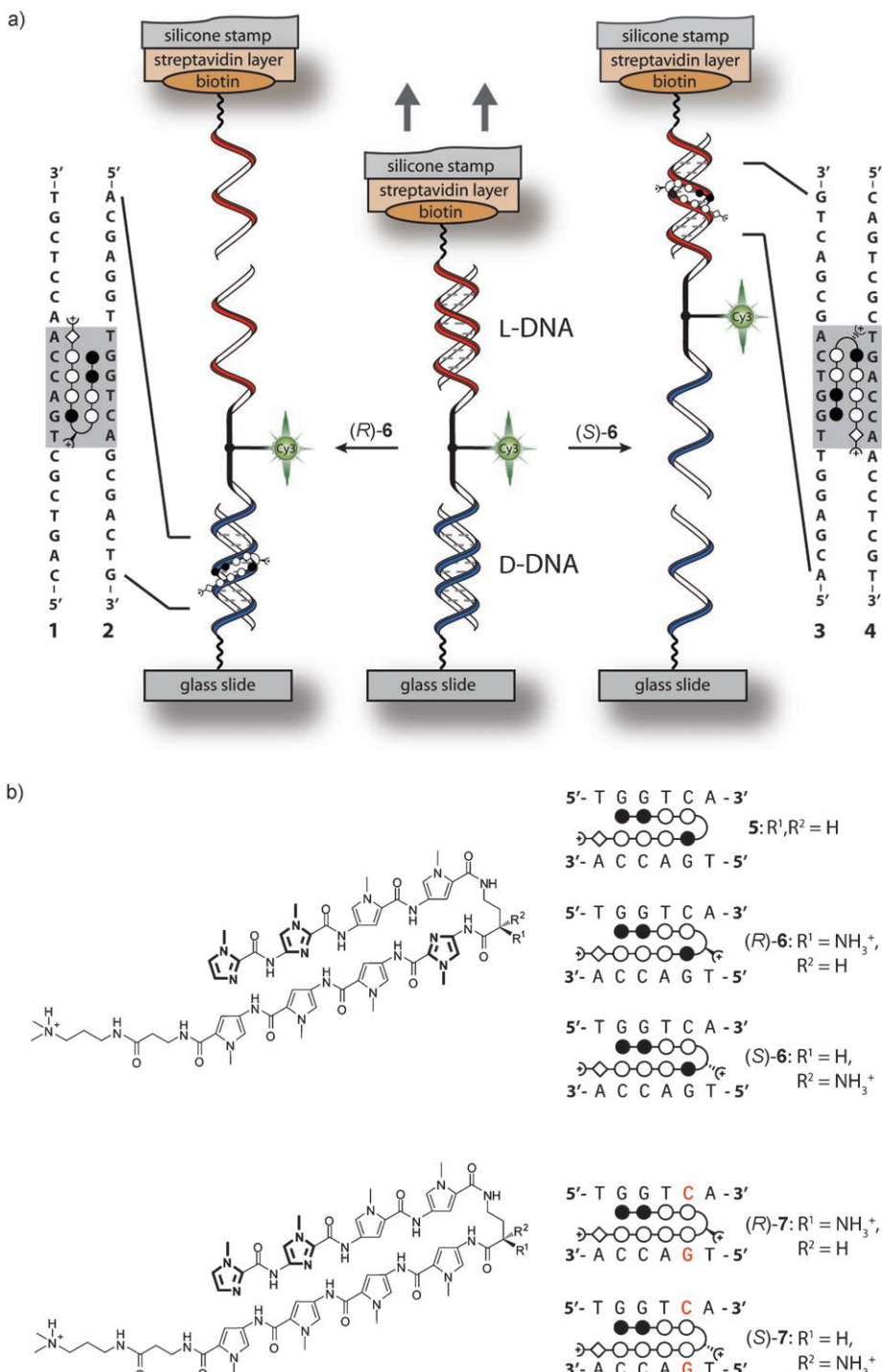


**Figure 1.** a) Schematic representation of the molecular force balance containing d-DNA and L-DNA duplexes in the presence of chiral hairpin polyamides (R)-6 or (S)-6; the bases indicated by filled circles are those highlighted in the corresponding structures shown in (b). b) Chemical structures and binding motifs of matched hairpin polyamides 5, (R)-6, (S)-6, and single-base-pair-mismatched compounds (R)-7, (S)-7. Mismatched positions are represented by red-colored base pairs.

single-base-pair-mismatched polyamides (R)-7 and (S)-7 to the molecular balance. Both chiral polyamides led to changes in survival probability: 0.59 and 0.27, respectively, at 25 nm concentration (Figure 3). Comparison to the matched polyamides revealed that the change in signal was decreased

approximately 0.6-fold. We assumed that the differences in survival probability were caused by less stabilized reference complexes as a result of the discriminative power arising from chirality and mismatched DNA base-pairing of polyamides (R)-7 and (S)-7. This combination reduces the sensitivity of the molecular force balance for measuring differences between matched and single-base-pair-mismatched DNA–polyamide complexes. To increase the sensitivity, we applied a mixture of matched R-configured polyamide (R)-6 and single-base-pair-mismatched S-configured polyamide (S)-7 to the molecular force balance (Figure 3). As a result, a single-base-pair-mismatched DNA–polyamide complex is directly compared with a perfectly matched DNA–polyamide complex. Indeed, using a 1:1 mixture of (R)-6:(S)-7 significantly increased the survival probability relative to the parent single-base-pair-mismatched analysis (0.66 at 25 nm concentration). An almost identical change (survival probability = 0.21) was observed by using the complementary polyamide mixture (S)-6:(R)-7. As a control, differential force analysis in the presence of enantiomeric mismatched polyamides (R)-7:(S)-7 gave a balanced ratio. It can be concluded that the resolution of the measurement for matched and single-base-pair-mismatched DNA–polyamide complexes is enhanced by applying mixtures of chiral hairpin polyamides. By this means, polyamides provide a versatile tool to modify reference duplexes for improving the sensitivity of the molecular force balance.

To ensure that the differences in rupture forces were a result of the DNA duplex stabilization by hairpin polyamides, we compared the melting temperatures ( $T_m$ ) of the DNA–polyamide complexes.<sup>[15]</sup>

Melting analysis containing nonchiral polyamide 5 revealed an identical increase of 7°C for complexes 1-2-5 ( $T_m = 77^\circ\text{C}$ ) and 3-4-5 ( $T_m = 77^\circ\text{C}$ ) relative to the d-DNA and L-DNA duplexes 1-2 and 3-4 ( $T_m = 70^\circ\text{C}$ ), respectively (Table 1). Addition of chiral polyamide (R)-6 to d-DNA duplex 1-2

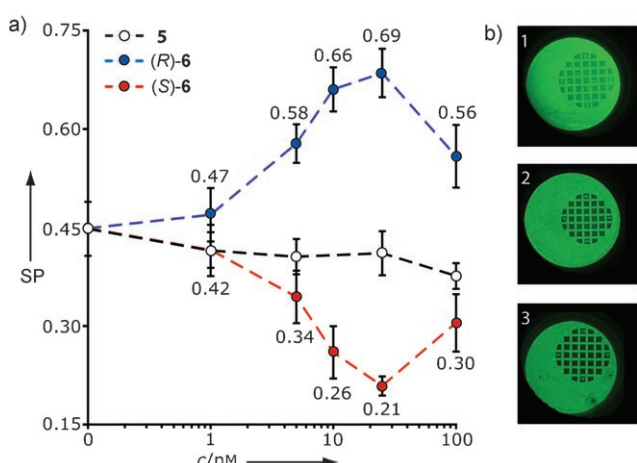


**Figure 2.** a) Molecular force balance analysis in the presence of increasing concentrations of polyamides 5 (white circles), (R)-6 (blue circles), and (S)-6 (red circles). The survival probability (SP) represents the Cy3-fluorescence intensity on the glass slide after separation of the silicone stamp. b) Cy3-fluorescence images of a spot on the glass slide showing the imprint of the silicone stamp after separation. Images 1, 2, and 3 represent the fluorescence intensities in presence of 25 nm polyamide (R)-6, 5, and (S)-6, respectively.

**Table 1:** Melting temperatures for DNA–polyamide complexes.<sup>[a]</sup>

Polyamide	D-DNA duplex [°C] 1·2	$\Delta T_m$ [°C]	L-DNA duplex [°C] 3·4
–	70	–	70
5	77	–	77
(R)-6	83	8	75
(S)-6	75	8	83
(R)-7	76	5	71
(S)-7	71	5	76

[a] Values reported are the mean values of at least three melting temperature measurements.

provided a higher stabilization leading to a  $T_m = 83^\circ\text{C}$  for complex **1·2-(R)-6**. In contrast, melting temperature of L-DNA–polyamide complex **3·4-(R)-6** was significantly lower ( $T_m = 75^\circ\text{C}$ ) and revealed a  $\Delta T_m$  value of  $8^\circ\text{C}$ , which confirms a binding preference of polyamide (R)-6 for D-DNA duplex **1·2**. An identical value of  $\Delta T_m = 8^\circ\text{C}$  was observed for DNA–polyamide complexes **1·2-(S)-6** and **3·4-(S)-6**. As expected, melting analysis of DNA–polyamide complexes **1·2-(R)-7** ( $T_m = 76^\circ\text{C}$ ) and **3·4-(R)-7** ( $T_m = 71^\circ\text{C}$ ), containing single-base-pair-mismatched polyamide (R)-7, revealed a decrease in stabilization leading to a reduced  $\Delta T_m$  value of  $5^\circ\text{C}$  relative to the matched complexes. This result was confirmed by an identical difference in  $T_m$  values for complexes **1·2-(S)-7** ( $T_m = 71^\circ\text{C}$ ) and **3·4-(S)-7** ( $T_m = 76^\circ\text{C}$ ).

In summary, we have introduced a symmetric molecular force balance by using the mirror-image forms of DNA as differentiation modules. A single chiral amine substituent of enantiomeric hairpin polyamides affords diastereoselective complexes for D-DNA and L-DNA duplexes. This feature expands the scope of polyamides and provides an easy tool to modify reference complexes to increase the rupture force resolution of the molecular force balance. The investigations

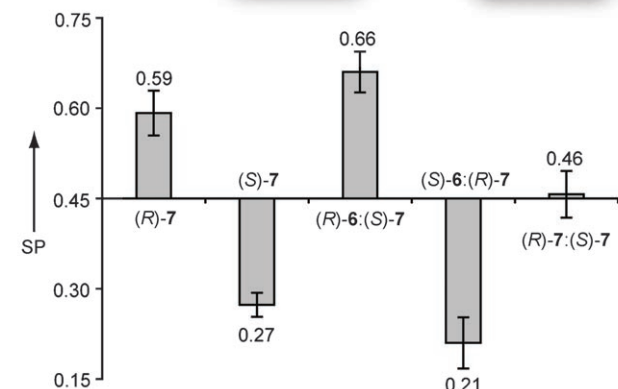
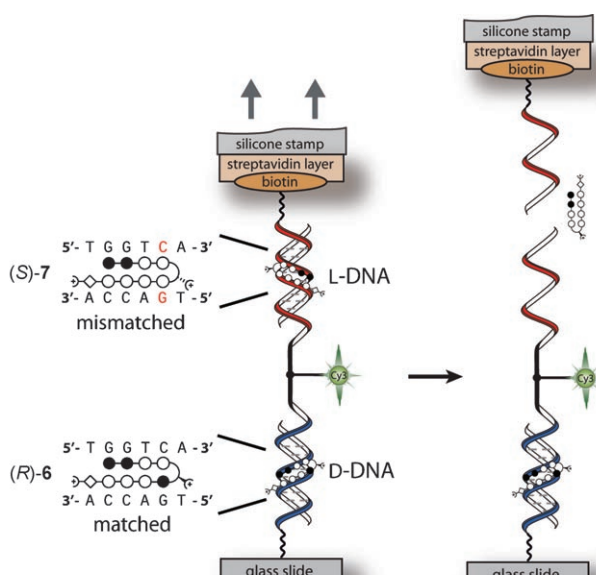


**Figure 3.** Schematic representation of the molecular force balance for measuring mixtures of polyamides and analysis data of single-base-pair-mismatched polyamides (R)-7 and (S)-7 as well as polyamide mixtures (1:1) of (R)-6, (S)-6, (R)-7, and (S)-7, respectively, at 25 nm concentration (SP = survival probability).

demonstrate the potential to determine effects of structural changes within a single experiment. Because of its sensitivity and amenability to high-throughput screenings, one could imagine exploring further chiral DNA-binding molecules by the molecular force balance, for example, intercalators, transcription factors, and restriction enzymes.

Received: July 6, 2007

Revised: August 8, 2007

Published online: September 26, 2007

**Keywords:** chiral resolution · DNA recognition · nanotechnology · polyamides · single-molecule studies

[1] J. W. Trauger, E. E. Baird, P. B. Dervan, *Nature* **1996**, 382, 559–561.

[2] P. B. Dervan, B. S. Edelson, *Curr. Opin. Struct. Biol.* **2003**, 13, 284–299.

- [3] D. M. Herman, E. E. Baird, P. B. Dervan, *J. Am. Chem. Soc.* **1998**, *120*, 1382–1391.
- [4] H. Urata, K. Shinohara, E. Ogura, Y. Ueda, M. Akagi, *J. Am. Chem. Soc.* **1991**, *113*, 8174–8175.
- [5] H. Urata, T. Kumashiro, T. Kawahata, T. Otake, M. Akagi, *Biochem. Biophys. Res. Commun.* **2004**, *313*, 55–61.
- [6] K. P. Williams, X. H. Liu, T. N. M. Schumacher, H. Y. Lin, D. A. Ausiello, P. S. Kim, D. P. Bartel, *Proc. Natl. Acad. Sci. USA* **1997**, *94*, 11285–11290.
- [7] S. Negi, M. Dhanasekaran, T. Hirata, H. Urata, Y. Sugiura, *Chirality* **2006**, *18*, 254–258.
- [8] H. Urata, Y. Ueda, Y. Usami, M. Akagi, *J. Am. Chem. Soc.* **1993**, *115*, 7135–7138.
- [9] a) N. C. Hauser, R. Martinez, A. Jacob, S. Rupp, J. D. Hoheisel, S. Matysiak, *Nucleic Acids Res.* **2006**, *34*, 5101–5111; b) G. Hayashi, M. Hagiwara, A. Kobori, K. Nakatani, *ChemBioChem* **2007**, *8*, 169–171.
- [10] a) V. T. Moy, E. L. Florin, H. E. Gaub, *Science* **1994**, *266*, 257–259; b) R. Merkel, P. Nassoy, A. Leung, K. Ritchie, E. Evans, *Nature* **1999**, *397*, 50–53; c) H. Clausen-Schaumann, M. Seitz, R. Krautbauer, H. E. Gaub, *Curr. Opin. Chem. Biol.* **2000**, *4*, 524–530; d) C. Bustamante, Z. Bryant, S. B. Smith, *Nature* **2003**, *421*, 423–427; e) P. B. Tarsa, R. R. Brau, M. Barch, J. M. Ferrer, Y. Freyzon, P. Matsudaira, M. J. Lang, *Angew. Chem.* **2007**, *119*, 2045–2047; *Angew. Chem. Int. Ed.* **2007**, *46*, 1999–2001; f) Y. J. Jung, B. J. Hong, W. Zhang, S. J. B. Tendler, P. M. Williams, S. Allen, J. W. Park, *J. Am. Chem. Soc.* **2007**, *129*, 9349–9355.
- [11] C. H. Albrecht, K. Blank, M. Lalic-Multhaler, S. Hirler, T. Mai, I. Gilbert, S. Schiffmann, T. Bayer, H. Clausen-Schaumann, H. E. Gaub, *Science* **2003**, *301*, 367–370.
- [12] C. H. Albrecht, H. Clausen-Schaumann, H. E. Gaub, *J. Phys. Condens. Matter* **2006**, *18*, S581–S599.
- [13] G. Neuert, C. H. Albrecht, H. E. Gaub, *Biophys. J.* **2007**, *93*, 1215–1223.
- [14] K. Blank, T. Mai, I. Gilbert, S. Schiffmann, J. Rankl, R. Zivin, C. Tackney, T. Nicolaus, K. Spinnler, F. Oesterhelt, M. Benoit, H. Clausen-Schaumann, H. E. Gaub, *Proc. Natl. Acad. Sci. USA* **2003**, *100*, 11356–11360.
- [15] D. S. Pilch, N. Poklar, C. A. Gelfand, S. M. Law, K. J. Breslauer, E. E. Baird, P. B. Dervan, *Proc. Natl. Acad. Sci. USA* **1996**, *93*, 8306–8311.



## Supporting Information

© Wiley-VCH 2007

69451 Weinheim, Germany

# **Recognition of “Mirror-Image” DNA by Small Molecules**

Christian Dose<sup>†</sup>, Dominik Ho<sup>‡</sup>, Hermann E. Gaub<sup>‡</sup>,

Peter B. Dervan<sup>†\*</sup> & Christian H. Albrecht<sup>‡\*\*</sup>

<sup>†</sup>Division of Chemistry and Chemical Engineering California Institute of Technology Pasadena, California 91125, USA, Fax: (+1) 626-683-8753, E-mail: dervan@caltech.edu

<sup>‡</sup>Lehrstuhl für Angewandte Physik and Center for Nanoscience Ludwig-Maximilians-Universität Amalienstrasse 54, 80799 Munich, Germany, Fax: (+49) 89-2180-2050, E-mail: christian.albrecht@physik.uni-muenchen.de

### General Procedures and Materials:

Polyamide conjugates were synthesized on solid-phase using published Boc-based protocols and purified by reverse-phase high pressure liquid chromatography (HPLC).<sup>[3]</sup> Analytical HPLC was performed on a Beckman Gold system equipped with a diode array detector using a Phenomenex Gemini column (5  $\mu$ m particle size, C18 110A, 250 x 4.6 mm, 5 micron). Preparative HPLC was performed on a Beckman Gold system equipped with a single-wavelength detector monitoring at 310 nm using a Phenomenex Gemini column (5  $\mu$ m particle size, C18 110A, 250 x 21.2 mm, 5 micron). For both analytical and preparative HPLC, solvent A was 0.1% (v/v) aqueous trifluoroacetic acid (TFA) and solvent B was acetonitrile. Solvent gradients were adjusted as needed. UV-Vis spectra were recorded in water on a Hewlett-Packard Model 8452 A diode array spectrophotometer. All polyamide concentrations were determined using an extinction coefficient of 69.200  $M^{-1}\cdot cm^{-1}$  at  $\lambda_{max}$  near 310 nm. Matrix-assisted, LASER desorption/ionization time-of-flight mass spectrometry (MALDI-TOF MS) was performed using an Applied Biosystems Voyager DR Pro spectrometer. Polyamide **5**: MALDI-TOF [M+H]<sup>+</sup> calcd for  $C_{57}H_{71}N_{22}O_{10}^+$  = 1223.6, observed = 1223.4; polyamide (**R**)-**6**: MALDI-TOF [M+H]<sup>+</sup> calcd for  $C_{57}H_{72}N_{23}O_{10}^+$  = 1238.6, observed = 1238.6; polyamide (**S**)-**6**: MALDI-TOF [M+H]<sup>+</sup> calcd for  $C_{57}H_{72}N_{23}O_{10}^+$  = 1238.6, observed = 1238.5; polyamide (**R**)-**7**: MALDI-TOF [M+H]<sup>+</sup> calcd for  $C_{58}H_{73}N_{22}O_{10}^+$  = 1237.6, observed = 1237.3; polyamide (**S**)-**7**: MALDI-TOF [M+H]<sup>+</sup> calcd for  $C_{58}H_{73}N_{22}O_{10}^+$  = 1237.6, observed = 1237.5.

D-DNA oligomers **1** and **2** were purchased HPLC purified from Integrated DNA Technologies (Coralville, USA). L-DNA oligomers **3**, **4**, and DNA-conjugates used for the molecular force balance 5'-H<sub>2</sub>N-TTTTTTTTCAGTCGCTGACCAACCTCGT-3', 3'-GTCAGCGACTGGTTGGAGCACTTTT-T-5'-5'-T(Cy3)TTTTCACGAGGTTGGTCAGCGACTG-3', 3'-TGCTCCAACCAGTCGCTGACTTTTT-TTTT-5'-biotin (italic letters represent L-DNA monomers) were purchased HPLC purified from IBA GmbH (Goettingen, Germany). The DNA-oligonucleotides for the molecular force balance containing the polyamide-binding motifs (gray) were aligned as shown in Figure S1.



**Figure S1.** DNA sequences and polyamide binding motifs of the molecular force balance.

The molecular force balance setup was performed according to literature [12]. A polymethylmethacrylat (PMMA) fluid cell placed on top of the glass slide was used for polyamide addition. Polydimethylsiloxane (PDMS) stamps were PEG-biotin functionalized using epoxy-trimethoxysilane (ABCR, Karlsruhe, Germany) and amino-PEG-biotin (mw: 3400 g/mol, Rapp Polymere, Goettingen, Germany). The PDMS stamps were incubated in 1x PBS (phosphate buffer saline) containing 15 nM streptavidin (Invitrogen, Karlsruhe, Germany) and 0.4% (w/w) bovine serum albumin (BSA) for at least one hour before use. Polyamides in 1x PBS buffer were added to the fluid cell 30 min prior to the experiment. Streptavidin coated PDMS stamps were approached to the force balances using high precision stepper motors (OWIS, Staufen, Germany) and a piezo actuator, monitored by reflection interference contrast microscopy (RICM). The biotinylated force balances and the streptavidin coated PDMS stamp were allowed to couple for 10 min, followed by retraction of the PDMS stamp at a velocity of 5 µm/s. Images of the molecular force balance glass slide were recorded by a confocal fluorescence scanner at 4 µm resolution (Tecan, Austria). Melting temperature analysis was monitored on a Beckman UV-Vis spectrometer at 260 nm within 25-90 °C by applying a heating rate of 0.5 °C/min. Measurements were performed in a degassed buffer containing 2 µM DNA duplex/polyamide (1:1), 10 mM NaCl, and 100 mM NaH<sub>2</sub>PO<sub>4</sub> at pH 7.0.  $T_m$ -values were defined as the maximum of the first derivative of the melting curve.

Polyamide ball-and-stick representation legend: Black and white circles represent imidazole and pyrrol rings, respectively, half-circles represent γ-aminobutyric acid, half-circles containing a cross represent positive charged amines, and white diamonds represent β-alanine moieties. All polyamides contain 3-(dimethylamino)-1-propylamine (Dp) as tail.

# Quantitative Detection of Small Molecule/DNA Complexes Employing a Force-Based and Label-Free DNA-Microarray

Dominik Ho,<sup>†‡</sup> Christian Dose,<sup>§</sup> Christian H. Albrecht,<sup>†</sup> Philip Severin,<sup>†</sup> Katja Falter,<sup>†</sup> Peter B. Dervan,<sup>§</sup> and Hermann E. Gaub<sup>†\*</sup>

<sup>†</sup>Lehrstuhl für Angewandte Physik and Center for Nanoscience Ludwig-Maximilians-Universität, 80799 Munich, Germany; <sup>‡</sup>Munich Center For Integrated Protein Science (CIPSM) Ludwig-Maximilians-Universität, 81377 Munich, Germany; and <sup>§</sup>Division of Chemistry and Chemical Engineering California Institute of Technology, Pasadena, CA 91125

**ABSTRACT** Force-based ligand detection is a promising method to characterize molecular complexes label-free at physiological conditions. Because conventional implementations of this technique, e.g., based on atomic force microscopy or optical traps, are low-throughput and require extremely sensitive and sophisticated equipment, this approach has to date found only limited application. We present a low-cost, chip-based assay, which combines high-throughput force-based detection of dsDNA·ligand interactions with the ease of fluorescence detection. Within the comparative unbinding force assay, many duplicates of a target DNA duplex are probed against a defined reference DNA duplex each. The fractions of broken target and reference DNA duplexes are determined via fluorescence. With this assay, we investigated the DNA binding behavior of artificial pyrrole-imidazole polyamides. These small compounds can be programmed to target specific dsDNA sequences and distinguish between D- and L-DNA. We found that titration with polyamides specific for a binding motif, which is present in the target DNA duplex and not in the reference DNA duplex, reliably resulted in a shift toward larger fractions of broken reference bonds. From the concentration dependence nanomolar to picomolar dissociation constants of dsDNA·ligand complexes were determined, agreeing well with prior quantitative DNAase footprinting experiments. This finding corroborates that the forced unbinding of dsDNA in presence of a ligand is a nonequilibrium process that produces a snapshot of the equilibrium distribution between dsDNA and dsDNA·ligand complexes.

## INTRODUCTION

Small DNA-binding molecules are in the spotlight of many fields of research. Whether it is genomics, systems biology, or molecular medicine, the knowledge if and how strong a molecule interacts with a specific DNA sequence is of utmost interest. The formation of such complexes is typically linked to changes in the double-helical structure and may even result in the displacement or blocking of other molecules. This enables important functions in e.g., transcription, recombination, and DNA repair (1,2).

Given the importance of understanding the basis of molecular recognition, assays are needed that allow for fast, sensitive, and quantitative detection of dsDNA·ligand complexes. Traditionally, DNase footprinting experiments are employed to identify the binding sites of a ligand on dsDNA and also quantify the respective affinities. Although certainly powerful, DNase footprinting is a complex procedure and requires several days of preparation (3). Very rapid and also label-free quantification of even minuscule amounts of ligand becomes possible with microcantilever arrays (4). They suffer, however, from the costs associated with the fabrication and chemical modification of large numbers of cantilevers.

It is often of importance to identify the full DNA recognition profile of a certain DNA binder to understand what kind

of role the binder plays within a living organism. Chip-based methods accommodate the need for massively parallel analysis of dsDNA·ligand interactions: chromatin immunoprecipitation-on-chip (ChIP-on-chip) is a widespread technique allowing for a genome-wide identification of protein-binding sites (5,6). ChIP-on-chip relies on nonspecific cross-linking of DNA with a DNA-binding molecule *in vivo*. Cross-linking efficiencies vary from molecule to molecule, and some interactions may even be missed (7). In particular, the detection of small molecules interacting with DNA is nontrivial. Today, a growing number of *in vitro* chip-based assays are available allowing for the analysis of dsDNA·ligand interactions under controlled experimental conditions. In an experiment by Warren et al. (8,9), all permutations of an eight basepair dsDNA sequence were displayed on a single chip. Ligand binding was detected directly by fluorescence and the cognate sites were ranked in the order of increasing affinity. However, fluorescence trades fast and sensitive readout for a labeled ligand, and the label may alter the sequence specificity profile of the ligand in an unbiased manner. A widespread label-free detection method is surface plasmon resonance imaging. Due to the small change in refractive index, the detection of small molecules with surface plasmon resonance imaging is complicated and requires larger features compared to fluorescence-based techniques (10,11). Depending on the application, the background signal caused by unwanted adsorption imposes a substantially challenge to all chip-based methods. The

---

Submitted November 4, 2008, and accepted for publication February 25, 2009.

\*Correspondence: [gaub@lmu.de](mailto:gaub@lmu.de)

Editor: Jane Clarke.

© 2009 by the Biophysical Society  
0006-3495/09/06/4661/11 \$2.00

---

doi: 10.1016/j.bpj.2009.02.059

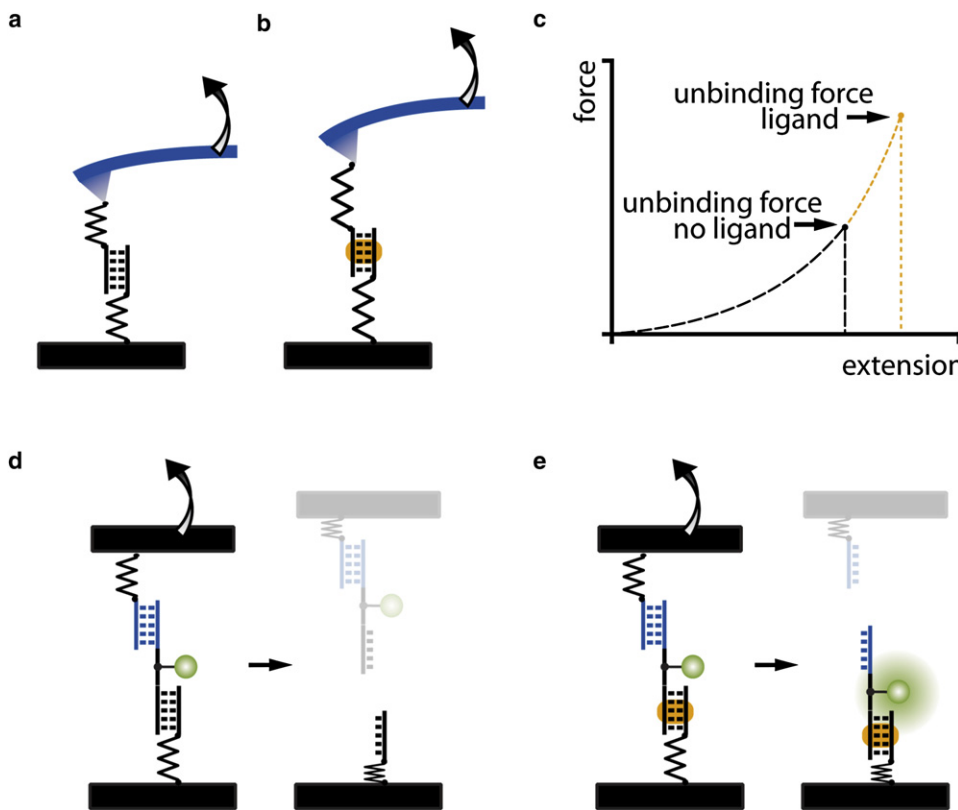


**FIGURE 1** (a) Conventional, AFM-based single molecule force spectroscopy, in which the force required to unbind a molecular bond, such as a target DNA duplex, is measured with a cantilever spring. (b) A ligand bound to the target DNA duplex alters the force required for unbinding. (c) Single molecule force spectroscopy data are typically presented as force-extension traces. From two absolute force measurements, the consequences of ligand binding can be investigated. (d) The CUFA replaces the cantilever spring by a known reference bond. Upon loading the chain of target DNA duplex and reference DNA duplex, the weaker of the two bonds has a higher probability of unbinding than the stronger one. (e) In case a ligand forms a complex with the target DNA duplex and stabilizes it, significantly more fluorophores end up on the side of the target DNA duplex after separation of the two surfaces.

fabrication of inert surfaces is even considered as the main bottleneck for further development of the latter (12).

Here, we present a microarray compatible dsDNA·ligand complex detection format, which is based on the comparative unbinding force assay (CUFA). CUFA has already been applied to detect single nucleotide polymorphisms (13), to study differences of antibody/antigen interactions (14), to eliminate cross-reactions on protein microarrays (15), and to investigate the chiral selectivity of small peptides (16). For dsDNA·ligand interaction detection, CUFA relies on the alteration of the unbinding forces of a target dsDNA as a result of ligand binding (17–19). This effect was demonstrated in single molecule experiments employing atomic force microscopy (AFM) (20) (21,22), optical tweezers (23), and magnetic tweezers (24) (Fig. 1, a–c).

Instead of a microscopic, spring-like object, e.g., a cantilever or a trapped bead, CUFA employs a precisely defined molecular bond as force sensor. Thereby, the target DNA duplex is directly compared against a reference DNA duplex and merely fluorescence is required to readout the experiment (Fig. 1, d and e). In comparison with conventional force-based measurements, many of the experimental uncertainties are removed. With no calibration offsets or instrument drift the comparative unbinding force experiments are more accurate and independent of the experimental apparatus. Naturally, such experiments are primed to be carried out in parallel by using a chip format with many duplicates (in the order of  $10^4/\mu\text{m}^2$ ) of the same experiment contributing to the excellent

sensitivity of the measurement. The resulting assay is fluorescence based; however, it does not require a labeled ligand. Only the DNA linker between the target and reference DNA duplex is conjugated to a fluorophore at a noninteracting basepair. Rather than detecting the mere presence of the ligand, the change of unbinding forces of the target DNA duplex due to ligand binding is detected. By this means the assay is insensitive to nonspecific adsorption and deals with one of the major bottlenecks of current biochips.

As a model system, we investigated sequence programmable pyrrole-imidazole hairpin polyamides (25). These molecules recognize the minor groove of DNA with affinities and specificities comparable to naturally occurring DNA-binding proteins (26,27). The sequence specificity arises from interactions of pairs of the aromatic amino acids *N*-methylpyrrole (Py), *N*-methylimidazole (Im), and *N*-methylhydroxypyrrrole (Hp) with the edges of the Watson-Crick DNA basepairs. A pairing of Im opposite to Py targets a G·C basepair, and Py/Im recognizes a C·G basepair, whereas a Py/Py pair comprises a preference for both A·T and T·A (28). The discrimination of T·A from A·T using Hp/Py pairs completes the four basepair letter code (29). Eight-ring hairpin polyamides provide a good compromise between synthetic ease and molecular recognition properties. In this binding motif, a  $\gamma$ -aminobutyric acid residue connects the carboxylic terminus of one strand to the amino terminus of the other (30). The turn residue also serves as a DNA recognition element for A·T and T·A basepairs. Further,

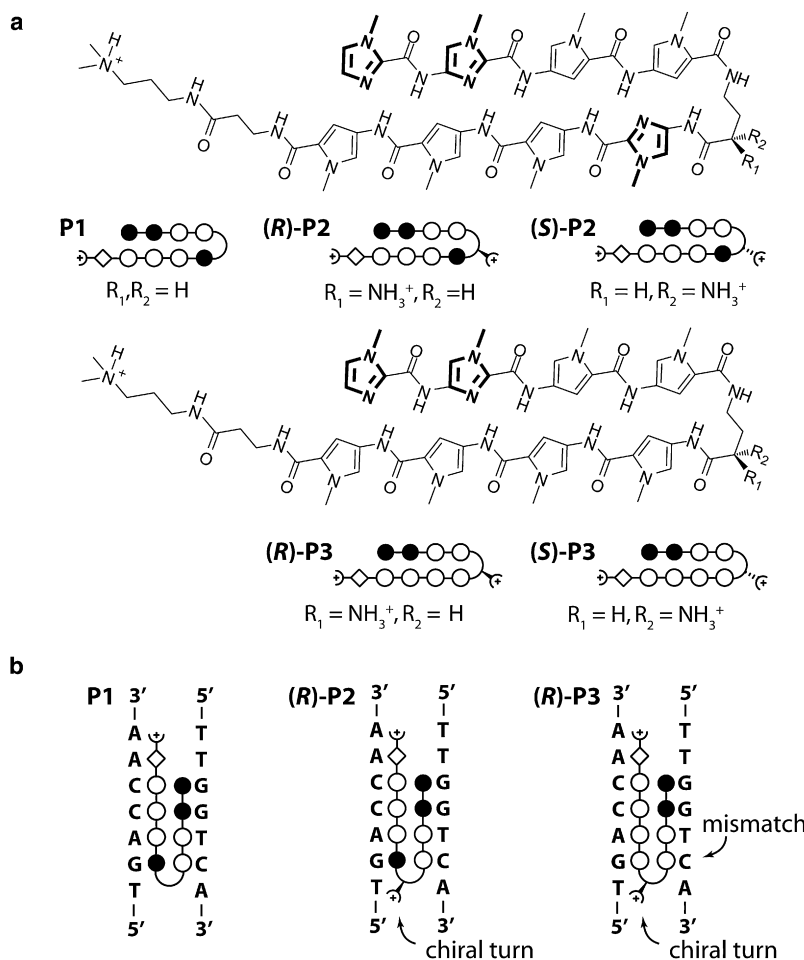


FIGURE 2 (a) Chemical structures of matched hairpin polyamides **P1**, **(R)-2**, and **(S)-2** as well as single basepair mismatched compounds **(R)-P3** and **(S)-P3**. The ball and stick model represents imidazole and pyrrole as solid and open circles, respectively. The  $\beta$ -alanine residue is shown as a diamond, and the dimethylaminopropylamide tail is shown as a half circle with a plus. The chiral diaminobutyric acid turn residue is represented as a turn, to which a semicircle with a plus is linked. *R* and *S* chirality is indicated by a solid and dashed connection of the semicircle to the turn, respectively. (b) Ball and stick representation for the three different hairpin motifs bound to the same target DNA sequence. **P1** binds sequence specific to the target DNA sequence. **(R)-2** is modified with a chiral diaminobutyric acid turn, which increases the overall binding affinity. **(R)-3** is also modified with a chiral diaminobutyric acid turn, however contains a single basepair mismatch that reduces the overall binding affinity.

a  $\beta$ -alanine residue and a dimethylaminopropylamide tail at the C-terminus each confer a specificity for A·T and T·A basepairs (31). This general addressability of the DNA minor groove is supported by x-ray and NMR structure studies (32,33) and has been utilized in several applications, including, for example, DNA nanostructures (34,35), recruitment of DNA-binding proteins (36,37), and the inhibition of gene expression within living cells (38–40).

Here we report the application of CUFA to accurately determine the thermal dissociation constant  $K_D$  of three different dsDNA·polyamide interactions (Fig. 2 a). In particular, we investigated the influence of a chiral turn as well as a single mismatch to the overall affinity of an eight-ring hairpin polyamide to the same target DNA sequence (Fig. 2 b).

## MATERIALS AND METHODS

### DNA constructs

DNA oligomers **1**:  $\text{NH}_2\text{-}(6\text{-hexaethyleneglycol})_5\text{-}5'\text{-TTT TTT TTT TCA GTC GCT GAC CAA CCT CGT-3'}$ , **2**:  $3'\text{-GTC AGC GAC TGG TTG GAG CAC TTT T(Cy3)\text{-5'}-5'\text{-TTT TTC TGC TCC AAC CAG TCG CTG AC -3'}$ , **3**: Biotin- $5'\text{-TTT TTT TTT TGT CAGCGACTGGTTGGAGCA}$ , **4**:  $3'\text{-GTC}$

AGC GAC TGG TTG GAG CAC TTT T(Cy3)- $5'\text{-5'-TTT TTC ACG AGG TTG GTC AGC GAC TG-3'}$ , and **5**: Biotin- $5'\text{-TTT TTT TTT TCA GTC GCT GAC CAA CCT CGT-3'}$  were purchased HPLC grade from IBA GmbH (Goettingen, Germany). Italic letters in oligomers **4** and **5** represent L-DNA bases. In upside-down experiments the  $\text{NH}_2\text{-}(6\text{-hexaethyleneglycol})_5$  (HEGL) and biotin modifications were exchanged.

### Molecular setup preparation (DNA slide)

Each individual molecular chain consisting of a reference and a target DNA duplex is referred to as a “molecular setup”. Oligomer **1** is amine-modified at the 5' end and allows covalent attachment to an aldehyde-functionalized glass slide (Schott GmbH, Jena, Germany). Two microliter drops of 5× phosphate buffered saline (PBS; Roche GmbH, Grenzach, Germany) containing 25  $\mu\text{M}$  oligomer **1** were spotted on an aldehyde glass slide in a 4 × 4 pattern and were incubated in a saturated NaCl ddH<sub>2</sub>O atmosphere overnight. After washing the slide with ddH<sub>2</sub>O containing 0.2% sodium dodecyl sulfate (VWR Scientific GmbH, Darmstadt, Germany) and thoroughly rinsing the slide in ddH<sub>2</sub>O, the resulting Schiff bases were reduced with 1% aqueous NaBH<sub>4</sub> (VWR Scientific GmbH, Darmstadt, Germany) for 20 min. After thoroughly rinsing the slide in ddH<sub>2</sub>O, the slides were blocked in 1× PBS containing 4% bovine serum albumin (Sigma-Aldrich GmbH, Munich, Germany) for 30 min. A custom-made 16-well silicone isolator (Grace-Biolabs, OR) was placed on the top of the immobilized DNA oligomer **1** spots. Three microliters of 1× PBS containing 1  $\mu\text{M}$  oligomer **2** and 2  $\mu\text{M}$  oligomer **3** were added to each well and incubated for 1 h, completing the **1**·**2**·**3** molecular setups. Then, the slide was washed with 1× PBS containing 0.05% sodium dodecyl sulfate and thoroughly rinsed with 1× PBS. The

silicon isolator remained on the slide throughout the experiment, and care was taken that after hybridization the slide always remained immersed in 1× PBS. The **1·4·5** and upside-down molecular setups were prepared accordingly.

## PDMS stamp

The polydimethylsiloxane (PDMS) stamp was fabricated by casting 10:1 (base/crosslinker) (Sylgard, Dow Corning, MI) into a custom-made micro- and millistructured silicon wafer (HSG-IMIT, Villingen-Schwenningen, Germany) (41). After curing was complete, the PDMS was taken out of the mold and cut into a 4 × 4 pillar arrangement. Each pillar is 1 mm diameter, is 1 mm high, and carries a microstructure on the flat surface: 100 × 100  $\mu\text{m}^2$  pads are separated by 41  $\mu\text{m}$  wide and 5  $\mu\text{m}$  deep trenches allowing for liquid drainage during the contact and separation process. Free polymers were extracted in toluene for at least 1 day (42). The PDMS was activated overnight in 12.5% hydrochloric acid and subsequently derivatized with (3-glycidoxypropyl)-trimethoxysilane (ABCR, Karlsruhe, Germany) to generate epoxide groups. NH<sub>2</sub>-PEG-Biotin (3400 g/mol; Rapp Polymere, Tübingen, Germany) was melted at 80°C, and ~1  $\mu\text{L}$  was spotted on each pillar followed by overnight incubation in argon atmosphere at 80°C. The excess polymers were thoroughly removed with ddH<sub>2</sub>O. Shortly before the experiment, the PDMS was incubated with 1  $\mu\text{g}/\text{ml}$  streptavidin (Thermo Fisher Scientific, Bonn, Germany) in 1× PBS and 0.4% bovine serum albumin for 30 min, washed with 1× PBS containing 0.05% Tween 20 (VWR Scientific GmbH, Darmstadt, Germany), with 1× PBS and gently dried with N<sub>2</sub> gas.

## Ligand incubation

Sixteen-well silicone isolators allowed the addition of up to 16 different concentrations of the dsDNA ligands within a single experiment. Because of technical convenience, we restricted ourselves to the addition of eight different concentrations. Fifty milliliters volume of polyamides in 1× PBS was circulated through each well for at least 2 h using a self-made fluidic system driven by a 16-channel peristaltic pump (Ismatec GmbH, Wertheim-Mondfeld, Germany).

## Coupling and separation

The streptavidin functionalized PDMS stamp was approached to the DNA slide using high-precision stepper motors (OWIS GmbH, Staufen, Germany) and a piezo actuator (Piezo Systems Jena, Jena, Germany), monitored by reflection interference contrast microscopy (43). The biotinylated molecular complexes and the multivalent streptavidin coated PDMS stamp were allowed to couple via a biotin-streptavidin-biotin complex for 10 min, followed by retraction of the PDMS stamp at a velocity of 5  $\mu\text{m}/\text{s}$ . Biotin-streptavidin is an extremely strong molecular interaction and is of significantly greater stability than short dsDNA at the applied separation velocity (44,45). In separate controls, we determined that no noteworthy amount of fluorescently labeled streptavidin was transferred from the PDMS to the DNA array during an experiment.

## Analysis

Fluorescence images of the DNA slide were recorded in solution using a confocal scanner with 4  $\mu\text{m}$  resolution (Tecan Austria GmbH, Austria) before and after the contact. The fluorescence per unit area was assumed to be proportional to the fluorescently labeled species per unit area (see Fig. S1 in the Supporting Material). The normalized fluorescence intensity (NF) is defined as the number of broken reference bonds normalized to the total number of individual molecular setups that have been under load. For the **1·2·3** molecular setups, it was determined as follows: initially, all molecular setups are present in the state S0 and were detected via the Cy3 labeled oligomer **2** (Fig. 3 a). After separation, the molecular setups on the glass slide exist in three different states, S0 (**1·2·3**), S1 (**1·2**), and S2

(**1**), as shown in Fig. 3 b. An unbinding force was applied only to the molecular setups in state S1 and S2. Molecular setups in state S0 did not couple to the PDMS streptavidin surface and therefore retained the biotinylated oligomer **3**. Because S1 and S0 cannot be distinguished, the latter was labeled with the spectrally distinct fluorescent marker streptavidin Alexa Fluor 647 (AF; Fig. 3 c). The labeling was performed subsequent to the Cy3 readout to avoid quenching or fluorescence resonance energy transfer effects. The Cy3 and AF fluorescence images allow the quantification of the relative amounts of S0, S1, and S2 (Fig. 3, d and e). The Cy3 and AF fluorescence images recorded after contact contain square-like features corresponding to the contacted area. From each square-like feature the Cy3<sub>Rem</sub> and AF<sub>Rem</sub> were determined individually. Cy3<sub>Initial</sub> and AF<sub>Initial</sub> were determined from the noncontacted regions adjacent to each square-like feature.

$$S0 = AF_{\text{Ratio}} \quad (1)$$

$$S1 = Cy3_{\text{Ratio}} - AF_{\text{Ratio}} \quad (2)$$

$$S2 = 1 - Cy3_{\text{Ratio}} \quad (3)$$

$$Cy3_{\text{Ratio}} = \frac{Cy3_{\text{Rem}}}{Cy3_{\text{Initial}}}, \quad (4A)$$

$$AF_{\text{Ratio}} = \frac{AF_{\text{Rem}}}{AF_{\text{Initial}}} \quad (4B)$$

S0, S1, and S2 are normalized such that the relation S0 + S1 + S2 = 1 is always true. As defined above, the NF is given by the number of broken **2·3** bonds (S1) normalized to the number of bonds that have been under load (S1 + S2):

$$NF = \frac{S1}{S1 + S2} = \frac{Cy3_{\text{Ratio}} - AF_{\text{Ratio}}}{1 - AF_{\text{Ratio}}} \quad (5)$$

The NF directly reflects the relative mechanical stability, a physical quantity inherent to a pair of molecular complexes, and is not influenced by the amount of molecules under load. The NF should not be confused with the Cy3<sub>Ratio</sub>. For a fixed mechanical stability, the latter depends on the number of coupled molecular complexes, whereas the NF does not. The NFs presented in this work are the averages of the NFs determined from all square-like features of an experiment. The **1·4·5** and upside-down molecular setups were analyzed accordingly.

## Polyamide synthesis

Polyamide conjugates were synthesized on solid-phase using published Boc-based protocols and purified by reverse-phase HPLC ( $\geq 95\%$  purity) (46). Ultraviolet-visible spectra were recorded in water on a Hewlett-Packard Model 8452 A diode array spectrophotometer. All polyamide concentrations were determined using an extinction coefficient of 69,200 M<sup>-1</sup>cm<sup>-1</sup> at  $\lambda_{\text{max}}$  near 310 nm. Matrix-assisted, LASER desorption/ionization time-of-flight mass spectrometry (MALDI-TOF MS) was performed using an Applied Biosystems Voyager DR Pro spectrometer. Polyamide **P1**: MALDI-TOF [M+H]<sup>+</sup> calcd for C<sub>57</sub>H<sub>71</sub>N<sub>22</sub>O<sub>10</sub><sup>+</sup> = 1223.6, observed = 1223.4, (**R**)-**P2**: MALDI-TOF [M+H]<sup>+</sup> calcd for C<sub>57</sub>H<sub>72</sub>N<sub>23</sub>O<sub>10</sub><sup>+</sup> = 1238.6, observed = 1238.6, (**S**)-**P2**: MALDI-TOF [M+H]<sup>+</sup> calcd for C<sub>57</sub>H<sub>72</sub>N<sub>23</sub>O<sub>10</sub><sup>+</sup> = 1238.6, observed = 1238.5, (**R**)-**P3**: MALDI-TOF [M+H]<sup>+</sup> calcd for C<sub>58</sub>H<sub>73</sub>N<sub>22</sub>O<sub>10</sub><sup>+</sup> = 1237.6, observed = 1237.3, (**S**)-**P3**: MALDI-TOF [M+H]<sup>+</sup> calcd for C<sub>58</sub>H<sub>73</sub>N<sub>22</sub>O<sub>10</sub><sup>+</sup> = 1237.6, observed = 1237.5.

## Melting temperature analysis

Melting temperatures were monitored on a Beckman ultraviolet-visible spectrometer at 260 nm within 25–90°C by applying a heating rate of

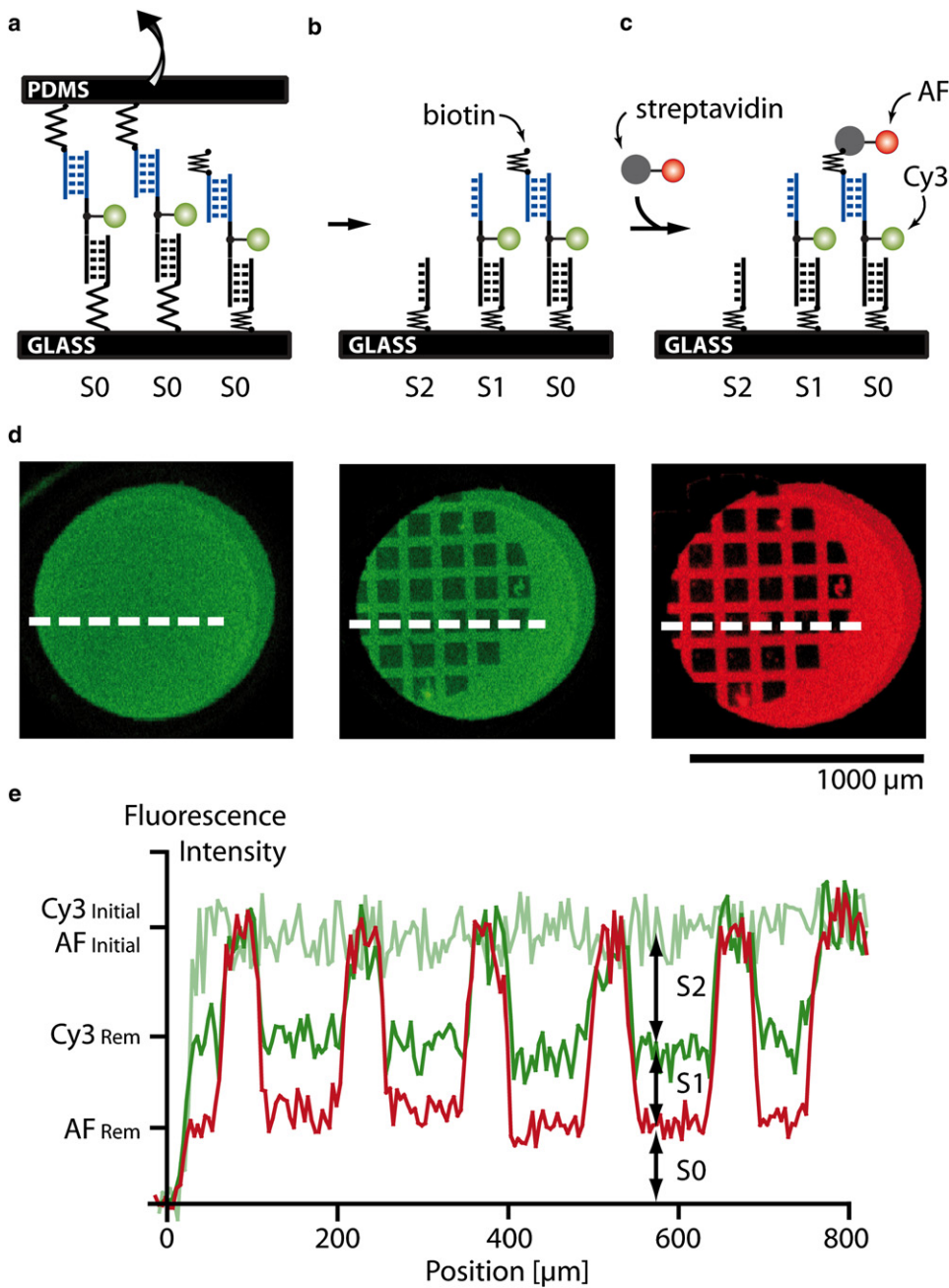


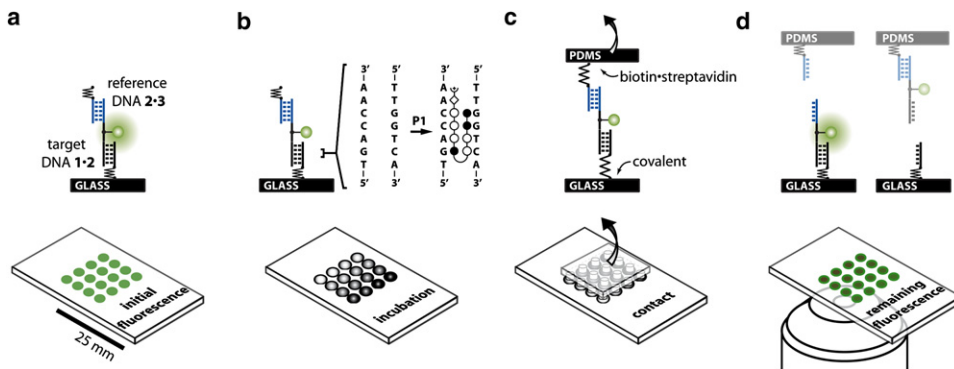
**FIGURE 3** Comparative unbinding force experiment on the molecular level. (a) Before separation of the two surfaces, all molecular setups are in the state S0. (b) After separation, either target (state S2) or reference (state S0) bond is broken or no coupling (state S0) occurred. (c) Because states S0 and S1 cannot be distinguished by fluorescence, the free biotin of state S0 is labeled with streptavidin Alexa Fluor 647 (AF). (d) Fluorescence images of the glass slide before and after separation as well as after incubation with AF. The dark square-like features correspond to the area contacted with a microstructured PDMS stamp. (e) Corresponding line plots. From the fluorescence intensities the relative amounts of the states S0, S1, and S2 can be determined.

0.5°C/min. Measurements were performed in a degassed buffer containing 2 μM DNA duplex/polyamide (1:1), 10 mM NaCl, and 100 mM NaH<sub>2</sub>PO<sub>4</sub> at pH 7.0.  $T_m$ -values are defined as the maximum of the first derivative of the melting curve.

## RESULTS AND DISCUSSION

Force-based ligand detection relies on the alteration of unbinding forces due to dsDNA·ligand complex formation. In the course of conventional single molecule experiments, one strand of a DNA duplex is immobilized to solid support via a polyethyleneglycole (PEG) linker. In the same way, the complementary strand is immobilized to a microscopic force

detector such as an AFM cantilever. Upon contacting the AFM cantilever with the solid support, the two complementary DNA strands hybridize. During separation of the support and the detector surface, the PEG linkers act like entropic springs (47,48), and an increasing force builds up until the DNA duplex unbinds (Fig. 1, a and b). The force extension curve is recorded and the unbinding force determined. Because unbinding is a thermally activated process (49) and the force detector is limited by thermal noise (50), several hundred experiments are typically performed to determine the unbinding forces with sufficient accuracy. As demonstrated by Krautbauer et al. (17) as well as Koch et al. (18), complex formation of a DNA duplex with a small



molecule or a protein is accompanied by a shift of the unbinding forces (Fig. 1 c). In our comparative unbinding force experiments, a known molecular bond carrying a fluorescent label replaces the microscopic force detector (Fig. 1, d and e).

Fig. 4 a illustrates the molecular setup schematically. Target DNA duplex **1·2** is immobilized to glass support via a (hexaethyleneglycol)<sub>5</sub> linker of oligomer **1**. Reference DNA duplex **2·3** is bridged to **1·2** via a 10 basepair single stranded polythymine linker carrying a Cy3 fluorescence label. Oligomer **3** carries a biotin modification at the end of another polythymine linker. Before the force experiment, a fluidic system allows for incubation of the molecular setups with different ligand concentrations (Fig. 4 b). In Fig. 4 c, a soft PDMS stamp is brought in contact with the **1·2·3** complexes on the glass slide analogously to a microcontact-printing experiment (51,52). **1·2·3** couples to the PDMS stamp via biotin-streptavidin complex formation. Upon retraction of the PDMS stamp at 5  $\mu\text{m}/\text{s}$  force is built up gradually acting along the molecular chain consisting of the linkers as well as the **1·2** and **2·3** duplexes until either **1·2** or **2·3** breaks (Fig. 4 d).

Approximately  $10^4$  duplicates of the same experiment are performed per  $\mu\text{m}^2$ . The absolute force needed to pull the two surfaces apart is neither recorded nor analyzed. Instead, the unbinding force of each target DNA duplex is compared individually against a separate reference duplex. For each molecular chain, the two possible experimental outcomes are distinguished by determining the location of the fluorescently labeled oligomer **2**. In case the fluorophore remained on the glass slide, the **2·3** DNA duplex is broken, and in case the fluorophore was transferred to the PDMS stamp, the **1·2** DNA duplex is broken.

The target and the reference DNA duplex are comprised of the same basepair composition, and the outcome “**1·2** is broken” should be close to equally likely to the outcome “**2·3** is broken” (53). Experimentally, we determined a NF (see Materials and Methods) of 38.4% with an error of 1.6%, which we estimated from repeated measurements (Fig. 5 a). We attribute this deviation from the expected

FIGURE 4 Schematics of CUFA experiments. (a) The molecular setup consists of two DNA duplexes, i.e., the **1·2** target and the **2·3** reference DNA duplex, linked in series. (b) A simple fluidic system allows incubation of 16 identical DNA spots with eight different polyamide **P1** concentrations. (c) The molecular setups are linked between glass support and PDMS. Separation of the surfaces applies a load to the chain of duplexes until the weaker fails. (d) The fluorescently labeled linking DNA oligomer **2** is more likely to remain on the side of the more stable DNA·ligand complex.

NF of 50% to the symmetry break due to the different surfaces to which the oligomers are attached. DNA duplexes are sensitive to solution conditions such as pH and ionic strength (54), which may differ depending on the proximity of the DNA duplex to the PDMS or the glass surface. This minor imbalance does not affect the quantitative detection of dsDNA·ligand complexes.

### Nonchiral hairpin polyamide

To investigate whether the CUFA is applicable to determine the thermal dissociation constant  $K_D$  of dsDNA·ligand interactions, we incubated **1·2·3** molecular setups with different concentrations of hairpin polyamide **P1**. Thereby, we make use of a symmetry breaking property, such that **P1** only binds to the target and not the reference DNA duplex: hairpin polyamides bind sequence specific with a preference for N→C orientation with respect to the 5'→3' direction of the adjacent DNA strand (55,56). The preferred binding motif 5'-TGAC-CAA-3' of polyamide **P1** is present in the **1·2** target DNA duplex, whereas the **2·3** reference DNA duplex contains the reverse-binding motif 5'-AACCAAGT-3', to which **P1** binds with significantly decreased affinity.

On a single chip, we incubated 16 identical spots of immobilized **1·2·3** molecular setups with eight different **P1** concentrations ranging from 0 to 2.7 nM and performed a CUFA experiment as described above. The NF increased with increasing polyamide concentration from 38.4% (Fig. 5 a) until it saturated at 63.1% (Fig. 5 b). This is in agreement with a stabilizing effect of **P1** on the **1·2** duplex. As it is common for quantitative dsDNA·polyamide interaction studies, we fitted the titration data to the Hill equation isotherm (a more detailed discussion follows at the end of this section) (9,58). The apparent thermal dissociation constant  $K_D$  was determined to be 105 pM with a 95% confidence interval of [65 pM, 169 pM] agreeing well with previously published quantitative DNase footprinting and microarray data (58). The NF data including the fit are shown in Fig. 5 c.

To ensure that the molecular setup responds as expected, we investigated the upside-down molecular setup **3·2·1**.

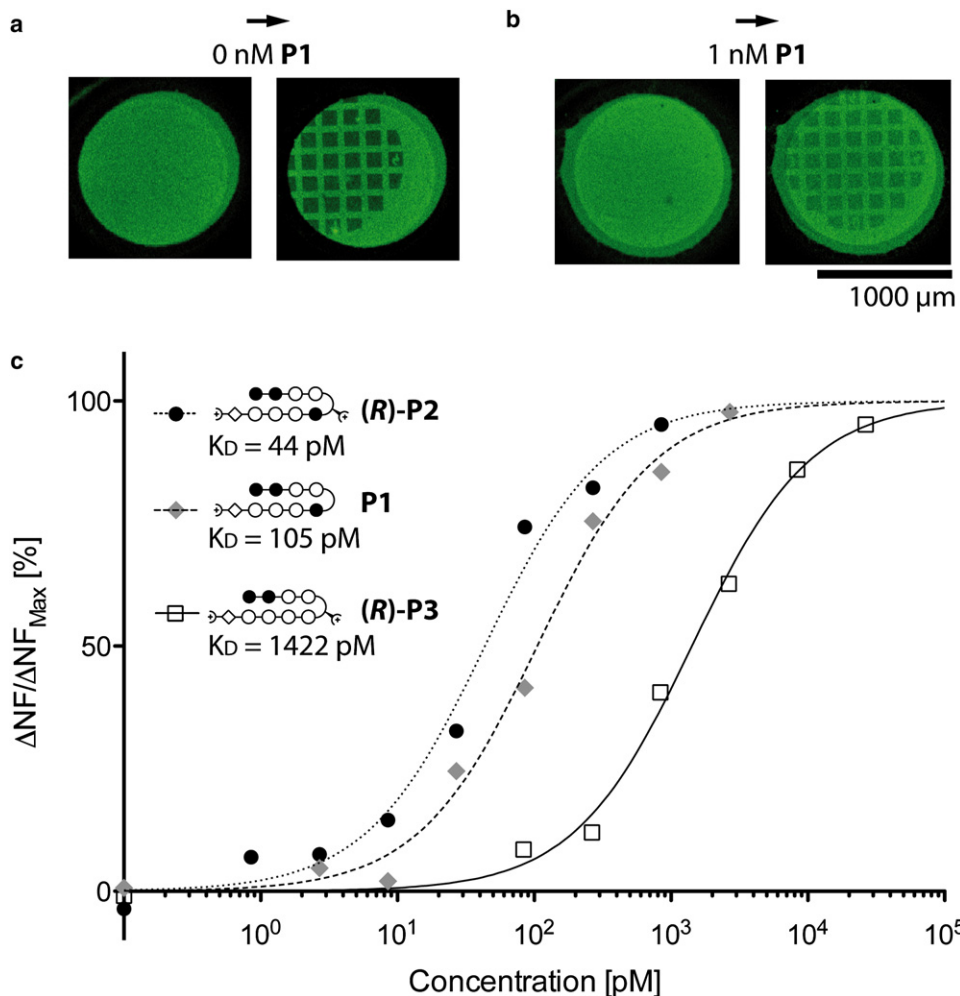


FIGURE 5 (a) Cy3 fluorescence image of **1·2·3** molecular setups on a glass slide before and after contact with a PDMS stamp in absence of **P1**. (b) Cy3 fluorescence image of **1·2·3** molecular setups on a glass slide before and after contact with a PDMS stamp in presence of 1 nM **P1**. The fluorescence intensity of the contacted area is higher compared to the 0 nM case. (c) Relative change in NF due to titration with three different polyamide compounds.

Here, the position of the target and the reference DNA duplex is exchanged, and thus the response to the addition of **P1** should be inverted. Indeed, the NF decreased from 31.9% to 7.7% upon increasing the **P1** concentration from 0 to 10 nM. In this case, the polyamide binds preferentially to the DNA duplex adjacent to the PDMS stamp, and therefore the amount of fluorescently labeled oligomer **2** transferred to the PDMS stamp was increased in presence of **P1**.

### Chiral hairpin polyamide

In previous work, we demonstrated that chiral hairpin polyamides distinguish between D- and L-DNA (16). Chiral selectivity is introduced by an amine substituent on the  $\gamma$ -turn amino acid of the hairpin polyamide that was also shown to lead to an increase in binding affinity (47). The chiral hairpin polyamide (**(R)-P2**), which recognizes the same sequence as **P1**, was examined employing the **1·4·5** molecular setup. **1·4** is identical to the **1·2** target DNA duplex, and **4·5** is the mirrored DNA duplex to **1·4**. (**(R)-P2**) binds preferentially to the **1·4·5'-TGACCAA-3'** binding motif, whereas **4·5** presents less optimal binding sites due to its opposite chirality.

Analogous to the previous experiment, an increase in concentration of (**R**)-**P2** from 0 to 1 nM lead to an increase of the NF from 47.1% to 80.3%, agreeing with a stabilizing effect on the D-DNA duplex **1·4**. Fitting the titration data to a Hill equation isotherm revealed an apparent thermal dissociation constant  $K_D$  of 44 pM with a 95% confidence interval of [23 pM, 83 pM]. The  $K_D$  for the (**R**)-**P2** hairpin polyamide has not been reported yet. However, a lowered  $K_D$  compared to **P1** is consistent with prior experiences with the addition of an amine substituent to the  $\gamma$ -turn amino acid of regular polyamide hairpins (47). The NF data including the fit are shown in Fig. 5 c.

For control, the **5·4·1** upside-down molecular setup in combination with (**R**)-**P2** was measured at 0 nM and 10 nM yielding 32.8% and 12.9%, respectively. The regular molecular setup **1·4·5** in combination with mirror imaged polyamide (**S**)-**P2** was also measured at 0 nM and 10 nM resulting in NF of 44.1% and 20.9%. The two controls demonstrated that the response of the assay was as expected: in the **5·4·1** upside-down molecular setup, the target and reference DNA duplex are essentially mirrored (target and reference are of identical sequence but opposite chirality).

In this case, the ligand recognizes the DNA duplex adjacent to the PDMS stamp and the change in NF due to ligand binding was inverted. In case the ligand was mirrored and incubated with the **1·4·5** molecular setup, the ligand recognized the reference bond as its preferential binding motif and the change in NF was also inverted.

### Mismatched hairpin polyamide

Introducing the single basepair mismatched polyamide (**R**)**-P3** to the **1·4·5** molecular setup is expected to form a DNA-ligand complex of lower affinity (57). In detail, **1·4** provides a binding motif for (**R**)**-P3** with a single basepair mismatch. The affinity to **4·5** is even further decreased, because the binding motif contains a single basepair mismatch and, in addition, is of opposite chirality. Incubation of the **1·4·5** molecular setup with increasing concentrations of (**R**)**-P3** increased the NF from 47.1% at 0 nM to 71.2% at 27 nM. The apparent  $K_D$ , determined from a fit of the NF to the Hill equation isotherm, was 1442 pM with a 95% confidence interval of [932 pM, 2169 pM]. The NF data including the fit are shown in Fig. 5 c.

Controls were performed with the **5·4·1** upside-down molecular setup in absence and presence of 10 nM (**R**)**-P3**, yielding NF of 32.8% and 15.4%, respectively. For the regular **1·4·5** molecular setup, the NF fluorescence also decreased from 47.1% in absence to 25.6% in presence of 10 nM mirrored compound (**S**)**-P3**. Both controls, in which either the molecular setup or the ligand was mirrored, produced an inverted change in NF as response to the addition of the ligand.

### Melting temperatures

To ensure that the differences in unbinding forces were a result of target DNA duplex stabilization by hairpin polyamides, the melting temperatures of the dsDNA·polyamide complexes were determined. The results clearly showed a larger increase in melting temperature for the target duplexes in presence of the polyamides compared to the reference duplexes (Fig. 6).

### Thermal dissociation constant

The affinity of a hairpin polyamide for its dsDNA binding site is characterized by the thermal dissociation constant  $K_D$ . The experimental data suggest that the Hill equation isotherm governs the response of the NF, from which the  $K_D$  characteristic for the dsDNA·polyamide complex under investigation is easily determined. In the following, we derive the response of CUFA beginning with the law of mass action.

The law of mass action describes the amounts of dsDNA·ligand complexes, unbound dsDNA, and free ligands at chemical equilibrium with a dsDNA·ligand complex characteristic thermal  $K_D$  defined as

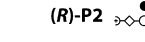
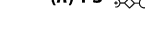
Polyamide	Target [°C] <b>1·2 / 1·4</b>	Reference [°C] <b>2·3</b>	Reference [°C] <b>4·5</b>
none	70	70	70
<b>P1</b> 	77	73	-
( <b>R</b> )- <b>P2</b> 	83	-	75
( <b>R</b> )- <b>P3</b> 	76	-	71

FIGURE 6 Melting temperatures of the target and reference DNA duplex in presence and absence of polyamides. The polyamides and DNA duplexes are mixed at a stoichiometry of 1:1 at 2  $\mu$ M.

$$K_D = \frac{k_{\text{off}}}{k_{\text{on}}} = \frac{[\text{dsDNA}][\text{ligand}]}{[\text{dsDNA} \cdot \text{ligand}]} \quad (6)$$

In our experiments, the total amount of added ligand exceeded the available dsDNA binding sites by at least two orders of magnitude. As a result, the probability  $p$  of a dsDNA binding site to be occupied by a ligand is given by the Hill equation isotherm and depends on the ligand concentration and  $K_D$  only (58):

$$p = \frac{[\text{ligand}]}{[\text{ligand}] + K_D} \quad (7)$$

For further analysis, it is crucial to compare the timescale of association to a single binding site to the timescale of the force probing. The apparent  $K_D$  determined from the CUFA experiment may vary from the initial thermal  $K_D$ , if the system is allowed to equilibrate during the application of the external force: at equilibrium and ligand concentrations around the thermal  $K_D$  the association rate, given by  $[\text{ligand}] \cdot k_{\text{on}}$ , is of the same order of magnitude as the dissociation rate  $k_{\text{off}}$ . The lifetime or inverse dissociation rate for a dsDNA·polyamide complex was experimentally determined to be  $\sim 500$  s (59). At 5  $\mu$ m/s separation velocity and similar linker lengths, the force needed to rupture a 20 basepair DNA duplex is built up on timescales in the order of  $\tau = 0.01$  s (44). The DNA duplex unbinding occurs therefore on a much faster timescale  $\tau$  than the association or dissociation of the dsDNA·ligand complex at relevant ligand concentrations:

$$\tau \ll \frac{1}{[\text{ligand}] \cdot k_{\text{on}}} \quad (8)$$

Although the natural off-rate of polyamides is very low, dissociation of the ligand from the DNA duplex during force probing may be nonnegligible. Studies suggest that the B-S transition of DNA under force can be explained by a tilt of the basepairs and a significant reorganization of the helical structure of the DNA (60–62). The B-S transition has not been observed for 20 basepair duplexes yet (44). However, even small deformations of the dsDNA helical structure may lead to the dissociation of the ligand, especially because hairpin polyamides are particularly sensitive to deformations

of the minor groove. This results in a decreased fraction of occupied binding sites at the time of dsDNA unbinding compared to the initial situation before force is applied. Given that the association rate is slow, rebinding of the ligand to the dsDNA is neglected and the fraction of occupied binding sites is reduced by a constant factor  $f$ .

$$p' = f \cdot p = f \cdot \frac{[\text{ligand}]}{[\text{ligand}] + K_D}, \quad (9)$$

where  $f$  lies within the interval [0,1]. The probability of a binding site to be occupied by a ligand is still governed by the Hill equation isotherm; however with increasing ligand concentration, the probability  $p'$  saturates at  $f < 1$  instead of 1. Importantly, the apparent  $K_D$  is identical with the thermal  $K_D$ .

The target DNA sequence was designed such that there is only one preferred polyamide-binding site. Without loss of generality, the no-ligand case is assumed to yield  $\text{NF}_0$ , whereas the bound-ligand case is assumed to yield  $\text{NF}_1$ . The fluorescence signals of these two states superimpose each other, and the expected total fluorescence signal as a function of the polyamide concentration is the sum of the NFs of the two states weighted by their relative occurrence:

$$\begin{aligned} \text{NF} &= p' \cdot \text{NF}_1 + (1 - p') \cdot \text{NF}_0 \\ &= \text{NF}_0 + f \cdot (\text{NF}_1 - \text{NF}_0) \cdot \frac{[\text{ligand}]}{[\text{ligand}] + K_D}. \end{aligned} \quad (10)$$

The dissociation of ligands from the DNA duplex results in a decrease of the maximal change in NF, whereas the apparent  $K_D$  is not affected. To conclude, in case Eq. 8 holds, the forced unbinding of dsDNA in presence of a ligand is a nonequilibrium process that produces a snapshot of the equilibrium distribution between dsDNA and dsDNA·ligand complexes from which the thermal dissociation constant  $K_D$  can be determined.

## CONCLUSION

The CUFA was successfully applied to quantify the thermal dissociation constants of three different dsDNA-polyamide complexes. For this purpose, polyamide concentrations as low as 10 pM were detected. This level of sensitivity is comparable to conventional chip methods, which work with fluorescently labeled ligands (9). Labeling, however, may alter the binding behavior compared with the unlabeled ligand and is not always applicable. Label-free high-throughput techniques, such as surface plasmon resonance, are challenged when they are confronted with small molecules like polyamides, which are easily detected employing CUFA. Our approach not only avoids labeling of the interacting molecules (a label is attached to linking DNA strand at a noninteracting basepair), but also permits the combination of different experiments as well as controls on one chip. The current DNA-feature size is hundreds of micrometers but can be

reduced to several micrometers using conventional microarray spotters. Miniaturization will allow for a high degree of parallelization and significantly reduced sample volumes.

We foresee CUFA in combination with microarray technology to be used as a tool to rapidly determine and quantify the sequence-recognition profile of small molecules like transcription factors, drugs, or other DNA-binding molecules. In separate experiments, we demonstrated that short-lived molecular interactions are captured in molecular crowded environments, as will be published elsewhere (63). Thus, the sensitivity range covers molecular complexes with micromolar to picomolar thermal dissociation constants and CUFA may prove to be the ideal tool for systems biologists, who have a growing interest in techniques that obtain affinity binder data with sufficient accuracy in a high-throughput fashion (64,65). The experimental procedure is as simple as contacting and separating two surfaces and can be implemented in any laboratory equipped with a quantitative fluorescence microscope.

## SUPPORTING MATERIAL

One figure is available at [http://www.biophysj.org/biophysj/supplemental/S0006-3495\(09\)00680-8](http://www.biophysj.org/biophysj/supplemental/S0006-3495(09)00680-8).

D. Ho and P. Severin are grateful to the Elite Network of Bavaria (IDK-NBT) for a doctoral fellowship. C. Dose is grateful to the Alexander von Humboldt foundation for a postdoctoral fellowship.

Financial support was provided by the Nanosystems Initiative Munich, the Deutsche Forschungsgemeinschaft, the Fonds der Chemischen Industrie, and the National Institutes of Health.

## REFERENCES

1. Gottesfeld, J. M., L. Neely, J. W. Trauger, E. E. Baird, and P. B. Dervan. 1997. Regulation of gene expression by small molecules. *Nature*. 387:202–205.
2. Majumdar, C. Y., and A. K. Mapp. 2005. Chemical approaches to transcriptional regulation. *Curr. Opin. Chem. Biol.* 9:467–474.
3. Connaghan-Jones, K., A. Moody, and D. Bain. 2008. Quantitative DNase footprint titration: a tool for analyzing the energetics of protein-DNA interactions. *Nat. Protocols*. 3:900–914.
4. Zhang, J., H. Lang, F. Huber, A. Bietsch, W. Grange, et al. 2006. Rapid and label-free nanomechanical detection of biomarker transcripts in human RNA. *Nat. Nanotechnol.* 1:214–220.
5. Ren, B. 2000. Genome-wide location and function of DNA binding proteins. *Science*. 290:2306–2309.
6. Harbison, C. T., D. B. Gordon, T. I. Lee, N. J. Rinaldi, K. D. Macisaac, et al. 2004. Transcriptional regulatory code of a eukaryotic genome. *Nature*. 431:99–104.
7. Solomon, M. J., and A. Varshavsky. 1985. Formaldehyde-mediated DNA-protein crosslinking: a probe for *in vivo* chromatin structures. *Proc. Natl. Acad. Sci. USA*. 82:6470–6474.
8. Warren, C., N. Kratochvil, K. Hauschild, S. Foister, M. Brezinski, et al. 2006. Defining the sequence-recognition profile of DNA-binding molecules. *Proc. Natl. Acad. Sci. USA*. 103:867–872.
9. Puckett, J., K. Muzikar, J. Tietjen, C. Warren, A. Ansari, et al. 2007. Quantitative microarray profiling of DNA-binding molecules. *J. Am. Chem. Soc.* 129:12310–12319.

10. Boozer, C., G. Kim, S. Cong, H. Guan, and T. Londergan. 2006. Looking towards label-free biomolecular interaction analysis in a high-throughput format: a review of new surface plasmon resonance technologies. *Curr. Opin. Biotechnol.* 17:400–405.
11. Wang, J., and H. S. Zhou. 2008. Aptamer-based Au nanoparticles-enhanced surface plasmon resonance detection of small molecules. *Anal. Chem.* 80:7174–7178.
12. Gurard-Levin, Z. A., and M. A. Mrksich. 2008. Combining self-assembled monolayers and mass spectrometry for applications in biochips. *Annu. Rev. Anal. Chem.* 1:767–800.
13. Albrecht, C., K. Blank, M. Lalic-Multhaler, S. Hirler, T. Mai, et al. 2003. DNA: a programmable force sensor. *Science.* 301:367–370.
14. Blank, K., T. Mai, I. Gilbert, S. Schiffmann, J. Rankl, et al. 2003. A force-based protein biochip. *Proc. Natl. Acad. Sci. USA.* 100:11356–11360.
15. Blank, K., A. Lankenau, T. Mai, S. Schiffmann, I. Gilbert, et al. 2004. Double-chip protein arrays: force-based multiplex sandwich immunoassays with increased specificity. *Anal. Bioanal. Chem.* 379:974–981.
16. Dose, C., D. Ho, H. E. Gaub, P. B. Dervan, and C. H. Albrecht. 2007. Recognition of “mirror-image” DNA by small molecules. *Angew. Chem.* 46:8384–8387.
17. Krautbauer, R., S. Fischerlander, S. Allen, and H. E. Gaub. 2002. Mechanical fingerprints of DNA drug complexes. *Single Mol.* 3:97–103.
18. Koch, S. J., A. Shundrovsky, B. C. Jantzen, and M. D. Wang. 2002. Probing protein-DNA interactions by unzipping a single DNA double helix. *Biophys. J.* 83:1098–1105.
19. Leuba, S. H., M. A. Karymov, M. Tomschik, and R. Ramjit. 2003. Assembly of single chromatin fibers depends on the tension in the DNA molecule: magnetic tweezers study. *Proc. Natl. Acad. Sci. USA.* 100:495–500.
20. Puchner, E. M., A. Alexandrovich, A. L. Kho, U. Hensen, L. V. Schäfer, B. Brandmeier, F. Gräter, H. Grubmüller, H. E. Gaub, and M. Gautel. 2008. Mechanoenzymatics of titin kinase. *Proc. Natl. Acad. Sci. USA.* 105:13385–13390.
21. Schlierf, M., F. Berkemeier, and M. Rief. 2007. Direct observation of active protein folding using lock-in force spectroscopy. *Biophys. J.* 93:3989–3998.
22. Wiita, A., R. Perez-Jimenez, K. Walther, F. Gräter, B. Berne, et al. 2007. Probing the chemistry of thioredoxin catalysis with force. *Nature.* 450:124–127.
23. Clemen, A. E. M., M. Vilfan, J. Jaud, J. S. Zhang, M. Barmann, et al. 2005. Force-dependent stepping kinetics of myosin-V. *Biophys. J.* 88:4402–4410.
24. Gosse, C., and V. Croquette. 2002. Magnetic tweezers: micromanipulation and force measurement at the molecular level. *Biophys. J.* 82:3314–3329.
25. Dervan, P. B., A. T. Poulin-Kerstien, E. J. Fechter, and B. S. Edelson. 2005. Regulation of gene expression by synthetic DNA-binding ligands. *Top. Curr. Chem.* 253:1–31.
26. Dervan, P. B., and B. S. Edelson. 2003. Recognition of the DNA minor groove by pyrrole-imidazole polyamides. *Curr. Opin. Struct. Biol.* 13:284–299.
27. Dervan, P. B. 2001. Molecular recognition of DNA by small molecules. *Bioorg. Med. Chem.* 9:2215–2235.
28. White, S., J. W. Szewczyk, J. M. Turner, E. E. Baird, and P. B. Dervan. 1998. Recognition of the four Watson-Crick base pairs in the DNA minor groove by synthetic ligands. *Nature.* 391:468–471.
29. Kielkopf, C. L., R. E. Bremer, S. White, J. W. Szewczyk, J. M. Turner, et al. 2000. Structural effects of DNA sequence on T.A recognition by hydroxypyrrrole/pyrrole pairs in the minor groove. *J. Mol. Biol.* 295:557–567.
30. Mrksich, M., M. E. Parks, and P. B. Dervan. 1994. Hairpin peptide motif - a new class of oligopeptides for sequence-specific recognition in the minor-groove of double-helical DNA. *J. Am. Chem. Soc.* 116:7983–7988.
31. Swalley, S. E., E. E. Baird, and P. B. Dervan. 1999. Effects of  $\gamma$ -turn and  $\beta$ -tail amino acids on sequence-specific recognition of DNA by hairpin polyamides. *J. Am. Chem. Soc.* 121:1113–1120.
32. Kielkopf, C. L., S. White, J. W. Szewczyk, J. M. Turner, E. E. Baird, et al. 1998. A structural basis for recognition of A center dot T and T center dot A base pairs in the minor groove of B-DNA. *Science.* 282:111–115.
33. deClairac, R. P. L., B. H. Geierstanger, M. Mrksich, P. B. Dervan, and D. E. Wemmer. 1997. NMR characterization of hairpin polyamide complexes with the minor groove of DNA. *J. Am. Chem. Soc.* 119:7909–7916.
34. Cohen, J. D., J. P. Sadowski, and P. B. Dervan. 2007. Addressing single molecules on DNA nanostructures. *Angew. Chem.* 46:7956–7959.
35. Schmidt, T. L., C. K. Nandi, G. Rasched, P. P. Parui, B. Brutschy, et al. 2007. Polyamide struts for DNA architectures. *Angew. Chem.* 46:4382–4384.
36. Arndt, H. D., K. E. Hauschild, D. P. Sullivan, K. Lake, P. B. Dervan, et al. 2003. Toward artificial developmental regulators. *J. Am. Chem. Soc.* 125:13322–13323.
37. Stafford, R. L., H. D. Arndt, M. L. Brezinski, A. Z. Ansari, and P. B. Dervan. 2007. Minimization of a protein-DNA dimerizer. *J. Am. Chem. Soc.* 129:2660–2668.
38. Olenyuk, B. Z., G. J. Zhang, J. M. Klco, N. G. Nickols, W. G. Kaelin, Jr., et al. 2004. Inhibition of vascular endothelial growth factor with a sequence-specific hypoxia response element antagonist. *Proc. Natl. Acad. Sci. USA.* 101:16768–16773.
39. Nickols, N. G., and P. B. Dervan. 2007. Suppression of androgen receptor-mediated gene expression by a sequence-specific DNA-binding polyamide. *Proc. Natl. Acad. Sci. USA.* 104:10418–10423.
40. Nickols, N. G., C. S. Jacobs, M. E. Farkas, and P. B. Dervan. 2007. Modulating hypoxia-inducible transcription by disrupting the HIF-1-DNA interface. *ACS Chem. Biol.* 2:561–571.
41. Albrecht, C. H., H. Clausen-Schaumann, and H. E. Gaub. 2006. Differential analysis of biomolecular rupture forces. *J. Phys. Condens. Matter.* 18:S581–S599.
42. Perutz, S., E. J. Kramer, J. Baney, and C. Y. Hui. 1997. Adhesion between hydrolyzed surfaces of poly(dimethylsiloxane) networks. *Macromolecules.* 30:7964–7969.
43. Wiegand, G., K. R. Neumaier, and E. Sackmann. 1998. Microinterferometry: three-dimensional reconstruction of surface microtopography for thin-film and wetting studies by reflection interference contrast microscopy (RICM). *Appl. Opt.* 37:6892–6905.
44. Morfill, J., F. Kuhner, K. Blank, R. Lugmaier, J. Sedlmair, et al. 2007. B-S transition in short oligonucleotides. *Biophys. J.* 93:2400–2409.
45. Merkel, R., P. Nassoy, A. Leung, K. Ritchie, and E. Evans. 1999. Energy landscapes of receptor-ligand bonds explored with dynamic force spectroscopy. *Nature.* 397:50–53.
46. Herman, D. M., E. E. Baird, and P. B. Dervan. 1998. Stereochemical control of the DNA binding affinity, sequence specificity, and orientation preference of chiral hairpin polyamides in the minor groove. *J. Am. Chem. Soc.* 120:1382–1391.
47. Kienberger, F., V. P. Pastushenko, G. Kada, and H. J. Gruber. 2000. Static and dynamical properties of single poly(ethylene glycol) molecules investigated by force spectroscopy. *Single Mol.* 78:123–128.
48. Friedsam, C., A. K. Wehle, F. Kuhner, and H. E. Gaub. 2003. Dynamic single-molecule force spectroscopy: bond rupture analysis with variable spacer length. *J. Phys. Condens. Matter.* 15:S1709–S1723.
49. Evans, E., and K. Ritchie. 1997. Dynamic strength of molecular adhesion bonds. *Biophys. J.* 72:1541–1555.
50. Viani, M., T. Schäffer, A. Chand, M. Rief, H. E. Gaub, and P. Hansma. 1999. Small cantilevers for force spectroscopy of single molecules. *J. Appl. Phys.* 86:2258–2262.
51. Xia, Y., and G. M. Whitesides. 1998. Soft lithography. *Annu. Rev. Mater. Sci.* 28:153–184.
52. Bernard, A., J. P. Renault, B. Michel, and H. R. Bosshard. 2000. Micro-contact printing of proteins. *Adv. Mater.* 12:1067–1070.

53. Neuert, G., C. H. Albrecht, and H. E. Gaub. 2007. Predicting the rupture probabilities of molecular bonds in series. *Biophys. J.* 93:1215–1223.
54. Rouzina, I., and V. A. Bloomfield. 2001. Force-induced melting of the DNA double helix. 2. Effect of solution conditions. *Biophys. J.* 80:894–900.
55. White, S., E. E. Baird, and P. B. Dervan. 1997. Orientation preferences of pyrrole-imidazole polyamides in the minor groove of DNA. *J. Am. Chem. Soc.* 119:8756–8765.
56. Hawkins, C. A., R. P. de Clairac, R. N. Dominey, E. E. Baird, S. White, et al. 2001. Controlling binding orientation in hairpin polyamide DNA complexes. *J. Am. Chem. Soc.* 122:5235–5243.
57. Hsu, C. F., J. W. Phillips, J. W. Trauger, M. E. Farkas, J. M. Belitsky, et al. 2007. Completion of a programmable DNA-binding small molecule library. *Tetrahedron*. 63:6146–6151.
58. Halperin, A., A. Buhot, and E. Zhulina. 2006. On the hybridization isotherms of DNA microarrays: the Langmuir model and its extensions. *J. Phys. Condens. Matter*. 18:S463–S490.
59. Baliga, R., E. Baird, D. Herman, C. Melander, P. B. Dervan, et al. 2001. Kinetic consequences of covalent linkage of DNA binding polyamides. *Biochemistry*. 40:3–8.
60. Rief, M., H. Clausen-Schaumann, and H. E. Gaub. 1999. Sequence dependent mechanics of single DNA molecules. *Nat. Struct. Biol.* 6:346–349.
61. Lebrun, A., and R. Lavery. 1996. Modeling extreme stretching of DNA. *Nucleic Acids Res.* 24:2260–2267.
62. Smith, S. B., Y. J. Cui, and C. Bustamante. 1996. Overstretching B-DNA: the elastic response of individual double-stranded and single-stranded DNA molecules. *Science*. 271:795–799.
63. Ho, D., K. Falter, P. Severin, and H. E. Gaub. 2009. DNA as a force sensor in an aptamer-based biochip for ATP. *Anal. Chem.* n press.
64. Titz, B., M. Schlesner, and P. Uetz. 2004. What do we learn from high-throughput protein interaction data? *Expert Rev. Proteomics*. 1:111–121.
65. Kitano, H. 2002. Systems biology: a brief overview. *Science*. 295:1662–1664.

Biophysical Journal, Volume 96

**Supporting Material**

**Quantitative detection of small molecule/DNA complexes employing a force-based and label-free DNA-microarray**

Dominik Ho, Christian Dose, Christian H. Albrecht, Philip Severin, Katja Falter, Peter B. Dervan, and Hermann E. Gaub

## SUPPLEMENTARY INFORMATION

### **“Quantitative detection of small molecule/DNA complexes employing a force-based and label-free DNA-microarray”**

*Dominik Ho<sup>1,2</sup>, Christian Dose<sup>3</sup>, Christian H. Albrecht<sup>1</sup>, Philip Severin<sup>1</sup>, Katja Falter<sup>1</sup>, Peter B. Dervan<sup>3</sup>, Hermann E. Gaub<sup>1</sup>*

[<sup>1</sup>] Lehrstuhl für Angewandte Physik and Center for Nanoscience  
Ludwig-Maximilians-Universität  
Amalienstrasse 54, 80799 Munich, Germany  
Fax: (+49) 89-2180-2050  
E-mail: gaub@lmu.de

[<sup>2</sup>] Munich Center For Integrated Protein Science (CIPSM)  
Ludwig-Maximilians-Universität  
Butenandtstrasse 5-13, 81377 Munich, Germany  
E-mail: dominik.ho@web.de

[<sup>3</sup>] Division of Chemistry and Chemical Engineering  
California Institute of Technology  
Pasadena, California 91125, USA  
Fax: (+1) 626-683-8753  
E-mail: dervan@caltech.edu

**DNA surface density.** Quantitative analysis of the fluorescence images relies on the assumption that the amount of fluorescently labeled species per unit area is proportional to the obtained fluorescence intensity per unit area. To investigate this relationship, we titrated identically prepared oligomer **1** spots on a glass slide with different amounts of oligomer **2** ranging from 0 to 0.6 pMol. After 2 hours of incubation the slide was washed thoroughly in 1x PBS and read out via fluorescence. The fluorescence intensities were summed over all pixels of each well divided by the fluorescence spot area, which was on average 1.8 mm of diameter. The fluorescence intensity was proportional to the amount of added ligand for amounts of DNA oligomer **2** less than 0.4 pMol. At higher amounts the fluorescence intensity saturated and deviated significantly from a line fit.

The observed saturation can be explained by electrostatic repulsion between the dsDNA. Short dsDNA is a rod like, cylindrical molecule, which is most densely packed in a parallel arrangement. Close packing of short dsDNA on a surface is thus equivalent to the problem of close packing of hard disks. The total hard disk radius is the sum of the dsDNA radius and the length of electrostatic repulsion. The former is known to be 0.95 nm [1] and the latter is best described by the Debye length that is approximately 0.62 nm at 147 mM Na<sup>+</sup> [2]. The total disk radius is therefore 1.57 nm. Randomly packing discs results in a packing efficiency of 82% [2]. The packing efficiency and the total disk radius yield the theoretical maximum in short dsDNA surface density  $\rho_{\text{Debye}}$  of 0.11 molecules per nm<sup>2</sup> in good agreement with literature values [3].

To compare whether the onset of fluorescence intensity saturation coincides with  $\rho_{\text{Debye}}$  the densities of **1·2** complexes per unit area were determined from the fluorescence spot size and the assumption that all oligomers **2** hybridized to free oligomers **1** immobilized to the surface. Further, the expected maximal fluorescence intensity was determined by extrapolating the line fit for low densities to  $\rho_{\text{Debye}}$  yielding  $I_{\text{Debye}}$ . In Figure S1 the fluorescence intensity ratio  $I/I_{\text{Debye}}$  was plotted against the corresponding calculated surface density ranging from 0 to 0.13 molecules per nm<sup>2</sup>. The observed saturation of fluorescence intensity at around 0.09 molecules per nm<sup>2</sup> is in good agreement with  $\rho_{\text{Debye}}$ . Remaining free ssDNA strands that also occupy a small fraction of the surface area may explain the slightly lower experimentally determined value.

It is entirely possible that a non-linearity between amount of oligomer **2** per unit area and fluorescence signal at high surface densities contributes to the observed saturation effect. Hence, the molecular setups in the present study were prepared at  $\rho_0$  of 0.06 molecular setups per nm<sup>2</sup>. This is a surface density for which we have shown the fluorescence per unit area to

be proportional to the fluorescently labeled species per unit area. Nonetheless, the surface density is rather high: the Flory radius, which is deduced from the radius of gyration, is a good measure of the volume a polymer encompasses [1] [4]. From the actual lengths and the persistence lengths of dsDNA [5], ssDNA [6] and PEG [7] we calculate a Flory radius of 9.38 nm for the **1·2·3** molecular setups used in our experiments. Assuming again a close packing of disks yields an upper limit of 0.003 molecular setups per nm<sup>2</sup> for the regime wherein the constructs do not interact with each other. The densities used in our experiments are an order of magnitude higher than that. This is a fact that should be kept in mind if the binding of larger and less robust ligands like proteins to dsDNA is going to be investigated. In this case, the surface densities of the molecular setups may have to be decreased further in order to avoid steric hindrance and unwanted interactions.

## REFERENCES

- [1] Halperin, A., A. Buhot and E. Zhulina. 2006. On the hybridization isotherms of DNA microarrays: the Langmuir model and its extensions. *J. Phys.: Condens. Matter*, 18:S463-S490.
- [2] Berryman, J. G. 1983. Random close packing of hard spheres and disks. *Phys. Rev. A*. 27:1053-1061.
- [3] Ray, S., S. Daube, G. Leitus, Z. Vager and R. Naaman. 2006. Chirality-Induced Spin-Selective Properties of Self-Assembled Monolayers of DNA on Gold. *Phys. Rev. Lett.* 96: 036101.
- [4] Israelachvili, J. N. 1991. *Intermolecular and Surface Forces*. Academic Press, New York.
- [5] Marko, J. F. and E. D. Siggia. 1995. Stretching DNA. *Macromolecules*. 28:8759-8770.
- [6] Rief, M., H. Clausen-Schaumann and H. E. Gaub. 1999. Sequence dependent mechanics of single DNA molecules. *Nat. Struct. Biol.* 6:346-349.
- [7] Oesterhelt, F., M. Rief and H. E. Gaub. 1999. Single molecule force spectroscopy by AFM indicates helical structure of poly (ethylene-glycol) in water. *New J. Phys.* 1:6.1-6.11.

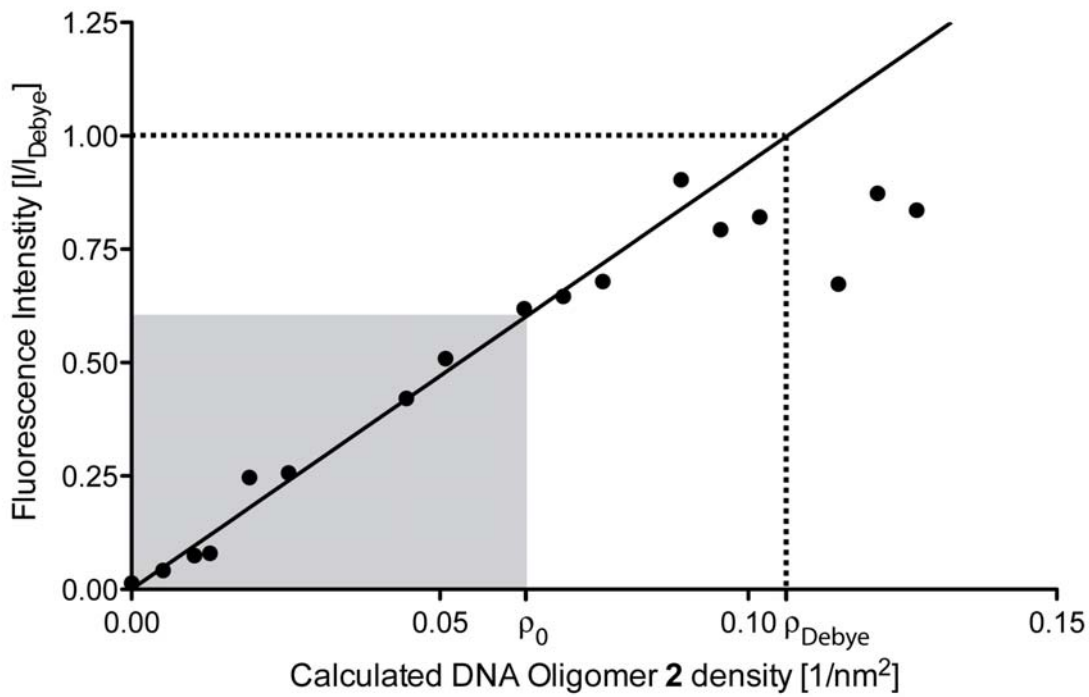


**Figure S1.** Different amounts of oligomer **2** were incubated with identically prepared oligomer **1** spots. The fluorescence intensities per unit area are plotted against the calculated surface densities. The dashed line indicates the highest possible density of oligomer **2** per unit area based on the electrostatic repulsion argument. The CUFA experiments are performed at densities of oligomer **2** per unit area, wherein the fluorescence intensity per unit area is proportional to the presence of fluorescently labeled oligomer **2** per unit area (highlighted in grey).

# DNA as a Force Sensor in an Aptamer-Based Biochip for Adenosine

**Dominik Ho, Katja Falter, Philip Severin, and Hermann E. Gaub\***

*Lehrstuhl für Angewandte Physik and Center for Nanoscience (CeNS), Ludwig-Maximilians-Universität, Amalienstrasse 54, 80799 Munich, Germany, and Munich Center For Integrated Protein Science (CIPSM), Ludwig-Maximilians-Universität, Butenandtstrasse 5-13, 81377 Munich, Germany*

Without prior signal amplification, small molecules are difficult to detect by current label-free biochip approaches. In the present study, we developed a label-free capture biochip based on the comparative measurement of unbinding forces allowing for direct detection of small-molecule–aptamer interactions. The principle of this assay relies on increased unbinding forces of bipartite aptamers due to complex formation with their cognate ligands. The bipartite aptamers are immobilized on glass support via short DNA duplexes that serve as references to which unbinding forces can be compared. In a simple model system, adenosine is captured from solution by an adenosine-selective aptamer. Linking the molecular chains, each consisting of a short DNA reference duplex and a bipartite aptamer, between glass and a poly(dimethylsiloxane) (PDMS) surface and subsequently separating the surfaces compares the unbinding forces of the two bonds directly. Fluorescence readout allows for quantification of the fractions of broken aptamer and broken reference bonds. The presence of micromolar adenosine concentrations reliably resulted in a shift toward larger fractions of broken reference bonds. Because of the force-based design, the interactions between the bipartite aptamer and the target, rather than the presence of the target, are detected and no washing step disturbing the equilibrium state prior to probing and no reporter aptamer or antibody is required. The assay exhibits excellent selectivity against other nucleotides and detects adenosine in the presence of a complex molecular background. Multiplexing was demonstrated by performing whole titration experiments on a single chip revealing an effective half-maximal concentration of 124.8 μM agreeing well with literature values.

A current goal within the field of bioanalytical methods is the development of label-free detection formats, which probe multiple interactions simultaneously employing massively parallel assays.<sup>1</sup> High impact of DNA biochips on the field of biology provides motivation to develop arrays for other classes of molecules,

including peptides, proteins, and small molecules.<sup>2</sup> DNA or RNA aptamers are promising candidates for fabrication of microarray surfaces, which simply and effectively capture above-mentioned analytes from solution. Numerous reports confirm that aptamers specifically respond to all kinds of molecules<sup>3</sup> such that they are increasingly recognized as rivals for antibodies in in vitro diagnostics<sup>4</sup> and molecular sensor applications,<sup>5–7</sup> surpassing them in terms of small molecular weight, ease of modification, and ability to detect toxins.<sup>8</sup> In contrast to proteins, which are difficult to immobilize on surfaces due to their tendency to adsorb nonspecifically and thus lose activity,<sup>9</sup> standard protocols for oligonucleotide microarrays are used for aptamer biochips.

The development of such arrays has proven to be more difficult than expected. Small molecules in particular are rarely detected due to several reasons: First, their small size induces only small signals using current biochip-compatible, label-free detection techniques (e.g., surface plasmon resonance,<sup>10</sup> electrochemical,<sup>11</sup> or cantilever bending<sup>12</sup> based sensors). Second, background signals are generally large in biochip assays due to the tendency of molecules to adsorb to basically all man-made surfaces.<sup>13–15</sup> Third, aptamers developed against small molecules are generally of low affinity,<sup>16</sup> prohibiting washing steps that would increase the signal-to-background ratio. The combination of small signal, high background, and no option for stringent washes creates an overwhelming technical hurdle for the quantification of small molecules without prior signal amplification. Here, we present a widely applicable strategy for the direct detection of small-

- (2) Lockhart, D. J.; Winzeler, E. A. *Nature* 2000, 405, 827–836.
- (3) Hermann, T.; Patel, D. J. *Science* 2000, 287, 820–825.
- (4) Rimmeli, M. *ChemBioChem* 2003, 4, 963–971.
- (5) Zhang, S.; Xia, J.; Li, X. *Anal. Chem.* 2008, 80, 8382–8388.
- (6) Wang, J.; Zhou, H. S. *Anal. Chem.* 2008, 80, 7174–7178.
- (7) Navani, N. K.; Li, Y. F. *Curr. Opin. Chem. Biol.* 2006, 10, 272–281.
- (8) Tang, J.; Xie, J.; Shao, N.; Yan, Y. *Electrophoresis* 2006, 27, 1303–1311.
- (9) Kusnezow, W.; Hoheisel, J. *J. Mol. Recognit.* 2003, 16, 165–176.
- (10) Boozer, C.; Kim, G.; Cong, S.; Guan, H.; Londergan, T. *Curr. Opin. Biotechnol.* 2006, 17, 400–405.
- (11) Xu, D.; Xu, D.; Yu, X.; Liu, Z.; He, W.; Ma, Z. *Anal. Chem.* 2005, 77, 5107–5113.
- (12) Zhang, J.; Lang, H.; Huber, F.; Bietsch, A.; Grange, W.; Certa, U.; Mckendry, R.; Güntherodt, H.; Hegner, M.; Gerber, C. *Nat. Nanotechnol.* 2006, 1, 214–220.
- (13) Haab, B. B.; Dunham, M. J.; Brown, P. O. *Genome Biol.* 2001, 2, 0004.10004.13.
- (14) Michaud, G.; Salsbury, M.; Zhou, F.; Bangham, R.; Bonin, J.; Guo, H.; Snyder, M.; Predki, P.; Schweitzer, B. *Nat. Biotechnol.* 2003, 21, 1509–1512.
- (15) Ma, H.; Horiuchi, K. *Drug Discovery Today* 2006, 11, 661–668.
- (16) Hamula, C.; Guthrie, J.; Zhang, H.; Li, X.; Le, X. *TrAC, Trends Anal. Chem.* 2006, 25, 681–691.

\* To whom correspondence should be addressed. Phone: +49 89 2180 3172. Fax: +49 89 21 80 2050. E-mail: gaub@physik.lmu.de.

(1) Gurard-Levin, Z. A.; Mrksich, M. *Annu. Rev. Anal. Chem.* 2008, 1, 767–800.

molecule–aptamer complex formation. Our approach reports interactions between small molecules and aptamers, rather than the mere presence of small molecules close to a sensor surface. Thereby, nonspecific adhesion, the major bottleneck in the development of next-generation biochips, is rendered insignificant.

For detection of the bound analyte we applied the comparative unbinding force assay (CUFA), which operates label-free and is insensitive to nonspecifically adsorbed target molecules. CUFA has already been applied to detect single-nucleotide polymorphisms,<sup>17</sup> to study differences of antibody/antigen interactions,<sup>18</sup> to eliminate cross-reactions on protein microarrays,<sup>19</sup> and to investigate the chiral selectivity of small peptides.<sup>20</sup> Whereas standard single-molecule force spectroscopy experiments measure the unbinding forces of molecular complexes by a microscopic, springlike object, e.g., an atomic force microscopy (AFM) cantilever<sup>21</sup> or a bead in an optical trap,<sup>22</sup> CUFA reduces the force detector to a single DNA reference duplex. Many molecular chains, each consisting of a bipartite aptamer and a DNA reference duplex, are grafted between two surfaces. The linker between the bonds is conjugated to a fluorophore. Upon separation of the surfaces, a force gradually builds up within the molecular chain and the unbinding forces of the bipartite aptamer structure are compared directly against the unbinding forces of the short DNA reference duplex. The result, i.e., the fractions of broken aptamer and broken reference bonds, is stored in a binary fluorophore distribution (fluorophore top or bottom surface). If complex formation between aptamer and ligand results in increased unbinding forces of the aptamer structure, a shift toward larger fractions of broken reference bonds is expected. Thereby, CUFA combines the advantages of fluorescence-based techniques, namely, fast and sensitive detection employing commercially available scanners or fluorescence microscopes, with the advantages of label-free methods, namely, no undesirable label interactions and the option for simultaneous detection of multiple analytes. Importantly, high specificity when investigating molecular interactions is a major strength of CUFA. Current fluorescent<sup>23</sup> and label-free biochip methods do not allow for discrimination between specifically and nonspecifically adhered analytes, which may lead to false-positives. Washing steps are performed to reduce non-specific adhesion. However, if molecular interactions with equilibrium dissociation constants in the micromolar range need to be characterized, specifically but weakly interacting molecules are also removed resulting in false-negatives. CUFA overcomes these difficulties by detecting the interaction between the capture

aptamer and its target and not merely the presence of the target.

In the present study, we investigated the interaction between adenosine and an adenosine-selective aptamer. This model system is instructive for the reasons that the aptamer is well-characterized,<sup>24–26,28</sup> the interaction is very weak, and the analyte is so small that it cannot be detected directly with surface plasmon resonance.<sup>6</sup>

## EXPERIMENTAL SECTION

**Immobilization of Aptamer–DNA Unbinding Force Complex on Slides (Bottom Surface).** DNA oligomers **1**, **2**, and **3** were purchased HPLC grade from IBA GmbH (Göttingen, Germany). Sequences and modifications of all oligonucleotides are the following: **1**, NH<sub>2</sub>-(hexaethyleneglycol)<sub>5</sub>-5'-TTT TTT TTT TCG GTC TGT CGC GTA CTT GCA-3'; **2**, 3'-GCC AGA CAG CGC ATG AAC GTT TTT T-5'-T(Cy3) TTT TTC AAC ATA CCT GGG GGA GTA TAT AAT GAC TGA CCC C-3'; **3**, biotin-5'-TTT TTT TTT TGG GGT CAG TCA TTA TAG CGG AGG AAG GTA TGT TG-3'. For the upside-down experiment the NH<sub>2</sub>-(hexaethyleneglycol)<sub>5</sub> (HEGL) and biotin modifications are exchanged. The five HEGL linkers are connected via phosphate groups. DNA oligomer **1** is amine-modified, which allows covalent linkage to aldehyde-functionalized glass slides (Schott GmbH, Jena, Germany). We spotted 2 μL drops of 5x SSC (saline sodium citrate; Sigma-Aldrich GmbH, Munich, Germany) containing 25 μM oligomer **1** on the aldehyde slide in a 4 × 4 pattern and incubated the slide in a saturated NaCl ddH<sub>2</sub>O atmosphere overnight. After washing the slide with ddH<sub>2</sub>O containing 0.2% sodium dodecyl sulfate (SDS; VWR Scientific GmbH, Darmstadt, Germany) and thoroughly rinsing the slide with ddH<sub>2</sub>O we reduced the resulting Schiff bases with 1% aqueous NaBH<sub>4</sub> (VWR Scientific GmbH, Darmstadt, Germany) for 20 min. Subsequently, the slide was washed with 1× SSC and thoroughly rinsed with ddH<sub>2</sub>O. In order to reduce nonspecific binding, the slides were blocked in 1× SSC containing 4% bovine serum albumin (BSA; Sigma-Aldrich GmbH, Munich, Germany) for 30 min. Custom-made 16-well silicone isolators (Grace-Biolabs, OR) were placed on top of the immobilized DNA oligomer **1**. The 0.1 μM Cy3-modified oligomer **2** and 0.2 μM biotin-modified oligomer **3** were hybridized to the latter for 1 h, completing the **1·2·3** complex on the glass slide. The slides were washed with 1× SSC containing 0.05% SDS and thoroughly rinsed with 1× SSC. The silicone isolators stayed on the slide throughout the experiment, and care was taken that after hybridization the slide remained immersed in 1× SSC.

**Ligand Incubation.** The 16-well silicon isolators allow for incubation with different concentrations of the ligand molecule on one slide. An amount of 100 μL of the respective solutions was circulated through the wells employing a self-made microfluidic system. The latter was driven by two 16-channel peristaltic pumps (Ismatec GmbH, Wertheim-Mondfeld, Germany) pumping the different solutions through tubing and blunt needles leading into and out of the wells in a closed circuit. The tubing was

- (17) Albrecht, C.; Blank, K.; Lalic-Multhaler, M.; Hirler, S.; Mai, T.; Gilbert, I.; Schiffmann, S.; Bayer, T.; Clausen-Schaumann, H.; Gaub, H. E. *Science* **2003**, *301*, 367–370.
- (18) Blank, K.; Mai, T.; Gilbert, I.; Schiffmann, S.; Rankl, J.; Zivin, R.; Tackney, C.; Nicolaus, T.; Spinnler, K.; Oesterhelt, F.; Benoit, M.; Clausen-Schaumann, H.; Gaub, H. E. *Proc. Natl. Acad. Sci. U.S.A.* **2003**, *100*, 11356–11360.
- (19) Blank, K.; Lankenau, A.; Mai, T.; Schiffmann, S.; Gilbert, I.; Hirler, S.; Albrecht, C.; Benoit, M.; Gaub, H. E.; Clausen-Schaumann, H. *Anal. Bioanal. Chem.* **2004**, *379*, 974–981.
- (20) Dose, C.; Ho, D.; Gaub, H. E.; Dervan, P. B.; Albrecht, C. *Angew. Chem., Int. Ed.* **2007**, *46*, 8384–8387.
- (21) Florin, E. L.; Moy, V. T.; Gaub, H. E. *Science* **1994**, *264*, 415–417.
- (22) Svoboda, K.; Schmidt, C. F.; Schnapp, B. J.; Block, S. M. *Nature* **1993**, *365*, 721–727.
- (23) Warren, C.; Kratochvil, N.; Hauschild, K.; Foister, S.; Brezinski, M.; Dervan, P.; Phillips, G., Jr.; Ansari, A. *Proc. Natl. Acad. Sci. U.S.A.* **2006**, *103*, 867–872.

(24) Huizenga, D. E.; Szostak, J. W. *Biochemistry* **1995**, *34*, 656–665.

(25) Lin, C. H.; Patel, D. J. *Chem. Biol.* **1997**, *4*, 817–832.

(26) Stojanovic, M. N.; de Prada, P.; Landry, D. W. *J. Am. Chem. Soc.* **2000**, *122*, 11547–11548.

(28) Jhaveri, S. D.; Kirby, R.; Conrad, R.; Maglott, E. J.; Bowser, M.; Kennedy, R. T.; Glick, G.; Ellington, A. D. *J. Am. Chem. Soc.* **2000**, *122*, 2469–2473.

passivated prior to use with 1× SSC containing 4% BSA for 30 min. Adenosine triphosphate (ATP), adenosine monophosphate (AMP), and guanosine triphosphate (GTP) were obtained from Roche (Roche GmbH, Grenzach, Germany).

#### Immobilization of Streptavidin on Poly(dimethylsiloxane)

**Stamp (Top Surface).** Micro- and macrostructured poly(dimethylsiloxane) (PDMS) stamps were fabricated by casting 1:10 cross-linker/base (Sylgard, Dow Corning, MI) into a custom-made Pyrex/silicon wafer (HSG-IMIT, Villingen-Schwenningen, Germany) according to standard procedures.<sup>29</sup> The resulting PDMS stamp carries pillars of 1 mm diameter and 1 mm height in a square pattern on a 3 mm thick basis. The spacing between two adjacent pillars is 3 mm. The flat pillar surface is microstructured with 100 μm × 100 μm pads separated by 41 μm wide and 5 μm deep rectangular trenches allowing for drainage of liquid during the contact and separation process. Before free polymers were extracted from the device in toluene using a Soxhlet device, the PDMS was cut in 4 × 4 pillar pieces. PDMS was then activated in 12.5% HCl overnight and derivatized with (3-glycidoxypropyl)-trimethoxysilane (ABCR, Karlsruhe, Germany) in order to generate epoxide groups. NH<sub>2</sub>-PEG-biotin (3400 g/mol; Rapp Polymere, Tübingen, Germany) was molten at 80 °C, and roughly 1 μL was spotted on each pillar followed by overnight incubation in argon atmosphere at 80 °C. The excess polymers were thoroughly removed with ddH<sub>2</sub>O. Shortly before the experiment the PDMS was incubated with 1 μg/mL streptavidin (Thermo Fisher Scientific, Bonn, Germany) in 1× SSC and 0.4% BSA for 30 min, washed with 1× SSC containing 0.05% Tween 20 (VWR Scientific GmbH, Darmstadt, Germany), and gently dried with N<sub>2</sub> gas.

**Contact Process and Fluorescence Readout.** On an inverted microscope (Carl-Zeiss MicroImaging GmbH, Göttingen, Germany) the slide was fixed on a stainless steel stage with permanent magnets. The PDMS device was placed upside down on a glass block connected to a xyz stepper motor system (OWIS GmbH, Staufen, Germany) and a closed-loop piezo (Piezo Systems Jena, Germany). Prior to the contact process, the slide and the PDMS stamp were aligned parallel to each other, employing reflection interference microscopy<sup>30</sup> and a commercially available gimbal adjustment system (OWIS GmbH, Germany) mounted to the piezo. With the use of the latter, contact was established. Care was taken that each individual pillar is compressed not more than 3 μm. The separation of the two surfaces was carried out at constant velocity of 1 μm/s. Fluorescence images were recorded before and after the contact process employing a Tecan microarray scanner (Tecan Austria GmbH, Grödig, Austria).

## RESULTS AND DISCUSSION

#### Detection Principle of the Force-Based Aptamer Sensor.

The implementation of this format is shown schematically in Figure 1. Although the instrumentation is almost identical to a microcontact printing setup,<sup>31</sup> the key to the comparable unbinding force assay lies within the molecular setup (Figure 1a). A short DNA duplex in shear geometry serves as a force reference. One

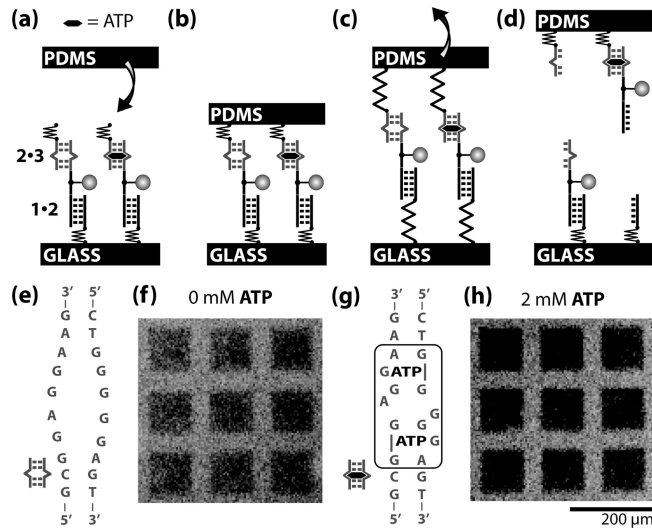


**Figure 1.** Schematic representation of the comparative unbinding force assay for the detection of small molecules. (a) DNA reference duplexes **1·2** and bipartite aptamers **2·3** are bound in series via PEG spacers to glass support. Depending on the presence of ATP, the aptamer is in its bound or free state. A streptavidin-functionalized PDMS surface is approached to the glass surface. (b) PDMS couples to the **3** oligomers of the bipartite aptamers via biotin-streptavidin complex formation. (c) The two surfaces are separated, and an increasing force builds up until either the reference duplex or the bipartite aptamer breaks. (d) Aptamer-ATP complex formation increases the unbinding forces of the bipartite aptamer. In comparison to the case that no ATP is present, a larger fraction of linking DNA strands conjugated to fluorophores is transferred from the glass to the PDMS. (e) At 0 mM ATP the bipartite aptamer is present as a loose bubble flanked by Watson-Crick base-paired stem regions. (f) Fluorescence on glass after contact without prior incubation with ATP. The squarelike features (100 × 100 μm<sup>2</sup>) correspond to the area contacted with microstructured PDMS. (g) At 2 mM ATP the bipartite aptamer bases show enhanced stacking upon binding of two molecules of ATP. (h) Fluorescence on glass after contact with prior incubation with 2 mM ATP. In comparison to the 0 mM ATP case, a larger fraction of fluorescence was transferred from the glass to the PDMS.

strand, oligomer **1**, is connected to glass support (bottom surface) via a (hexaethyleneglycol)<sub>5</sub> spacer. The complementary strand, oligomer **2**, which also carries a Cy3 fluorescence label, possesses an overhang containing the sequence of one part of the bipartite ATP aptamer. The complementary aptamer strand, oligomer **3**, is biotin-modified at the end of a polythymine linker and completes the **1·2·3** complex on the glass slide. We chose the reference force duplex and the stem regions flanking the aptamer such that their calculated free energies<sup>32</sup> are similar, assuming that similar free energies also imply similar unbinding forces under an external load. The spontaneous off-rates are sufficiently slow such that the complex is stable for days under physiological conditions.

In Figure 1b the **1·2·3** complex on the glass surface was brought into contact with a PDMS surface functionalized with streptavidin attached to 3400 g/mol PEG linkers, allowing for biotin-streptavidin complexation. After 10 min, the surfaces were separated at a constant velocity of 1 μm/s (Figure 1c). Thereby, the polymeric anchors were stretched and a force gradually built up until the chain of molecular complexes ruptured either at the

- (29) Wilbur, J. L.; Kumar, A.; Kim, E.; Whitesides, G. M. *Adv. Mater.* **1994**, *6*, 600–604.
- (30) Wiegand, G.; Neumaier, K. R.; Sackmann, E. *Appl. Opt.* **1998**, *37*, 6892–6905.
- (31) Bernard, A.; Renault, J. P.; Michel, B.; Bosshard, H. R. *Adv. Mater.* **2000**, *12*, 1067–1070.

(32) Kibbe, W. A. *Nucleic Acids Res.* **2007**, *35*, 43–46.

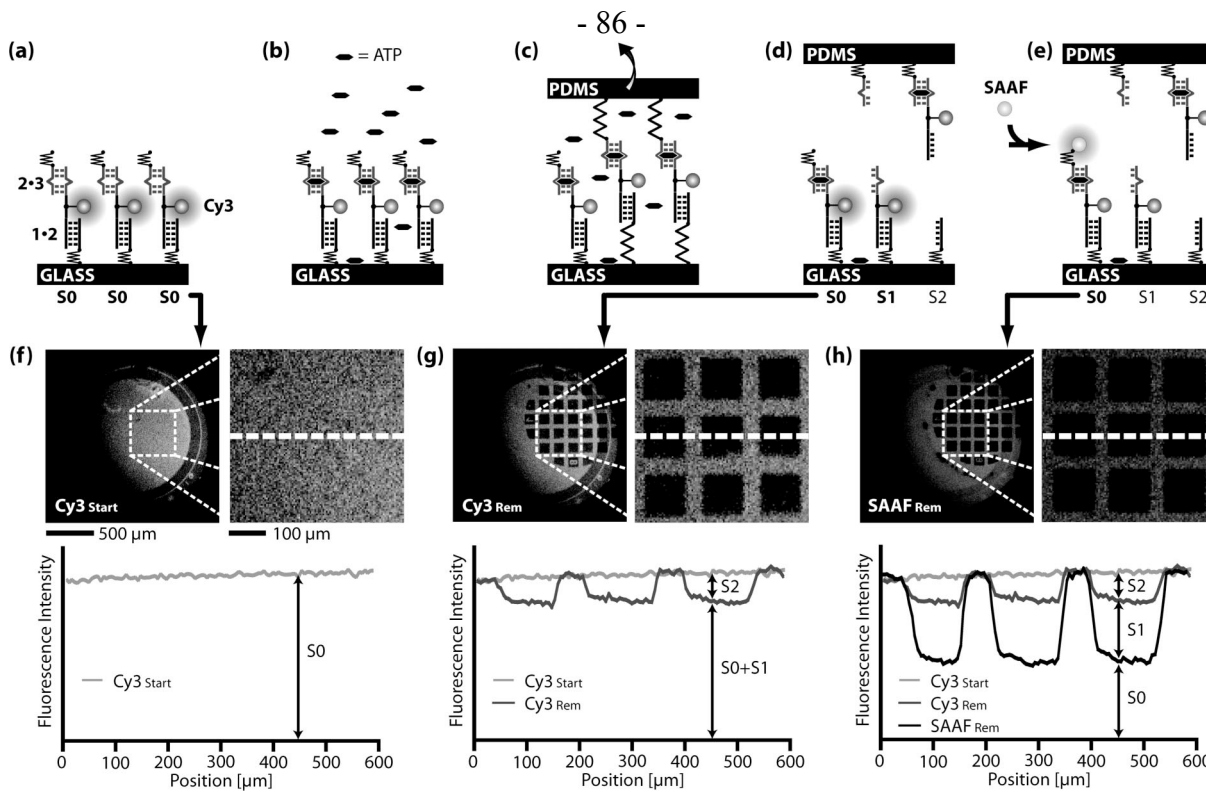


**Figure 2.** Detailed schematic of data acquisition and processing. (a) Initially all DNA-hybrids are in the state S0. The chip fluorescence is recorded at 550–600 nm ( $\text{Cy3}_{\text{Start}}$ ). (b) Incubation with ATP. (c) Coupling of the DNA-hybrids to a second surface and separation of the surfaces in the presence of ATP. (d) DNA-hybrids appear in the states S0, S1, and S2. The chip fluorescence is recorded again at 550–600 nm ( $\text{Cy3}_{\text{Rem}}$ ). (e) Labeling of noncoupled DNA-hybrids with streptavidin Alexa Fluor 647 (SAAF) and recording of fluorescence at 655–695 nm ( $\text{SAAF}_{\text{Rem}}$ ). (f)  $\text{Cy3}_{\text{Start}}$  chip fluorescence image and corresponding line profile allowing for determination of the initial amount of DNA-hybrids. (g)  $\text{Cy3}_{\text{Rem}}$  chip fluorescence image and corresponding line profile allowing for determination of the fraction S2. (h)  $\text{SAAF}_{\text{Rem}}$  chip fluorescence image and corresponding line profile allowing for determination of the fractions S0 and S1. The fluorescence line profiles are averaged over 40  $\mu\text{m}$ .

1·2 reference or at the 2·3 aptamer. We neither recorded nor analyzed the macroscopic force needed to pull the two surfaces apart. The unbinding forces are compared intrinsically and independently for each molecular chain. Aptamer–ATP complex formation is expected to increase the aptamer unbinding forces and as a result increase the fraction of the broken reference bonds (Figure 1d). Macroscopically, the fractions of broken reference bonds and broken aptamer bonds were determined via the location of the fluorescently labeled oligomers **2**. Parts f and h of Figure 1 show the fluorescence intensity of the DNA-hybrids after contact with and without the presence of 2 mM ATP. The squarelike features correspond to the contacted area. It is qualitatively observed that without the presence of ATP a smaller fraction of fluorophores is transferred from the glass slide to the PDMS compared to the case when the spot is incubated with 2 mM ATP. This is in agreement with ATP stabilizing the aptamer bond and thus an increased probability that the reference bonds fail. Consequently, the fraction of retained oligomers **2** and thus fluorophores on the glass slide is reduced.

The breakage of the biotin–streptavidin bond may be neglected since it unbinds at significantly higher forces than short double-stranded DNA. However, unbinding forces strongly depend on the applied force loading rates. Since in our case the force loading rates were not recorded, they are estimated from single-molecule experiments. For the combination of an applied separation velocity of 1  $\mu\text{m}/\text{s}$ , a combined PEG linker of 10 000 g/mol and a 20 bp DNA duplex, a force-loading rate in the order of  $10^3$  pN/s is

typically obtained.<sup>33</sup> Under these conditions a 20 bp DNA duplex unbinds at around 40 pN,<sup>33</sup> whereas biotin–streptavidin unbinds at around 80 pN or even higher forces.<sup>34,35</sup>

**Quantitative Fluorescence Analysis.** Quantitative determination of the ratio between broken aptamer bonds and broken reference bonds requires a more complex analysis, since it cannot be assumed that all DNA-hybrids physically connect to both surfaces via the biotin–streptavidin bond. Uncoupled DNA-hybrids result in a background signal. In our experiments, we determined and subtracted the latter for each squarelike feature individually in order to calculate the normalized fluorescence (NF). The NF is defined as the ratio between broken 2·3 complexes and total amount of DNA-hybrids, to which a load was applied, and is determined as follows: Initially, when the 1·2·3 DNA-hybrids are immobilized on glass, a fluorescence image is taken (Figure 2, parts a and f). The DNA-hybrids are incubated with ATP (Figure 2b). The PDMS stamp is lowered toward the glass surface allowing the DNA-hybrids to couple to the PDMS via biotin–streptavidin complexation. In the presence of the ATP the PDMS is retracted (Figure 2c), and an increasing force is built up until one of the links breaks. Not all of the DNA-hybrids are coupled via the biotin–streptavidin bond. As illustrated in Figure 1d, the DNA-hybrids appear in three different states 1·2·3 (S0), 1·2 (S1),

(33) Morfill, J.; Kuhner, F.; Blank, K.; Lugmaier, R.; Sedlmair, J.; Gaub, H. E. *Biophys. J.* 2007, 93, 2400–2409.

(34) Merkel, R.; Nassoy, P.; Leung, A.; Ritchie, K.; Evans, E. *Nature* 1999, 397, 50–53.

(35) Pincet, J. *Biophys. J.* 2005, 89, 4374–4381.

and **1** (S2) on the glass slide. For simplicity we refer to the amounts of S0, S1, and S2 as fractions normalized to all DNA-hybrids, i.e., the relation  $S_0 + S_1 + S_2 = 1$  is always true. Only molecules in state S1 and S2 were exposed to an unbinding force. Molecules in the state S0 were not coupled to the PDMS surface and therefore retained the biotinylated oligomer **3**. From the Cy3 fluorescence intensity per unit area the fraction of S2 is determined (Figure 2, parts d and g, eq 3). In order to distinguish S0 and S1, the former is labeled with the spectrally distinct fluorescent marker streptavidin Alexa Fluor 647 (SAAF, Figure 2, parts e and h). The labeling is performed subsequent to the Cy3 readout in order to avoid quenching or fluorescence resonance energy transfer (FRET) effects. This allows us to determine the fractions of S0 and S1 from SAAF fluorescence (eqs 1 and 2).

$$S_0 = \text{SAAF}_{\text{Ratio}} \quad (1)$$

$$S_1 = \text{Cy3}_{\text{Ratio}} - \text{SAAF}_{\text{Ratio}} \quad (2)$$

$$S_2 = 1 - \text{Cy3}_{\text{Ratio}} \quad (3)$$

$$\text{Cy3}_{\text{Ratio}} = \frac{\text{Cy3}_{\text{Result}}}{\text{Cy3}_{\text{Start}}} \quad (4a)$$

$$\text{SAAF}_{\text{Ratio}} = \frac{\text{SAAF}_{\text{Result}}}{\text{SAAF}_{\text{Start}}} \quad (4b)$$

For the analysis only the  $\text{Cy3}_{\text{Rem}}$  and  $\text{SAAF}_{\text{Rem}}$  fluorescence images are employed.  $\text{SAAF}_{\text{Start}}$  and  $\text{Cy3}_{\text{Start}}$  are determined from the noncontacted regions adjacent to each squarelike feature. The NF is given by the fraction of broken **2·3** bonds (S1) normalized to the fraction of bonds that have been under load (S1 + S2).

$$\text{NF} = \frac{S_1}{S_1 + S_2} = \frac{\text{Cy3}_{\text{Ratio}} - \text{SAAF}_{\text{Ratio}}}{1 - \text{SAAF}_{\text{Ratio}}} \quad (5)$$

The NF directly reflects the relative unbinding forces, a physical quantity inherent to a pair of molecular complexes, and is not influenced by the number of molecules under load. The NF should not be confused with  $\text{Cy3}_{\text{Ratio}}$ . For a fixed mechanical stability, the latter depends on the fraction of coupled DNA-hybrids, whereas the NF does not. The NFs presented in this work are the averages of all squarelike features contacted properly within an experiment. The NF experimental error is estimated from repeated blank measurements yielding a standard deviation of 0.018.

**CUFA Detects the Concentration of Adenosine.** Varying concentrations of ATP (0–2000  $\mu\text{M}$ ) were applied to the different DNA-hybrid spots on one slide (Figure 3a). This way a whole concentration range was measured within a single experiment. Under physiological buffer conditions (15 mM sodium citrate, 150 mM NaCl, 1 mM MgCl<sub>2</sub>, pH 7.4), the **1·2·3** sensor reliably reported the presence of its target. At zero concentration the normalized fluorescence was  $0.792 \pm 0.018$ . Upon addition of micromolar concentrations of ATP, the normalized fluorescence decreased and reached its minimum of  $0.683 \pm 0.018$  at 0.5 mM as shown in Figure 3b. This is in agreement with a stabilizing effect of ATP on the aptamer structure. Fitting the ATP titration data to the Hill equation with slope  $n = 2$  revealed a half-

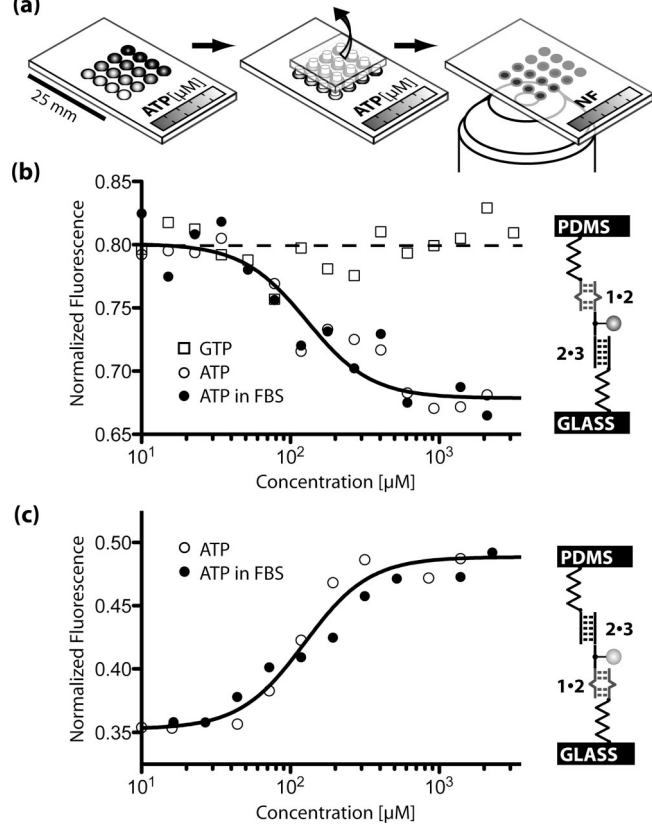


**Figure 3.** (a) Self-made microfluidic device allows incubation of 16 identical DNA-hybrid spots with different concentrations of ATP on a single chip. In the presence of ATP, the chip is contacted with a 16 pillar PDMS contact device and read out via fluorescence. (b) Normalized fluorescence for increasing concentrations of ATP and GTP in the regular configuration **1·2·3**. The solid line is the corresponding fit to the Hill equation. (c) Upside-down configuration **3·2·1**.

maximal effective concentration  $\text{EC50} = 124.8 \mu\text{M}$  with a 95% confidence interval of  $[102.8 \mu\text{M}, 151.4 \mu\text{M}]$ . Huizenga and Szostak demonstrated that the equilibrium dissociation constant of the adenosine–aptamer interaction depends upon the specific salt and Mg<sup>2+</sup> concentrations.<sup>24</sup> For the present buffer conditions, the experimentally obtained EC50 value is in agreement with previously published values of the equilibrium dissociation constant.<sup>24–28</sup>

In order to ensure that the molecular setup responds as expected, we investigated, analogously to the regular configuration **1·2·3**, the upside-down configuration **3·2·1**. Here, the position of the target and reference bond is exchanged, and thus the response to the addition of adenosine should be inverted. Indeed, the NF increased from  $0.353 \pm 0.018$  to a maximal NF of  $0.489 \pm 0.018$  upon increasing the ATP concentration from 0 to 0.5 mM (Figure 3c). The aptamer bond is now adjacent to the glass slide. Upon binding of the target molecule, the aptamer is less likely to break and a larger fraction of fluorophores remains on the glass slide.

**Sensitivity.** The sensitivity of our assay is estimated from the signal-to-noise ratio. For ATP concentrations below 53.5  $\mu\text{M}$  the latter is lower than 1, and thus ATP is not detectable. From 53.5

(27) Stojanovic, M. N.; de Prada, P.; Landry, D. W. *J. Am. Chem. Soc.* 2001, 123, 4928–4931.

to 310.3  $\mu\text{M}$ , ATP is quantified via the change in normalized fluorescence. At higher ATP concentrations the change in normalized fluorescence saturates, and thus ATP is detected; however, it cannot be quantified. This is comparable to fluorescent sensors based on aptamer assembly<sup>26</sup> or folding.<sup>27,28</sup> In recent publications, several groups demonstrated the use of structure-switching aptamer sensors in combination with signal amplification techniques using gold nanoparticles. For these assays larger ranges of sensitivity were reported.<sup>5,6</sup>

**Selectivity.** To demonstrate the selectivity of our force-based assay, separate experiments were conducted on GTP (Roche GmbH, Grenzach, Germany) and AMP (Roche GmbH, Grenzach, Germany). Since the aptamer recognizes adenosine, the addition of AMP resulted in a similar response like ATP (Supporting Information Figure S1). Conversely GTP, where the adenosine base is exchanged with a guanosine base, produced no detectable response (Figure 3c). The results demonstrated that the developed strategy has sufficient selectivity to detect the interaction between adenosine and the antiadenosine aptamers immobilized on the chip surface.

**Detection of Adenosine in Molecular Crowded Environment.** The experiments presented above were performed in pure 1× SSC buffer. However, because of the force-based design, the experimental result should only be susceptible to molecules interacting directly with the aptamer structure. In order to demonstrate this, we repeated the ATP experiments in 1× SSC buffer and 10% fetal bovine serum (FBS, Sigma-Aldrich, Germany). While the force comparison was carried out in the presence of the ligand and a molecular crowded solution, the readout of the result occurred subsequently and is therefore insensitive to additional washing steps, as long as these do not dissociate the DNA-hybrids. As shown in Figure 3, parts b and c, the same response is observed in the presence of FBS as for the FBS-free measurements.

## CONCLUSIONS

In the present study, we employed the CUFA as a label-free aptamer-based capture biochip. The design relies on an increased stability of bipartite aptamers upon binding of its target molecules. The assay reliably reported the presence of adenosine for concentrations above 53.5  $\mu\text{M}$  and allowed quantitative detection of adenosine for concentrations between 53.5 and 310.3  $\mu\text{M}$ . The

Hill equation governs the response of the assay with an EC50 = 124.8  $\mu\text{M}$  agreeing well with literature values for the equilibrium dissociation constant of the antiadenosine aptamer.

The limited sensitivity range and the dependence of the equilibrium constant (and thus of the assay response) upon specific salt and Mg<sup>2+</sup> concentrations renders quantitative detection of adenosine impracticable. Ionic concentrations of real samples are hardly ever known, and adenosine detection assays with superior sensitivity ranges are available. The strength of the assay lies within the fast and reliable characterization of the equilibrium dissociation constant of the interaction between a small molecule and a low-affinity aptamer. This was demonstrated in pure SSC buffer as well as in a molecular crowded solution. Producing reliable equilibrium binding data within the micromolar regime still poses a challenge for existing high-throughput techniques.<sup>36</sup> Conversely, implementing aptamers of higher affinity can yield more sensitive sensors for their cognate molecules. Due to the label-free, microarray-compatible design, it is easily imaginable to test the presence of various analytes in parallel—basically only limited by the number of available aptamer structures. Detection of proteins and peptides, simultaneous detection of multiple analytes, and miniaturization will be reported elsewhere.

## ACKNOWLEDGMENT

We thank P. Tinnefeld, F. Weinert, P. Baaske, S. Duhr, U. Steinbach, F. Dehmelt, J. Vogelsang, S. Kufer, and C. Albrecht for helpful discussions. Support was provided by the Nanosystem Initiative Munich and the Deutsche Forschungsgemeinschaft. D.H. and P.S. are grateful to the Elite Network of Bavaria (IDK-NBT) for a doctoral fellowship. K.F. is grateful for a Max-Weber fellowship.

## SUPPORTING INFORMATION AVAILABLE

Additional information as noted in text. This material is available free of charge via the Internet at <http://pubs.acs.org>.

Received for review December 31, 2008. Accepted February 24, 2009.

AC802766J

(36) Titz, B.; Schlesner, M.; Uetz, P. *Expert Rev. Proteomics* 2004, 1, 111–121.

# Supporting Information

## DNA as a force sensor

### in an aptamer-based biochip for adenosine

*Dominik Ho, Katja Falter, Philip Severin and Hermann E. Gaub\**

Lehrstuhl für Angewandte Physik and Center for Nanoscience (CeNS), Ludwig-Maximilians-  
Universität, Amalienstrasse 54, 80799 Munich, Germany

Munich Center For Integrated Protein Science (CIPSM), Ludwig-Maximilians-Universität,  
Butenandtstrasse 5-13, 81377 Munich, Germany

gaub@physik.lmu.de

## CONTENTS

Experiments with AMP (S2)

## Experiments with AMP

Additional to the experiments with ATP, we conducted experiments on the **1•2•3** molecular setup in presence and absence of 2 mM AMP. Within the experimental error, the change in normalized fluorescence was identical compared to the addition of 2 mM ATP. Explicitly, the normalized fluorescence was  $0.80 \pm 0.018$  for the 0 mM case and  $0.67 \pm 0.018$  for the 2 mM case.

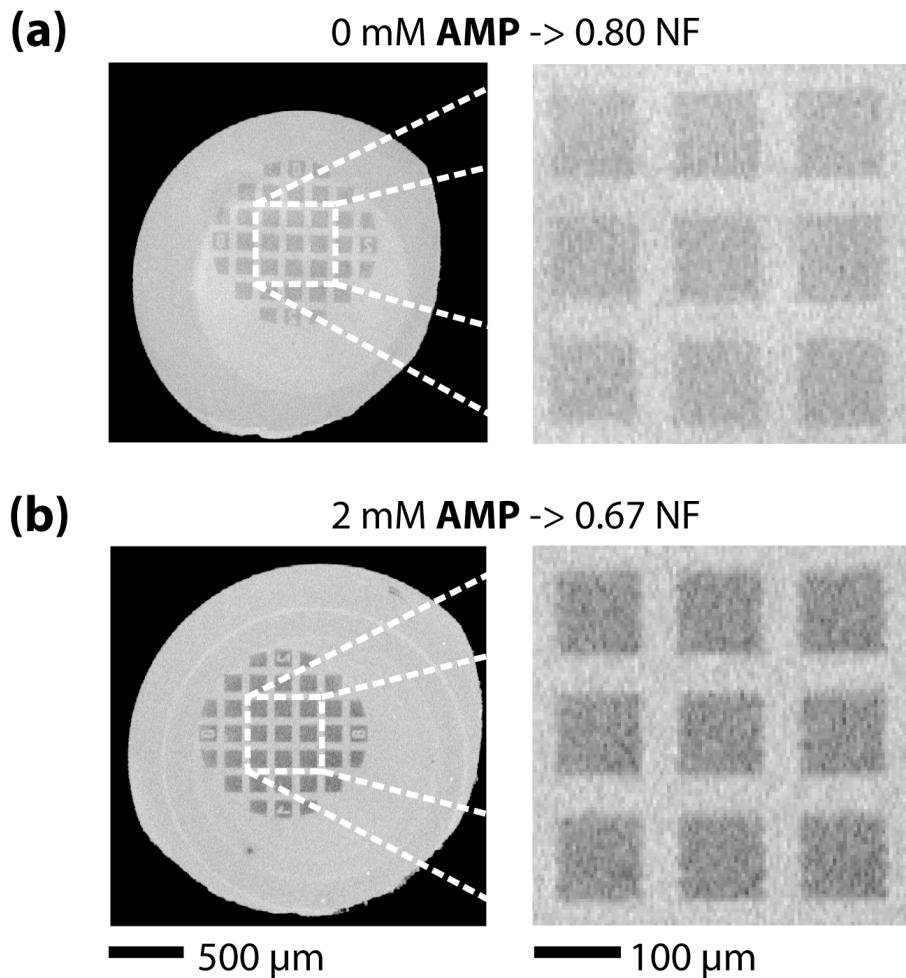


**Figure S1.** (a) Fluorescence on glass after contact without prior incubation with AMP. The square-like features ( $100 \times 100 \mu\text{m}^2$ ) correspond to the area contacted with microstructured PDMS. (b) Fluorescence on glass after contact with prior incubation with 2 mM AMP. Compared to the 0 mM AMP case, a larger fraction of fluorescence was transferred from the glass to the PDMS.

## A.2. MANUSKRIPTE

### M1:

**Ho, D.**, J. L. Zimmermann, F. A. Dehmelt, U. Steinbach, M. Erdmann, P. Severin, K. Falter, H. E. Gaub. 2009. Force-driven separation of short double stranded DNA.

Bemerkung: Eingereicht am 7.7.2009 beim Biophysical Journal. Die Revision (minor Revisions) liegt derzeit wieder bei den Referees.

## TITLE PAGE

### “Force-driven separation of short double stranded DNA”

*Dominik Ho<sup>1,2</sup>, Julia L. Zimmermann<sup>1,3</sup>, Florian A. Dehmelt<sup>1</sup>, Uta Steinbach<sup>1</sup>, Matthias Erdmann<sup>1</sup>, Philip Severin<sup>1</sup>, Katja Falter<sup>1</sup>, Hermann E. Gaub<sup>1</sup>*

[<sup>1</sup>] Lehrstuhl für Angewandte Physik and Center for Nanoscience  
Ludwig-Maximilians-Universität  
Amalienstrasse 54, 80799 Munich, Germany  
Fax: (+49) 89-2180-2050  
E-mail: gaub@lmu.de

[<sup>2</sup>] Munich Center For Integrated Protein Science (CIPSM)  
Ludwig-Maximilians-Universität  
Butenandtstrasse 5-13, 81377 Munich, Germany  
E-mail: dominik.ho@web.de

[<sup>3</sup>] present address: Max-Planck-Institut für extraterrestrische Physik  
Giessenbachstrasse, 85748 Garching, Germany

## ABSTRACT

Short double stranded DNA is used in a variety of nanotechnological applications and for many of them it is of importance to know for which forces and which force loading rates the DNA duplex remains stable. In this work we develop a theoretical model describing the force-dependent dissociation rate for tens of base-pair long DNA duplexes under tension along their axis (“shear geometry”). Explicitly, we set up a three state equilibrium model and apply the canonical transition state theory in order to calculate the kinetic rates for strand unpairing as well as the rupture force distribution as a function of the separation velocity of the end-to-end distance. Theory is in excellent agreement with actual single molecule force spectroscopy results and even allows for the prediction of the rupture force distribution for a given DNA duplex sequence and separation velocity. We further show that, for the description of double stranded DNA separation kinetics, our model is a significant refinement of the conventionally used Bell-Evans model.

## INTRODUCTION

Double stranded DNA (dsDNA) is an extensively studied polymer offering a number of striking properties. Among them is inter-strand recognition according to the Watson-Crick base-pairing rules, stability under a broad range of conditions and ease of synthesis allowing for a fast and cost-efficient production of any desired sequence with almost any kind of chemical modification. Within the past several years, various areas of application of DNA have been found and specifically nanotechnology is increasingly harnessing the potential of this versatile polymer [1]. Whereas in earlier published work DNA merely served as simple molecular handles for single molecule experiments [2] [3], today DNA serves as molecular building blocks for complex self-assembled nanostructures [4] [5] [6] [7] as well as DNA computing [8]. In our laboratory, DNA was even used as a programmable force sensor for the detection of single nucleotide polymorphisms [9], multiplexed antibody sandwich assays [10] [11], investigation of chiral preference of small DNA binding molecules [12], quantitative detection of DNA binding molecules [13] and aptamer sensors [14]. Recently, our laboratory applied this DNA force sensor concept to “single molecule cut and paste” experiments [15] for the bottom up assembly of nanoparticles [16] and single molecule fluorescence applications [17]. For many of the abovementioned applications, it is insightful if not even critical to know what forces a given DNA duplex may withstand: Particularly, such knowledge would not only allow to predict, tune and analyze DNA force sensor experiments, but also to design more stable DNA scaffolds.

The elastic response and force dependent dissociation rate of DNA duplexes has been extensively studied in micromanipulation experiments employing atomic force microscopy (AFM) [18] [19], magnetic beads [20], glass micro needles [21], and optical tweezers [22] [23]. Here, we will only discuss the stretching of dsDNA along its axis (“shear geometry”) in contrast to the gradual unzipping of DNA perpendicular to its axis (“unzip geometry”). Stretching DNA duplexes with thousands of base-pairs along its axis, results in an elastic response with a distinct force plateau at 60-65 pN [18] [21] [22]. During this elongation at almost constant force the DNA molecule stretches up to a factor of 1.7 of its contour length. This behavior is highly reproducible, independent of the stretching velocity and commonly attributed to a highly cooperative conversion from regular B-DNA into an overstretched conformation called S-DNA [24] [25] [26] [27]. On the contrary, Rouzina and Bloomfield [28] as well as Piana [29] argue that S-DNA is not a distinct conformation of the polymer, but simply the melting of the dsDNA into two single strands. However, the B-S transition not only appears to be too cooperative for a common melting process but it was also shown that dsDNA remains stable at forces significantly higher than 65 pN [30] with an elastic response distinct from one single stranded DNA (ssDNA)

polymer or two parallel ssDNA polymers [24]. Further support for S-DNA being a distinct conformation is provided by the experimental observation of a second transition in the range between 150 and 200 pN, which, instead of the B-S transition, is thought to be the final melting transition [18] [24]. Based on the assumption that S-DNA is in fact a distinct conformation, several recent theoretical studies modeled the elongation of DNA duplexes applying three state (B-DNA, S-DNA and ssDNA) equilibrium approaches [24] [25]. These studies concluded that S-DNA is the thermodynamically preferred and stable state for forces between 65 and 130 pN.

Individual base-pairing interactions are relatively weak (free energy around 1-3  $k_B T$ ) and thermal fluctuations cause opening (“breathing”) of the DNA duplex from its ends as well as the formation of bubbles, which are regions of ssDNA (opened base-pairs) in between regions of dsDNA. The shorter the DNA duplex the more likely it is that for an instant all base-pairs open up and the two strands separate even at forces well below 130 pN. For tens of base-pair long DNA duplexes Strunz and colleagues [31] as well as Morfill and colleagues [32] observed strand separation already at forces between 40 to 70 pN. Repeated measurements resulted in rupture force distributions, which were shifted to higher forces for higher separation velocities. From a theoretical point of view, this can be described as a thermally driven escape process from a free energy potential and has typically been discussed within the framework of the Bell-Evans model. Herein, the trapping potential is assumed to be a one-dimensional harmonic free energy potential and strand separation is treated as the crossing of an energy barrier following an Arrhenius-law-like time dependence [31] [32] [33] [34] [35]. Application of a force tilts the energy landscape, reduces the energy barrier proportional to the applied force and, therefore, increases the dissociation rate of the DNA duplex. According to the experimental data, the model predicts higher rupture forces for higher separation velocities [33]. Although the experiments are explained quite well by the Bell-Evans model, the latter does not allow for the prediction of rupture forces for a given DNA duplex sequence and separation velocity. Apart from the Bell-Evans theory, molecular dynamics simulations provided insight into the DNA separation process employing force fields and initial molecular structures. Unfortunately, these simulations cost a significant amount of computation time such that the timescales accessible for in-silico experiments are much shorter than what is experimentally observable [26] [27]. Therefore, it is apparent that a theory is missing that fills the gap between the Bell-Evans model, which is too simplistic, and the detailed molecular dynamics simulations, with which mechanics can currently be simulated on very short timescales only.

In the present work, we develop a model that describes and predicts the DNA duplex rupture forces for any given sequence and experimentally accessible pulling velocities. Explicitly, we derive the dissociation rate as a function of the applied force based on a combination of recent work on DNA

equilibrium theory and the canonical transition state theory. On this basis, we calculate the force extension traces and the rupture force distribution for a twenty and a thirty base-pair long DNA duplex and compare the obtained results to actual single molecule experimental data. Further, we are able to show that, for the description of double stranded DNA separation kinetics, our model is a significant refinement of the conventionally used Bell-Evans model.

## RESULTS AND DISCUSSION

The result of the present work is a theoretical model, which predicts the rupture force of tens of base-pairs long dsDNA as they appear in DNA force sensor, DNA nanostructure and DNA computing applications. For this purpose, we first set up a three state equilibrium model similar to a model, which was used before for the description of the force extension traces of long dsDNA [24]. Second, we apply the canonical transition state theory to this equilibrium model, which in turn permits the calculation of the rate of duplex dissociation at a given force  $f$ . Theoretical results are compared to actual AFM experiments on the twenty base-pair **1·2** and the thirty base pair **1·3** duplex. Details about the DNA oligomers **1**, **2** and **3** as well as details about the experimental procedures are provided in the supplementary information.

### I. Equilibrium theory

Analogous to the Bragg-Zimm theory [36] and a variety of work that has been published recently on the force-induced opening of dsDNA in unzip geometry [37] [39] [40] and shear geometry [28] as well as the opening of coiled coils [41] [42] we calculate the equilibrium free energy of DNA duplexes: The DNA duplex is described as a one dimensional polymer, for which every base-pair  $i$  is considered to be present in one of three discrete states, namely regular B-DNA ( $s_i = 0$ ), overstretched S-DNA ( $s_i = 1$ ) and single stranded DNA ( $s_i = 2$ ) conformation. Thus, any configuration  $s$  of a  $N$  base pair DNA duplex is represented by a  $N$ -tuple

$$(Equation 1) \quad s = (s_1, s_2, \dots, s_N),$$

where the  $i$ th entry represents the state of the  $i$ th base pair, counting from the 5' to the 3' end.

Two contributions to the free energy per base-pair are taken into account:  $w$ , the elastic free energy per base pair at a given force  $f$  and  $j$ , the base-pairing free energy that we derive from a nearest neighbor model and assume to be independent of the applied force. The free energy of the  $i$ th base pair therefore equals

$$(Equation 2) \quad g_{s_i, s_{i+1}}(f) = w_{s_i, s_{i+1}}(f) + j_{s_i, s_{i+1}}$$

These two energy contributions yield the total free energy  $G_{total}(s, f)$  for any possible configuration  $s$  at any force  $f$ .

$$(Equation 3) \quad G_{total}(s, f) = \sum_{i=1}^{N-1} g_{s_i, s_{i+1}}(f) + w_{s_N}(f),$$

where the term  $w_{s_N}(f)$  corresponds to the  $N$ th base-pair, which does not have a next neighbor it may interact with such that  $j_{s_N, s_{N+1}} = 0$ .

**Elastic energy.** The free energies due to the elastic deformation of the three different DNA conformations are obtained by simply integrating their extensions with respect to the force.

$$(Equation\ 4) \quad w(f) = - \int_0^f x(f') df'$$

Phenomenological polymer extension models reproduce the force extension traces well (Figure 2a). In the supplemental information, we derive the elastic free energy per base-pair from such polymer extension models for B-DNA ( $w_B$ ), S-DNA ( $w_S$ ) and ssDNA ( $w_{ss}$ ) explicitly. Assuming an average base pairing energy of  $2.4\ k_B T$ , as it is the case for the **1·2** and **1·3** DNA duplexes, Figure 2b illustrates, which DNA configuration is most favorable for forces between 0 and 200 pN: B-DNA remains thermodynamically stable for forces below 60 pN. S-DNA is stable between 60 and about 130 pN and above 130 pN ssDNA is the energetically most favorable state. Since we employ a nearest neighbor model for the calculation of the partition sum of the system, it is convenient to represent the free energy due to the elastic behavior of DNA in a 3x3 matrix form.

$$(Equation\ 5) \quad w_{s_i, s_{i+1}}(f) = \begin{bmatrix} w_B(f) & w_B(f) & w_B(f) \\ w_S(f) & w_S(f) & w_S(f) \\ w_{ss}(f) & w_{ss}(f) & w_{ss}(f) \end{bmatrix},$$

where the rows correspond to the state of base pair  $i$  and the columns to the state of base-pair  $i + 1$ . Thus, in our model, the elastic free energy of base pair  $i$  is independent of the state of base-pair  $i + 1$ .

**Interaction free energy.** Experimentally, it was observed that the stability of a given base-pair not only depends on whether the base-pair itself is A·T or G·C, but also on the identity and orientation of adjacent base-pairs, presumably due to the differences in free energy for the different possible stacking interactions [43]. In our model, we employ the nearest neighbor model of SantaLucia, which takes these experimental observations into account [44]. The stacking free energy between each base-pair  $i$  and  $i + 1$  is given by the constant  $J_i$  in case both are either B-DNA or S-DNA. Although the stacking free energies for B-DNA and S-DNA are independent parameters, for simplicity, we assume them to be identical.

In addition, the boundaries between regions of different states are associated with energy penalties.  $C_{B-S}$  is the energy cost associated with a boundary between B-DNA and S-DNA regions. Cluzel and colleagues estimated the B-S boundary energy from the cooperativity of the B-S transition to be close to  $3.4\ k_B T$  [21]. Unlike the non-nearest neighbor models for which the latter value was derived, for our nearest neighbor model, the total energy penalty is given by  $C_{B-S}$  along with the loss of one additional base stacking interaction. The average energy lost in base stacking interaction is  $2.4\ k_B T$  for the **1·2** as well as the **1·3** duplex, which is why we set  $C_{B-S}$  to  $2.2\ k_B T$  (half a base stacking interaction free energy subtracted from each boundary).

Furthermore, the boundaries between double stranded and between single stranded regions of DNA are associated with the free energy cost  $C_{ds-ss}$ . According to SantaLucia [44] this value is close to  $1 k_B T$ . For any given state  $s$ , there are always two boundaries at each side of the dsDNA region and, therefore, the parameter  $C_{ds-ss}$  has an impact only on the likelihood of bubbles. Within polymer theory, the latter are commonly referred to as loops. Since bubbles come along with additional degrees of freedom, polymer theory predicts an entropic energy contribution proportional to the logarithm of the bubble size, which favors the creation of bubbles.

$$(Equation 6) \quad \Delta G_{loop}(n_{loop}) = k_B T \ln n_{loop}^{-c},$$

where  $n_{loop}$  is the number of opened base-pairs within the bubble and  $c$  is the loop exponent. The value of loop exponent is  $c = 3/2$  for an ideal loop and  $c = 2.1$  for a self-avoiding loop [45]. The exact value of  $c$  for dsDNA is still under debate. Recent theoretical calculations by Einert and colleagues imply that data for long dsDNA is best fit by setting  $c = 0$ , which may be explained by the fact that DNA contains a significant numbers of nicks. Such a long ranged interaction cannot be implemented into our nearest neighbor model. Therefore, we simply chose the parameter such that theory agreed best with actual experiments and estimated a value of  $-0.25 k_B T$  for  $C_{ds-ss}$ , corresponding to an average bubble size of 4 base pairs. Note that the theoretical predictions [46] [47] [48] of longer ranged entropic contribution to partially melted DNA is in agreement with experimental data obtained by Altan and colleagues [49]. Based on foerster energy transfer measurements on tracts of A·T base pairs, they argue that initiating a bubble requires a free energy much larger than  $k_B T$ , while extending this bubble requires only free energies in the range of (0.05-1.0)  $k_B T$  per base-pair.

In matrix form, the interaction free energy contributions based on the SantaLucia nearest neighbor model and the boundary free energy penalties are

$$(Equation 7) \quad j_{s_i, s_{i+1}} = \begin{bmatrix} -J_i & C_{B-S} & C_{ds-ss} \\ C_{B-S} & -J_i & C_{ds-ss} \\ C_{ds-ss} & C_{ds-ss} & 0 \end{bmatrix},$$

where the rows correspond to the state of base pair  $i$  and the columns to the state of base-pair  $i + 1$ . Thus, if base pair  $i$  and base-pair  $i + 1$  are B-DNA then an energy gain of  $J_i$  is introduced to the base stacking interaction. The same is true for two adjacent S-DNA base-pairs. Boundaries between base-pairs are associated with an energy penalty  $C_{B-S}$  or  $C_{ds-ss}$ , where  $C_{B-S}$ , as discussed above, is  $3.4 k_B T$  and  $C_{ds-ss}$  is  $-0.25 k_B T$ .

**Partition Sum.** From the total free energy  $G_{total}$  (Equation 2 and 3) of each possible state  $s$  we calculate the partition sum, which in turn allows for determination of the force extension trace and the likelihoods of the states  $s$ .

$$\begin{aligned}
 Z(f) &= \sum_s P(s, f) = \sum_s \exp(-G_{total}(s, f)) = \sum_s \prod_{i=1}^N \exp(-g_{s_i, s_{i+1}}(f)) \\
 (\text{Equation 8}) \quad &= \sum_{\substack{\text{all matrix } i=1 \\ \text{elements}}} \prod_{i=1}^N \begin{bmatrix} \exp(-w_B(f) + J_i) & \exp(-w_B(f) - C_{B-S}) & \exp(-w_B(f) - C_{ds-ss}) \\ \exp(-w_S(f) - C_{B-S}) & \exp(-w_S(f) + J_i) & \exp(-w_S(f) - C_{ds-ss}) \\ \exp(-w_{ss}(f) - C_{ds-ss}) & \exp(-w_{ss}(f) - C_{ds-ss}) & \exp(-w_{ss}(f)) \end{bmatrix}
 \end{aligned}$$

Thus the partition sum may be considered as the sum over all matrix elements of the product of  $N$   $3 \times 3$  matrices [50]. Thereby, the  $i$ th matrix of the  $N$  matrices represents the  $i$ th base-pair containing nine entries. Each entry represents the Boltzmann factor of one of the nine possible combinations of states that base pair  $i$  and base pair  $i + 1$  may adopt. We make two corrections to Equation 8, which we explain in more detail in the supplementary information. First, we introduce two additional base-pairs at  $i = 0$  and  $i = N + 1$ , which are single stranded. This takes care of the boundary conditions at the end of the DNA duplex. Second, we do not count the states, for which two or less base-pairs are remaining. These states, as we will discuss in more detail in the next chapter, correspond to already separated strands.

**Stretching Curves.** From the partition sum of our model we derive the force-extension trace for a given sequence and compare it to experimentally obtained data. The equilibrium force-extension trace follows directly from the derivative of the partition sum with respect to the force [51]:

$$(\text{Equation 9}) \quad x_{DNA\,duplex}(f) = k_B T \frac{\partial \ln Z(f)}{\partial f}.$$

The AFM experiments were prepared according to the materials and methods section and are schematically shown in Figure 1a. The two complementary single strands **1** and **2** were coupled to the cantilever tip and a substrate via long poly(ethylene glycol) linkers (5 kDa). In a typical experiment, the tip is brought into contact with the glass slide, the two complementary strands hybridize and form the **1·2** duplex. Upon retraction at constant velocity the PEG spacer and dsDNA elongates, building up an increasing force until the duplex dissociates. Figure 3 shows an average of 20 force extension curves. Experimentally, one measures the elasticity of a chain of four elements: the dsDNA duplex, the PEG linker, the ssDNA linker, and the cantilever. The force-extension trace is a superposition of the extension profile of all four of them.

$$(\text{Equation 10}) \quad x(f) = x_{DNA\,duplex}(f) + x_{DNA\,linker}(f) + x_{PEG\,linker}(f) + x_{cantilever}(f),$$

where  $x_{DNA\,duplex}$  is specified by Equation 9 and  $x_{cantilever}$  is the deflection of the cantilever, which is proportional to the cantilever stiffness  $k_{cantilever} = 8$  pN/nm. The polymer models from which  $x_{DNA\,linker}$  and  $x_{PEG\,linker}$  are derived are described in the supplemental information. We used the number of monomers within the PEG polymer  $N_{PEG}$  as a fitting parameter since PEG polymers are typically synthesized with a rather broad size distribution [32]. Fitting of the whole system resulted in a monomer

number of 255, which agrees well with the expected monomer number of 227 for a total PEG linker with a molecular weight of 10 kDa.

Figure 3 shows that the theory fits the experimental data very well for forces above 30 pN. However, for lower forces the theoretical fit underestimates the experimentally obtained forces. The 10-15 pN plateau between 10 and 20 nm extension at the beginning of the stretching curve is typical for a DNA desorption process from a surface [52]. For higher extensions, we attribute this deviation between theory and experiment to nonspecific interactions and entanglements of the strands with each other on the surface. This is entirely possible, since the contour length of the surface anchored DNA strands is larger than 50 nm and the spacing between two of these strands is typically about 10 nm [12] [15] [16].

## II. Canonical Transition State Theory

For an average base-pairing free energy of  $2.4 k_B T$ , dsDNA is thermodynamically stable for forces smaller than 130 pN [18] [24] [25]. Still, Strunz and colleagues [31] as well as Morfill and colleagues [32] observed bond breakage at forces between 40 and 70 pN for 20 and 30 base-pair dsDNA. They accounted this effect to thermal fluctuations like the opening or “breathing” of dsDNA from its ends as well as the formation of bubbles, which are regions of ssDNA in between regions of dsDNA. Some of these fluctuations are so large that the whole duplex opens and the two strands separate.

Such a thermally activated escape process can be described employing the canonical transition state theory [53] [54]. This theory is purely classical and based on two assumptions: (1) The bond is trapped in a free energy potential and thermodynamic equilibrium prevails. (2) Once the system has crossed a dividing surface in state space, i.e. the transition state, it will not return to the metastable state. The rate of escape follows directly from the flux through this dividing surface.

Within the next paragraphs, we first define the dividing surface, i.e. the transition states, for the dsDNA equilibrium model described in the previous chapter. Subsequently, we calculate the equilibrium flux through this dividing surface and thus the rate of escape. We explicitly calculate the rupture force distributions for the two DNA duplexes **1·2** as well as **1·3** and compare it to experimental data. At the end of this chapter, we discuss why the canonical transition state theory is an appropriate description of our system.

**Transition States.** In the case of a  $N$  base-pair long DNA duplex the free energy potential is  $N$ -dimensional and the corresponding coordinate is the state  $s$ . A dividing surface between the reactants (double stranded DNA) and the products (single stranded DNA) has to be chosen such that once the system has crossed this surface, chances of recrossing are negligible. In our system this dividing surface is spanned by the states  $s_{tst}$ , for which there is exactly one base stacking interaction left. One base stacking interaction corresponds to either two adjacent B-DNA or S-DNA base-pairs. Therefore, there are  $2(N - 1)$  distinct states through which the reaction may occur. For illustrative purposes we can collapse the free energy landscape onto one coordinate:  $n$ , the number of remaining base-pairs. Within this picture (Figure S1) we identify the transition state as  $n_{tst} = 2$ . If another base-pair opens up, the two DNA strands dissociate, i.e. the polymers will immediately reduce their end-to-end distance and reannealing of the two stands is literally impossible.

**Equilibrium Flux.** The rate of escape is given by the equilibrium flux through the transition states  $s_{tst}$  in direction of the product (two separate strands). The flux is essentially twice the base-pair opening rate

(either one of the two remaining base-pairs may open), which, for simplicity, we assume to be the same for all  $s_{tst}$ . This allows us to use the collapsed free energy landscape with only one reaction coordinate  $n$ , the number of remaining base-pairs. The equilibrium flux through the transition states  $s_{tst}$  becomes the probability of the system to be in the collapsed transition state  $n_{tst}$  multiplied by  $\dot{n}_+$ , twice the base pair opening rate. The result for the rate of escape at a given force  $f$  is

$$(Equation 11) \quad k(f) = \left\langle \delta[n - n_{tst}] \dot{n}_+ \right\rangle_{equilibrium} \\ = \frac{1}{Z(f)} \sum_{s_{tst}} \dot{n}_+ \exp(-\Delta G_{total}(s_{tst}, f))$$

The calculations are shown explicitly in the supplementary information. To our knowledge, the base-pair opening rate of a single base-pair stacking interaction has never been determined experimentally. From literature we estimate the base-pair opening rate at the ends of dsDNA to be in between  $10^3 \text{ s}^{-1}$  and  $10^9 \text{ s}^{-1}$ : Bockelmann and colleagues performed optical tweezers measurements from which we estimate an opening rate of at least  $10^3 \text{ s}^{-1}$  [55]. Fluorescence measurements investigating the end fraying of the dsDNA could not resolve any base-pair opening rates on time scales shorter than  $10^9 \text{ s}^{-1}$  [56]. In a paper, which discusses the unzipping of DNA, Cocco and colleagues assumed a value of  $10^8 \text{ s}^{-1}$  [24] and nuclear magnetic resonance imino proton exchange studies yielded rates in the order of  $10^7 \text{ s}^{-1}$  [57]. For a base-pair opening rate of  $\dot{n}_+ = 5 \cdot 10^8 \text{ s}^{-1}$  our theory agrees very well with the experimentally determined rupture forces [32]. Note that the rate depends on the applied force, but since the force dependence is rather weak [40], we assume the rate to be constant. In principle all calculations could also be performed with force and sequence dependent rates.

**Rupture Forces.** Based on the canonical transition state theory, we derive the rupture force distributions obtained for two given sequences, namely the **1·2** as well as the **1·3** DNA duplex, and different pulling velocities  $v$ . Experimentally, we control the separation velocity between cantilever and substrate. Thus, the end-to-end distance  $x$  of a system composed of dsDNA, ssDNA linker, PEG linker and AFM cantilever continuously increases in time with constant velocity  $v$ . From the end-to-end distance  $x$  we derive the force acting along this chain of elastic elements. The force in turn allows us to determine the escape rate  $k$  as a function of time. The resulting differential equation describes the decay from a metastable state  $N_{\text{duplex}}$  with a time-dependent rate [33].

$$(Equation 12) \quad dN_{\text{duplex}} = N_{\text{duplex}} k(t) dt,$$

where  $k(t) = k(f(v \cdot t))$  and  $f(x)$  follows from Equation 10.

For the **1·2** as well as the **1·3** DNA duplex and separation velocities between  $10 \text{ nm/s}$  and  $10 \mu\text{m/s}$  we numerically solved this differential equation. The obtained rupture force distributions are shown in Figure 4a. Strikingly, the rupture force distribution of the **1·2** DNA duplex broadens with increasing

force loading rate, while the rupture force distribution of the **1·3** DNA duplex is almost independent of this parameter. We attribute this behavior to the crossing of the B-S transition at around 65 pN, which is only observed for the **1·2** DNA duplex for the experimentally applied force loading rates. For forces above 65 pN and thus above the B-S transition the slope of force-extension profile increases significantly resulting in a wider distribution of the obtained rupture forces. In order to verify that the broadening of the rupture force distribution is indeed due to the crossing of the B-S transition, we calculated the **1·3** DNA duplex rupture force distributions for force loading rates higher than what was experimentally achievable. In agreement with this interpretation, the rupture force distribution of the **1·3** DNA duplex broadens correspondingly for rupture forces above the B-S transition (data not shown). The experimentally obtained rupture force distributions are further broadened by the thermal and instrumentation noise introduced to the cantilever. According to Morfill and colleagues [32] the total experimental noise was Gaussian with a width of 4.7 pN. Therefore, in order to compare theory with experiment, we convolved the theoretically obtained rupture force distribution with the latter (Figure 4b). From these distributions we determined the most probable rupture force via a Gaussian fit. Figure 4c shows the latter plotted against the corresponding most probable force loading rate for the theoretically predicted and the experimental data. The theory reproduces the data quite well within the experimental error.

Systematic errors on the experimental side are mainly due to errors of the cantilever calibration, which introduces an error of up to 5-10% [58]. The presented AFM force data was performed with two different AFM cantilever tips, one for all the **1·2** DNA duplex data and one for all the **1·3** DNA duplex data. Therefore the set of most probable rupture forces may be shifted by up to 5-10%. Further, a small error is introduced due to pulling angles that are not perpendicular to the substrate, which is typically in the order of 2% [59].

Systematic errors on the theoretical side include the following: We chose the base-pair opening rate for the B-DNA and the S-DNA conformation to be identical, although they are completely independent parameters. Further, the S-DNA polymer elasticity model is very crude for several other reasons. First, according to Cocco and colleagues [24], we approximated the force-extension curve of S-DNA to be linear. Second, the base-pair free energy was assumed to be identical to the B-DNA interaction. Furthermore, there are most likely two types of S-DNA depending on whether the force is applied at the 5' or the 3' ends of the dsDNA [26] [60]. Finally, the nearest neighbor model does not account for long ranged interactions as they are experimentally observed in DNA bubbles, which has a strong influence on the boundary energy  $C_{ss-ds}$  and thus on how cooperative DNA strand separation occurs. From our calculations, we observed that a more cooperative transition between single stranded and double stranded DNA, i.e. a larger value for  $C_{ss-ds}$ , leads to a reduced DNA duplex length dependence on the

rupture force distribution. For values of  $C_{ss-ds}$  in the range of a few  $k_B T$ , the rupture force distributions of the **1·2** and one the **1·3** DNA duplex almost superimpose.

**Thermodynamic Equilibrium Prevails.** To appropriately describe the separation of dsDNA employing the canonical transition state theory, thermodynamic equilibrium must prevail within the binding potential [54]. Two scenarios would contradict such an assumption: Either, the changes of state occur on timescales equal to or slower than the rate of escape or, in order to reach the transition states, an intermediate free energy barrier needs to be crossed. Within the supplemental information, we discuss these scenarios and conclude that, for the experimentally observed force range between 0 and 100 pN, the canonical transition state theory is applicable.

### III. Comparison to the Bell-Evans model.

Typically, the rupture of molecular bonds is described employing the Bell-Evans model [34]. Like our model, the latter is based on transition state theory assuming a thermally activated escape from a free energy potential. Within the following chapter we discuss the differences between the Bell-Evans model and our model, how they compare and why our model is a significant refinement for the description of the force-induced separation of short dsDNA.

The main difference between the two models lies within the approximation of the Bell-Evans trapping potential as a harmonic free energy landscape, which is simply tilted by an external force. As a result of this approximation, the free energy difference between the equilibrium and the transition state decreases proportional to the applied force.

$$(Equation\ 13) \quad \Delta G(f) = \Delta G_0 - f \cdot x_{ts},$$

where  $\Delta G_0$  is the free energy difference at zero force and  $x_{ts}$  is a force-independent distance between the equilibrium state and the transition state. The force dependent rate is given by

$$(Equation\ 14) \quad k(f) = k_0 \cdot \exp(-\Delta G(f)),$$

where  $k_0$  is the natural attempt frequency of the molecular bond. Within our work, we explicitly model the evolution of the DNA duplex free energy landscape with increasing force. In order to see what differences arise in comparison to the Bell-Evans approach, we calculate an effective barrier height of the transition state from the sum of the Boltzmann probabilities for the states  $s_{ts}$ .

$$(Equation\ 15) \quad \Delta G(f) = -\ln \left( \sum_{s_{ts}} \frac{\exp(-\Delta G_{total}(s_{ts}, f))}{Z} \right)$$

As shown in Figure 5a, the force-dependent evolution of the effective barrier height according to Equation 15 does exhibit significant differences from the Bell-Evans approach (Equation 13). Below 10 pN the free energy difference between the equilibrium state and transition state increases with applied force. This is in agreement with Figure 2b, which shows that for increasing applied forces the absolute value of the free energy difference per base-pair between B-DNA (equilibrium state for low forces) and ssDNA (transition state) increases for forces below 10 pN before it decreases for forces above 10 pN. The microscopic origin of this effect is the following: although the contour length of ssDNA is longer compared to B-DNA, the contour length of ssDNA projected onto the direction of applied force, i.e. the end-to-end distance, is shorter for low forces due to its much shorter persistence length. Thus, low forces stabilize DNA duplexes, a result that was previously shown experimentally [61] [62] and discussed theoretically [28] [63]. Between 10 and 60 pN the free energy decreases roughly proportionally to the applied force  $f$ . Above 65 pN, i.e. above the B-S transition, the energy decreases linearly again, yet with a smaller slope. Taking the negative derivative of the calculated free energy

barrier height with respect to the force yields an effective distance between the equilibrium state and the transition state  $x_{tst}$ .

$$(Equation\ 16) \quad x_{tst} = -\frac{\partial \Delta G(f)}{\partial f}$$

$x_{tst}$  does exhibit a rather odd force dependency (Figure 5b), which we explain according to geometrical considerations: Strunz and colleagues estimated an upper limit for  $x_{tst}$  assuming that the equilibrium state is B-DNA with a contour length of 0.34 nm/base-pair and that the transitions state is all-ssDNA (apart from two residual base-pairs) with a contour length of about 0.7 nm/base-pair [31]. In case of the thirty base-pair 1·2 DNA duplex, this corresponds to a total length difference between these two states of about 10 nm, which is significantly larger than the corresponding values of  $x_{tst}$  obtained from our calculations and obtained from actual experiments [31] [32]. Two effects contribute to this deviation. First,  $x_{tst}$  is the projection of the distance between the equilibrium state and the transition state onto the direction of applied force. Therefore, a more accurate estimate of  $x_{tst}$  is the difference in end-to-end distance according to our polymer models for B-DNA and ssDNA (Figure 5b). Second, within the range of 60 to 65 pN, the equilibrium state switches from a predominantly B-DNA duplex to a predominantly S-DNA duplex. The difference in end-to-end distance between the equilibrium state and the transition states is much smaller for a S-DNA duplex than for a B-DNA duplex (Figure 5c). Consequently,  $x_{tst}$  decreases to a fraction of a nanometer during the B-S transition.

Due to the force-dependence of  $x_{tst}$ , we conclude that the standard Bell-Evans model is only a good description of the force-induced separation of DNA duplexes for forces between 10 and 50 pN as well as between 65 and roughly 100 pN. However, for both scenarios a different set of free energy landscape parameters, i.e. free energy barrier at zero force and distance between equilibrium and transition state, need to be chosen. On the contrary our refined model provides a reliable description for forces between 0 and approximately 100 pN. Our results are in agreement with recent literature. Hyeon and Thirumalai [64] argue that  $x_{tst}$  changes considerably if the molecular bond is soft or plastic as it is the case for dsDNA. Further, Dudko and colleagues [65] report that the position of the equilibrium state may depend on the applied force leading to a force dependence of the distance between the equilibrium state and the transition state and thus to a nonlinear dependence of the barrier height on the applied force.

## CONCLUSION

The result of the present work is a theoretical model that employs a combination of a three state equilibrium model and the canonical transition state theory in order to describe the force induced strand separation of tens of base pair long dsDNA. The three state equilibrium model serves as basis for a free energy trapping landscape. Double strand separation occurs through transition states, which we identified as the states with two adjacent base-pairs remaining, i.e. one remaining stacking interaction. We calculated the rate of escape as a function of force from the total flux through these transition states assuming a base-pair opening rate of  $5 \cdot 10^8$  s<sup>-1</sup>. The rate of escape in turn allowed us to explicitly calculate the rupture force distribution for two DNA duplexes, **1·2** and **1·3**. The theoretically obtained results and actual single molecule atomic force microscopy experiments are in excellent agreement. We argue that, in case of the force-induced DNA strand separation, our model is a significant refinement of the Bell-Evans model and provides a reliable description for forces between 0 and 100 pN. In future, we foresee this theory to be applied to predict, tune and analyze the behavior of DNA force sensors.

## **SUPPLEMENTARY MATERIAL**

To view all of the supplemental files associated with this article, visit [www.biophysj.org](http://www.biophysj.org).

## **ACKNOWLEDGEMENTS**

Financial support was provided by the Nanosystems Initiative Munich. D. Ho, P. Severin and K. Falter are grateful to the Elite Network of Bavaria (IDK-NBT) for a doctoral fellowship.

## REFERENCES

- [1] Seeman, N. 2003. DNA in a material world. *Nature* 421:427-431.
- [2] Martin, M. 2000. DNA Handles for Single Molecule Experiments. *Single Mol.* 1:139-144.
- [3] Essevaz-Roulet, B., U. Bockelmann, and F. Heslot. 1997. Mechanical separation of the complementary strands of DNA. *Proc. Natl. Acad. Sci. USA*. 94:11935-11940.
- [4] Yan, H. 2003. DNA-Templated Self-Assembly of Protein Arrays and Highly Conductive Nanowires. *Science* 301:1882-1884
- [5] Cohen, J.D., J. P. Sadowski, and P. B. Dervan. 2007. Addressing Single Molecules on DNA Nanostructures. *Angew. Chem. Int. Ed.* 46:7956-7959.
- [6] Winfree, E., F. Liu, L. A. Wenzler, and N. C. Seeman. 1998. Design and self-assembly of two-dimensional DNA crystals. *Nature*. 394:539-544
- [7] Shawn, M. D., H. Dietz, T. Liedl, B. Höglberg, F. Graf, and W. M. Shih. 2009. Self-assembly of DNA into nanoscale three-dimensional shapes. *Nature*. 459:414-418.
- [8] Liu, Q., L. Wang, A. Frutos, A. Condon, R. Corn, and L. Smith. 2000. DNA computing on surfaces. *Nature*. 403:175-179
- [9] Albrecht, C., K. Blank, M. Lalic-Multhaler, S. Hirler, T. Mai, I. Gilbert, S. Schiffmann, T. Bayer, H. Clausen-Schaumann, and H. E. Gaub. 2003. DNA: a programmable force sensor. *Science*. 301:367-370.
- [10] Blank, K., A. Lankenau, T. Mai, S. Schiffmann, I. Gilbert, S. Hirler, C. Albrecht, M. Benoit, H. E. Gaub, and H. Clausen-Schaumann. 2004. Double-chip protein arrays: force-based multiplex sandwich immunoassays with increased specificity. *Anal. Bioanal. Chem.* 379:974-981.
- [11] Blank, K., T. Mai, I. Gilbert, S. Schiffmann, J. Rankl, R. Zivin, C. Tackney, T. Nicolaus, K. Spinnler, F. Oesterhelt, M. Benoit, H. Clausen-Schaumann, and H. E. Gaub. 2003. A force-based protein biochip. *Proc. Natl. Acad. Sci. USA*. 100:11356-11360.
- [12] Dose, C., D. Ho, H. E. Gaub, P. B. Dervan, and C. H. Albrecht. 2007. Recognition of "Mirror-Image" DNA by Small Molecules. *Angew. Chem.* 46:8384-8387.
- [13] Ho, D., C. Dose, C.H. Albrecht, P. Severin, K. Falter, P.B. Dervan, and H. E. Gaub. 2009. Quantitative Detection of Small Molecule/DNA Complexes Employing a Force-Based and Label-Free DNA-Microarray. *Biophys. J.* 96:4661-4671.
- [14] Ho, D., K. Falter, P. Severin, H. E. Gaub. 2009. DNA as a Force Sensor in an Aptamer-Based Biochip for Adenosine. *Anal. Chem. Int. Ed.* 81:3159-3164.
- [15] Kufer, S. K., E. M. Puchner, H. Gumpp, T. Liedl, and H. E. Gaub 2008. Single-Molecule Cut-and-Paste Surface Assembly. *Science* 319:594-596.

- [16] Puchner, E., S. Kufer, M. Strackharn, S. Stahl, and H. E. Gaub. 2008. Nanoparticle self-assembly on a DNA-scaffold written by single-molecule cut-and-paste. *Nano Letters* 8:3692-3695
- [17] Kufer, S., M. Strackharn, S. Stahl, H. Gumpf, E. M. Puchner and H. E. Gaub 2009. Optically monitoring the mechanical assembly of single molecules. *Nature Nanotechnology* 4:45-49.
- [18] Rief, M., H. Clausen-Schaumann, and H. E. Gaub. 1999. Sequence dependent mechanics of single DNA molecules. *Nat. Struct. Biol.* 6:346-349.
- [19] Cao, Y., T. Yoo, and H. Li. 2008. Single molecule force spectroscopy reveals engineered metal chelation is a general approach to enhance mechanical stability of proteins. *Proc. Natl. Acad. Sci. USA.* 105:11152-11157.
- [20] Smith, S., L. Finzi, and C. Bustamante. 1992. Direct mechanical measurements of the elasticity of single DNA molecules by using magnetic beads. *Science* 258:1122-1126.
- [21] Cluzel, P., A. Lebrun, C. Heller, R. Lavery, J. Viovy, D. Chatenay and F. Caron. 1996. DNA: an extensible molecule. *Science* 271:792-794.
- [22] Smith, S. B., Y. J. Cui, and C. Bustamante. 1996. Overstretching B-DNA: the elastic response of individual double-stranded and single-stranded DNA molecules. *Science*. 271:795-799.
- [23] Wang, M., H. Yin, R. Landick, J. Gelles and S. M. Block. 2005. Stretching DNA with optical tweezers. *Biophys. J.* 72:1335-1346.
- [24] Cocco, S., J. Yan, J. Léger, D. Chatenay, J. Marko. 2004. Overstretching and force-driven strand separation of double-helix DNA. *Phys. Rev. E.* 70:011910.
- [25] Storm, C and P. C. Nelson. 2003. Theory of high-force DNA stretching and overstretching. *Phys. Rev. E.* 67:051906.
- [26] Lebrun, A. and R. Lavery. 1996. Modelling extreme stretching of DNA. *Nucleic Acids Res.* 24:2260-2267
- [27] Konrad, M. and J. Bolonick. 1996. Molecular dynamics simulation of DNA stretching is consistent with the tension observed for extension and strand separation and predicts a novel ladder structure. *J. Am. Chem. Soc.* 118:10989-10994.
- [28] Rouzina, I. and V. A. Bloomfield. 2001. Force-Induced Melting of the DNA Double Helix 1. Thermodynamic Analysis. *Biophys. J.* 80:882-893.
- [29] Piana, S. 2005. Structure and energy of a DNA dodecamer under tensile load. *Nucleic Acids Res.* 33:7029-7038.
- [30] Clausen-Schaumann, H., M. Rief, C. Tolksdorf and H. E. Gaub. 2000. Mechanical Stability of Single DNA Molecules. *Biophys. J.* 78:1997-2007.
- [31] Strunz, T., K. Oroszlan, R. Schäfer and H. Güntherodt. 1999. Dynamic force spectroscopy of single DNA molecules. *Proc. Natl. Acad. Sci. USA.* 96:11277-11282.

- [32] Morfill, J., F. Kuhner, K. Blank, R. Lugmaier, J. Sedlmair and H. E. Gaub. 2007. B-S Transition in Short Oligonucleotides. *Biophys. J.* 93:2400-2409.
- [33] Friedsam, C., A. K. Wehle, F. Kuhner and H. E. Gaub. 2003. Dynamic single-molecule force spectroscopy: bond rupture analysis with variable spacer length. *J. Phys.: Condens. Matter*, 15:S1709-S1723.
- [34] Evans, E. and K. Ritchie. 1997. Dynamic strength of molecular adhesion bonds. *Biophys. J.*, 72:1541-1555.
- [35] Merkel, R., P. Nassoy, A. Leung, K. Ritchie, E. Evans. 1999. Energy landscapes of receptor-ligand bonds explored with dynamic force spectroscopy. *Nature*. 397:50-53.
- [36] Oesterhelt, F., M. Rief, and H. E. Gaub. 1999. Single molecule force spectroscopy by AFM indicates helical structure of poly(ethylene- glycol) in water. *N. J. Phys.* 1:1-11.
- [37] Zimm, B. H., and J. K. Bragg. 1959. Theory of the phase transition between helix and random coil in polypeptide chains. *J. Chem. Phys.* 31:526 –535.
- [38] Bockelmann, U., B. Essevaz-Roulet and F. Heslot 1997. Molecular Stick-Slip Motion Revealed by Opening DNA with Piconewton Forces. *Phys. Rev. Lett.* 79:4489-4492.
- [39] Bockelmann, U., B. Essevaz-Roulet and F. Heslot. 1998. DNA strand separation studied by single molecule force measurements. *Phys. Rev. E.* 58:2386-2394.
- [40] Cocco, S., R. Monasson and J. F. Marko. 2001 Force and kinetic barriers to unzipping of the DNA double helix. *Proc. Natl. Acad. Sci. USA.* 98:8608-8613.
- [41] Bornschloegl, T. and M. Rief. 2006. Single Molecule Unzipping of Coiled Coils: Sequence Resolved Stability Profiles. *Phys. Rev. Lett.* 96:118102.
- [42] Bornschloegl, T. and M. Rief. 2008. Single-Molecule Dynamics of Mechanical Coiled-Coil Unzipping. *Langmuir* 24:1338-1342.
- [43] Gotoh, O. and Y. Tagashira. 1981. Stabilities of nearest-neighbor doublets in double-helical DNA determined by fitting calculated melting profiles to observed profiles. *Biopolymers*. 20:1033-1042.
- [44] SantaLucia, J. 1998. A unified view of polymer, dumbbell, and oligonucleotide DNA nearest-neighbor thermodynamics. *Proc. Natl. Acad. Sci. USA.* 95:1460-1465.
- [45] Kafri, Y., D. Mukamel, and L. Peliti. 2000. Why is the DNA Denaturation Transition First Order? *Phys. Rev. Lett.* 85:4988.
- [46] Hanke, A., M. G. Ochoa and, R. Metzler. 2008. Denaturation Transition of Stretched DNA. *Phys. Rev. Lett.* 100: 018106.
- [47] Y. Kafri, D. Mukamel, and L. Peliti. 2002. Melting and unzipping of DNA. *Eur. Phys. J. B.* 27:135-146.

- [48] T. R. Einert, P. Naeger, H. Orland, and R. R. Netz. 2008. Impact of Loop Statistics on the Thermodynamics of RNA Folding. *Phys. Rev. Lett.* 101:048103.
- [49] Altan-Bonnet, G., A. Libchaber, and O. Krichevsky. 2003. Bubble dynamics in double-stranded DNA. *Phys. Rev. Lett.* 90:138101.
- [50] Lifson, S. 1964. Partition functions of linear-chain molecules. *J. Chem. Phys.* 40:3705.
- [51] Rubinstein, M., and R. H. Colby. 2003. *Polymer Physics*. Oxford University Press, Oxford.
- [52] Kuhner, F., M. Erdmann, L. Sonnenberg, A. Serr, J. Morfill, and H. E. Gaub. 2006. Friction of single polymers at surfaces. *Langmuir*. 22:11180-11186.
- [53] Polanyi, M., and E. Wigner. 1928. *Z. Phys. Chem. Abt. A*. 139:439.
- [54] Hänggi, P., P. Talkner, and M. Borkovec. 1990. Reaction-rate theory: fifty years after Kramers. *Rev. Mod. Phys.* 62:251-342.
- [55] Bockelmann, U., P. Thomen, and F. Heslot. 2008. Dynamics of the DNA Duplex Formation Studied by Single Molecule Force Measurements. *Biophys. J.* 87:3388-3396.
- [56] Andreatta, D., S. Sen, J. Lustres, S. Kovalenko, N. Ernsting, C. Murphy, R. Coleman, and M. Berg. 2006. Ultrafast Dynamics in DNA: “Fraying” at the End of the Helix. *J. Am. Chem. Soc.* 128:6885-6892.
- [57] Guéron, M., and J. L. Leroy. 1995. Studies of base pair kinetics by NMR measurement of proton exchange. *Methods Enzymol.* 261:383-413.
- [58] Butt, H. J., and M. Jaschke. 1995. Calculation of thermal noise in atomic-force microscopy. *Nanotechnology*. 6:1-7.
- [59] Kühner, F., M. Erdmann, and H. E. Gaub. 2006. Scaling Exponent and Kuhn Length of Pinned Polymers by Single Molecule Force Spectroscopy. *Phys. Rev. Lett.* 97: 218301.
- [60] Albrecht, C., G. Neuert, R. Lugmaier, and H. E. Gaub. 2008. Molecular Force Balance Measurements Reveal that Double-Stranded DNA Unbinds Under Force in Rate-Dependent Pathways. *Biophys. J.* 94: 4766-4774.
- [61] Birshtein, T. M., and O. B. Ptitsyn. 1966. *Conformations of Macromolecules*. John Wiley, New York.
- [62] Rupprecht, A., J. Piskur, J. Schultz, L. Nordenskiöld, Z. Song, and G. Lahajnar. 1994. Mechanochemical study of conformational transitions and melting of Li-, Na-, K-, and CsDNA fibres in water-ethanol solutions. *Biopolymers*. 34:897-920.
- [63] Buhot, A., and A. Halperin. 2000. Extension of rod-coil multiblock copolymers and the effect of the helix-coil transition. *Phys. Rev. Lett.* 84:2160-2163.

- [64] Hyeon, C. and D. Thirumalai. 2007. Measuring the energy landscape roughness and the transition state location of biomolecules using single molecule mechanical unfolding experiments. *J. Phys. Condens. Matter.* 19:113101.
- [65] Dudko, O. K., A. E. Filippov, J. Klafter J and M. Urbakh. 2003. Beyond the conventional description of dynamic force spectroscopy of adhesion bonds. *Proc. Natl. Acad. Sci. USA.* 100: 11378-11381.

## FIGURE LEGENDS

**Figure 1.** (a) Schematic of a single molecule DNA stretching experiment. The 5' ends of a short double stranded DNA duplex are attached to a surface and an atomic force microscope cantilever via elastic poly(ethylene glycol) (PEG) polymers. Separation of the substrate and the cantilever at constant velocity leads to an increasing end-to-end distance and thus to an increasing force. (b) Superposition of twenty experimentally obtained force-extension traces obtained from the same 30 base-pair **1·2** DNA duplex with a separation velocity of 1  $\mu$  m/s. The duplex dissociates at around 60-65 pN. (c) Schematic of the three state model. Every base-pair of the DNA duplex appears in one of three states: B-DNA, S-DNA or single stranded DNA. Every state  $s$  of a  $N$  base-pair long DNA may thus be represented by a list of length  $N$  with entries 0 (B-DNA), 1 (S-DNA) and 2 (ssDNA) for every base-pair.

**Figure 2.** (a) Force-extension traces obtained from phenomenological models for the three different states of double stranded DNA. (b) Corresponding free energy difference per base-pair between B-DNA and ssDNA as well as between S-DNA and ssDNA. A free energy penalty of  $2.4 k_B T$ , the average base-pair free energy of the **1·2** and **1·3** DNA duplexes, is introduced to the free energy of ssDNA due to the loss of base-pairing interactions. Highlighted in black is the state, which is thermodynamically most favorable. The most favorable state is B-DNA for forces below 60 pN, S-DNA for forces between 60 pN and 130 pN and single stranded DNA for forces above 130 pN.

**Figure 3.** Force-extension data of short double stranded DNA attached to a surface and an atomic force microscope cantilever via 5 kDa poly(ethylene glycol) linkers each. Data of twenty pulling experiments at a separation velocity of 1  $\mu$ m/s was binned into 1 pN intervals and averaged (circles). The solid line is the corresponding fit of our model. The dashed line represents the fit in case the DNA duplex remains in its canonical B-form. Below 30 pN the fit underestimates forces, an observation that we attribute to nonspecific interactions and entanglements with neighboring constructs on the surface. The inset shows that for forces above 30 pN theory and experimental data agree within the experimental error.

**Figure 4.** (a) Calculated rupture force distribution for the **1·2** and the **1·3** duplex for 50, 500 and 5000 nm/s pulling velocity. (b) Comparison of the experimental and calculated rupture force distribution for the **1·2** and **1·3** duplex at 895 nm/s and 1007 nm/s respectively. The calculated rupture force distributions were convolved with a Gaussian cantilever detection noise of 4.7 pN. (c) Comparison of the experimental and calculated most probable rupture forces for different most probable loading rates.

The grey data points refer to the experimental data and the black data points to the theory data. Squares refer to the 30 base-pair DNA **1·2** duplex and triangles to the 20 base-pair **1·3** duplex.

**Figure 5.** (a) Calculated effective barrier height, according to the standard Bell-Evans model. Between 10 and 50 pN the free energy decreases proportionally to the applied force  $f$ . Above 65 pN, when B-DNA is converted into S-DNA, the energy decreases linearly again, yet with a significantly smaller slope. (b) The negative derivative of the force versus free energy profile yields  $x_{tsf}$ , the effective distance between the equilibrium state and the transition state. The dashed line represents the difference in end-to-end distance for B-DNA and ssDNA for the **1·2** DNA duplex as a function of force. (c) For forces below 60 pN,  $x_{tsf}$  reflects the increase in end-to-end distance from B-DNA to ssDNA. (d) For forces above 65 pN,  $x_{tsf}$  reflects the increase in end-to-end distance from S-DNA to ssDNA.

**Figure 1**

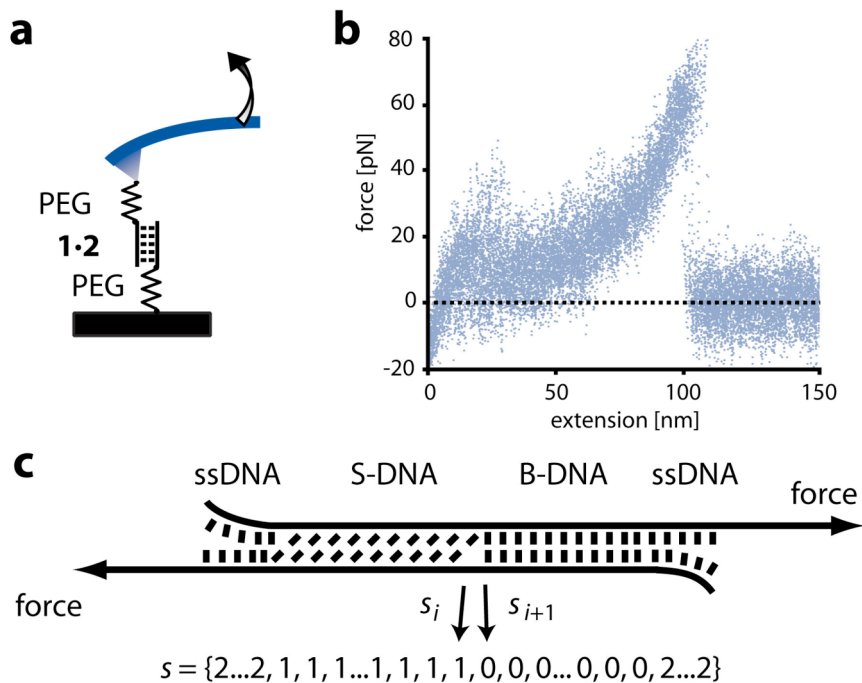


**Figure 2**

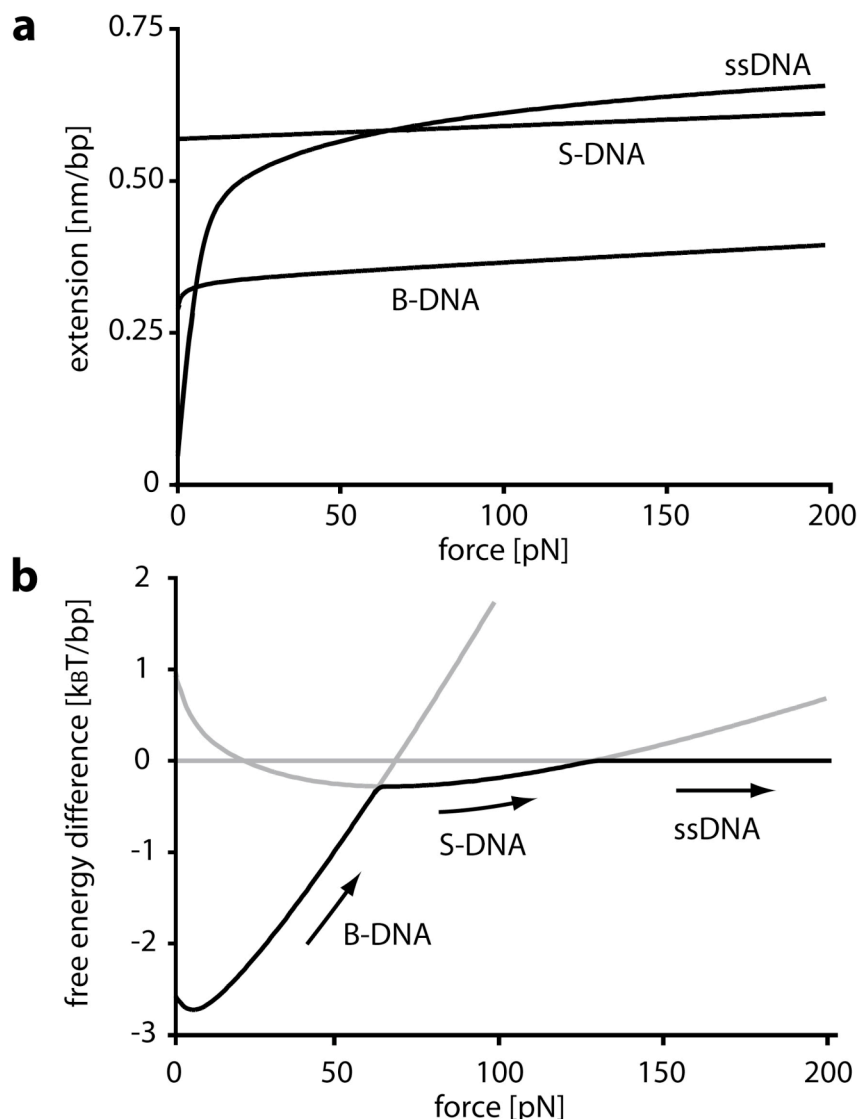


**Figure 3**

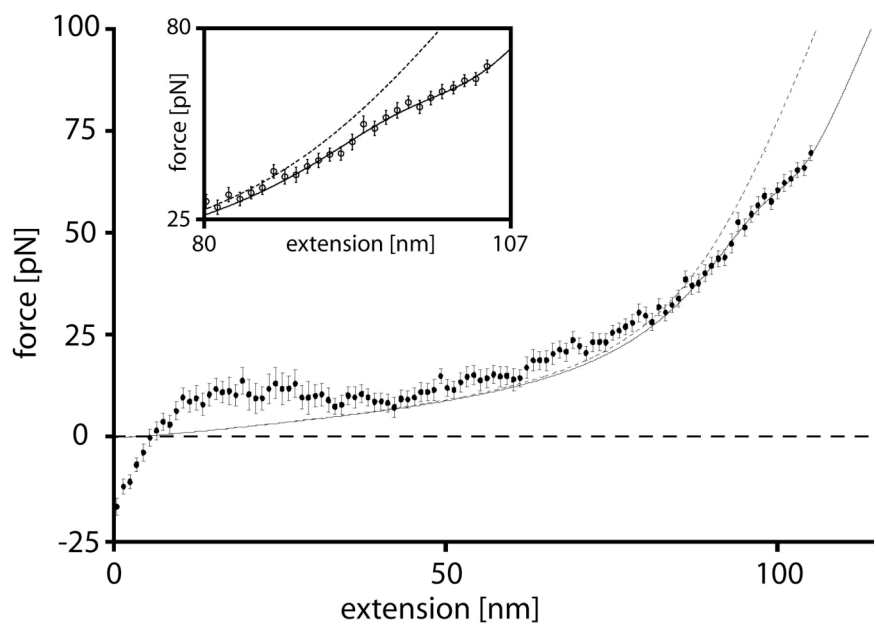


**Figure 4**

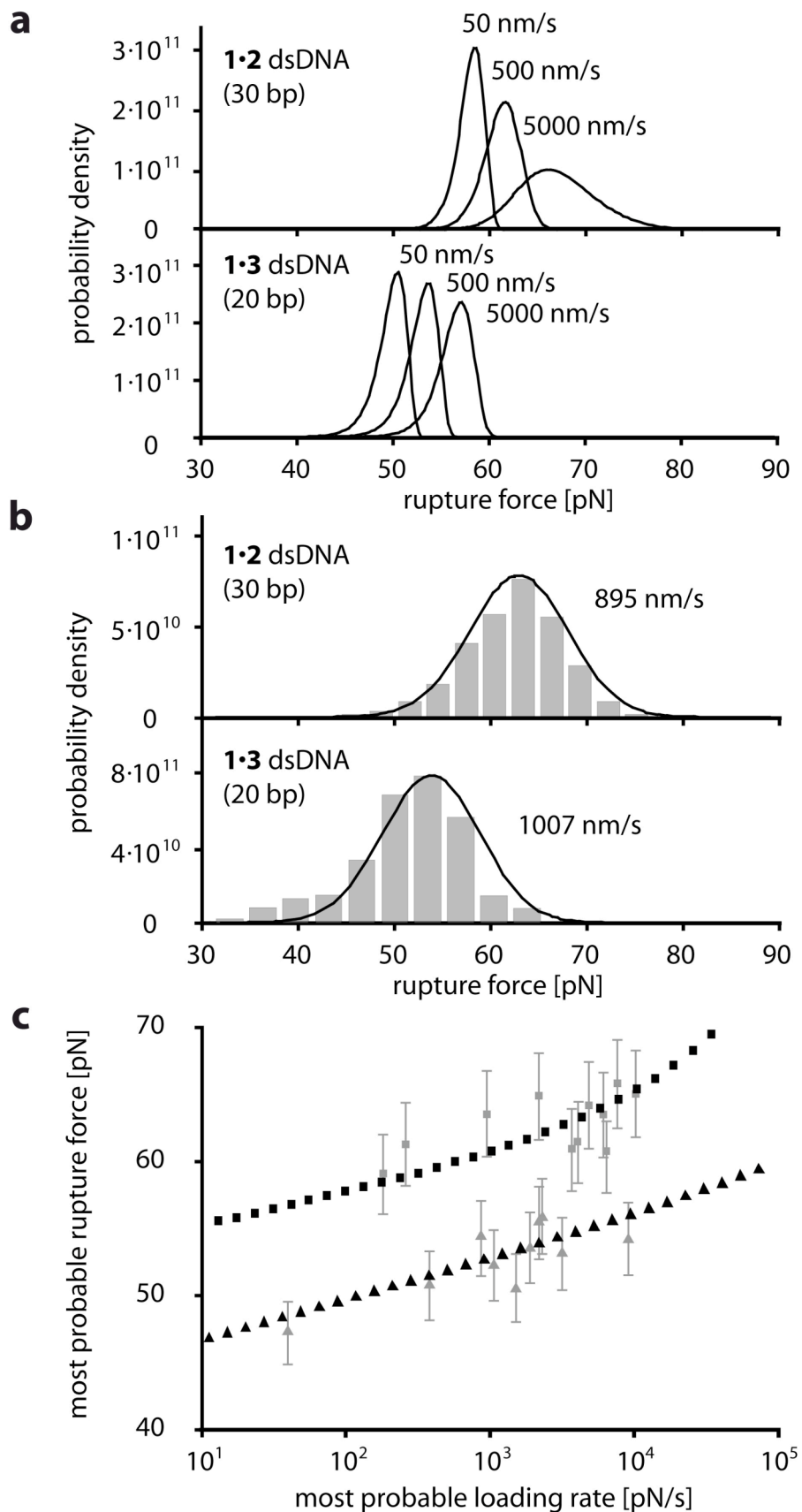
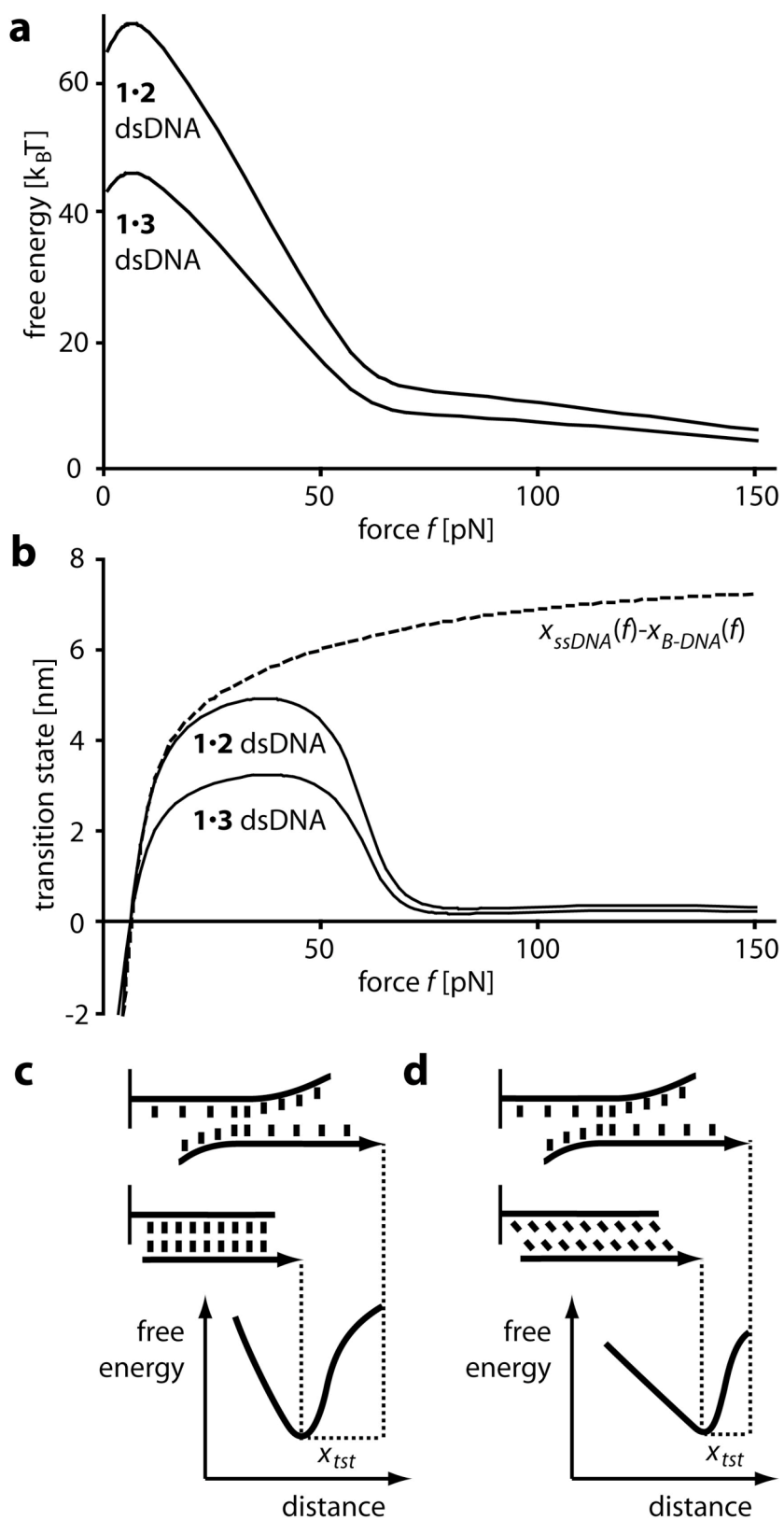


**Figure 5**



## SUPPLEMENTARY INFORMATION

### “Force-driven strand separation of short double stranded DNA”

*Dominik Ho<sup>1,2</sup>, Julia L. Zimmermann<sup>1,3</sup>, Florian A. Dehmelt<sup>1</sup>, Uta Steinbach<sup>1</sup>, Matthias Erdmann<sup>1</sup>, Philip Severin<sup>1</sup>, Katja Falter<sup>1</sup>, Hermann E. Gaub<sup>1</sup>*

[<sup>1</sup>] Lehrstuhl für Angewandte Physik and Center for Nanoscience  
Ludwig-Maximilians-Universität  
Amalienstrasse 54, 80799 Munich, Germany  
Fax: (+49) 89-2180-2050  
E-mail: gaub@lmu.de

[<sup>2</sup>] Munich Center For Integrated Protein Science (CIPSM)  
Ludwig-Maximilians-Universität  
Butenandtstrasse 5-13, 81377 Munich, Germany  
E-mail: dominik.ho@web.de

[<sup>3</sup>] present address: Max-Planck-Institut für extraterrestrische Physik  
Giessenbachstrasse, 85748 Garching, Germany

## CONTENTS

- Materials and Methods (S2)
- Polymer Models (S4)
- Partition Sum Corrections (S6)
- Transition State Theory (S7)
- References (S10)

## MATERIALS AND METHODS

Theoretical calculations were performed using Mathematica version 5.1 (Wolfram Research, Champaign, IL). The experimental data presented in this study was obtained according to Morfill and colleagues [1]. In the following paragraphs we briefly discuss the experimental setup and data analysis.

**DNA constructs.** DNA oligomers **1**: SH-5'-TTT TTT TTT TTT TTT TTC GTT GGT GCG GAT ATC TCG GTA GTG GGA TAC GAC GAT ACC GAA GAC AGC TCA TGT TAT ATT ATG-3', **2**: SH-5'-TTT TTT TTT TTA TCC CAC TAC CGA GAT ATC CGC ACC AAC G-3' and **3**: SH-5'-TTT TTT TCC GAG ATA TCC GCA CCA ACG-3' were purchased HPLC grade from IBA GmbH (Goettingen, Germany).

**Preparation of slides and cantilevers.** The used oligonucleotides modified with a thiol group at their 5'-termini were immobilized on amino-functionalized surfaces using a hetero-bifunctional poly(ethylene glycol) (PEG) spacer [2]. Oligonucleotide **1** was immobilized on the cantilever and oligonucleotide **2**, respectively **3**, was coupled to the surface. Before use, the cantilevers (Bio-lever, Olympus) were cleaned as described earlier [3]. After this cleaning procedure, amino-modified cantilevers were prepared using 3-aminopropyltrimethylethoxysilane (ABCR GmbH, Karlsruhe, Germany). For the surface-coupling of oligonucleotide **2**, respectively **3**, commercially available amino-functionalized slides (Slide A, Nexterion, Mainz, Germany) were used. From now on, both surfaces (cantilever and slide) were treated in parallel as described previously [4]. They were incubated in borate buffer pH 8.5 for 1 h in order to deprotonate the amino groups to ensure coupling to the N-hydroxysuccinimide (NHS) groups of the heterobifunctional NHS-PEG-maleimide (molecular weight, 5000 g/mol; Nektar, Huntsville, AL). After dissolving the PEG at a concentration of 50 mM in borate buffer at pH 8.5, this solution was incubated on the surfaces for 1 h. In parallel, the thiol groups of oligonucleotides **1**, **2** and **3** were recovered from disulfide bonds. Oligonucleotides were reduced using tris (2-carboxyethyl) phosphine hydrochloride beads (Perbio Science, Bonn, Germany). After washing the surfaces with ultrapure water, a solution of the oligonucleotides **1** and **2**, respectively **3**, (1.75 mM) was incubated on the cantilever tip and the surfaces for 1 h. During this incubation time, the free functional maleimide group of the PEG was allowed to react with the 5'-thiol end of the respective oligonucleotide, yielding a thioester bond. Finally, the cantilever and the surfaces were rinsed with PBS to remove noncovalently bound oligonucleotides and stored in PBS until use.

**Force spectroscopy.** The force measurements were performed in PBS containing 150 mM NaCl at room temperature using an MFP-3D AFM (Asylum Research, Santa Barbara, CA). Cantilever spring constants were measured as described previously [5] [6]. During one experiment, the approach and retract velocity were held constant. To obtain measurements over a broad range of different loading rates, several experiments were performed each at a different retract velocity ranging from 50 nm/s to 10 mm/s.

**Data Analysis.** The obtained data were converted into force-extension curves. From these force-extension curves, the rupture force (the force at which the dsDNA separates into two single strands) and the corresponding loading rate were determined using the software Igor Pro 5.0 (Wavemetrics, Lake Oswego, OR) and a custom-written set of procedures. The rupture force is defined as described previously [7]. To determine the loading rate, the freely jointed chain model was used, according to previous studies [9].

## POLYMER MODELS

Herein, we employ polymer extension models for B-DNA, S-DNA and single stranded DNA according to the three-state equilibrium model of Cocco and colleagues [8]. The poly(ethylene-glycol) is modeled according to Oesterhelt and colleagues [9].

**Double-stranded B-DNA.** B-DNA elasticity is very well described by chain bending fluctuations leading to an entropic elasticity, while elastic stretching of the double helix generates the roughly linear stretching between 20 and 50 pN with a spring constant per base pair of  $f_B/C_B = 1200/0.34$  pN/nm. According to previous work [10], the extension per base-pair is

$$x_B(f) = C_B \left( 1 - \sqrt{\frac{k_B T}{4 A_B f}} + \frac{f}{f_B} \right),$$

where the persistence length is  $A_B = 50$  nm, the force constant  $f_B = 1230$  pN and the contour length  $C_B = 0.34$  nm. The free energy correspondingly becomes

$$w_B(f) = - \int_{f'=0}^f x_B(f') df'$$

**Double-stranded S-DNA.** For S-DNA elasticity a linear response to elongation was suggested [8] with an extension per base pair of

$$x_S(f) = x_0 + \frac{f - f_0}{S},$$

and a free energy function of

$$w_S(f) = w_B(f_0) - \frac{1}{2} \left( (x_0 + x_1)(f_1 - f_0) + 2x_1(f - f_1) + (f - f_1)^2 / S \right)$$

where the parameters are  $x_0 = 0.32$  nm,  $x_1 = 0.58$  nm,  $f_0 = 62$  pN,  $f_1 = 68$  pN and  $S = 4700$  pN/nm. The values for  $f_0$  and  $f_1$  are salt dependent parameters and given for a salt concentration of 500 mM. They shift down by 5 pN for each decade reduction in NaCl concentration. Thus the above set of parameters is chosen such that experimental data on the B-S transition, the salt dependence [11] and the stretching data for forces between 68 and 150 pN [12] are reproduced well.

**Single-stranded DNA.** The ssDNA polymer model is phenomenological [8] and includes the logarithmic dependence of extension on force seen at >50 mM NaCl concentration [13] as well as the reduction in contour length generated at low force by self-adhesion (“folding”) of the chain. The extension per base pair is

$$x_{ss}(f) = C_{ss} \left( \frac{a_1 \ln(f/f_1)}{1 + a_3 \text{Exp}(-f/f_3)} \right),$$

where  $C_{ss} = 0.34$  nm,  $a_1 = 0.21$ ,  $a_2 = 0.34$ ,  $f_1 = 0.0037$  pN,  $f_2 = 2.9$  pN and  $f_3 = 8000$  pN. The parameter  $a_3 = 2.1 \ln(M/0.0025)/\ln(0.15/0.0025) - 0.1$  depends on NaCl concentration  $M$  (mol). The free energy correspondingly becomes

$$w_{ss}(f) = - \int_{f'=0}^f x_{ss}(f') df'.$$

**Poly(ethylene glycol).** For the PEG extension per monomer we used a two state model develop by Oesterhelt and colleagues [1].

$$x_{PEG}(f) = \left( \frac{C_{planar}}{\text{Exp}(\Delta G(f)/k_B T) + 1} + \frac{C_{helical}}{\text{Exp}(-\Delta G(f)/k_B T) + 1} \right) \cdot \left( \coth\left(\frac{f \cdot A_{PEG}}{k_B T}\right) - \frac{k_B T}{f \cdot A_{PEG}} \right) + \frac{f}{K_{PEG}},$$

where  $C_{planar} = 3.58$  Å,  $C_{helical} = 2.8$  Å,  $A_{PEG}$  of 7 Å,  $K_{PEG} = 150$  N/m and

$$\Delta G(f) = \Delta G_0 - f(C_{planar} - C_{helical}),$$

where  $\Delta G_0 = 3.3 k_B T$ . This model takes into account that the PEG monomers appear in two conformations.

## PARTITION SUM CORRECTIONS

**Boundary Condition.** The partition sum of Equation 8 does not account for the boundary conditions at the end of the DNA duplex yet. As boundary conditions, we therefore introduce two additional base-pairs at  $i = 0$  and  $i = N + 1$ , which are single stranded. The partition sum  $Z'$  including the two boundary base pairs becomes

$$Z' = \sum_{\substack{\text{allmatrix} \\ \text{elements}}} \begin{bmatrix} 0 & 0 & 0 \\ 0 & 0 & 0 \\ \exp(-w_{ss}(f) - C_{ds-ss}) & \exp(-w_{ss}(f) - C_{ds-ss}) & \exp(-w_{ssDNA}(f)) \end{bmatrix} \times Z \times \begin{bmatrix} 0 & 0 & 0 \\ 0 & 0 & 0 \\ 0 & 0 & \exp(-w_{ssDNA}(f)) \end{bmatrix}.$$

**Strand-separated states.** All states with less than two remaining base-pairs are already strand separated. We subtract the Boltzmann probabilities of these states from the partition sum such that the partition sum that we use for all further calculations becomes

$$Z'' = Z' - (Z_0 + Z_1),$$

$$\text{where } Z_0 = \sum_{\substack{\text{allmatrix} \\ \text{elements}}} \begin{bmatrix} 0 & 0 & 0 \\ 0 & 0 & 0 \\ \exp(-w_{ss}(f) - C_{ds-ss}) & \exp(-w_{ss}(f) - C_{ds-ss}) & \exp(-w_{ss}(f)) \end{bmatrix}^{N+1} \times$$

$$\begin{bmatrix} 0 & 0 & 0 \\ 0 & 0 & 0 \\ \exp(w_{ss}(f) - C_{ds-ss}) & \exp(w_{ss}(f) - C_{ds-ss}) & \exp(w_{ss}(f)) \end{bmatrix}^i \times$$

$$\begin{bmatrix} 0 & 0 & 0 \\ 0 & 0 & 0 \\ \exp(w_{ss}(f) - C_{ds-ss}) & \exp(w_{ss}(f) - C_{ds-ss}) & \exp(w_{ss}(f)) \end{bmatrix} \times$$

$$\text{and } Z_1 = \sum_{i=1}^N \sum_{\substack{\text{allmatrix} \\ \text{elements}}} \begin{bmatrix} 0 & 0 & 0 \\ 0 & 0 & 0 \\ \exp(w_{ss}(f) - C_{ds-ss}) & \exp(w_{ss}(f) - C_{ds-ss}) & \exp(w_{ss}(f)) \end{bmatrix}^{N-i} \times$$

$$\begin{bmatrix} 0 & 0 & 0 \\ 0 & 0 & 0 \\ \exp(w_{ss}(f) - C_{ds-ss}) & \exp(w_{ss}(f) - C_{ds-ss}) & \exp(w_{ss}(f)) \end{bmatrix}$$

## TRANSITION STATE THEORY

**Equilibrium Flux.** The equilibrium flux is simply the sum of the Boltzmann probabilities of all states  $s_{tst}$  times the base pair opening rate:

$$k(f) = \langle \delta[n - n_{tst}] \dot{n}_+ \rangle_{equilibrium}$$

$$= \frac{1}{Z(f)} \sum_{s_{tst}} \dot{n}_+ \exp(-\Delta G_{total}(s_{tst}, f))$$

$$k(f) = \frac{1}{Z''} \dot{n}_+ \sum_{k=1}^{N-1} \sum_{\substack{\text{all matrix} \\ \text{elements}}}^{\text{elements}} \begin{bmatrix} 0 & 0 & 0 \\ 0 & 0 & 0 \\ \exp(-g_{ss}(f) - C_{ds-ss}) & \exp(-g_{ss}(f) - C_{ds-ss}) & \exp(-g_{ss}(f)) \end{bmatrix}^k \times$$

$$\begin{bmatrix} \exp(-g_B(f) + J_k) & \exp(-g_B(f) + J_k - C_{B-S}) & \exp(-g_B(f) - C_{ds-ss}) \\ \exp(-g_S(f) + J_k - C_{B-S}) & \exp(-g_S(f) + J_k) & \exp(-g_S(f) - C_{ds-ss}) \\ 0 & 0 & 0 \end{bmatrix} \times$$

$$\begin{bmatrix} \exp(-g_B(f) + J_{k+1}) & \exp(-g_B(f) + J_{k+1} - C_{B-S}) & \exp(-g_B(f) - C_{ds-ss}) \\ \exp(-g_S(f) + J_{k+1} - C_{B-S}) & \exp(-g_S(f) + J_{k+1}) & \exp(-g_S(f) - C_{ds-ss}) \\ 0 & 0 & 0 \end{bmatrix} \times$$

$$\begin{bmatrix} 0 & 0 & 0 \\ 0 & 0 & 0 \\ \exp(-g_{ss}(f) - C_{ds-ss}) & \exp(-g_{ss}(f) - C_{ds-ss}) & \exp(-g_{ss}(f)) \end{bmatrix}^{N-k-1} \times \begin{bmatrix} 0 & 0 & 0 \\ 0 & 0 & 0 \\ 0 & 0 & \exp(-g_{ss}(f)) \end{bmatrix}$$

**Thermodynamic Equilibrium Prevails.** To appropriately describe the separation of dsDNA employing the canonical transition state theory, thermodynamic equilibrium must prevail within the binding potential. Two scenarios would contradict such an assumption: Either, the changes of state occurred on timescales equal to or slower than the rate of escape or if, in order to reach the transition states, an intermediate free energy barrier needs to be crossed. In the following, we discuss these scenarios and conclude that, for the experimentally observed force range between 0 and 100 pN, the canonical transition state theory is applicable.

The changes in state from dsDNA to ssDNA occur at base-pair opening and closing rates. Within the present work, we assumed that these rates are in the order of  $10^8$  s<sup>-1</sup>. From our numerical calculations, we deduce that the base-pair opening rate is about two orders of magnitude faster than the rate at which short dsDNA dissociates for forces below 100 pN. We therefore conclude that the escape process does not critically disturb the thermodynamic equilibrium.

Due to the base-pair heterogeneity the transition state might only be reached by crossing intermediate free energy barriers [8]. In this case, this intermediate barrier crossing would become rate limiting and the populations of states would not be Boltzmann distributed. In order to investigate this effect, we calculated the free energy as a function of the open base-pairs explicitly for the two dsDNAs used here

(Figure S1). Hereby, we neglected the simultaneous formation of more than one DNA bubble. Figure S1b illustrates that no significant energy barriers appear for forces up to 100 pN.

Since the changes in state occur much faster than the separation of the strands and, apart from the transition state, no significant energy barriers arises along the reaction coordinate, we conclude that the canonical transition state theory is appropriate for modeling the rate of strand separation for tens of base-pair long dsDNA. However, for forces significantly higher than 100 pN, the requirements for the canonical transition state theory fail: The rate of escape becomes comparable to the timescale of internal fluctuations, i.e. the base-pair opening and closing rates. Further, rate-dominating barriers apart from the transition state arise. Both effects result in a significant perturbation of the equilibrium distribution and consequently in the breakdown of the canonical transition state theory.

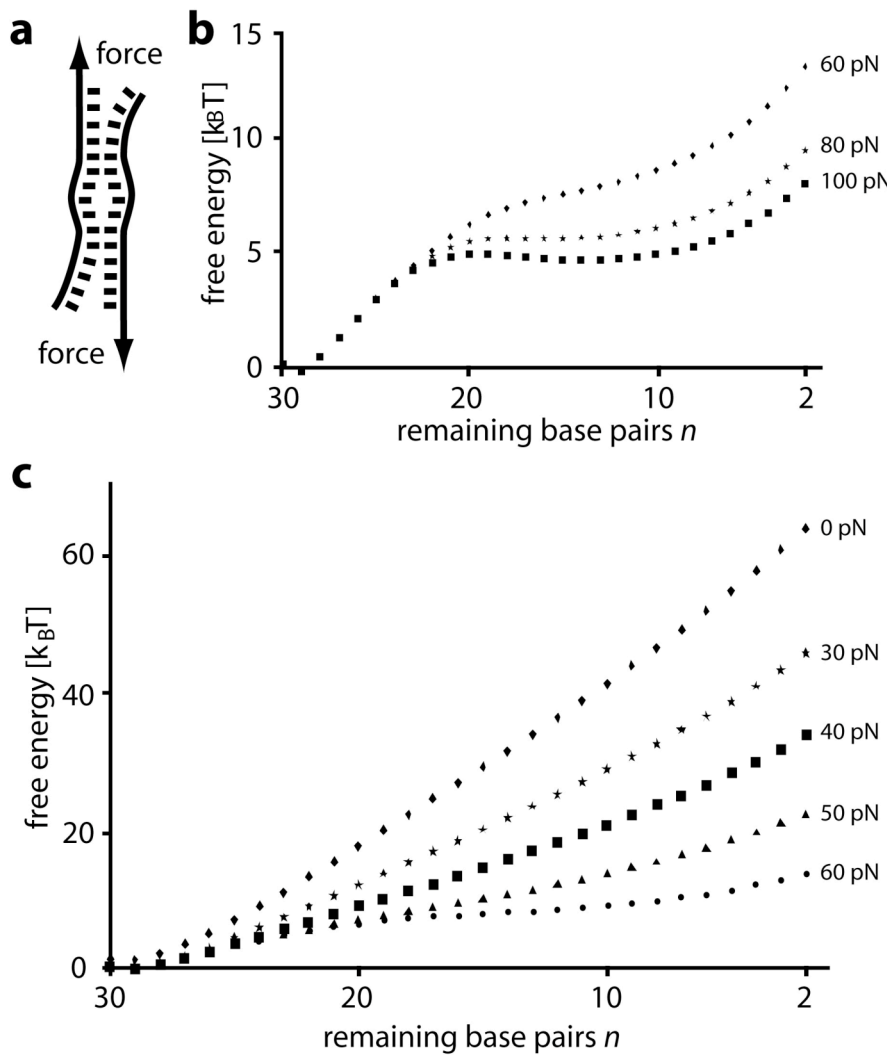


**Figure S1.** (a) The calculated energy landscape collapsed onto one coordinate *n*, the number of remaining base pairs, is calculated from equilibrium theory. Thereby, we allow the double strand to open up from its ends as well as to form a bubble of ssDNA. In order to speed up the numerical calculations, we do not account for the simultaneous opening of more than one bubble. (b) Free energy landscape of the **1·2** DNA duplex at 60, 80 and 100 pN calculated from the partition sum. (c) Free energy landscape of the **1·2** DNA duplex at forces smaller than 60 pN. The transition state is located at *n*<sub>ts</sub> = 2 and no significant barriers apart from the transition state are observed for forces up to 100 pN.

## REFERENCES

- [1] Morfill, J., F. Kuhner, K. Blank, R. Lugmaier, J. Sedlmair and H. E. Gaub. 2007. B-S Transition in Short Oligonucleotides. *Biophys. J.* 93:2400-2409.
- [2] Kuehner, F., J. Morfill, R. A. Neher, K. Blank, and H. E. Gaub. 2007. Force-induced DNA slippage. *Biophys. J.* 92:2491–2497.
- [3] Neuert, G., C. Albrecht, E. Pamir, and H. E. Gaub. 2006. Dynamic force spectroscopy of the digoxigenin-antibody complex. *FEBS Lett.* 580:505–509.35.
- [4] Blank, K., J. Morfill, and H. E. Gaub. 2006. Site-specific immobilization of genetically engineered variants of *Candida Antarctica* lipase B. *ChemBioChem.* 7:1349–1351.11180–11186.
- [5] Butt, H. J., and M. Jaschke. 1995. Calculation of thermal noise in atomic-force microscopy. *Nanotechnology.* 6:1–7.
- [6] Hugel, T., and M. Seitz. 2001. The study of molecular interactions by AFM force spectroscopy. *Macromol. Rapid Commun.* 22:989–1016.
- [7] Evans, E., and K. Ritchie. 1999. Strength of a weak bond connecting flexible polymer chains. *Biophys. J.* 76:2439–2447.
- [8] Cocco, S., J. Yan, J. Léger, D. Chatenay, J. Marko. 2004. Overstretching and force-driven strand separation of double-helix DNA. *Phys. Rev. E.* 70:011910.
- [9] Oesterhelt, F., M. Rief, and, H. E. Gaub. 1999. Single molecule force spectroscopy by AFM indicates helical structure of poly(ethylene- glycol) in water. *N. J. Phys.* 1:1–11.
- [10] Marko, J., and E. Siggia. 1995. Stretching DNA. *Macromolecules.* 28:8759-8770.
- [11] Wenner, J. R., M. C. Williams, I. Rouzina, and V. A. Bloomfield. 2002. *Biophys. J.* 82:3160.
- [12] Leger, J.-F., G. Romano, A. Sarkar, J. Robert, L. Bourdieu, D. Chatenay, and J. F. Marko. 1999. *Phys. Rev. Lett.* 83:1066.
- [13] Y. Zhang, H. J. Zhou, and Z. C. Ou-Yang. 2001. *Biophys. J.* 81:1133.

### A.3. PUBLIKATIONEN UNABHÄNGIG VON DER DISSERTATION

#### P4:

Valero, V., T. Nevian, **D. Ho**, and M. Lindau. 2008. Tethering Forces of Secretory Granules Measured with Optical Tweezers. *Biophysical Journal*. 95:4972-4978.

#### P5:

Muñoz Javier, A., P. Del Pino, M. F. Bedard, **D. Ho**, A. G. Skirtach, G. B. Sukhorukov, C. Plank, and W. J. Parak. 2008. Photoactivated release of cargo from the cavity of polyelectrolyte capsules to the cytosol of cells. *Langmuir*. 24:12517-12520.

# Tethering Forces of Secretory Granules Measured with Optical Tweezers

Vicente Valero, Thomas Nevian, Dominik Ho, and Manfred Lindau  
School of Applied and Engineering Physics, Cornell University, Ithaca, New York 14853

**ABSTRACT** Fusion of a vesicle with its target membrane is preceded by tethering or docking. However, the physical mechanism of vesicle-tethering is unknown. To study this mechanism, we used eosinophil secretory granules, which undergo stimulated homotypic fusion events inside the cell during degranulation. Using a dual optical trap system, we observed tether formation between isolated eosinophil secretory granules. The results show that secretory granules interact stochastically with a target membrane forming physical tethers linking the vesicle and target membrane, rather than via interactions with the cytoskeleton. The necessary components are membrane-associated, and the addition of cytosolic components is not required. Tether-lifetime measurements as a function of applied mechanical force revealed at least three kinetically distinct tethered states. The tethered-state lifetimes of isolated eosinophil granules match the residence times of chromaffin granules at the plasma membrane in intact cells, suggesting that the tethering mechanisms reported here may represent the physiological mechanisms of vesicle-tethering in the cell.

## INTRODUCTION

Vesicular transport entails a sequence of steps including vesicle formation, transport, tethering and docking, and eventually fusion. Although the fusion steps (in particular, exocytic fusion pore openings) have been studied in great detail (1), there is little functional information available on tethering, the step that precedes vesicle fusion. Tethering and docking are terms describing the association of a vesicle with its target membrane. Tethering has been considered a link that extends over distances of more than 25 nm, whereas docking is thought of as a state where the vesicle and target membrane are held together within <5–10 nm (2). Thus, the term “tethering” refers to the initial interaction of a vesicle with its target membrane, whereas “docking” is widely thought to involve the trans-pairing of soluble *N*-ethylmaleimide-sensitive factor attachment receptors (SNAREs) (3,4). Although a number of tethering factors were identified, it remains unclear what their molecular mechanism of vesicle tethering is, and which (if any) of these proteins and multi-subunit complexes physically link a vesicle to its target membrane (5). In chromaffin cells, new vesicles approaching the membrane are docked or tethered (6), jittering as if they were in a small cage or as if attached to the plasma membrane via a tether ~70 nm long (7). This type of movement does not depend on intact SNAREs (8). It is unknown whether tethering involves a physical link between the membranes or else

a cytoskeletal cage keeping the vesicle in place. Here we report on the first measurements, to our knowledge, of tethering forces between isolated horse eosinophil granules, using a dual optical trap.

## MATERIALS AND METHODS

### Cell preparation

Eosinophils were isolated from 125 mL of fresh blood from the jugular veins of horses (Equine Research Center, Cornell University, Ithaca, NY). During spontaneous sedimentation of red blood cells, the plasma, which contains leukocytes, was rapidly collected. The remaining erythrocytes were lysed by osmotic shock, and the final pellet was washed in Hanks' solution. To obtain 98% pure eosinophils, the solution was centrifuged over discontinuous Percoll (Biochrom, Berlin, Germany) gradients (9).

### Granule isolation

To isolate granules,  $\sim 5 \times 10^6$  purified horse eosinophils (Fig. 1 a) were suspended in 1 mL KCl-based buffer (125 mM KCl, 10 NaCl, 7 MgCl<sub>2</sub>, 2 CaCl<sub>2</sub>, 10 HEPES, and 5 EGTA) containing 140 nM free Ca<sup>2+</sup> (calculated using WebMaxC, version 2.10, Stanford University, <http://maxchelator.stanford.edu>), protease inhibitors (pepstatin A, TPCK, aprotinin, leupeptin, and dithiothreitol, from Sigma, St. Louis, MO), and DNase I (grade II, Roche Boehringer, Indianapolis, IN), and disrupted by ~25 passages through a 25.5 syringe needle (Fig. 1 b). The suspension was then placed on top of a discontinuous Percoll gradient of 2 mL 79% Percoll at the bottom, overlaid with 1 mL 20% Percoll in a 15-mL Falcon tube, and centrifuged for 10 min at 500 rpm. The top 1 mL of buffer was removed, and the next 500  $\mu$ L containing isolated granules, as well as small pieces from broken cells, were collected. The collected 500- $\mu$ L suspension was gently mixed with 1 mL of KCl buffer and centrifuged at 500 rpm for 10 min in an Eppendorf centrifuge. We removed 1.2 mL of buffer from the top, leaving 300  $\mu$ L of suspension at the bottom containing the granules. These 300  $\mu$ L were then placed on top of 500  $\mu$ L of fresh KCl buffer in an Eppendorf tube and centrifuged for 2 min at 500 rpm. The top 400  $\mu$ L of buffer were discarded, leaving 400  $\mu$ L of granule suspension. A sample chamber was filled with ~300  $\mu$ L of an appropriately diluted solution containing granules at low concentration (~1 granule in 0.01 mm<sup>2</sup> of area) (Fig. 1 c). The chamber had a cover glass bottom, and was mounted on the stage of the inverted microscope (Axiovert 135 TV, Zeiss, Thornwood, NY).

Submitted March 3, 2008, and accepted for publication August 5, 2008.

Address reprint requests to Manfred Lindau, School of Applied and Engineering Physics, 212 Clark Hall, Cornell University, Ithaca, NY 14853. Tel.: 607-255-5264; Fax: 607-255-7658; E-mail: ml95@cornell.edu.

Thomas Nevian's present address is the Institute for Physiology, Bern University, Bühlpark 5, CH-3012 Bern, Switzerland.

Dominik Ho's present address is the Dept. of Physics, Ludwig-Maximilians-University, Amalienstrasse 54, D-80799 Munich, Germany.

Editor: Joshua Zimmerberg.

© 2008 by the Biophysical Society  
0006-3495/08/11/4972/07 \$2.00

doi: 10.1529/biophysj.108.132670

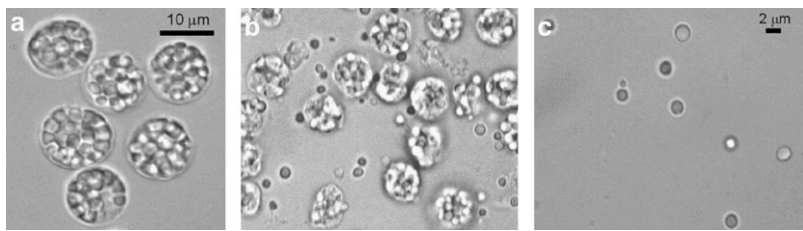


**FIGURE 1** Horse eosinophil granule isolation. Purified horse eosinophils (*a*) were disrupted by passages through a syringe needle (*b*), and were purified (*c*) by Percoll centrifugation.

### Dual optical trap setup

A dual optical trap was built, with one fixed and one steered trap. A diode-pumped neodymium-doped orthovanadate (Nd/YVO<sub>4</sub>) infrared-laser emitting at 1064 nm, Millenia IR, Spectra-Physics, Mountain View, CA was used as the light source for optical trapping. The beam was split by a polarizing beam-splitter. One beam was fixed in position, and the other was steered by a pair of acousto-optical deflectors (AODs) (see the Supplementary Material, Data S1, for details). A program was written in Visual Basic (Microsoft, Redmond, WA) to control the AODs and to acquire the video images. The program also controlled the piezo-electric translators for trap stiffness calibration.

### Video imaging

Bright-field images of trapped granules were taken at 26–28 frames/second with a CCD video camera (SSC-M370, Sony, Niles, IL), using a digital video processor (DVP-32, InstruTECH, Great Neck, NY). With the objective used here (Zeiss Plan-Neofluar 100×13 Oil), pixels size corresponded to 97 nm/pixel in the object plane. Regions of interest of 60 × 100 pixels were saved for offline analysis.

### Calibration of trap stiffness

For each granule in the fixed trap, trap stiffness was determined by experimental calibration, using a viscous-drag method. The optical trap held the vesicle 4–5 μm above the coverslip surface. Viscous drag forces were applied by moving a microscope substage with the sample chamber by 100 μm at different speeds, via attached piezo-electric translators (P-282, Physik Instrumente, Auburn, MA). The applied viscous-drag forces were estimated

by applying Stokes' law  $F = 6\pi\eta rv$ , where  $\eta$  is the viscosity of the buffer,  $r$  is the radius of the vesicle, and  $v$  is the velocity of the flow. The granule was imaged while the substage was moved by 100 μm at various velocities, and displacement was determined as a function of applied force as calibration for the tethering experiment. This procedure was performed for each granule because trap stiffness may vary, depending on granule refractive index as well as laser power and focusing. The laser power was changed manually, using neutral density filters to modify trap stiffness.

The contour lines in Fig. 2, *b–d*, indicate the best fit of the displaced image of the resting granule (Fig. 2 *a*) (for details, see Calibration Image Analysis). Fig. 2 *e* shows the movement of the sample chamber (*black trace*) and granule displacement in the vertical direction (*red*, direction of viscous drag force) and horizontal direction (*blue*, perpendicular to viscous drag force). The position of the granule clearly follows the drag force. For a particular sweep, the downward displacement is rather constant, whereas the upward displacements show a slope (Fig. 2 *e*). This slope reflects a slope in velocity, and thus in applied force because of the hysteresis of the open-loop piezo movement (data not shown). For the quantitative analysis, only the linear parts (downward displacements) were used. The granule diameter was estimated as the distance between the intensity minima on each side of the granule image. The accuracy of this procedure was confirmed using polystyrene beads of known radius. Knowing the velocity of the chamber movement and the granule diameter, the viscous drag force can be estimated. Fig. 2 *f* shows that the displacement is proportional to the applied force, with a trap stiffness (inverse slope) of 25 pN/μm. For the range of granules used in our experiments (1.0–2.5-μm diameter), trap stiffness showed no systematic dependence on granule diameter (data not shown). Out of 111 granules, 74 (67%) had diameters between 1.3–1.8 μm, and the trap stiffness was 15–25 pN/μm. Using 2-μm-diameter polystyrene beads, the average trap stiffness using the same intensity was ~45 pN/μm, corresponding to their higher refractive index.

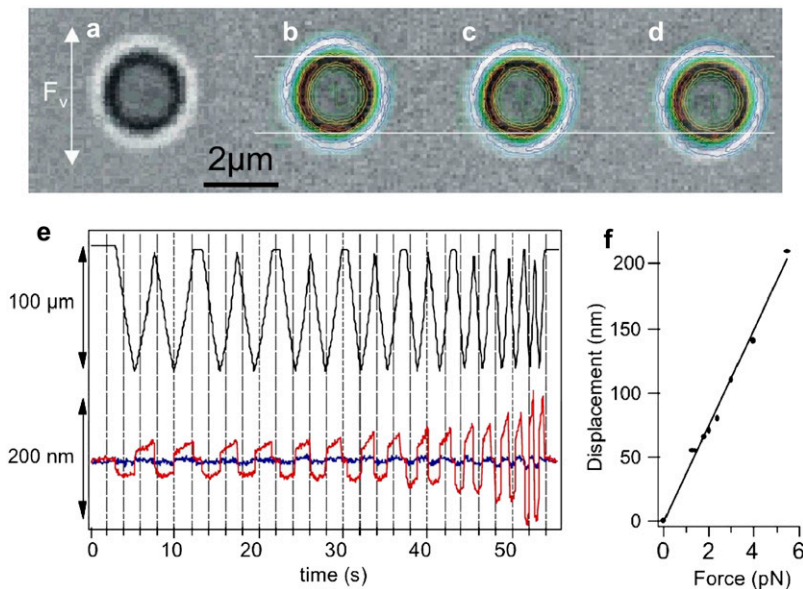


**FIGURE 2** Calibration of trap stiffness for an individual granule by video-imaging of trapped granule. (*a*) Resting position in absence of friction force. (*b–d*) During movement of experimental chamber, the granule is displaced because of friction force  $F_v$ , depending on velocity of movement. To determine displacement, image (*a*) is used as a template (contour lines) to fit images of displaced granule (*b–d*). Horizontal white lines indicate position of granule at zero force. (*e*) Displacement of the microscope stage versus time (*black trace*) and displacement of granule in the direction of stage movement (*red*) and in the perpendicular direction (*blue*). Displacement of granule is proportional to viscous drag force (*f*), calculated from velocity  $v$  of stage movement  $F = 6\pi\eta rv$ .

## Calibration image analysis

When a viscous drag force was applied, the granule was displaced from its resting position. To characterize the displacement of a granule with high precision, a video image of the trapped granule was taken at its resting position, averaging  $\sim 10$  acquired frames. To determine displacement while a force was applied, the image of the displaced granule was fitted using the image taken at resting position as a template. The fit parameters were the displacements  $\Delta x$  and  $\Delta y$ , an intensity scaling factor and a variable intensity offset to account for fluctuations in illumination. The image fitting was programmed in IGOR (WaveMetrics, Lake Oswego, OR), using only a selected region (typically,  $40 \times 40$  pixels) containing the trapped granule. The initial guesses were updated from frame to frame, according to the fit result of the preceding frame. Moreover, the region of interest was updated and recentered according to the calculated displacement. To ensure that the algorithm did not provide values reflecting spurious local minima, some image sequences were fitted not only in the order in which they were acquired, but also in reverse order. The results showed stable positions, independent of sequence order. The automatic algorithm worked well when the frame-to-frame displacements were small. When the displacement of the granule from one frame to the next was too large, the granule was “lost” by the fit program, and new manual initial guesses had to be entered.

## Measurement of tethering forces

To measure tethering forces, a granule was trapped with the fixed trap, and trap stiffness was calibrated. A second granule was subsequently trapped with the steered trap. The granules were then positioned at some distance and brought into contact for a defined time interval, using the automatic control program. The steered granule was moved in 15-nm steps by changing the frequency in the acoustic-optic deflector in 10-kHz increments. Granule-granule contact was indicated by observable movements of the granule in the fixed trap. After contact was observed, the direction of trap movement was reversed, pulling the steered granule back in 15-nm steps and 5-s or 20-s time intervals. The actual trap movement was performed at a speed of 90 nm/s. The determination of displacement of granules was similar to that for the calibration. However, the regions of interest were chosen such that the area of interest covered only  $\sim 70\text{--}80\%$  of the image of the granule, excluding the part in contact with the second granule. This method ensured that the position determination for a granule was accurate, and was not disturbed by the presence of the second granule in the image. The measured displacement was converted to applied force, using the trap-stiffness calibration. All experiments were performed at room temperature ( $22\text{--}25^\circ\text{C}$ ).

## RESULTS

### Tethering forces between isolated secretory granules

Eosinophil granules perform homotypic granule-granule fusion events in the cell (9–12) to achieve high local concentrations of the released cytotoxic proteins by formation of degranulation sacs (13–15). Isolated horse eosinophil granules were used to determine if physical tethers are formed, linking their membranes. These granules have a high refractive index, and can be manipulated using a dual optical trap. A 1064-nm laser beam was split into two beams, with one beam fixed and the other steered by acousto-optical deflectors. The two granules shown in Fig. 3 a were trapped, with the left granule in the steered trap. The steered granule was then brought into contact with the granule in the fixed trap (Fig. 3 b), pushing it slightly to the right. When the

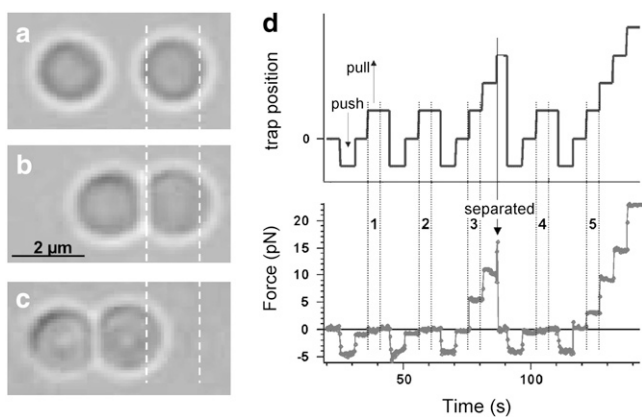


**FIGURE 3** Granule-granule tether formation. (a) Right granule is held in stationary optical trap, and left granule in a steered optical trap. (b) Steered trap brings left granule in contact with right granule, pushing right granule slightly to right. (c) When steered trap pulls left granule back, right granule is pulled away from its resting position, indicating that a tether has been formed. Vertical dashed lines are provided to aid in identifying displacement of right granule. (d) Representative tethering force experiment. Steered optical trap was moved in steps of 25 nm (top) at 5-s intervals, and the force on the granule in stationary trap is analyzed (bottom). Force on the granule in stationary trap is exerted by interaction with granule in steered trap. Numbers indicate pushing attempts to form a tether bond. Attempts 3 and 5 were successful. A tether dissociation event is indicated by arrow (*separated*).

steered granule was pulled back, the second granule was pulled to the left (Fig. 3 c), indicating that the granules were strongly tethered to each other.

To determine the applied force, the fixed trap stiffness was calibrated, applying a viscous drag force to the granule in the fixed trap (see Calibration of Trap Stiffness in Materials and Methods). A computer-controlled protocol was executed to move the granule in the steered trap stepwise at time intervals of 5 s or 20 s and increments of 15 nm, bringing it in contact with the granule in the fixed trap. After the contact time interval, the granule was pulled back, again at the same time intervals and increments as for the approach and contact. When a tether was formed, the granule in the fixed trap was pulled away from its resting position, following the steered granule. The applied forces were determined from measurements of the displacement of the granule in the stationary trap, using the trap stiffness from the calibration.

Fig. 3 d shows a representative experiment. The upper trace indicates the steered trap position, and the lower trace indicates the force applied to the granule in the fixed trap via its interaction with the granule in the steered trap. The first push and pull are indicated by arrows. Granules were pushed together with a force of  $\sim 4$  pN. This trial, as well as the second trial, did not produce a tethered state, and no force was applied to the granule in the fixed trap when the steered granule was pulled back. The third trial, however, produced a tethered state, and the pull of the steered granule exerted a force of  $\sim 5$  pN on the granule in the fixed trap. After 5 s, the steered granule was moved another step, and the force was increased to  $\sim 10$  pN. When the steered granule was moved

again, the force increased again, but shortly afterward, the granules separated (arrow in Fig. 3 d), and the granule in the fixed trap moved back to its resting position. In the fourth trial, there was again no tethering. In the fifth trial, even larger forces could be applied to the tether, and a 23-pN force was applied for 5 s without separation. When the steered granule was moved farther, the granule in the fixed trap exceeded the escape force, and the experiment was terminated. Tethering forces could be analyzed in 81 of 111 experiments, giving a total of 368 force measurements. In the remaining 30 experiments, there was either no detectable tethering interaction, or the image quality was insufficient to fit the granule positions properly. Tether separations were observed for forces between 0.3 pN (no detectable tether formation) and 38 pN.

### Force dependence of tether dissociation

The force dependence of tether-dissociation kinetics allows for a determination of tether-bond properties. For a simple bond, the dissociation rate constant  $k$  should depend on the applied force as

$$k = k_0 \exp\left(\frac{Fx}{k_B T}\right), \quad (1)$$

where  $k_0$  is the rate constant at zero force,  $F$  the applied force,  $x$  the amount the bond needs to be stretched to reach the activation energy (energy landscape maximum),  $k_B$  the Boltzmann constant, and  $T$  the absolute temperature (16). To analyze the dependence of the dissociation rate constant on the applied force, we determined for each applied force the survival time of the tether. In Fig. 4 a, a pulling force of 7.7 pN was applied for 5 s without separation. Thus, the lifetime of this tether at this force was  $\geq 5$  s. The force was then increased in the next step to 13.2 pN. The lifetime of the tether at this larger force was 4.1 s, at which time the two granules separated. Survival curves were constructed, pooling the measured tether lifetimes in three groups of applied pulling force: 1–5 pN, 5–10 pN, and >10 pN. The average applied forces in these three pools were 2.4 pN, 6.7 pN, and 15.1 pN, respectively. Fig. 4, b–d, shows the survival curves for these three pools. A single exponential fit of the function

$$N(t) = N_D \exp(-kt) + N_S \quad (2)$$

of the low-force group (Fig. 4 b) gave a dissociation rate constant  $k = 0.39 \pm 0.05 \text{ s}^{-1}$ , with  $N_D = 145 \pm 5$  and  $N_S = 163 \pm 7$ . The large value for the offset  $N_S$  represents a subset of  $\sim 50\%$  of more strongly tethered vesicles that do not dissociate within a few seconds in this force range. For larger

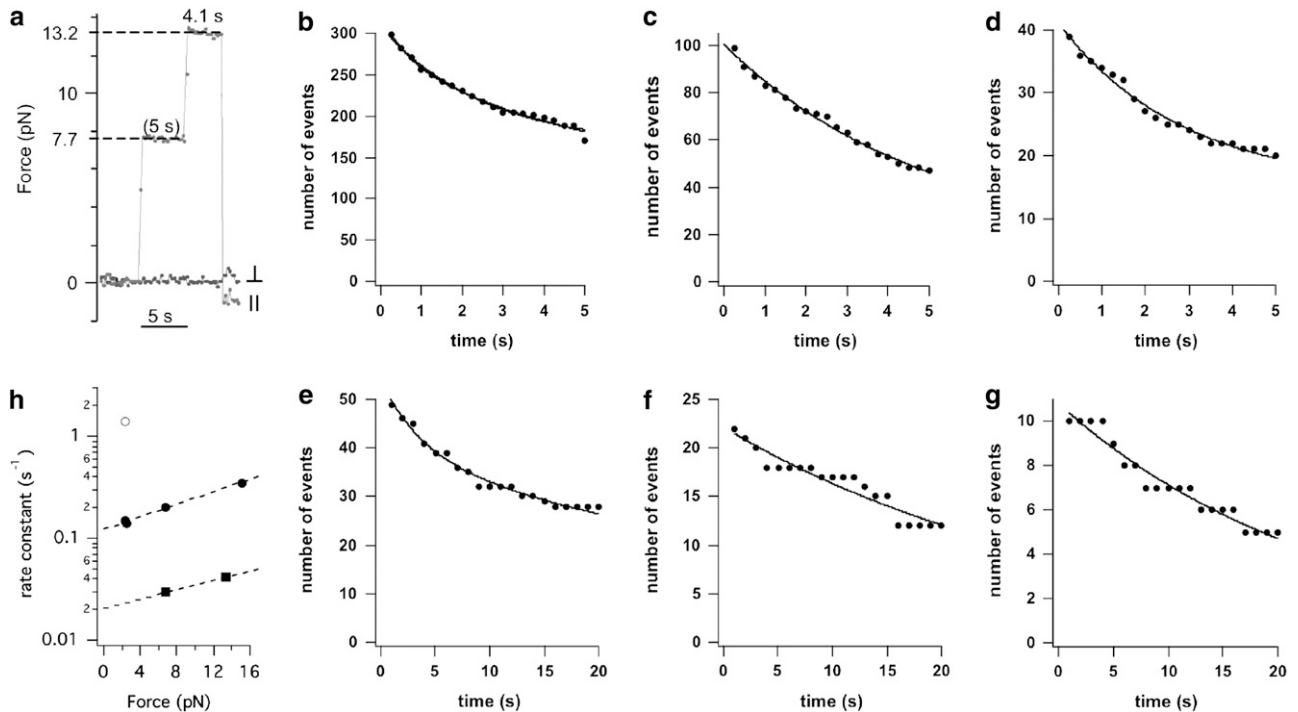


FIGURE 4 Kinetic analysis of tether disruption. (a) Trapped granule displacement converted to applied pulling force, exerted by steered tethered granule in direction of applied force (marked ||) and in perpendicular direction (marked ⊥). For each time interval, applied force was determined (horizontal dashed lines), and time was measured (as indicated) for which the granule remained tethered at this force. (b–g) Tether survival curves for 5-s time-interval protocol (b–d) and for 20-s time-interval protocol (e–g) in force groups, with mean values as indicated. Fitted curves are single exponential fits. (b) Double exponential fit is also superimposed (see text for fit details). (h) Force dependence of tether-dissociation rate constants (open circle, weak component, solid circles, intermediate main component, solid squares, strong component).

forces, a fraction of vesicles remained tethered at the end of the 5-s intervals. Combined exponential fits of these two groups indicate rate constants of  $0.20 \pm 0.04 \text{ s}^{-1}$  and  $0.35 \pm 0.05 \text{ s}^{-1}$  for the 5–10 pN and  $>10$  pN groups, respectively, and a pool of  $\sim 15$  more strongly tethered granules. This finding and the apparently rapid kinetics in the low-force group indicate heterogeneity in the tethering states, suggesting at least three distinct tethered states that dissociate at different forces and with different kinetics. The groups of Fig. 4, c and d, had mean applied forces of 6.7 pN and 15.1 pN, respectively. Substituting the corresponding average forces and rate constants in Eq. 1 provides a value for the length  $x$  by which the tethering bond needs to be stretched to reach the peak of the energy barrier

$$x = \frac{k_B T}{\Delta F} \ln \left[ \frac{k(15.1 \text{ pN})}{k(6.7 \text{ pN})} \right] = 2.7 \text{ \AA}.$$

This leads to an expected rate constant for the low-force  $k(2.5 \text{ pN}) = 0.15 \text{ s}^{-1}$ , which differs from the result of the single exponential fit. The rapid dissociation kinetics in the low-force group thus reflect disruption of a more loosely tethered state. The data in Fig. 4 b were therefore refitted, assuming a double exponential decay, with one rate constant fixed at  $0.15 \text{ s}^{-1}$ , the value expected for the more tightly tethered state. The result of this fit indicated that 53% of tethered granules dissociated with the  $0.15 \text{ s}^{-1}$  rate constant, 16% had a faster rate constant of  $1.4 \text{ s}^{-1}$ , indicating a weakly tethered state, and 31% were more strongly tethered ( $N_S$ ). The data are thus consistent with at least three different tethered states where the kinetics of the intermediate state are described by the relation

$$k = k_0 \exp \left( \frac{Fx}{k_B T} \right), \quad \text{with } k_0 \sim 0.13 \text{ s}^{-1} \quad \text{and} \quad x \sim 2.7 \text{ \AA}.$$

To test if a dissociation rate constant of  $\sim 0.15 \text{ s}^{-1}$  is indeed the main component in the 1–5-pN force group, the time intervals during which the vesicles were pushed together, as well as the time intervals to apply a particular pulling force to the tethers, were increased to 20 s. Kinetic data are shown in Fig. 4, e–g, for the same force groups as before. The average applied forces in the three groups were 2.5 pN, 6.6 pN, and 13.4 pN, respectively. A single exponential fit to the data in the 1–5-pN group (Fig. 4 e) yielded a rate constant  $k = 0.14 \pm 0.01 \text{ s}^{-1}$ , in excellent agreement with the expected main component in this force group from the data obtained with the 5-s interval. Thus, with this protocol, most of the tethers in this main group are dissociated in the low-force regime during the 20-s time interval. The data in Fig. 4, f and g, provide information on the more strongly tethered state. These data could be well-fitted, assuming an exponential decay to zero giving rate constants of  $0.030 \pm 0.002 \text{ s}^{-1}$  and  $0.042 \pm 0.002 \text{ s}^{-1}$  for the groups with 6.6 pN and 13.4 pN, respectively. For the tightly tethered state, this corresponds to values of  $x = 2.0 \text{ \AA}$  and  $k_0 = 0.022 \text{ s}^{-1}$  in Eq. 1. The data

strongly suggest at least three differently tethered states that dissociate with rate constants of  $\sim 1.4 \text{ s}^{-1}$ ,  $0.13 \text{ s}^{-1}$ , and  $0.024 \text{ s}^{-1}$  for low applied force (Fig. 4 h).

## Elastic properties of tethered granules

In eight experiments, the same position-fitting algorithm that was used for the granule in the fixed trap could also be applied to the granule in the steered trap, to reveal a linear relationship between applied force and the change in the relative distance between the tethered granules (Fig. 5). Linear regression provided the slope or reciprocal “spring constant” of the tethered vesicles, which is  $1/C_S = 13.2 \pm 1.3 \text{ nm/pN}$ . This spring constant presumably reflects the elastic properties of the tethers linking the granules, as well as the elastic properties of the granules themselves.

## DISCUSSION

### Tethering involves formation of physical links

Vesicular fusion is preceded by tethering of the vesicle to its target membrane (3,4), but it was unknown whether tethering involved physical links between the two membranes (5). The localization of chromaffin granules near the plasma membrane was studied extensively, and was found to be consistent with granules that were held at the plasma membrane by a tether  $\sim 70 \text{ nm}$  long or by a molecular cage that would restrict granule motion in a similar way (7,8,17,18). We show here that isolated eosinophil granules form physical links when brought into contact with optical tweezers. All components required for the formation of strongly tethered states

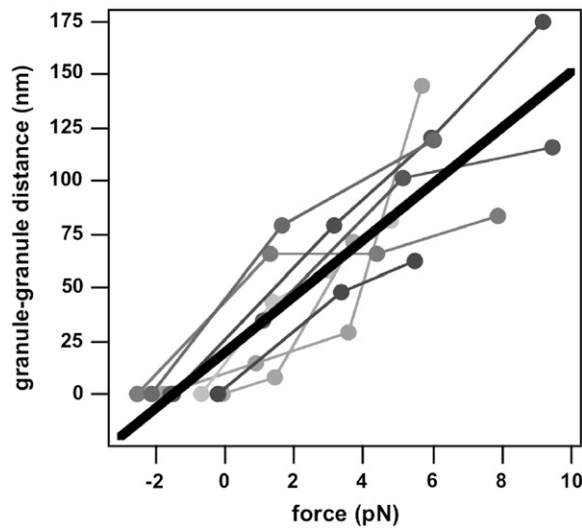


FIGURE 5 Force dependence of relative distance between two tethered granules. Measurements from same tether pair are connected by straight lines. Positions obtained when vesicles were slightly pushed against each other were arbitrarily taken as zero distance. Thick diagonal line is linear regression fit.

are retained on the membrane of the granules, and the addition of cytosol or cytosolic components is not required.

Horse eosinophil granules have a typical diameter of  $\sim 1.5 \mu\text{m}$ . Because of the small curvature, bringing them into contact creates a large contact area. When two spheres of radius  $r$  are brought into contact in the absence of applied force deforming the spheres, the radial distance  $s$  from the contact point to a point where the surfaces of the two spheres are separated by a distance  $2d$  is  $s = \sqrt{2rd - d^2}$ . If we take  $2d$  to be  $\sim 10 \text{ nm}$ , a distance that should be close enough for membrane-protein interactions to occur, a value  $s = 86 \text{ nm}$  is obtained for spheres with radius  $r = 750 \text{ nm}$ . The corresponding estimate for the contact area would thus be  $\sim 0.023 \mu\text{m}^2$ . The elastic properties of tethered granules are characterized by a reciprocal spring constant of  $\sim 13 \text{ nm/pN}$  (Fig. 5). When the two granules are pushed together by a typical force of  $2\text{--}5 \text{ pN}$ , we thus estimate that the distance between granule centers would be pushed together  $\sim 25\text{--}65 \text{ nm}$ . The contact area where two membranes are within a 10-nm distance would then increase to  $\sim 0.08\text{--}0.17 \mu\text{m}^2$ . Even the contact area of  $0.023 \mu\text{m}^2$  in the absence of granule deformation would obviously be large enough to include a very large number of proteins, and many tether-forming proteins could be present within the contact area. However, as indicated in the experiment shown in Fig. 3, formation of tethers was actually not a very frequent event. It is, of course, possible that the frequency of tether formation was low because of missing cytosolic components, and that in the presence of such components, tether formation frequency would increase markedly.

Tether formation is presumably a consequence of molecular binding events between tethering components present in the two interacting membranes. Such binding events were stochastic in nature, and when granules were brought into contact, most trials failed to produce a tethering interaction. When granules were pushed together for  $\sim 5 \text{ s}$  with a force of  $\sim 10 \text{ pN}$ , only 33% of the trials led to tether formation. This stochastic behavior suggests that under the conditions of our experiments, there is a rather limited probability of forming a tether bond, and that the experiments reflect the properties of individual tethers rather than multiple tethers or nonspecific membrane interactions. It is, however, also possible that tethering components in the granule membrane are present in clusters that could form multiple tether bonds. Variability in the number of tether bonds formed may then give rise to kinetically distinct components.

Nevertheless, it appears likely that the tethering interactions are mediated by specific protein components associated with the membranes. The molecular identity of the specific components associated with or integral to the membranes that form the granule tethers and their regulation are still unknown. Further direct measurements of tethering forces, using biochemical and molecular manipulations, will be needed to demonstrate the physiological role of the granule tethering interaction described here. We anticipate that

such experiments will provide much further insight into the molecular components and mechanisms of vesicle tethering.

### Kinetics of tether dissociation

The tether dissociations show at least three kinetically distinct components with lifetimes of  $0.7 \text{ s}$ ,  $7.7 \text{ s}$ , and  $42 \text{ s}$  at low force. Residence times of secretory granules at plasma membrane docking sites, recently determined in chromaffin cells using total internal reflection fluorescence microscopy (17), show three kinetically distinct states with similar lifetimes. The chromaffin granules arriving at the plasma membrane were grouped into three classes (visiting vesicles, with residence times  $<1 \text{ s}$ ; short-retained tethered, between  $1\text{--}10 \text{ s}$ ; and long-retained tethered,  $>10 \text{ s}$ ). Our experiments suggest three states with tether lifetimes of  $0.7 \text{ s}$ ,  $7.7 \text{ s}$ , and  $42 \text{ s}$ , which correspond well to the three states reported previously (17). The chromaffin granules with residence times  $<1 \text{ s}$  were considered unrestrained (17). Our measurements indicate that tethering interactions with lifetimes  $<1 \text{ s}$  involving physical links do occur, and raise the possibility that some of the visitor granules in chromaffin cells may actually form a tether with lifetimes  $<1 \text{ s}$ . The good agreement of tether lifetimes observed for eosinophil granule interactions with the granule residence times at docking sites reported for intact chromaffin cells (17) suggests that the tethering interactions characterized here represent the properties of physiologically relevant tethers. They indicate that the mechanism keeping secretory granules in place at their target membrane involves physical links that are formed by membrane components, rather than mechanisms involving the cytoskeleton.

### Biophysical properties of tethered granules

The force dependence of tether-dissociation kinetics yielded values of  $x$  at  $\sim 2.7 \text{ \AA}$  and  $\sim 2.0 \text{ \AA}$  by which tethering bonds must be stretched to reach the transition state for intermediate and strongly tethered states, respectively. The physical meaning of these values, however, should be interpreted with caution. The tether bond may very well not be a simple bond, but may have rather complex properties and, as discussed above, even the presence of multiple tether bonds cannot be excluded, in particular for the more tightly tethered states. Therefore, the values for  $x$  should be considered apparent  $x$  values.

The  $x$  values are remarkably close to those reported for single Fv-chain antibody binding (19). In contrast to the measurements of antibody-antigen interactions using atomic force microscopy (19), our experiments were performed using optical trapping, and involved elastic elements in the tether and/or granules such that tethered granules behaved as if connected via an elastic spring with spring constant  $C_S = 0.076 \pm 0.008 \text{ pN/nm}$ . However, the forces applied to granules will nevertheless appear at the critical bond linking two granules. The similarity of  $x$  values obtained here with those obtained for antibody-antigen interactions may be taken as evidence that

our experiments reveal the properties of individual tether complexes. However, definitive proof for this hypothesis must await experiments with defined isolated tethering proteins.

The work  $W$  to stretch an elastic spring with spring constant  $C_S$  by distance  $l$  is  $W = 1/2Fl = 1/2F^2/C_S$ . The data in Fig. 3 include forces up to  $\sim 9$  pN stretching the tether by  $\sim 120$  nm, which corresponds to a mechanical work of  $W \sim 5.3 \times 10^{-19}$  Nm or  $\sim 130 k_B T$ . However, only a small fraction of this work will actually stretch the tether bond. The kinetic analysis indicated that for the most tightly tethered state, the tether bond may be stretched by only  $\sim 2$  Å to reach the peak of the activation energy. The largest force we applied to tethered granules was 38 pN, which reduced the activation energy for tether dissociation by  $7.6 \times 10^{-21}$  Nm, which is  $\sim 2 k_B T$ . Given the slow dissociation kinetics of the tightly tethered state, the activation energy is presumably much larger, indicating that in the experiments described here, the tether bond was stretched only slightly.

If a granule is tethered to its target membrane via an elastic element, thermal motion would be expected, depending on the stiffness of the elastic element, such as for particles in an optical trap. The mean-squared displacement  $\langle \Delta s^2 \rangle$  of these fluctuations would thus be expected to be  $\langle s^2 \rangle = k_B T/C_S$  or  $\sim 50$  nm $^2$ , corresponding to root mean-square position fluctuations of  $\sim 7$  nm. Although this value is much smaller than the 70-nm tether length obtained from imaging the jittering motion of chromaffin granules at the plasma membrane in the  $x/y$  plane (7,8,17,18), it is rather close to the rapid jittering motion in the direction perpendicular to the plasma membrane, i.e.,  $\sim 4$  nm (18). It is thus possible that the rapid jittering motion of secretory granules perpendicular to the plasma membrane is attributable in part to the elastic properties of vesicle tethers.

## SUPPLEMENTARY MATERIAL

To view all of the supplemental files associated with this article, visit [www.biophysj.org](http://www.biophysj.org).

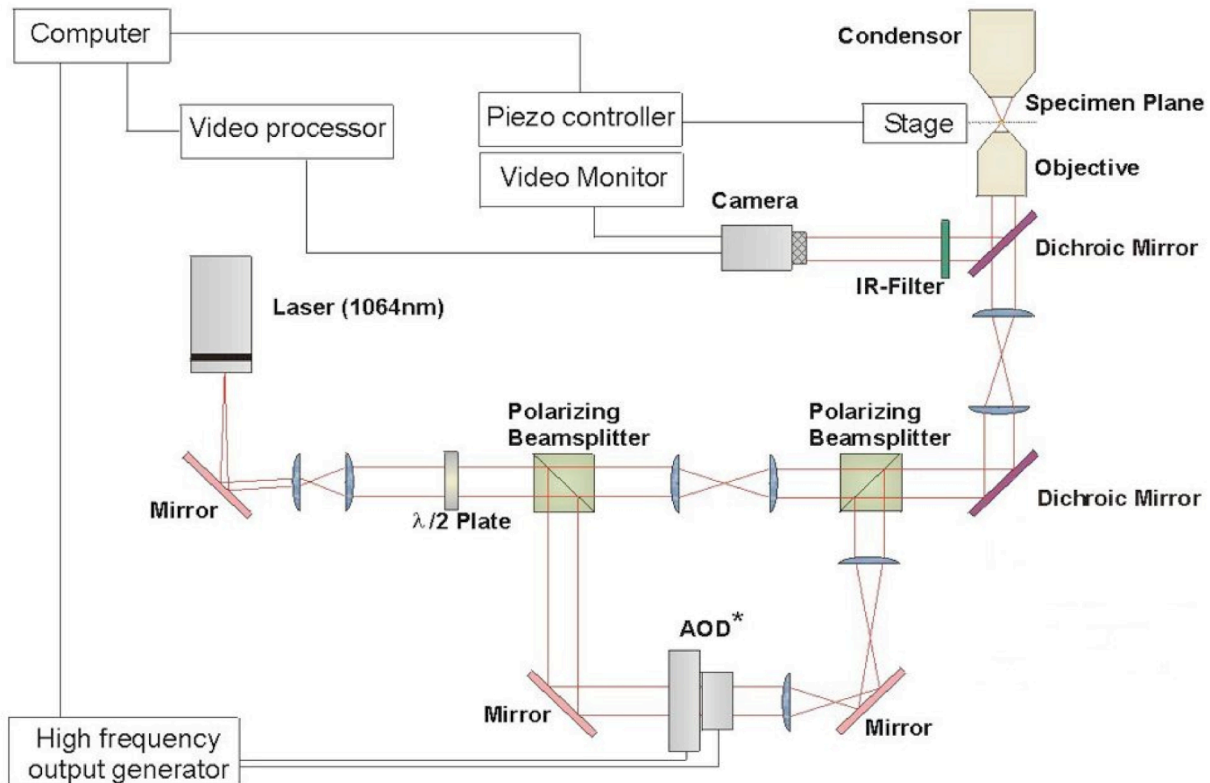
We thank Carol Collyer, director of Equine Research Services (Cornell University), for supplying horse blood; Jonathan King and Joan Lenz for improvement of cell isolation; and Guillermo Alvarez de Toledo, Gregor Dernick, and Ismail Hafez for helpful discussions.

This work was supported by the Human Frontier Science Program (grant RG0227/98), the National Institutes of Health (grant R01 NS38200), the Nanobiotechnology Center (an STC program of NSF Agreement No. ECS-9876771), and the Secretaría de Estado de Universidades, Investigación, y Desarrollo of Spain.

## REFERENCES

1. Lindau, M., and G. Alvarez de Toledo. 2003. The fusion pore. *Biochim. Biophys. Acta*. 1641:167–173.
2. Pfeffer, S. R. 1999. Transport-vesicle targeting: tethers before SNAREs. *Nat. Cell Biol.* 1:E17–E22.
3. Pfeffer, S. 2001. Vesicle tethering factors united. *Mol. Cell.* 8:729–730.
4. Cai, H., K. Reinisch, and S. Ferro-Novick. 2007. Coats, tethers, Rabs, and SNAREs work together to mediate the intracellular destination of a transport vesicle. *Dev. Cell.* 12:671–682.
5. Haas, A. K., and F. A. Barr. 2007. COP sets TRAPP for vesicles. *Dev. Cell.* 12:326–327.
6. Steyer, J. A., H. Horstmann, and W. Almers. 1997. Transport, docking and exocytosis of single secretory granules in live chromaffin cells. *Nature*. 388:474–478.
7. Steyer, J. A., and W. Almers. 1999. Tracking single secretory granules in live chromaffin cells by evanescent-field fluorescence microscopy. *Biophys. J.* 76:2262–2271.
8. Johns, L. M., E. S. Levitan, E. A. Shelden, R. W. Holz, and D. Axelrod. 2001. Restriction of secretory granule motion near the plasma membrane of chromaffin cells. *J. Cell Biol.* 153:177–190.
9. Scepe, S., and M. Lindau. 1993. Focal exocytosis by eosinophils: compound exocytosis and cumulative fusion. *EMBO J.* 12:1811–1817.
10. Hafez, I., A. Stolpe, and M. Lindau. 2003. Compound exocytosis and cumulative fusion in eosinophils. *J. Biol. Chem.* 278:44921–44928.
11. Hartmann, J., S. Scepe, I. Hafez, and M. Lindau. 2003. Differential regulation of exocytotic fusion and granule-granule fusion in eosinophils by Ca<sup>2+</sup> and GTP analogs. *J. Biol. Chem.* 278:44929–44934.
12. Scepe, S., and M. Lindau. 1997. Exocytotic competence and intergranular fusion in cord blood-derived eosinophils during differentiation. *Blood*. 89:510–517.
13. Henderson, W. R., E. Y. Chi, A. Jörg, and S. J. Klebanoff. 1983. Horse eosinophil degranulation induced by the ionophore A23187: ultrastructure and role of phospholipase A<sub>2</sub>. *Am. J. Pathol.* 111:341–349.
14. Tai, P.-C., and C. J. F. Spry. 1981. The mechanisms which produce vacuolated and degranulated eosinophils. *Br. J. Haematol.* 49:219–226.
15. Scepe, S., R. Moqbel, and M. Lindau. 1994. Compound exocytosis and cumulative degranulation by eosinophils and its role in parasite killing. *Parasitol. Today*. 10:276–278.
16. Bell, G. I. 1978. Models for the specific adhesion of cells to cells. *Science*. 200:618–627.
17. Toonen, R. F., O. Kochubey, H. de Wit, A. Gulyas-Kovacs, B. Konijnenburg, J. B. Sorensen, J. Klingauf, and M. Verhage. 2006. Dissecting docking and tethering of secretory vesicles at the target membrane. *EMBO J.* 25:3725–3737.
18. Allersma, M. W., M. A. Bittner, D. Axelrod, and R. W. Holz. 2006. Motion matters: secretory granule motion adjacent to the plasma membrane and exocytosis. *Mol. Biol. Cell.* 17:2424–2438.
19. Schwesinger, F., R. Ros, T. Strunz, D. Anselmetti, H. J. Guntherodt, A. Honegger, L. Jermutus, L. Tiefenauer, and A. Pluckthun. 2000. Unbinding forces of single antibody-antigen complexes correlate with their thermal dissociation rates. *Proc. Natl. Acad. Sci. USA*. 97:9972–9977.

## Supplemental Online Material



Schematic diagram illustrating the experimental set-up configuration for the dual optical traps. The solid lines represent the light path; the dashed lines represent controlled devices. A diode pumped neodymium doped orthovanadate (Nd:YVO<sub>4</sub>) infrared-laser emitting at 1064nm (Millenia IR, Spectra-Physics) was used as the light source for optical trapping. The beam was split by a polarizing beam splitter (PB1). The relative intensities of the two beams could be controlled by a rotatable λ/2 waveplate (Model 5540, New Focus, CA) that rotates the linear polarization vector. One beam was steered by a pair of acousto-optical deflectors (AODs) (DTD-274HA6, IntraAction) controlled with a PC via a frequency synthesizer card (DVE-40, IntraAction Corp., IL). The AODs are located in a plane conjugate to the microscope objective's back focal plane (BFP). Therefore, changes in the laser beam's angle at the AOD's do not produce changes in position at the objective's BFP. However, changes in beam angle in the BFP result in changes of position in the object plane and thus the trap position can be conveniently controlled by the AODs. The steered beam was combined with the fixed beam by a polarizing beam splitter PB2 and both were directed into the objective (100x 1.3 NA oil immersion Plan-Neofluar, Zeiss) via the epifluorescence port of the inverted microscope. The total power of the fixed and steered beam before the objective was typically 80 and 200 mW, respectively.

# Photoactivated Release of Cargo from the Cavity of Polyelectrolyte Capsules to the Cytosol of Cells

A. Muñoz Javier,<sup>†,‡,§,∇</sup> P. del Pino,<sup>†,‡,∇</sup> M. F. Bedard,<sup>§</sup> D. Ho,<sup>||</sup> A. G. Skirtach,<sup>§</sup>  
G. B. Sukhorukov,<sup>⊥</sup> C. Plank,<sup>‡</sup> and W. J. Parak<sup>\*,†,||,#</sup>

Fachbereich Physik, Philipps Universität Marburg, Marburg, Germany, Technische Universität München, Germany, Max-Plank-Institut für Kolloid- und Grenzflächenforschung, Golm, Germany, Center for Nanoscience, Ludwig Maximilians Universität München, Munich, Germany, Queen Mary, University of London, London, U.K., and Wissenschaftliches Zentrum für Materialwissenschaften, Philipps Universität Marburg, Marburg, Germany

Received July 30, 2008. Revised Manuscript Received September 4, 2008

Polyelectrolyte capsules with metal nanoparticles in their walls and fluorescently labeled polymers as cargo inside their cavity were prepared. Capsules were ingested by living cells with no uncontrolled release of the cargo upon the incorporation process. Photoinduced heating of the metal nanoparticles in the capsule walls lead to rupture of the capsule walls, and the polymeric cargo was released to the whole cytosol. Viability tests demonstrate that opening of capsules at moderate light intensities does not impair the cellular metabolism, whereas capsule opening at high light intensities ultimately leads to cell death.

## Introduction

For the time-resolved investigation of stimulated reactions inside living cells, it is desirable to be able to control the release of the stimulant that triggers the reaction.<sup>1,2</sup> A prominent example is caged calcium. Calcium is administered to cells while it is caged in a chelating complex. Upon a flash of light, calcium is released from the chelating complex by photolysis and can trigger Ca-dependent processes inside the cell.<sup>3</sup> To our knowledge, such light-controlled remote release of molecules so far has been demonstrated only for some relatively small molecules, such as Ca<sup>2+</sup>,<sup>4</sup> Mg<sup>2+</sup>,<sup>5</sup> nitric oxygen (NO),<sup>6</sup> glutamate,<sup>7</sup> or adenosin triphosphate (ATP).<sup>8</sup>

In this manuscript, we describe an alternative container that allows for light-controlled local release of (macro)molecules inside and outside cells. For this purpose, the molecule to be released is put as cargo into the cavity of polyelectrolyte capsules that have been assembled by layer-by-layer deposition.<sup>9</sup> The cargo molecule is enclosed and trapped inside the capsules, as it is too big to be able to diffuse through the polyelectrolyte network forming the walls of the capsules. The walls of the capsules are functionalized with metal nanoparticles. Upon

illumination with light, the metal nanoparticles will get heated, which leads to ruptures in the capsule walls and, finally, to release of the cargo out of the cavity of the capsule.

In the presented concept, stimulants are embedded in the cavity of capsules functionalized with metal nanoparticles in their walls. When cells are incubated with capsules, the capsules are internalized by the cells and remain in endosomal/lysosomal/phagosomal compartments. As the stimulants are embedded inside the capsules, they cannot trigger any reaction inside the cells. Upon irradiation of selected individual capsules with a light pointer and thus heating of the metal particles, the capsule wall and also the local membrane of the compartment in which the capsules are stored break, and the stimulant is released to the cytosol where it can trigger cellular reactions.

Several steps of this concept have been already demonstrated previously by several groups. The assembly of functionalized polyelectrolyte capsules has been pioneered by the group of Möhwald.<sup>9</sup> Nowadays, several procedures have been described to load the cavity of such capsules with (macro)molecules<sup>10,11</sup> and to functionalize their walls with colloidal nanoparticles, such as gold or silver nanocrystals.<sup>12–17</sup> Capsules with metal particles in their wall could be opened upon laser irradiation as a result

\* Corresponding author. E-mail: wolfgang.parak@physik.uni-marburg.de.

† Fachbereich Physik, Philipps Universität Marburg.

‡ Technische Universität München.

§ Max-Plank-Institut für Kolloid- und Grenzflächenforschung.

|| Ludwig Maximilians Universität München.

⊥ Queen Mary College.

# Wissenschaftliches Zentrum für Materialwissenschaften, Philipps Universität Marburg.

∇ These authors contributed equally to this study.

(1) Kaplan, J. H.; Somlyo, A. P. *Trends Neurosci.* **1989**, 12(2), 54–59.  
(2) Ellis-Davies, G. C. R. *Nat. Methods* **2007**, 4(8), 619–628.  
(3) Gurney, A. M.; Charnet, P.; Pye, J. M.; Nargeot, J. *Nature* **1989**, 341(6237), 65–68.

(4) Momotake, A.; Lindegger, N.; Niggli, E.; Barsotti, R. J.; Ellis-Davies, G. C. R. *Nat. Methods* **2006**, 3(1), 35–40.

(5) Ellis-Davies, G. C. R. *Cell Calcium* **2006**, 39(6), 471–473.

(6) Yip, K. P. *Am. J. Physiol.: Regul. Integr. Comp. Physiol.* **2005**, 289(2), R620–R626.

(7) Callaway, E. M.; Katz, L. C. *Proc. Natl. Acad. Sci. U.S.A.* **1993**, 90(16), 7661–7665.

(8) Yamakawa, M.; Goldman, Y. E. *J. Gen. Physiol.* **1991**, 98(4), 657–679.

(9) Sukhorukov, G. B.; Donath, E.; Davis, S.; Lichtenfeld, H.; Caruso, F.; Popov, V. I.; Möhwald, H. *Polym. Adv. Technol.* **1998**, 9(10–11), 759–767.

(10) Sukhorukov, G. B.; Möhwald, H. *Trends Biotechnol.* **2007**, 25(3), 93–98.  
(11) Kreft, O.; Muñoz Javier, A.; Sukhorukov, G. B.; Parak, W. J. *J. Mater. Chem.* **2007**, 17, 4471–4476.

(12) Rivera Gil, P.; del Mercato, L. L.; del Pino, P.; Munoz Javier, A.; Parak, W. J. *Nano Today* **2008**, 3(3–4), 12–21.

(13) Wang, D.; Rogach, A. L.; Caruso, F. *Nano Lett.* **2002**, 2(8), 857–861.

(14) Skirtach, A. G.; Dejugnat, C.; Braun, D.; Susha, A. S.; Rogach, A. L.; Sukhorukov, G. B. *J. Phys. Chem. C* **2007**, 111(2), 555–564.

(15) de Geest, B. G.; Sanders, N. N.; Sukhorukov, G. B.; Demeester, J.; Smedt, S. C. *D. Chem. Soc. Rev.* **2007**, 36, 636–649.

(16) de Geest, B. G.; Skirtach, A. G.; De Beer, T. R. M.; Sukhorukov, G. B.; Bracke, L.; Baeyens, W. R. G.; Demeester, J.; de Smedt, S. C. *Macromol. Rapid Commun.* **2007**, 28(1), 88–95.

(17) Johnston, A. P. R.; Cortez, C.; Angelatos, A. S.; Caruso, F. *Curr. Opin. Colloid Interface Sci.* **2006**, 11(4), 203–209.

(18) Skirtach, A. G.; Antipov, A. A.; Shchukin, D. G.; Sukhorukov, G. B. *Langmuir* **2004**, 20(17), 6988–6992.

(19) Radt, B.; Smith, T. A.; Caruso, F. *Adv. Mater.* **2004**, 16(23–24), 2184–2189.

(20) Angelatos, A. S.; Radt, B.; Caruso, F. *J. Phys. Chem. B* **2005**, 109, 3071–3076.

(21) Skirtach, A. G.; Dejugnat, C.; Braun, D.; Susha, A. S.; Parak, W. J.; Möhwald, H.; Sukhorukov, G. B. *Nano Lett.* **2005**, 5(7), 1371–1377.

of the temperature increase of the metal particles upon light absorption.<sup>18–22</sup> Capsules have also been demonstrated to be spontaneously internalized by a huge variety of cells.<sup>23–26</sup> Finally, capsules with metal nanoparticles in their walls that had been internalized by cells could be opened inside the cells upon laser irradiation, and fluorescent cargo was released from the cavity of the capsules.<sup>27</sup>

Although the concept of light-activated release of (macro)molecules from the cavity of polyelectrolyte capsules inside living cells has been already demonstrated,<sup>27</sup> some basic questions of this technique have not yet been addressed. Most prominently missing is information about the fate of the released cargo and about possible impairment of cells upon the release process. Concerning cell impairment, it has been demonstrated by other groups that local heat generation by irradiated Au nanoparticles can kill surrounding cells, and this effect (called “hyperthermia”) is used on purpose for the destruction of cancerous tissue.<sup>28</sup> For the controlled opening of capsules therefore, control of the light-generated heat is crucial in a way that the metal particles are heated enough to open the capsules but not enough to kill the cells. When capsules have been internalized by cells, they are stored in intracellular vesicular structures (endosomal, lysosomal, and phagosomal compartments).<sup>26</sup> This means that, effectively, the cargo inside the cavity of the capsules is also encapsulated by intracellular membrane-surrounded compartments. Heating of the metal nanoparticles in the walls of internalized capsules upon light illumination thus might lead to two different scenarios. Partial disintegration of the capsule walls due to the heat created in the nanoparticles<sup>18,19</sup> would release the cargo into the endosomal, lysosomal, and phagosomal compartments to which the capsules are confined. However, the heat transferred by the Au nanoparticles to the surrounding environment might not only open the walls of the capsules but might additionally cause local ruptures in the membrane of the surrounding vesicular compartment in which the capsules are trapped. Opening also the membrane around the capsules would lead to a release of the cargo from the cavity of the capsules to the cytosol. Although release of the cargo to the cytosol is preferred compared to release in confined endosomal, lysosomal, or phagosomal structures, the question arises whether cells would tolerate such harsh interference.

In this report, experimental evidence is presented that it is possible to release macromolecular cargo (in particular, dextran) from the cavity of internalized capsules into the cytosol of cells, without impairing cell viability on the time scale of hours.

## Materials and Methods

**Capsule Synthesis.** Polyelectrolyte multilayers were assembled on SiO<sub>2</sub> (4.78 μm) by the layer-by-layer deposition technique using solutions of polydiallyl dimethyl ammonium chloride (PDADMAC;

(22) Radziuk, D.; Shchukin, D. G.; Skirtach, A.; Mohwald, H.; Sukhorukov, G. *Langmuir* **2007**, 23(8), 4612–4617.

(23) Muñoz Javier, A.; Kreft, O.; Alberola, A. P.; Kirchner, C.; Zebli, B.; Susha, A. S.; Horn, E.; Kempfer, S.; Skirtach, A. G.; Rogach, A. L.; Rädler, J.; Sukhorukov, G. B.; Benoit, M.; Parak, W. J. *Small* **2006**, 2(3), 394–400.

(24) de Geest, B. G.; Vandenbroucke, R. E.; Guenther, A. M.; Sukhorukov, G. B.; Hennink, W. E.; Sanders, N. N.; Demeester, J.; de Smedt, S. C. *Adv. Mater.* **2006**, 18, 1005–1009.

(25) Cortez, C.; Tomaskovic-Crook, E.; Johnston, A. P. R.; Radt, B.; Cody, S. H.; Scott, A. M.; Nice, E. C.; Heath, J. K.; Caruso, F. *Adv. Mater.* **2006**, 18(15), 1998–2003.

(26) Muñoz Javier, A.; Kreft, O.; Semmling, M.; Kempfer, S.; Skirtach, A. G.; Bruns, O.; del Pino, P.; Bedard, M. F.; Rädler, J.; Käs, J.; Plank, C.; Sukhorukov, G.; Parak, W. J. *Advanced Materials*, in press.

(27) Skirtach, A. G.; Javier, A. M.; Kreft, O.; Köhler, K.; Alberola, A. P.; Möhwald, H.; Parak, W. J.; Sukhorukov, G. B. *Angew. Chem., Int. Ed.* **2006**, 45, 4612–4617.

(28) Huang, X.; Jain, P.; El-Sayed, I.; El-Sayed, M. *Lasers Med. Sci.* **2007**, 23(3), 217–228.

2 mg/mL, 0.5 M NaCl) and (2 mg/mL, 0.5 M NaCl), starting from PDADMAC. Following the deposition of the third layer, the particles were resuspended in a solution of gold sulfide/gold nanoparticles ( $\sim 1 \times 10^{15}$  NPs/mL).<sup>29–31</sup> The final multilayer composition was PDADMAC/PSS/PDADMAC/AuS<sub>2</sub>(PSS/PDADMAC)<sub>2</sub>/PSS [PSS = poly(styrene sulfonate)]. The sacrificial SiO<sub>2</sub> template was dissolved in hydrofluoric acid (HF, 0.3 M), leaving a polyelectrolyte hollow shell that was sedimented and resuspended in water several times to remove any traces of acid. Solutions of labeled dextran ( $M_w = 10$  kDa, 0.5 mg/mL) conjugated to red (Alexa Fluor 594) or blue fluorophores (Cascade Blue) were prepared. Encapsulation of fluorescently labeled dextran was accomplished by first incubating a solution of microcapsules and the desired labeled dextran, and second, by heating the solution to 64 °C for 20 min.<sup>32</sup> Exchanging the supernatant with water by carefully sedimenting and resuspending the capsules in water yielded filled capsules, whereby the fluorescently labeled dextran remained inside the wall of polyelectrolyte layers.<sup>11</sup> The geometry of the resulting capsules with dextran in their cavity and AuS<sub>2</sub> particles embedded in their walls is depicted in Figure 1. A more detailed protocol can be found in the Supporting Information.

**Capsule Internalization by Living Cells.** A total of  $3 \times 10^4$  MDA-MB-435s breast cancer cells (ATTC, USA) per square centimeter were seeded on culture dishes (22.1 cm<sup>2</sup>, #93060 from TPP) and were incubated with capsules ( $48 \times 10^4$  capsules per cm<sup>2</sup>, 16 capsules per cell) for about 24 h. After a washing step to remove free capsules, the culture dish was attached to the x-y-z-stage of the microscope, and cells with incorporated capsules were identified using phase contrast. Si substrates with native silicon oxide surface were attached to the bottom surface of the culture dishes, as they led to better phase contrast images of cells than plane glass substrates.

**Microscopy Setup with Laser for Capsule Exposure.** A 100 mW laser (830 nm wavelength) was coupled to an upright microscope (Axitotech, Zeiss, 40× objective) leading to a focused light spot of a few micrometers in diameter in the image plane. By changing the operation voltage of the laser, the resulting power of the focused light spot could be tuned in the range of 0–31 mW. Note that this range corresponds to intensities measured in the image plane after coupling the laser to the microscope and therefore, because of the optics used for the coupling, these values are attenuated in respect to the intensities measured directly after the diode laser. The microscope was equipped with filters for blue, green, and red fluorescence and with phase contrast. A beam splitter was used to allow for simultaneous excitation of the capsules via the laser and recording the phase contrast and fluorescence images of cells and capsules. A typical series of images was obtained in the following sequence. In-phase contrast mode cells with incorporated capsules were moved with an x-y-z-stage to the focus of the microscope. The laser was then turned on and moved with a separate x-y-stage so that selected capsules were exposed to the laser light. Directly after light-exposure of the capsules, a phase contrast image and images of all channels of fluorescence were recorded. For time-resolved series, phase contrast and fluorescence images were recorded at different points of time. A detailed sketch of the setup is shown in the Supporting Information.

**Viability Test.** In order to probe the cell viability upon opening of capsules, the LIVE/DEAD Viability/Cytotoxicity Assay Kit (from Molecular Probes Invitrogen, catalog number L3224) was applied. This test was either added before or directly after laser-exposure of the capsules (0.1 μL/mL calcein AM 4 mM in anhydrous dimethyl sulfoxide (DMSO) and 0.5 μL/mL ethidium homodimer-1 2 mM in DMSO/H<sub>2</sub>O 1:4 (v/v)). According to the manufacturer, the kit comprises two probes: calcein AM and ethidium homodimer (EthD-1). Calcein AM is a fluorogenic esterase substrate that is hydrolyzed by esterases to a green-fluorescent product (calcein) and thus, green

(29) Zhou, H. S.; Honma, I.; Komiyama, H.; Haus, J. W. *Phys. Rev. B* **1994**, 50(16), 12052–12056.

(30) Averitt, R. D.; Sarkar, D.; Halas, N. J. *J. Phys. Rev. Lett.* **1997**, 78(22), 4217–4220.

(31) Norman, T. J.; Grant, C. D.; Magana, D.; Zhang, J. Z.; Liu, J.; Cao, D. L.; Bridges, F.; Van Buuren, A. *J. Phys. Chem. B* **2002**, 106(28), 7005–7012.

(32) Köhler, K.; Möhwald, H.; Sukhorukov, G. B. *J. Phys. Chem. B* **2006**, 110(47), 24002–24010.

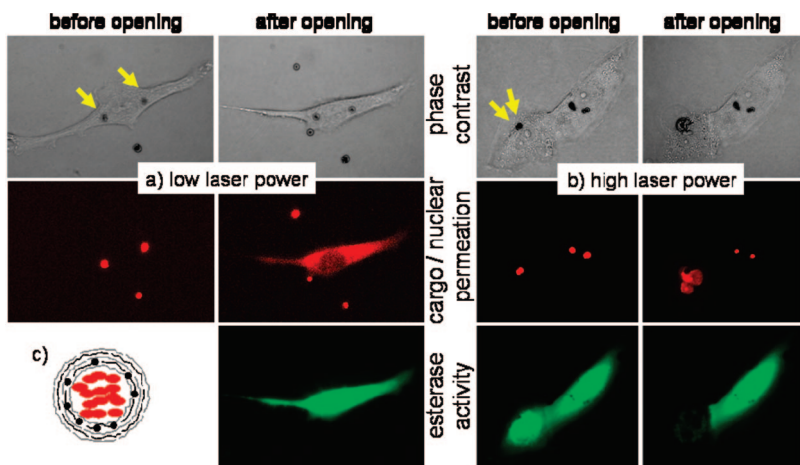


**Figure 1.** Cargo release and viability/cytotoxicity experiments with capsules filled with red Alexa Fluor 594 dextran as cargo and  $\text{AuS}_2$  particles embedded in their walls. Capsules were illuminated with (a) low laser power (2.3 mW), the minimum power needed to open the capsules, and (b) high laser power (31 mW), the maximum power output reachable with the laser diode used in these experiments. Phase contrast images show cells that have incorporated capsules (yellow arrows) before and after laser illumination. Red fluorescence images show the cargo release and the nuclear permeation (Ethd-1) in cases where capsules trapped in cells were excited with low laser power and high laser power, respectively. In the case of high power illumination, permeation of the cell membrane leads to loss of fluorescent cargo by diffusion out of the cell. Green fluorescence images indicate decrease of esterase activity in cells where capsules were excited with high and low laser power, respectively. (c) Sketch of the geometry of capsules with Alexa Fluor 594 dextran (red ellipsoids) in their cavity and  $\text{AuS}_2$  particles (black circles) embedded in their walls.

fluorescence is an indicator of cells that have esterase activity as well as an intact membrane to retain the esterase products. EthD-1 is a high-affinity, red-fluorescent nucleic acid stain that is only able to pass through the compromised membranes of dead cells and thus red fluorescence located in the nucleus is an indicator of dead cells.

## Results

The ability to mechanically disintegrate metal nanoparticle-functionalized capsules depends on the applied power of the light spot. Whereas light spots of 0.7 mW power were typically not sufficient to rupture the wall of capsules, light spots of more than around 2.3 mW power typically lead to deformation and disintegration of the illuminated capsules (see the Supporting Information for images). For the opening exposure times, less than 1 s were sufficient. Control experiments in which cells were exposed up to 30 min with a light spot of 31 mW power (maximum power output with the setup used) did not show any effect on cells (see the Supporting Information for images).

For experiments with cells, two ranges of laser spot power were used. In the first sets of experiments, the power of the laser spots was chosen to be just sufficient to open the capsules inside cells (see Figure 1). Typically, after opening of the capsules, a release of the fluorescence labeled dextran to the whole cytosol of the cells was observed. The nuclei of the cells were not stained with the fluorescence labeled dextran. Application of the viability/cytotoxicity kit demonstrated continuous esterase activity of the cells (visible via green fluorescence) after capsule opening for the investigated time periods of up to 2 h after capsule opening. Also no red fluorescence due to ethidium homodimer-1 staining of the nuclei was observed. This corresponds to the data obtained with untreated cells to which the viability/cytotoxicity kit had been applied for up to 2 h (see Supporting Information). From these data we conclude that the dextran has been released to the cytosol, which consequently must have involved local ruptures in the membranes of the vesicular structures in which the internalized capsules are trapped inside the cells. The viability/cytotoxicity data also suggest that in many, there is no impairment of the viability of the cells within the investigated time of up to 2 h after capsule opening. However, we have to point out that in 30% of our experiments opening of capsules with a laser spot

of 2.3 mW also impaired cells, as indicated by decreasing esterase activity and ethidium homodimer-1 staining of the nuclei.

The situation changes for higher laser power (31 mW). In this case, after capsule opening, changes in the cell morphology can be frequently observed with phase contrast microscopy. Also the data of the viability/cytotoxicity kit show decreasing esterase activity and ethidium homodimer-1 staining of the nuclei after capsule opening (see the Figure 1). Similar data were found in 100% of the experiments, and they clearly suggest cell death upon light-exposure of the capsules. Whether cell death originates directly from the heat released of the illuminated metal-particles (analogue to hyperthermia) or indirectly from mechanical rupture of the cellular organelles around the capsules cannot be determined from our data.

Similar data were obtained for capsules loaded with red and blue fluorescent dextran (see Figure 2). Although in the case of red fluorescence-labeled dextran, there is a spectral overlap between the red fluorescent cargo of the capsules and the red fluorescent ethidium homodimer-1 staining of the nucleus, release of cargo and nuclear staining of dead cells could be distinguished. This is due to the fact that cargo released to the cytosol does not stain the nucleus, whereas ethidium homodimer-1 exclusively stains the nucleus of dead cells. In the case of capsules with blue fluorescent cargo, the problem of spectral overlap was circumvented in first place.

These data suggests that there is a window in the applied laser power in which the heat created by illuminated capsules is large enough to locally disintegrate the walls of capsules and surrounding membranes to release the cargo of the capsules to the cytosol, but too low to cause cell death. Though the range of applicable laser power is reproducible, it significantly varies with the batch of capsules used. Inhomogeneities in capsule preparation (presumably due to different metal particle densities in the capsule walls) sometimes lead to destruction of cells after capsule opening with low laser power. However, the majority of cells (70%) in which capsules have been opened with low laser power (2.3 mW) are not impaired by the opening procedure. It can be pointed out that thermal energy input in the system is proportional to concentration of nanoparticles, their size and incident laser power.<sup>21</sup> Therefore, the laser intensity range in

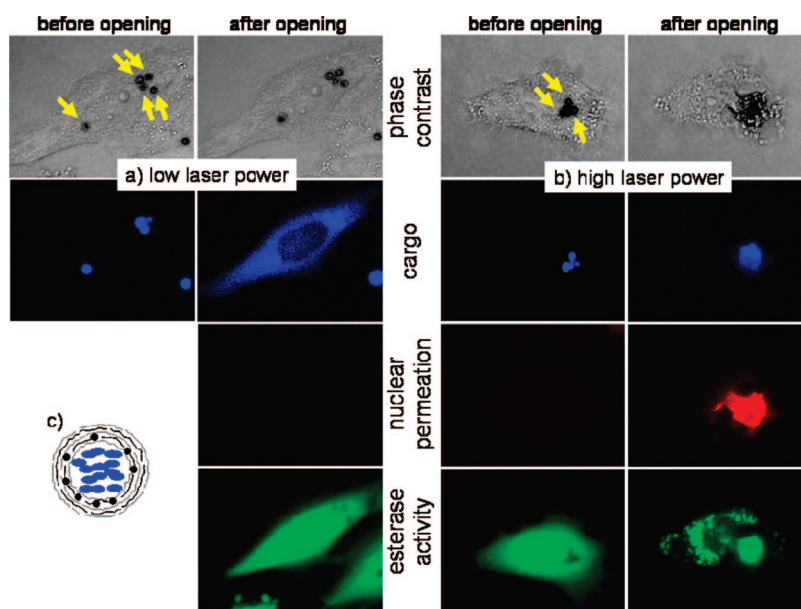


**Figure 2.** Cargo release and viability/cytotoxicity experiments with capsules filled with blue Cascade Blue dextran as cargo and AuS<sub>2</sub> particles embedded in their walls. Capsules were illuminated with (a) low laser power (2.3 mW), the minimum power needed to open the capsules, and (b) high laser power (31 mW), the maximum power output reachable with the laser diode used in these experiments. Phase contrast images show cells that have incorporated capsules (yellow arrows) before and after laser illumination. Blue fluorescence images display the fate of capsule's cargo at high and low laser power. Red fluorescence images show nuclear permeation (Ethd-1) in the case where capsules trapped in cells were excited with high laser power, whereas at low laser power, no nuclear permeation can be detected. Green fluorescence images indicate decrease of esterase activity in cells where capsules were excited with high and low laser power respectively. (c) Sketch of the geometry of capsules with Cascade Blue dextran (blue ellipsoids) in their cavity and AuS<sub>2</sub> particles (black circles) embedded in their walls.

which cells survive can be tuned by the combination of these parameters.

## Discussion

Photoactivated release of labeled dextran from the cavity of polyelectrolyte capsules to the cytosol of living cells works with good reproducibility and reliability as demonstrated in this work. Although this is exciting from the technological point of view, arguably dextran is not the most interesting molecule to be released inside cells. Therefore the question arises to which extent the technology platform described here can be transferred for releasing other molecules. Certainly release will not work for very small molecules, as, due to their size, they would diffuse through the porous polymer network out of which the capsule walls are formed. Molecules of high enough molecular weight can be loaded into the cavity of capsules either with a co-precipitation method with calcium carbonate<sup>10,11</sup> or by regulating capsule permeability via pH or temperature.<sup>10,32</sup> Certainly different cargo molecules might require modified encapsulation strategies, but the encapsulation of cargo in the capsule cavity clearly is not limited to dextran. Because the polyelectrolyte layers which are forming the capsule walls are highly charged, release of charged macromolecules might also be affected by charge interaction between the cargo and the capsule walls. Interaction of the cargo with the capsule walls also may be the reason why, in many experiments, incomplete release of the (dextran) cargo to the cytosol was observed (see Supporting Information). Quantitative release, i.e., always the same amount of cargo released upon the

opening of one capsules, thus seems very problematic. Also the details of the physics of the opening process of the capsules inside cells are not fully understood yet. Clearly the conditions (e.g., required exposure intensity) depend on the metal particle concentration and distribution inside the walls of the capsules. In order to obtain capsules with more precisely defined conditions for opening the capsule, synthesis has to be made more homogeneous. At any rate, the experiments presented here demonstrate that macromolecules can also be released with flash photolysis using polymer capsules as carrier system. While the system reported here is designed for the opening of individual capsules in single cells, the approach could be generalized for opening a large number of capsules inside tissue. In this case, light-induced heating of Au particles in the shell of the capsules could be replaced by heating of magnetic particles in the shell of the capsules with high frequency fields.

**Acknowledgment.** The authors are grateful to Dr. Loretta del Mercato and Dr. Pilar Rivera Gil for helpful discussions. This work was supported by the European Union (sixth framework STREP project Nanointeract) and by the German Research foundation (DFG, Forschungsschwerpunkt SPP 1313).

**Supporting Information Available:** More technical information about the experiments and images of capsule opening are shown. This information is available free of charge via the Internet at <http://pubs.acs.org>.

LA802448Z

## LEBENSLAUF

### Persönliche Daten.

Dominik Ho

Arcisstraße 40, 80799 München

Geboren am 14.10.1981 in Heidelberg

### Ausbildung.

- **Doktor rer. nat. (Physik)**, voraussichtlich Oktober 2009  
Ludwig-Maximilians-Universität, Lehrstuhl Gaub, München
- **Master of Engineering (Engineering Physics)**, 2006  
Cornell University, College of Engineering, Ithaca
- **Vordiplom (Physik)**, 2003  
Universität Heidelberg, Fakultät der Physik, Heidelberg
- **Abitur**, 2001  
Gymnasium Überlingen, Überlingen

### Stipendien & Preise.

- IDK Nano-Bio-Technologie, Doktorandenstipendium, 2006-2009
- MBPW - Gewinner der Ideas Stage, 2009
- Heidelberg-Cornell Exchange Fellow, 2004-2005
- Fulbright Fellow, 2004-2005
- e-fellows, 2004-2009

### Forschung.

- **Doktorand**, Professor Hermann E. Gaub  
Ludwig-Maximilians-Universität, München, 2006-heute
- **Gastwissenschaftler**, Professor Peter B. Dervan  
California Institute of Technology, Pasadena, Sommer 2007
- **Wissenschaftlicher Mitarbeiter**, Professor Manfred Lindau  
Cornell University, Ithaca, 2004-2006
- **Werkstudent**, Professor Augusto Mangini  
Ruprecht-Karls-Universität, Heidelberg, 2003-2004

### **Arbeitserfahrung.**

- **Praktikant**, EADS ST - Department Life Sciences  
Friedrichshafen, Februar-April 2004
- **Praktikant**, Senovation AG  
Ludwigshafen, Juni-September 2001

### **Lehre.**

- **Tutor**, Grundpraktikum Experimentalphysik, LMU, SS 2009
- **Tutor**, Thermodynamik und Elektrodynamik, LMU, SS 2008
- **Tutor**, Biophysik Praktikum, LMU, WS 2006, SS 2007, WS 2007
- **Tutor**, Biophysik Praktikum, Cornell University, WS 2004, WS 2005

### **Eingeladene Vorträge.**

- Randox Laboratories, Belfast, UK, 5.8.2009  
“Sandwich ELISA Biochips: Solution to the Cross-Reaction Problem”
- Modern Topics in Bio-Soft Matter, TUM, München, 16.7.2009  
“Force-driven separation of short double stranded DNA:  
Theory and Experiment”
- Biophysics Colloquium, Cornell University, Ithaca, NY, 28.8.2007  
“The molecular force balance: lab-on-a-chip force spectroscopy”

## DANKSAGUNG

An dieser Stelle möchte ich mich bei all denjenigen bedanken, die mich in meinen drei Jahren am Lehrstuhl Gaub begleitet und diese Zeit so lehrreich, kollegial, kameradschaftlich und unvergesslich gestaltet haben.

Mein größter Dank gilt natürlich Hermann Gaub, der mich in all meinen wissenschaftlichen Vorhaben mit Rat und Tat angeleitet und unterstützt hat. Er versteht es wie kein zweiter eine angenehm kreative und gleichzeitig produktive Atmosphäre an seinem Lehrstuhl zu schaffen.

Insbesondere bedanke ich mich bei meiner Familie, für die anhaltende Unterstützung während meines Studiums in Heidelberg und Ithaca sowie meiner Promotion in München: Allen voran meinen Eltern, Beate und Hans, denen ich so vieles verdanke. Meiner Schwester Sirikit, meinen Cousins Jennifer und Daniel, meinem Onkel Tony und meiner Tante Emmie, die mir immer Vorbild und Inspiration waren. Meinen Großeltern Wolfgang, Alice und Liselotte für viel Zuspruch und Unterstützung.

Des Weiteren danke ich in chronologischer Reihenfolge des Aufeinandertreffens:

Meinen Freunden aus Überlingen, Philipp, Daniel, Nicole, Isabella und Alexander, für die anhaltende Freundschaft und Unterstützung in allen Lebenslagen.

Christian Albrecht dafür, dass er mich mit viel Einsatz in seine Arbeit am DNA-Kraftsensor eingewiesen hat, für Schweinebauch beim Koreaner und Nürnberger Lebkuchen.

Martin Benoit, für geschmackvolle Musikeinlagen am Abend, seinen ständigen Einsatz für den Lehrstuhl und die gute Stimmung, die er verbreitet, und dafür, dass er und Tom meine Überschwemmung im Chemielabor beseitigt haben!

Sabine, Angelika, Verena und Tom dafür, dass sie den Lehrstuhl am Laufen halten.

Wolfgang Parak für die abendliche Lo-Studenten Besuche, humoristische Lehrstuhlgeschichten und viele hilfreiche Ratschläge.

Almudena und Pablo für spanische Abende bis 6 Uhr morgens.

Julia Sedlmair für nette Abende am Gärtnerplatz, Pommes-Schranke, Kuchen und dafür, dass wir trotz großer Distanz immer noch gut befreundet sind.

Julia Zimmermann für die schöne Farbgebung in unserem Büro, eine tolle Gartenparty und die Daten des DNA-Separationsartikels.

Hermann Gumpf für entspannte Jazz-, Scotch- und Japanabende.

Elias Puchner für viele lehrreiche Diskussionen, eine angenehme Zeit in Venedig und Boston, das Korrekturlesen meines DNA-Separationsartikels und Fluppen.

Matthias Erdmann für eine klasse Zeit am Lehrstuhl und in Venedig, fortwährende moralische Unterstützung, Läufe im Englischen Garten und viele Espressos im Spoon.

Stefan Kufer für eine schöne Zeit in Edmonton und ermutigende Worte.

Franz Weinert für eine klasse Zeit am Lehrstuhl, Poker-, Starcraft- Volleyball- und Pizzaabende. Viel Erfolg in Pasadena!

Katja Falter für die produktive Zeit während der Diplomarbeit und Verpflegung mit Schweinebraten, Käsespätzle, Kuchen und vielem mehr.

Philip Severin für seinen Einsatz an den experimentellen Aufbauten und guten Zeiten in der Vega-Bar.

Florian Dehmelt für eine super Zusammenarbeit während seiner Diplomarbeit, dem Gewinn des MBPW-Ideas-Stage und dafür, dass er mir viel über das Verfassen von Artikeln beigebracht hat.

Uta Steinbach für eine produktive Zeit während ihrer Diplomarbeit und ihre angenehme und ausgeglichene Art.

Ralf David für unterhaltsame Mittagessen, Kaffeepausen, Fußballspielen, gutes Essen auf der Weihnachtsfeier und dafür, dass er Sicherheit und Ordnung in unser Chemielabor gebracht hat.

Hans Heus für Käse aus Holland, lehrreiche Diskussionen, Ratschläge und das Korrekturlesen meiner Artikel.

Christian Dose und Peter Dervan für eine erfolgreiche Zusammenarbeit, einen interessanten Aufenthalt in Pasadena und eine super Feier im Strandhaus in Laguna Beach.

Jan Vogelsang für eine klasse Zeit am Lehrstuhl, lehrreiche Diskussionen, Pizza-, Poker-, Starcraft- und Shishaabende.

Philip Tinnefeld für hilfreiche Diskussionen und das Korrekturlesen unseres Aptamerartikels.

Stephan Heucke für Fußballspielen im Englischen Garten und gute Feiern.

Carolin und Stefan dafür, dass sie jetzt in München sind. Schön, bekannte Gesichter aus Heidelberg wieder zu sehen!

Jana für einen wunderschönen Urlaub auf Sylt, ihren Humor und anhaltende Unterstützung während des Schreibens meiner Doktorarbeit.